Structure, Function, and Application of Bacterial ABC Transporters

Thesis by

Chengcheng Fan

In Partial Fulfillment of the Requirements for the degree of

Doctor of Philosophy

CALIFORNIA INSTITUTE OF TECHNOLOGY

Pasadena, California

2020

(Defended May 5th, 2020)

Chengcheng Fan

ORCID: 0000-0003-4213-5758

ACKNOWLEDGMENTS

I would like to thank my PhD advisor, Prof. Doug Rees, for his research guidance, tireless patience and unconditional support over the past seven years. I am also grateful that he is always holding me to the highest standard, always encourages me to pursue further and push harder. Not only he gives me a lot of freedom to pursue new avenues of my research projects, he is also a very thoughtful and critical scientist, making sure the researches are done with quality and integrity. More importantly, he saw my interest in X-ray crystallography before I even realized. He not only taught me crystallography himself, but also sent me to workshops and synchrotrons to learn from the experts. I am forever thankful for everything he did for me!

I'm also very appreciative of my committee: Profs. Bil Clemons, Shu-ou Shan and David Chan, for their thoughtful advices and helpful discussions over the years. I would also like to thank Prof. Henry Lester for a very fruitful collaboration, and for always being caring and supportive, and Prof. Pamela Bjorkman for her enlightenments and support. I could not be more grateful for my undergraduate advisor, Prof. Jim Bowie, for his encouragement and support to go to graduate school. Without him, I will not be in Caltech at the first place.

I'm very thankful for all the mentors I had since undergraduate studies. They together shaped my approaches to science, especially to membrane proteins. Thank you to Dr. Heedeok Hong, Dr. Rachna Ujwal, and Dr. Jonas Lee, for the tremendous amount of training on membrane proteins, from expression to crystallization. I want to thank Dr. Jens Kaiser for all his advices, encouragements and support, for tirelessly teaching me crystallography, and for always being a great listener. I would also like to thank the Rees lab members for the happy working environment, especially Dr. Nadia Herrera and Dr. Phong Nguyen for their friendships, discussions and support, and Dr. Limei Zhang for her encouragement and support. I also really appreciate all the computer support from Welison Floriano. Thank you, Phoebe Ray, Allen Lee, and Jeff Lai for keeping everything in good order.

I'm very grateful of having two of the most amazing and awesome BMB classmates, Dr. Ferdinand Huber and Dr. Belinda Wenke. I am more than thankful for their friendship and endless support. I must also thank Grigor Varuzhanyan, for his friendship and for always reminding me not to work too hard. I am very thankful for Dr. Haoqing Wang, Dr. Shuai Wang, Zhi Yang, Ruohan Wang, Ailiena Maggiolo, Dr. Nadia Riera, Dr. Aye Myat Thinn, Dr. Hyun Gi Yun, and Dr. Kyu Hyun Lee, for their friendship and moral support. Besides, I really appreciate all the help and support from the members of the Bjorkman, Chan, Clemons, Hoelz, Jensen, and Lester labs.

All the crystallographic work could not be done without the help from beamline scientists from SSRL, APS and ALS. I am very thankful for their support during all of my data collections. I would also like to express my gratitude to two of my favorite crystallographers, Dr. Paul Adams and Dr. Jim Pflugrath. Thank you for not only teaching me crystallography, but also for having me as TA for the Cold Spring Harbor Laboratory X-ray Methods course; I truly appreciate that. The single-particle cryoEM work would not have been done without the help from Dr. Haoqing Wang and Dr. Andrey Malyutin. I am more than thankful for their support during the cryo-EM sample preparation and data collection.

Most importantly, my endless thanks go to my parents, Sue Dai and Dajun Fan, for all of their encouragement, love, wisdom, and support. Their caring, fearless, hardworking, strong, and thoughtful personalities shaped who I am today. I am forever learning from them. I am also grateful to my little brother, Shibo Fan, always being bright, happy, and kind. Although he always teases me for going to school for almost my whole life, I know he is very proud of his sister. I feel very thankful, lucky, and proud to be in this family!

ABSTRACT

The ATP-binding cassette (ABC) transporter of mitochondria (Atm1) mediates iron homeostasis in eukaryotes, while the prokaryotic homolog from *Novosphingobium aromaticivorans* (*Na*Atm1) can export glutathione derivatives and confer protection against heavy metal toxicity. To establish the structural framework underlying the *Na*Atm1 transport mechanism, we determined eight structures by X-ray crystallography and single particle cryo-EM in distinct conformational states, stabilized by individual disulfide crosslinks and nucleotides. As *Na*Atm1 progresses through the transport cycle, conformational changes in transmembrane helix 6 (TM6) alter the glutathione binding site and the associated substrate binding cavity. Significantly, kinking of TM6 in the post-ATP hydrolysis state stabilized by $MgADPVO_4$ eliminates this cavity, precluding uptake of glutathione derivatives. The presence of this cavity during the transition from the inward-facing to outward-facing conformational states, and its absence in the reverse direction, thereby provides an elegant and conceptually simple mechanism for enforcing the export directionality of transport by *Na*Atm1. One of the disulfide crosslinked *Na*Atm1 variants characterized in this work retains significant glutathione transport activity, suggesting ATP hydrolysis and substrate transport by Atm1 may involve a limited set of conformational states with minimal separation of the nucleotide binding domains in the inward-facing conformation.

The ATPase kinetic data was fit to a non-essential activator model with expansion to two substrate binding sites. While the structural data suggests that MgATP and GSSG bind to distinct states, outward- and inward-facing conformations, respectively, and hence might be expected to exhibit negative cooperativity, the kinetic data support a more complex interplay and also the importance of lipid molecule presence. How GSSG binding stimulates ATPase activity remains an open question and highlights the importance of the still elusive ternary complex with both MgATP and GSSG bound to *Na*Atm1.

Besides the structural and functional characterizations of the ABC exporter, *Na*Atm1, we additionally determined crystal structures of the repurposed periplasmic binding protein (PBP) from the ABC importer system. These PBPs are designed with circularly permutated GFP to act as biosensors to sense the concentrations of smoking cessation drugs and neurotransmitters under cellular conditions. The crystal structures determined for the nicotine and acetylcholine biosensors not only revealed the key residues in ligand binding, but also demonstrated similar ligand induced conformational changes as seen in other PBPs by following the Venus-flytrap mechanism.

PUBLISHED CONTENT AND CONTRIBUTIONS

1. Fan, C., Kaiser, J.T. and Rees, D.C. "A structural framework for the unidirectional transport by a bacterial ABC exporter." *In review*.

   C.F. participated in the conception of the project, solved and analyzed the crystal and single-particle cryo-EM structures, performed all the biochemical experiments, and participated in the writing of the manuscript.

2. Fan, C. and Rees, D.C. "A kinetic model for the ATPase stimulation of the ABC exporter *Na*Atm1 by the transported substrate GSSG." *In preparation*.

   C.F. participated in the conception of the project, performed all the biochemical experiments, and participated in the writing of the manuscript.

3. Fan, C. and Rees, D.C. "Crystal structure of the *Escherichia coli* transcription termination factor Rho." *Submitted*.

   C.F. participated in the conception of the project, solved and analyzed the crystal structure, and participated in the writing of the manuscript.

4. Fan, C.*, Nichols, A.*, Muthusamy, A., Bera, K., Shivange, A.V., Luebbert, L., Gao, F., Beatty, Z., Unger, E., Marvin, J.S., Tian, L., Looger, L.L, Rees, D.C., and Lester, H.A. "A family of iDrugSnFRs, nearly modular fusion of evolved periplasmic binding proteins and circularly permutated GFP for subcellular and supercellular dynamical measurements of drugs." *In preparation*.

   C.F. solved and analyzed the crystal structures and participated in the writing of the manuscript.

5. Borden, P.M., Zhang, P., Shivange, A.V., Marvin, J.S., Cichon, J., Dan, C., Podgorski, K., Figueiredo, A., Novak, O., Tanimoto, M., Shigetomi, E., Lobas, M.A., Kim, H., Zhu, P.K., Zhang, Y., Zheng, W.S., Fan, C., Wang, G., Xiang, B., Gan, L., Zhang, G., Guo, K., Lin, L., Cai, Y., Yee, A.G, Aggarwal, A., Ford, C.P., Rees, D.C., Dietrich, D, Khakh, B.S., Dittman, J.S., Gan, W., Koyama, M., Jayaraman, V., Cheer, J.F., Lester, H.A., Zhu, J.J. and Looger, L.L. "A fast genetically encoded fluorescent sensor for faithful *in vivo* acetylcholine detection in mice, fish, worms and flies." *In review*.

   C.F. solved the crystal structure of acetylcholine bound PBP domain of iAChSnFR.

TABLE OF CONTENTS

Chapter 1

INTRODUCTION

1.1 ATP-Binding Cassette (ABC) Transporter Overview

ABC transporters were first identified in bacterial uptake systems in the 1970s during the examination of energy coupling for amino acid transport (Berger and Heppel 1974). Later studies on different bacterial systems revealed a family of proteins that have highly homologous ATP-binding subunits (Higgins et al. 1986). Studies at the time on P (permeability)-glycoprotein (Pgp/ABCB1) also revealed that it contained similar nucleotide-binding domains as the bacterial ATP-binding subunits in nutrient uptake, suggestive of a common evolutionary ancestor (Chen et al. 1986). The name "ATP-Binding Cassette (ABC) transporters" was later acquired during the prediction of the tertiary structure for the nucleotide binding domain (NBD) of those bacterial uptake systems, and the eukaryotic multidrug transporter P-glycoprotein and CFTR (cystic fibrosis transmembrane conductance regulator) (Hyde et al. 1990). By then, it was known that ABC transporters are membrane transport proteins that are ubiquitously present in all domains of life with important roles in the translocation of a variety of substrates through coupling to the binding and hydrolysis of ATP (Higgins 1992).

Among ABC transporters, the ABC importers are present only in prokaryotes and they are involved in importing ions, amino acids, and nutrients, such as iron, molybdate, methionine, arabinose, vitamin B_{12}, etc. In contrast, ABC exporters are not only present in prokaryotes; they are also found in eukaryotes. The exporters are associated with key roles in multidrug resistance, fatty acid trafficking and mitochondrial iron homeostasis by exporting toxic substances and large macromolecules to the outside of the cell or a cellular compartment (Higgins 1992, Biemans-Oldehinkel, Doeven, and Poolman 2006, Davidson et al. 2008, Rees, Johnson, and Lewinson 2009, Theodoulou and Kerr 2015, Locher 2016).

Despite the different transport directionalities between importers and exporters, they share the same characteristic core domains, including two variable transmembrane domains (TMDs) embedded in the lipid bilayer that provides the translocation pathway and sometimes the substrate binding sites for exporters, and two highly conserved soluble nucleotide-binding domains (NBDs) located on the inside of the cell or compartment, providing the binding sites for ATP (Figure 1a). The catalytic domain of the conserved NBDs consists of a conserved P-loop, also known as the Walker-A motif (GxxxxGK(S/T), where x is any residue), associated with the stabilization of the phosphate group during ATP binding; a Walker-B motif (hhhhDE, where h is a hydrophobic residue), providing a glutamate residue for catalyzing the hydrolysis of ATP; an H-motif providing a histidine residue to stabilize the transition state for ATP hydrolysis; an aromatic residue in A-loop that stabilizes the adenine ring of bound ATP; and an ABC signature motif (LSGGQ) that, together with its dimeric NBD counterpart, is important in binding ATP (Figure 1b) (Rees, Johnson, and Lewinson 2009, Locher 2016). Besides the core domains, the ABC importer systems have additional periplasmic binding proteins that are essential for substrate delivery to the cognate transporter, as well as additional cytoplasmic regulatory domains (Biemans-Oldehinkel, Doeven, and Poolman 2006, Davidson et al. 2008, Rees, Johnson, and Lewinson 2009). Similar to the importers, there may also be extra domains fused to the NBD and/or TMD of ABC exporters with additional functions (Biemans-Oldehinkel, Doeven, and Poolman 2006).

In humans, there are 48 different ABC transporters that are classified into seven subfamilies (ABCA-ABCG). Transporters in the ABCA subfamily are thought to be important in lipid trafficking, and mutations can lead to genetic diseases such as Tangier disease and age-related macular degeneration (Vasiliou, Vasiliou, and Nebert 2009). ABCB subfamily transporters are involved in multidrug resistance (Borst and Schinkel 2013) and mitochondrial iron homeostasis (Pondarre et al. 2006). ABCC family members are not only important in multidrug resistance (Cole 2014), but also important in ion conductance (Kleizen et al. 2020, Babenko and Bryan 2003). Transporters in the ABCD subfamily are primarily found in peroxisome, endoplasmic reticulum and lysosome with roles in lipid trafficking; mutations in ABCD1 can lead to the buildup of fatty acids in the brain, leading to X-linked adrenoleukodystrophy (Hlavac and Soucek 2015). In contrast, members in the ABCE and ABCF subfamilies lack the transmembrane domains, and they are thought to promote interferon activity and inflammatory activities, respectively (Vasiliou, Vasiliou, and Nebert 2009). Lastly, the ABCG transporters are important in the sterol transport and multidrug resistance (Moitra et al. 2011) and mutations are associated with diabetes (ABCG1) (Schou et al. 2012) and sitosterolemia (ABCG5 and ABCGG8) (Yoo 2016).

1.2 ABC Importers

As recently as the early 2000s, structural determinations of membrane proteins were still considered to be extremely challenging. Instead of obtaining the entire structure of a transporter, efforts were first made to structurally characterize the soluble NBDs, along with any soluble transport-relevant protein, including the periplasmic binding proteins (PBPs) that provide the binding site for substrates. As the PBP carries a variety of substrates from small ions to large macromolecules, they present more substrate-specific biochemical information than the NBDs. The first structure of PBP determined was the structure of an arabinose binding protein at 5 Å resolution in 1976 (Phillips et al. 1976) and finally at 1.7 Å resolution in 1984 (Quiocho and Vyas 1984) with the crystallographic data first collected in 1974 (Quiocho et al. 1974). Following the groundbreaking work done in structurally characterizing the PBPs for amino acids (Saper and Quiocho 1983), ions (Pflugrath and Quiocho 1985) and sugars (Quiocho and Vyas 1984) by the Quiocho group, structures of many PBPs has been determined since then (Figure 2).

PBPs generally consist of two lobes that can adopt open and closed conformations. To bind substrate in the closed conformation, the two lobes in the open conformation would have to come together; this substrate-induced conformational change of bringing the two lobes together is commonly described as the Venus-flytrap mechanism (Felder et al. 1999), which has been seen in many PBPs (Sack, Saper, and Quiocho 1989, Kandt, Xu, and Tieleman 2006, Gonin et al. 2007, Aktas et al. 2011). The PBPs were initially classified into two classes in 1999 based on sequence alignments and overall structures (Fukami-Kobayashi, Tateno, and Nishikawa 1999). With more available structures in 2010, the PBPs were further classified into six different groups solely based on the alignments of the 3D structures (Berntsson et al. 2010). The classification information is as follows: i) Group 1 PBPs are important in metal binding and they have an α-helix serving as the hinge between the two lobes. ii) Group 2 PBPs mainly bind to carbohydrates and their N and C-termini are located in separate lobes. iii) Group 3 PBPs are generally bigger than other PBPs with molecular weight ranging from 55 to 70 kDa, and they bind to different substrates including oligopeptides, nickel ions, and arginine. The extra domain is thought to extend the binding cavity for oligopeptide binding. iv) Group 4 PBPs' hinge regions consist of two strands with 4-5 amino acids long, and their substrate ranges from carbohydrates, polyamines, tetrahedral oxyanions, to ferrous or ferric iron. v) Group 5 PBPs are part of the tripartite ATP-independent periplasmic transporter, they have distinctive β-strand orders and a long helix spanning over both lobes. vi) Group 6 PBPs can bind small anions and amino acids, such as nitrate and glycine betaine (Berntsson et al. 2010).

Although PBPs could bind similar substrates, such as metals, amino acids and carbohydrates, the overall structures of these PBPs are rather diverse. Examples of the similarities and differences in the structures of PBPs are presented in Figure 2. In the mononuclear metal ion binding proteins, the zinc-binding protein (Figure 2a) (Lee et al. 1999) has a long helix over the binding protein, but this long helix is not observed in the iron-binding protein (Figure 2b) (Koropatkin et al. 2007). The structures of the oxyanion binding proteins, including sulfate (Figure 2c) (He and Quiocho 1993), phosphate (Figure 2d) (Ledvina et al. 1998) and molybdate (Figure 2e) (Hu et al. 1997), are also structurally different from the mononuclear ion binding proteins (Figure 2ab). Similarly, structural differences are also evident in the various amino acid binding proteins, including the leucine/isoleucine/valine-binding protein (Figure 2f) (Trakhanov et al. 2005), the cysteine-binding protein (Figure 2g) (Muller et al. 2005), the histidine-binding protein (Figure 2h) (Yao, Trakhanov, and Quiocho 1994) and the methionine-binding protein (Figure 2i) (Nguyen et al. 2015). In addition to the ion and amino acid binding proteins, the sugar binding proteins, including the arabinose-binding protein (Figure 2j) (Quiocho and Vyas 1984), ribose-binding protein (Figure 2k) (Bjorkman et al. 1994), maltose-binding protein (Figure 2l) (Quiocho, Spurlino, and Rodseth 1997), and chitin-binding protein (Figure 2m) are also structurally distinct. Interestingly, an oligopeptide-binding protein (Figure 2n) (Levdikov et al. 2005) shares a similar overall structure as the chitin-binding protein (Figure 2m). The ectoine-binding protein is structurally distinct from all the other binding proteins with the long bending helix spanning over the whole binding protein (Figure 2o) (Lecher et al. 2009). Lastly, the vitamin B_{12}-binding protein (Figure 2p) (Borths et al. 2002) shares similar an overall structure with the zinc-binding protein (Figure 2a), and based on the recent classification (Berntsson et al. 2010), these two binding proteins belong to the same group.

So far, there have been four types of structurally characterized ABC importers with type I shown in Figure 3abcd, type II shown in Figure 3ef, type III shown in Figure 3g and type IV shown in Figure 3h. The classification information is summarized in Table 1. The first structure determined of an ABC importer was the *Escherichia coli* vitamin B_{12} transporter $BtuC_2D_2$ in the substrate and nucleotide free conformation (Locher, Lee, and Rees 2002), and it is now classified as a type II importer. $BtuC_2D_2$ consist of two TMDs, BtuC, and two NBDs, BtuD. BtuC consist of 10 TMHs per TMD, together a full transporter has 20 TMHs in total. The highly conserved NBD, BtuD is also in a dimeric form, where the Walker A-motif of BtuD is in close proximity to the ABC signature motif of the dimeric BtuD counterpart (Locher, Lee, and Rees 2002) and this positioning of the BtuD dimer is important in the binding of the two molecules of ATP. During substrate translocation, the vitamin B_{12}-binding protein, BtuF, delivers the vitamin B_{12} molecule to the $BtuC_2D_2$ transport system, leading to $BtuC_2D_2F$ complex formation (Figure 3e) (Hvorup et al. 2007). Other than $BtuC_2D_2F$, the *Burkholderia cenocepacia* hemin transporter, $BhuU_2V_2T$ (Figure 3f) (Naoe et al. 2016), the *Haemophilus influenzae* metal transporter, HI1470/1471 (Pinkett et al. 2007) and the heme transporter, $HmuU_2V_2$ from *Yersinia pestis* all share the same type II importer fold (Woo et al. 2012) (Table 1).

In comparison to type II importers, the type I importer fold consists of less TMHs in total. The first type I importer fold was revealed in the structure of a molybdate ABC importer $ModB_2C_2$ from *Archaeoglobus fulgidus* complexed with its periplasmic binding protein, ModA (Figure 3a) (Hollenstein, Frei, and Locher 2007). Besides the highly conserved NBD, the TMD (ModB) of $ModB_2C_2$ only consists of six TMHs and a full transporter consists of 12 TMHs in total. Later structures on the *Sphingomonas* alginate transporter system revealed a similar fold with six TMHs per TMD (Figure 3ab) (Maruyama et al. 2015). Interestingly, there are also heterodimeric type I importers. One example is the *Escherichia coli* maltose transport system. The two distinct TMDs (MalF and MalG) contain eight and five TMHs, respectively (Figure 3c) (Oldham et al. 2007). Lastly, the TMDs in the *Escherichia coli* methionine transport system consist of five TMHs per

TMD (Figure 3d) (Kadaba et al. 2008, Nguyen et al. 2018) and this same fold was also seen in an arginine/histidine transporter, $ArtQ_2N_2$ from *Caldanaerobacter subterraneus* (Yu et al. 2015).

In contrast, type III importers present a different case where one TMD contains eight helices with five TMHs and three additional helices almost diagonally spanning over the membrane, and a second TMD containing seven helices with four TMHs as shown in the cobalt energy-coupling factor transporter, CbiMNQO from *Rhodobacter capsulatus* (Figure 3g) (Bao et al. 2017). A similar type III importer fold has also been reported for the folate ECF transporter from *Lactobacillus brevis* (Wang et al. 2013) and the cobalamin ECF transporter from *Lactobacillus delbrueckii* (Santos et al. 2018). Besides type I, II, and III importer folds, the type IV importer fold has only been seen with the *Escherichia coli* siderophore importer, YdtPQ. Each TMD of YdtPQ consists of six TMHs (Figure 3h) and each TMD is fused to a NBD, forming a half-transporter and the full transporter is a dimer of two half-transporters (Figures 3h) (Wang, Hu, and Zheng 2020); this architecture is a surprisingly similar architecture to the type I ABC exporters (Figures 4 and 5, Tables 1 and 2).

1.3 ABC Exporters

Similar to the ABC importers, structural analysis of prokaryotic ABC exporters revealed a significant amount of structural diversity (Table 2). The type I ABC exporter fold was first revealed through the structure of the bacterial multidrug transporter Sav1866 from *Staphylococcus aureus* (Dawson and Locher 2006). Each TMD of Sav1866 consists of six TMHs, five of which are long helices that extrude out from the membrane toward the NBDs (Figure 4a) and each of the TMDs is fused with an NBD, forming a half-transporter which makes the whole Sav1866 transporter a homodimeric exporter. Subsequent structural analysis of a polypeptide transporter, PCAT1 from *Hungateiclostridium thermocellum*, also revealed a similar TMD fold, but it has additional peptidase domains on the N-termini of the TMDs (Figure 4b) (Lin, Huang, and Chen 2015). Similarly, the lipid-linked oligosaccharide flippase transporter, PglK from *Campylobacter jejuni* has extra helices on the periplasmic side of the membrane (Figure 4c) (Perez et al. 2015). Besides the homodimeric type I exporters, there are heterodimeric transporters consisting of two different half-transporters, such as the *Thermus thermophilus* multidrug transporter, TmrAB (Noll et al. 2017).

Unlike type I exporters, the prokaryotic type II exporters have six short TMHs per TMD, and the TMDs are separated from the NBD. Some of the type II exporters included the polysaccharide transporter (Figure 4d) (Bi et al. 2018), the wall teichoic acid transporter (Figure 4e) (Chen et al. 2020), the lipopolysaccharide transporter (Figure 4fg) (Li, Orlando, and Liao 2019, Owens et al. 2019) and the toluene tolerance efflux MLA complex (Figure 4g) (Kamischke et al. 2019). In addition, extra domains can form complexes with the transporters, which were revealed in the lipopolysaccharide transporter, LptB$_2$FGC (Figure 4g) and the MLA complex for toluene tolerance efflux (Figure 4h). Lastly, the type III exporter fold was first seen in MacB, a bacterial tripartite transporter, consisting of two short TMHs and two long TMHs that extruded to the periplasm and are fused with additional periplasmic domains that could together form the multidrug efflux complex with MacA and TolC (Fitzpatrick et al. 2017) (Figure 4i). This type III exporter fold was also later seen in a similar type of efflux pump from *Streptococcus pneumoniae* (Yang et al. 2018).

So far, human ABC transporters and their eukaryotic homologs from the ABCA, ABCB, ABCC, ABCD and ABCG subfamilies have been structurally characterized as either type I or II exporters (Figure 5, Table 3). In eukaryotes, the exporters may either be encoded in two separate polypeptide chains or in a single polypeptide chain. ABCA1, a phospholipid exporter, is encoded as a single polypeptide chain and its single-particle cryo-EM structure revealed not only the core domains, but also two extracellular domains with an enclosed hydrophobic tunnel and an intracellular regulatory domain (Figure 5a) (Qian et al. 2017). The multidrug resistance transporter, ABCB1 (also known as the P-glycoprotein), is encoded in one single chain containing just the core domains of two TMDs and two NBDs (Figure 5b) (Kim and Chen 2018). The peptide transporter, ABCB2/3 (TAP) is a heterodimer, encoded by two separate polypeptides (Figure 5c) (Oldham, Grigorieff, and Chen 2016). Besides ABCB2/3, ABCB4 (Figure 5d) (Olsen et al. 2020), ABCB7 homolog (Atm1 from *Saccharomyces cerevisiae* (Srinivasan, Pierik, and Lill 2014)) (Figure 5e), ABCB8 (Figure 5f) and ABCB10 (Figure 5g) (Shintre et al. 2013) all share the same overall architecture as ABCB1 (Figure 5b), which is the type I exporter fold. Members in the ABCC family, including the multidrug resistance protein homolog (MRP1, ABCC1) from *Bos taurus* (Figure 5h) (Johnson and Chen 2017), the cystic fibrosis transmembrane conductance regulator (CFTR, ABCC7) (Figure 5i) (Zhang, Liu, and Chen 2018), and ABCC8 (SUR1) in the KATP complex that functions as an ADP sensor for the potassium channel, Kir 6.2 (Figure 5j) (Lee, Chen, and MacKinnon 2017), all share the same type I exporter fold. The only structurally characterized ABCD family member, ABCD4, a lysosomal cobalamin exporter (Figure 5k) (Xu et al. 2019), also has long TMHs seen in other type I exporters in ABCB and ABCC families. In contrast to the type I exporters of the ABCB, ABCC and ABCD family transporters, the xenobiotics transporter, ABCG2 (Figure 5l) (Manolaridis et al. 2018), and the sterol transporter, ABCG5/8 (Figure 5m) (Lee et al. 2016) in ABCG family present all short TMs, which is a signature of a type II exporter.

1.4 ABC Transporter Transport Mechanism

The alternating access mechanism has been the most influential model to describe the transport mechanism of ABC transporters (Jardetzky 1966). In the basic mechanism, ABC transporters exhibit two major conformational states, an inward-facing conformation that opens toward the inside of a cell or a compartment, and an outward-facing conformation that opens toward the outside of a cell or a compartment. The conformational change between these two states is driven by the binding and hydrolysis of ATP. Structural analysis of various transporters, especially the exporters, revealed that in addition to the inward- and outward-facing conformations, there are also intermediate occluded conformational states that do not open toward either side of the membrane. In the updated alternating access mechanism for an ABC exporter (Figure 6a), the transported substrate binds to the inward-facing conformation from the inside of a given compartment. Binding of ATP drives dimerization of the NBDs, leading to the occluded conformation with both substrate and nucleotide bound, followed by transition through the occluded conformation to the outward-facing conformation that will release the substrate to the outside compartment. ATP hydrolysis resets the transporter and the transport cycle starts again following the exchange of nucleotide (Figure 6a) (Rees, Johnson, and Lewinson 2009, Locher 2016). For an importer, substrate is delivered to the transporter by the PBP when the transporter occupies the outward-facing conformation (Figure 6b). Upon ATP hydrolysis, the transporter adopts the inward-facing conformation, accompanying by substrate release and dissociation of the binding protein. The transport cycle could reinitiate upon the nucleotide exchange.

Although this simplified alternating access model has been used to describe the substrate translocation mechanisms for both importers and exporters, the detailed molecular mechanism, including the structures of the relevant intermediates, remain less studied. Recent structural studies of various transporter systems and the proposed transport mechanisms emphasize that these transporters utilize multiple transport mechanisms. For example, the structural analysis of the *Escherichia coli* vitamin B_{12} transporter, $BtuC_2D_2F$, revealed an asymmetric transport mode within the alternating access framework, and the asymmetric state is important in preventing the leakage of small molecules (Korkhov, Mireku, and Locher 2012). The structural analysis of a lipid-linked oligosaccharide (LLO) flippase from *Campylobacter jejuni* supported an outward-only transport mechanism, in which only the outward-facing conformation of the transporter is required for the lipid flipping. The transporter can still alternate between the inward, and outward-facing conformations (Perez et al. 2015). This outward-only mechanism was subsequently invoked as the transport mechanism for the bacterial efflux pump, MacB (Fitzpatrick et al. 2017). On the other hand, a trap and flip model was proposed for the *Escherichia coli* lipid A transporter, MsbA (Mi et al. 2017) in addition to the already proposed alternating access mechanism (Ward et al. 2007). A crankshaft conrod mechanism was proposed for the wall teichoic acid transporter, $TarG_2H_2$ (Chen et al. 2020). Further, the switch model (Higgins and Linton 2004), the constant contact model (George and Jones 2012), and the reciprocating twin-channel model (Jones and George 2014) have been proposed for ABC transporters. This variety of transport mechanisms highlights that it is easier to propose a model than to experimentally demonstrate the validity of a model, thereby emphasizing the importance of detailed molecular understanding for reconstructing the transport cycle for each transport system.

1.5 ABC Transporter Coupling Efficiencies

In addition to the structural analysis of various ABC transporters, the functional aspects of these transporters are critical for understanding the transport mechanism. The central functions of an ABC transporters are their ATPase activities and transport activities. The ATPase activities of ABC transporters can be measured robustly in detergent, nanodiscs, and proteoliposomes using various methods for quantifying the release of inorganic phosphate. In contrast, the transport activity measurements present a bigger challenge as the reaction setup requires two separate compartments to measure substrate translocation. As a consequence, these reactions are typically conducted with either proteoliposomes or membrane vesicles (Geertsma et al. 2008, Glavinas et al. 2008).

ABC transporters are generally associated with basal ATPase activities, that is the turnover of ATP in the absence of substrates. The basal activities of these transporters can vary greatly depending on the membrane environments. For example, the basal activity of the *Escherichia coli* vitamin B_{12} importer $BtuC_2D_2$ in proteoliposomes is 180 nmole/min/mg transporter, but in different detergents, the basal ATPase activity varies from ~300 to ~1,000 nmole/min/mg transporter (Borths et al. 2005). In addition, the measured basal ATPase activity for P-glycoprotein was ~100 to ~200 nmole/min/mg transporter in proteoliposomes with the variability resulted from the lipid composition, and ~1,450 to ~2,450 nmole/min/mg if the transporter is only embedded in plasma membrane (Dong, Penin, and Baggetto 1996). The origin of these basal activities of ABC transporters are unclear, but studies on $BtuC_2D_2$ revealed that its basal ATPase activity is important in keeping a more functional and stable transporter, which would become more active during substrate translocation (Livnat-Levanon et al. 2016). The basal ATPase activity in the *Lactococcus lactis* amino acid transporter GlnPQ was caused by the docking of unliganded PBP (Lycklama et al. 2018). These substrate-stimulated ATPase activities are generally within a few folds of increases of the basal activities of the transporters. In the case of $BtuC_2D_2$, the ATPase rate increased by about one-fold in proteoliposomes, but decreased by about two-fold and stimulated by about 50% depending on the detergent condition (Borths et al. 2005). The stimulation of drugs on the basal ATPase rates of P-glycoprotein varied from one to two fold with dependence on the membrane lipid composition (Dong, Penin, and Baggetto 1996), and the stimulation could be as high as about eight times in detergent for P-glycoprotein (Aller et al. 2009). A summary of the ATPase activities measured for different transporters in the presence of substrates is shown in Table 4.

In order for substrate transport to happen for an ABC transporter, it requires its transport activity to be driven by the hydrolysis of ATP by providing the driving force for translocation. The transport activities of ABC transporters are usually measured in reconstituted proteoliposomes or membrane vesicles, in which there will be two separate compartments, namely, the inside and outside of the proteoliposomes or membrane vesicle. In the case of proteoliposomes, it is commonly assumed that the orientation of the transport is 50% NBD-in and 50% NBD-out per reconstituted proteoliposome (Geertsma et al. 2008). But in the case with membrane vesicles, all transporters in the membrane will have the same orientation, either NBD-in or NBD-out (Glavinas et al. 2008). As ATP binds to the NBD of ABC transporters, it is required that ATP is placed on the same side as the NBD. One of the possible setups for an ABC importer is making use of the transporters with NBDs positioned on the inside of the proteoliposomes by supplying an ATP-regeneration system on the inside and the substrate on the outside of the proteoliposomes. The amount of imported substrate could be quantified by measuring the amount of accumulated substrate on the inside by collecting the proteoliposomes. In comparison, the exporter function is easier to test. One can make use of the transporters with NBDs positioned on the outside of the proteoliposomes and supply both substrate and ATP on the outside. The exported substrate will accumulate on the inside of the proteoliposomes and the amount of substrate could be quantified (Geertsma et al. 2008).

Although the transport assay is rather easy to set up, there are different factors that could affect the final transport activity. One factor is the reconstitution efficiency. During reconstitution of transporters into liposomes, not all transporters will get incorporated. This will result in a lower reconstitution efficiency as seen in the $BtuC_2D_2$ reconstitution (Borths et al. 2005). But this could be easily corrected by analyzing the amount of protein in the total reconstitution and in the proteoliposomes-only samples using SDS-PAGE. One other factor related to the reconstitution is the orientation effects. Transporters may preferentially be inserted into the membrane in one way or another, and thus the assumption of 50% in and 50% out would be incorrect. Further, the reconstituted proteoliposomes are highly unstable, the unilamella proteoliposomes may not only fuse with each other forming large unilamella vesicles, but they may also form multilamellar vesicles which will result in underestimation of the actual transport activities. Some of the transport activities of ABC transporters are summarized in Table 4. The transport activities of different transporters range from 0.03 to 1,200 nmole/min/mg transporter. With an estimate molecular weight of 120 kDa (1 mg protein $\cong$ 8 nmole protein) for most of these ABC transporters, the transport rates are estimated to be 0.004 min^{-1} to 150 min^{-1} or 0.0001 s^{-1} to 2.5 s^{-1}. This is significantly slower than the P-type ATPases that have a transport rate of about 10^2 s^{-1} (Skou 1998). In addition, secondary transporters can exhibit much higher rates, such as the band 3 anion exchanger with a transport rate on the order of 10^4 s^{-1} (Brahm 1977, Hsu 2018), the chloride channels has a rate close to 10^3 s^{-1} (Jayaram et al. 2008), the glucose transporter has a transport rate on the order of 10^3 s^{-1} (Mueckler and Thorens 2013), and the lactose transporter has a transport rate of ~20 s^{-1} (Viitanen, Garcia, and Kaback 1984). These different membrane transport systems are significantly faster than ABC transporters, which raise the questions of why ABC transporters are so slow and what are some factors that could limit their rate of transport.

The ATPase and transport activities of a given transporter may be used to calculate the coupling efficiency, which is given by the ATPase rate divided by the transport rate, to yield the number of ATP molecules hydrolyzed for one substrate molecule translocated. As ABC transporters present two NBDs, it is commonly thought that two ATP molecules are required per substrate translocation, but coupling efficiency of 2 has only been realized for the amino acid importer, GlnPQ (Lycklama et al. 2018), P-glycoprotein (Eytan, Regev, and Assaraf 1996), and the sterol transporter ABCG5/8 (Wang et al. 2006) (Table 4). In other transporter systems, significant variations in the coupling efficiency have been reported. For example, the coupling efficiency for the maltose transporter $MalFGK_2$ in different studies ranges from 1.4 to over 3000 ATP/transported substrate (Table 4), which must arise from differences in the experimental protocols for reconstitution and transport characterization. The uncoupled activity could reflect the operation of two parallel, functionally relevant pathways for ATP hydrolysis that differ by the presence or absence of the transported substrate as proposed for certain ABC importers (Lewinson and Livnat-Levanon 2017) and ABC exporters (Hofmann et al. 2019). The inefficient coupling of ABC transporters is also reminiscent of the properties of binding protein independent variants of the maltose transporter that exhibit constitutive ATPase activity (Covitz et al. 1994); this suggests that the uncoupled ATPase activity may also be associated with the ability to transport more weakly bound substrates in the absence of a binding protein. Understanding the origins of this uncoupling will be critical for the detailed dissection of the transport mechanism to assure that the ATP-dependent steps are indeed relevant to substrate translocation.

1.6 Mitochondrial ABC Transporters

The ABC transporter of mitochondria (Atm1) was first identified in *Saccharomyces cerevisiae* with localization to the inner membrane of mitochondria as a homodimer (Lill and Kispal 2001). Atm1-deficient mitochondria accumulate ~30x more non-heme iron (II) (Miao et al. 2009) than wild type mitochondria (Kispal et al. 1997), suggestive of an important role in mitochondrial iron homeostasis. In addition, while depletion of Atm1 from mitochondria has no effect on assembly of mitochondrial iron-sulfur cluster proteins, the biosynthesis of cytosolic iron-sulfur cluster proteins is significantly impaired. This observation suggests that Atm1 participates in the maturation of cytosolic iron-sulfur cluster proteins through the transport of one or more essential components or perhaps a regulatory species (Miao et al. 2009). Later studies demonstrated that thiol compounds, including cysteine, glutathione, oxidized glutathione (Kuhnke et al. 2006), and the glutathione persulfide (Riedel et al. 2019) could stimulate the ATPase activities of Atm1 and are thus potential substrates for Atm1. Additional studies on the *Arabidopsis* homolog atm3 revealed that it is not only important in iron-sulfur cluster biogenesis (Bernard et al. 2009, Zuo et al. 2017), but also in molybdenum cofactor biosynthesis (Teschner et al. 2010).

Humans contain four mitochondrial ABC transporters: ABCB6, ABCB7, ABCB8 and ABCB10. Among the four, ABCB7 and ABCB6 share 50% and 40% sequence identities with yeast Atm1, respectively. Studies on ABCB7 and its orthologs have shown that this transporter has an essential role in iron-sulfur cluster biogenesis (Pondarre et al. 2006) and heavy metal detoxification (Lerebours, To, and Bourdineaud 2016). Mutations in ABCB7 are associated with X-linked sideroblastic anemia in humans (Bekri et al. 2000). ABCB6 was first found to be a porphyrin transporter (Krishnamurthy et al. 2006) in the outer membrane of mitochondria, and was subsequently shown to protect cells against arsenic toxicity (Chavan, Oruganti, and Krishnamurthy 2011) and to have a role in cadmium detoxification (Rakvacs et al. 2019). In addition to mitochondria, ABCB6 has also been demonstrated to localize to the plasma membrane (Paterson et al. 2007), the Golgi apparatus (Tsuchida et al. 2008), and lysosome (Kiss et al. 2012).

In an effort to structurally characterize Atm1 and its homologs to understand the underlying transport mechanism, previous efforts from our lab set the groundwork by characterizing a bacterial homolog of Atm1/ABCB7/ABCB6. Through a funnel approach optimizing cloning, expression, purification, and crystallization, an Atm1 homolog from *Novosphingobium aromaticavorans (Na*Atm1) was selected which shares sequence identities of ~45% with the yeast Atm1 and the human ABCB7 and ABCB6. The structure of *Na*Atm1 was determined in the inward-facing conformation, in apo, glutathione (GSH), oxidized glutathione (GSSG), and glutathione-mercury complex (GS-Hg) bound states (Lee et al. 2014). The structural studies established that *Na*Atm1 folds as a homodimer with two identical half-transporters and is a member of the type I exporter family containing six TMHs in the TMDs (Figure 7ab). *In vitro* assays revealed that the ATPase activities of *Na*Atm1 could be greatly stimulated by glutathione-silver and glutathione-mercury complexes, while *in vivo* assays demonstrated that overexpression of *Na*Atm1 in heavy metal sensitive *Escherichia coli* strains conferred protection against toxic concentrations of Ag^+ and Hg^{2+}. These observations are suggestive of a heavy-metal detoxification function for *Na*Atm1, plausibly by exporting heavy metal derived GSH complexes (Lee et al. 2014). Two GSSG binding sites were identified in the structure (Figure 7a), a primary binding site deep into the lipid bilayer and a secondary binding site with a relatively lower occupancy closer to the cytoplasm. In both sites, GSSG forms extensive interactions with residues in the binding pocket (Figure 7cd). The relative positions of the two GSSG molecules are suggestive of a potential binding mode of a $[2Fe{:}2S][GS^-]_4$ complex that has been proposed as a potential substrate for Atm1 (Qi et al. 2012).

1.7 Purpose of Study

There has been a recent explosion in the structure determinations of ABC transporters, reflecting the resolution revolution in the field of single-particle cryo-electron microscopy. Despite these structural advances, functional characterizations of ABC transporters have been more challenging. This is largely because characterizing the functional aspects of ABC transporters necessitates measurement of the transport activity. As discussed above, transport measurements are challenging due to the requirement to faithfully reconstitute transporters into proteoliposomes and because of the high basal ATPase rate. As a consequence, fundamental questions concerning the transport mechanism remain unclear. The mechanistic questions are compounded by the variety of transport mechanisms that have been proposed for ABC transporters, including the alternating access model (Ward et al. 2007, Khare et al. 2009, Nguyen et al. 2018), the outward only model (Perez et al. 2015, Fitzpatrick et al. 2017), and the trap and flip model (Mi et al. 2017). The diversity of mechanistic proposals reinforces the concept that despite having a common nucleotide driven engine, details of the transport mechanism may differ significantly among the ABC transporter family. Even such basic questions as the location(s) of the substrate binding site(s) and the origins of the transport directionality of importers and exporters, are not well understood.

In consideration of the current state of the ABC transporter field, *Na*Atm1 presents a great opportunity since substrates have been defined, and the structure has been characterized to high resolution with X-ray crystallography. Consequently, I set out to use *Na*Atm1 as a model system to understand the transport mechanism for human ABC transporter homologs with two objectives:

1) elucidate the transport mechanism of *Na*Atm1 by structurally characterizing other conformational states in the transport cycle in the presence and absence of substrates and various nucleotides, using X-ray crystallography and single-particle cryo-electron microscopy, and
2) functionally characterize *Na*Atm1 through both ATPase and transport assays.

In addition to my studies on the *Na*Atm1 exporter system, many PBPs from the ABC importer systems have been recently redesigned as biosensors for cellular usages because of their substrate diversity. The Lester group has been actively working on developing and characterizing biosensors for smoking cessation drugs and neurotransmitters in collaboration with the Looger group at HHMI. Structures of the liganded states of the biosensors are crucial in the directed evolution of these biosensors. I thus set out to determine structures of these biosensors to guide its design for better binding specificity.

1.8 Figures

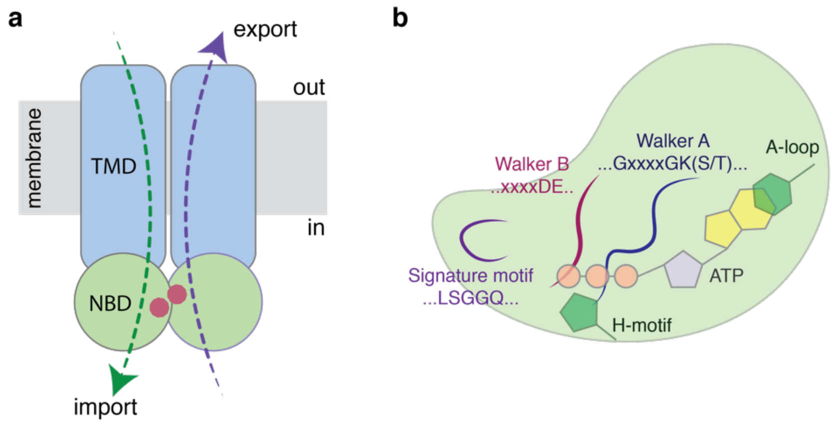

Figure 1. Overview of ABC transporter.

(**a**) ABC transporter overall architecture illustrating the directions of import and export. (**b**) Structural features of a nucleotide-binding domain present in ABC transporters. The conserved sequences motifs are labeled.

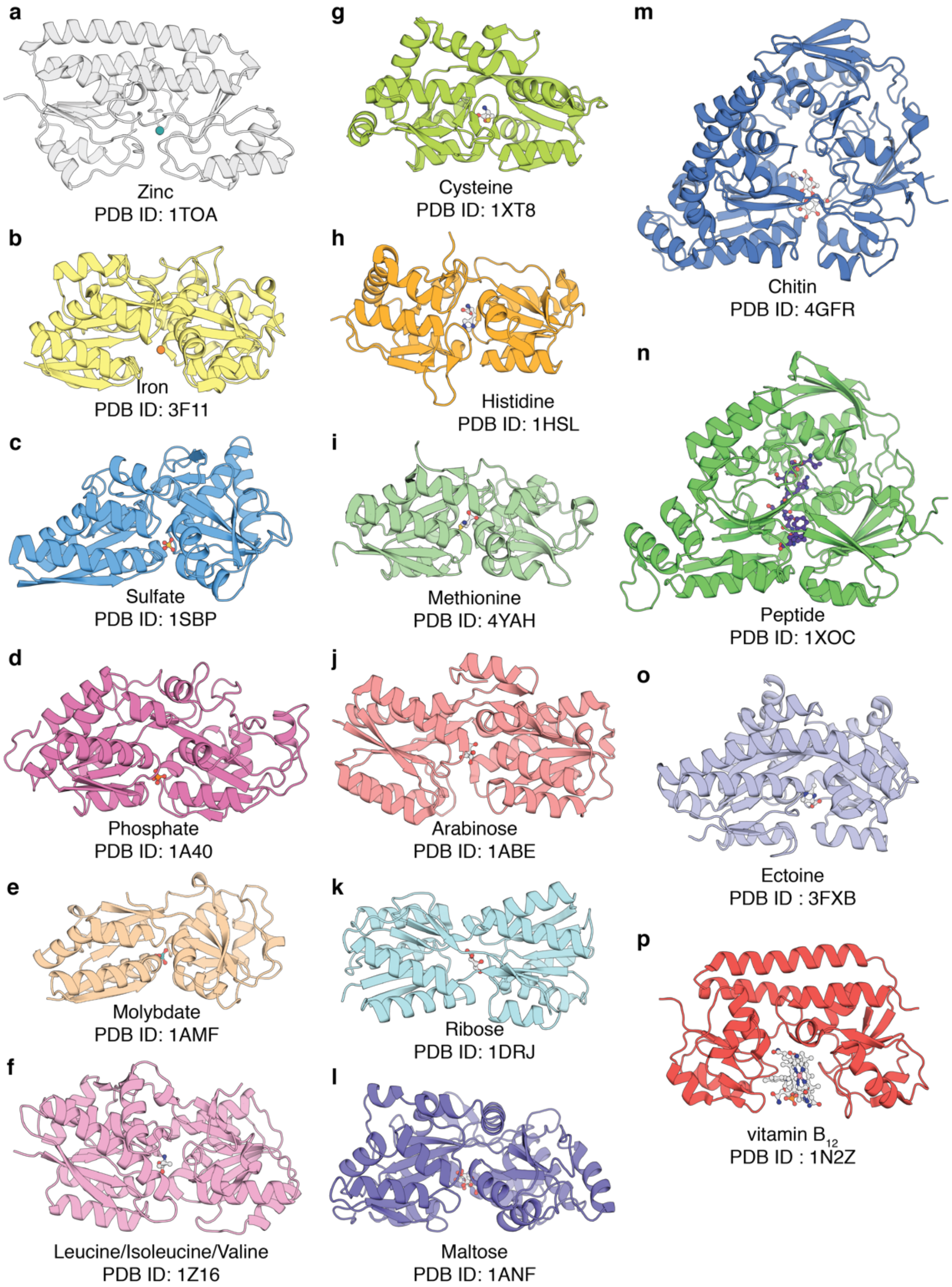

Figure 2. Crystal structures of periplasmic binding proteins.

Structures of (**a**) the zinc-binding protein from *Treponema pallidum*, (**b**) the iron-binding protein from *Synechocystis*, (**c**) the sulfate-binding protein from *Salmonella typhimurium*, (**d**) the phosphate-binding protein from *Escherichia coli*, (**e**) the molybdate-binding protein from *Escherichia coli*, (**f**) the leucine/isoleucine/valine-binding protein from *Escherichia coli*, (**g**) the cysteine-binding protein from *Campylobacter jejuni*, (**h**) the histidine-binding protein from *Escherichia coli*, (**i**) the methionine-binding protein from *Escherichia coli*, (**j**) the arabinose-binding protein from *Escherichia coli*, (**k**) the ribose-binding protein from *Escherichia coli*, (**l**) the maltose-binding protein from *Escherichia coli*, (**m**) the chitin-binding protein from *Vibrio cholerae*, (**n**) the peptide-binding protein from *Bacillus subtilis*, (**o**) the ectoine-binding protein from *Ruegeria pomeroyi*, and (**p**) vitamin B_{12}-binding protein from *Escherichia coli.* The corresponding PDB IDs are labeled below each structure.

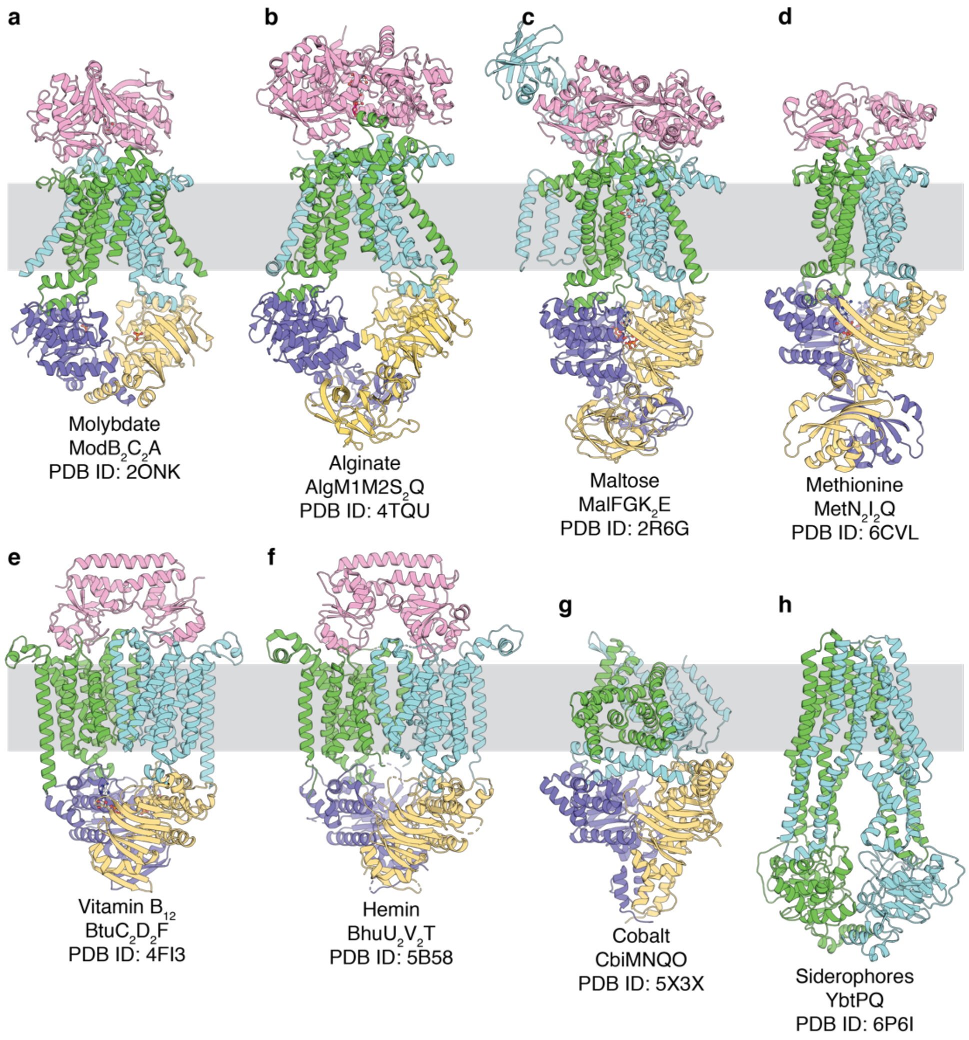

Figure 3. Structures of the prokaryotic ABC importers.

(**a**) Crystal structure of the *Archaeoglobus fulgidus* molybdate importer complex, ModB$_2$C$_2$A. (**b**) Crystal structure of the *Sphingomonas sp.* alginate importer complex, AlgM1M2S$_2$Q. (**c**) Crystal structure of the *Escherichia coli* maltose importer complex, MalFGK$_2$E. (**d**) Crystal structure of the *Escherichia coli* methionine importer complex, MetN$_2$I$_2$Q. (**e**) Crystal structure of the *Escherichia coli* vitamin B$_{12}$ importer complex, BtuC$_2$D$_2$F. (**f**) Crystal structure of the *Burkholderia cenocepacia* hemin importer complex, BhuU$_2$V$_2$T. (**g**) Crystal structure of the *Rhodobacter capsulatus* energy-coupling-factor (ECF), CbiMNQO. (**h**) Single-particle cryo-EM structure of the *Escherichia coli* siderophore importer, YbtPQ. The corresponding PDB IDs are labeled below each structure.

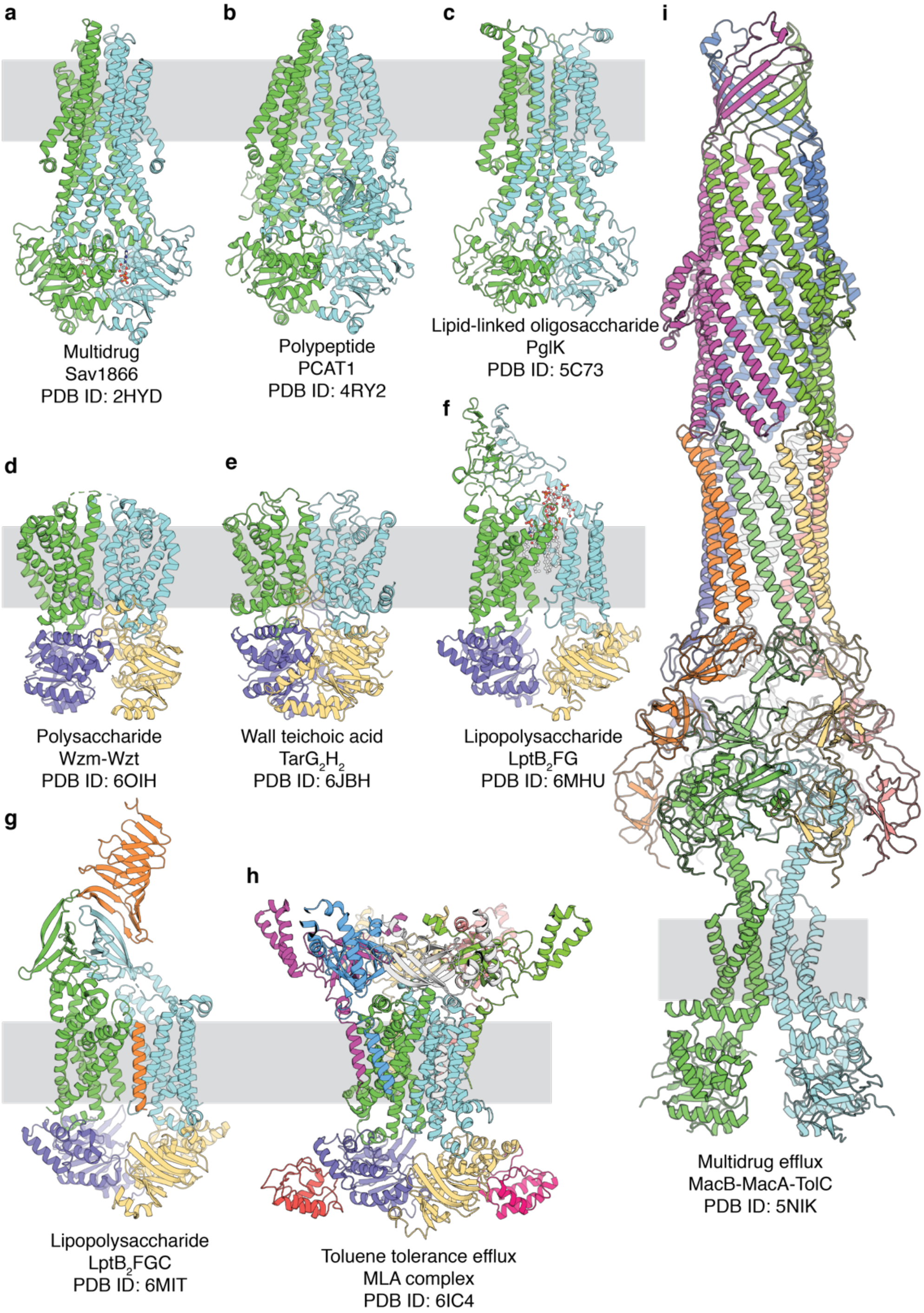

Figure 4. Structures of the prokaryotic ABC exporters.

(**a**) Crystal structure of the *Staphylococcus aureus* multidrug transporter, Sav1866. (**b**) Crystal structure of the *Hungateiclostridium thermocellum* PCAT1. (**c**) Crystal structure of the *Campylobacter jejuni* lipid-linked oligosaccharide transporter, PglK. (**d**) Crystal structure of the

Aquifex aeolicus O-antigen polysaccharide exporter, Wzm-Wzt. (**e**) Single-particle cryo-EM structure of the *Alicyclobacillus herbarius* wall teichoic acid exporter, $TarG_2H_2$. (**f**) Single-particle cryo-EM structure of the *Escherichia coli* lipopolysaccharide exporter, $LptB_2FG$. (**g**) Single-particle cryo-EM structure of the *Enterobacter cloacae* lipopolysaccharide exporter, $LptB_2FGC$. (**h**) Single-particle cryo-EM structure of the *Acinetobacter baumannii* MLA complex. (**i**) Single-particle cryo-EM structure of the *Escherichia coli* tripartite efflux pump, MacB in complex with MacA and TolC. The corresponding PDB IDs are labeled below each structure.

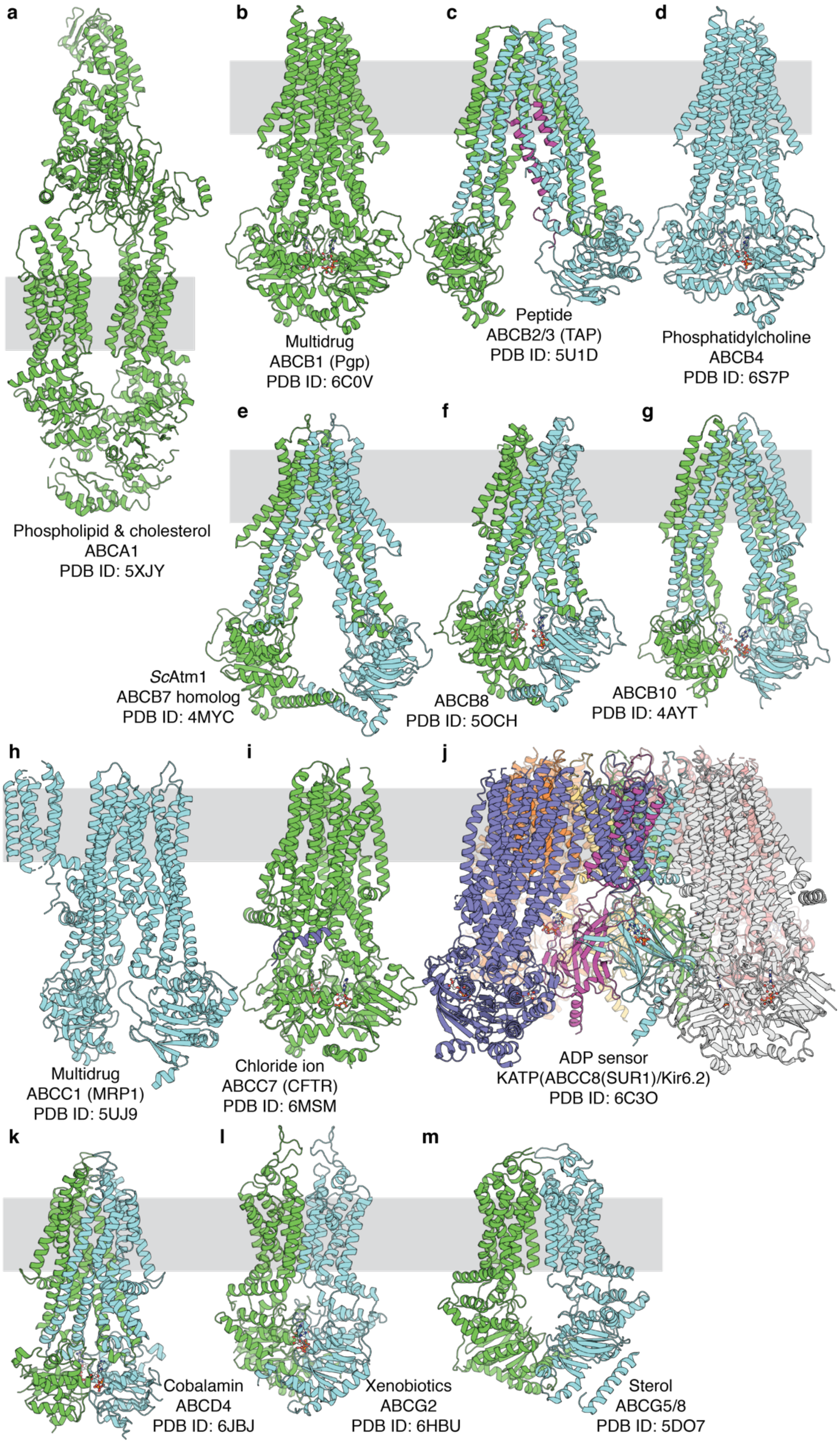
a
Phospholipid & cholesterol
ABCA1
PDB ID: 5XJY
b
Multidrug
ABCB1 (Pgp)
PDB ID: 6C0V
c
Peptide
ABCB2/3 (TAP)
PDB ID: 5U1D
d
Phosphatidylcholine
ABCB4
PDB ID: 6S7P
e
*Sc*Atm1
ABCB7 homolog
PDB ID: 4MYC
f
ABCB8
PDB ID: 5OCH
g
ABCB10
PDB ID: 4AYT
h
Multidrug
ABCC1 (MRP1)
PDB ID: 5UJ9
i
Chloride ion
ABCC7 (CFTR)
PDB ID: 6MSM
j
ADP sensor
KATP(ABCC8(SUR1)/Kir6.2)
PDB ID: 6C3O
k
Cobalamin
ABCD4
PDB ID: 6JBJ
l
Xenobiotics
ABCG2
PDB ID: 6HBU
m
Sterol
ABCG5/8
PDB ID: 5DO7

Figure 5. Structures of the eukaryotic ABC exporters.

(**a**) Single-particle cryo-EM structure of the human phospholipid and cholesterol transporter, ABCA1. (**b**) Single-particle cryo-EM structure of the human multidrug transporter, ABCB1 (Pgp, P-glycoprotein). (**c**) Single-particle cryo-EM structure of the human peptide transporter, ABCB2/3 (TAP-transporter associated with antigen processing). (**d**) Single-particle cryo-EM structure of the human phosphatidylcholine transporter, ABCB4. (**e**) Crystal structure of the human glutathione and derivatives transporter ABCB7 homolog (Atm1- ABC transporter of mitochondria) from *Saccharomyces cerevisiae*. (**f**) Single-particle cryo-EM structure of the human ABCB8. (**g**) Single-particle cryo-EM structure of the human ABCB10. (**h**) Single-particle cryo-EM structure of the human multidrug transporter, ABCC1 (MRP1-multidrug resistance protein) homolog from *Bos Taurus*. (**i**) Single-particle cryo-EM structure of the human chloride channel, ABCC7 (CFTR). (**j**) Single-particle cryo-EM structure of KATP channel, a SUR1 (ABCC8) and Kir6.2 complex. (**k**) Single-particle cryo-EM structure of the human cobalamin transporter, ABCD4. (**l**) Single-particle cryo-EM structure of the human xenobiotic transporter, ABCG2. (**m**) Crystal structure of the human sterol transporter, ABCG5/8. The corresponding PDB IDs are labeled below each structure.

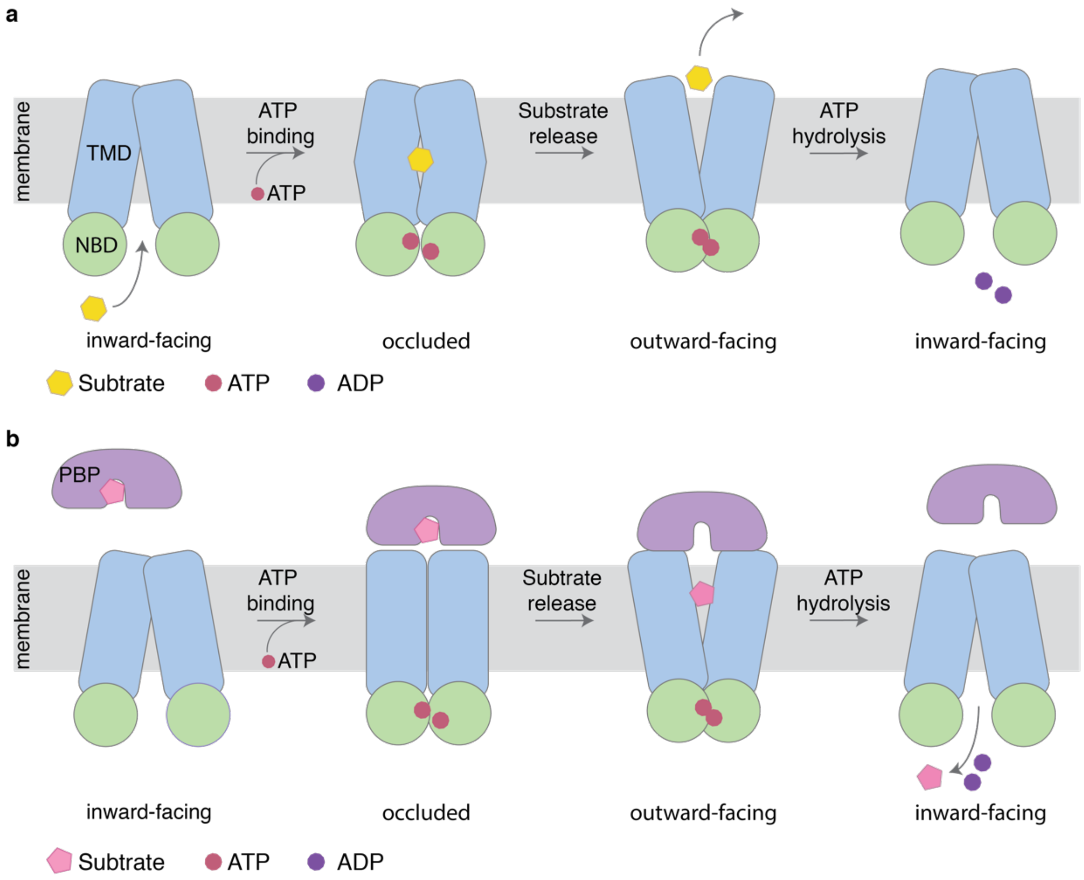

Figure 6. The alternating access transport model.

The alternating access mechanism for (**a**) an ABC exporter, and (**b**) an ABC importer.

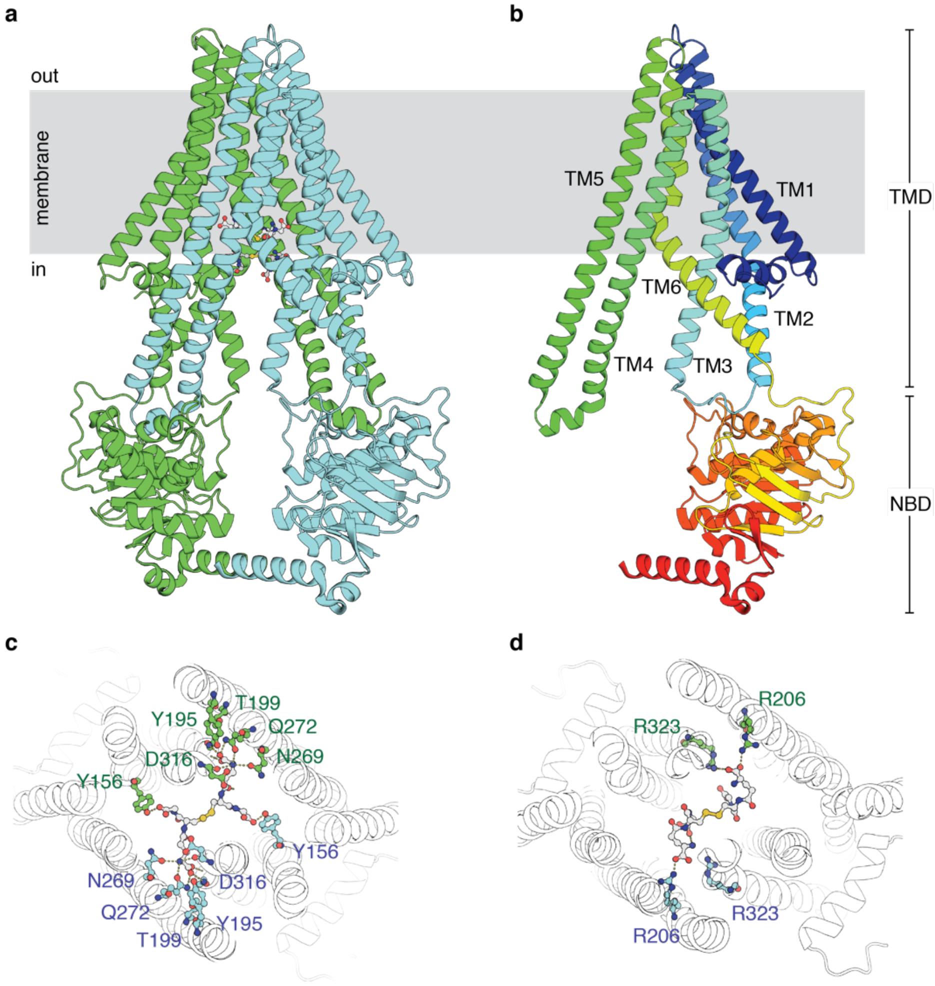

Figure 7. Crystal structure of *Na*Atm1 in the inward-facing conformation.

(**a**) Overall cartoon representation of *Na*Atm1 with two GSSG bound. One half-transporter is shown in green and the second half-transporter is shown in cyan. (**b**) *Na*Atm1 half-transporter with the TMD and NBD labeled. (**c**) GSSG in the primary binding site with interactions to the nearby residues. (**d**) GSSG in the secondary binding site with interactions to the nearby residues. Residues from the two chains are labeled in green and cyan, respectively. PDB ID: 4MRS.

1.9 Tables

Table 1. Summary of ABC importer structures.

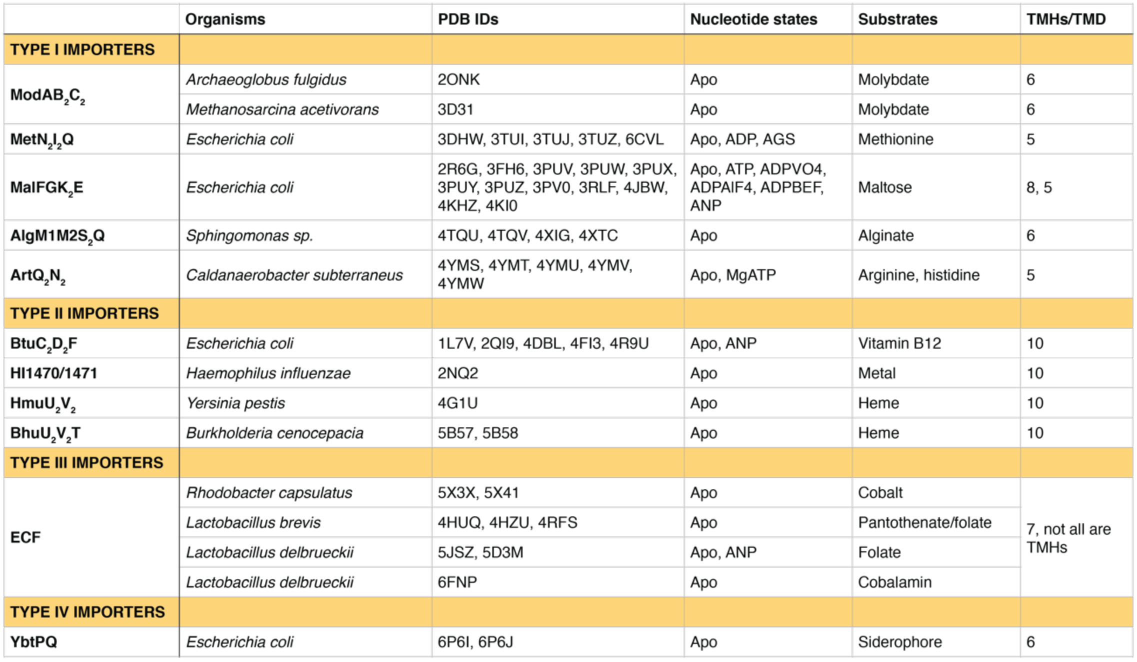

	Organisms	PDB IDs	Nucleotide states	Substrates	TMHs/TMD
TYPE I IMPORTERS					
ModAB$_2$C$_2$	*Archaeoglobus fulgidus*	2ONK	Apo	Molybdate	6
	Methanosarcina acetivorans	3D31	Apo	Molybdate	6
MetN$_2$I$_2$Q	*Escherichia coli*	3DHW, 3TUI, 3TUJ, 3TUZ, 6CVL	Apo, ADP, AGS	Methionine	5
MalFGK$_2$E	*Escherichia coli*	2R6G, 3FH6, 3PUV, 3PUW, 3PUX, 3PUY, 3PUZ, 3PV0, 3RLF, 4JBW, 4KHZ, 4KI0	Apo, ATP, ADPVO4, ADPAlF4, ADPBEF, ANP	Maltose	8, 5
AlgM1M2S$_2$Q	*Sphingomonas sp.*	4TQU, 4TQV, 4XIG, 4XTC	Apo	Alginate	6
ArtQ$_2$N$_2$	*Caldanaerobacter subterraneus*	4YMS, 4YMT, 4YMU, 4YMV, 4YMW	Apo, MgATP	Arginine, histidine	5
TYPE II IMPORTERS					
BtuC$_2$D$_2$F	*Escherichia coli*	1L7V, 2QI9, 4DBL, 4FI3, 4R9U	Apo, ANP	Vitamin B12	10
HI1470/1471	*Haemophilus influenzae*	2NQ2	Apo	Metal	10
HmuU$_2$V$_2$	*Yersinia pestis*	4G1U	Apo	Heme	10
BhuU$_2$V$_2$T	*Burkholderia cenocepacia*	5B57, 5B58	Apo	Heme	10
TYPE III IMPORTERS					
ECF	*Rhodobacter capsulatus*	5X3X, 5X41	Apo	Cobalt	7, not all are TMHs
	Lactobacillus brevis	4HUQ, 4HZU, 4RFS	Apo	Pantothenate/folate	
	Lactobacillus delbrueckii	5JSZ, 5D3M	Apo, ANP	Folate	
	Lactobacillus delbrueckii	6FNP	Apo	Cobalamin	
TYPE IV IMPORTERS					
YbtPQ	*Escherichia coli*	6P6I, 6P6J	Apo	Siderophore	6

Table 2. Summary of prokaryotic ABC exporter structures.

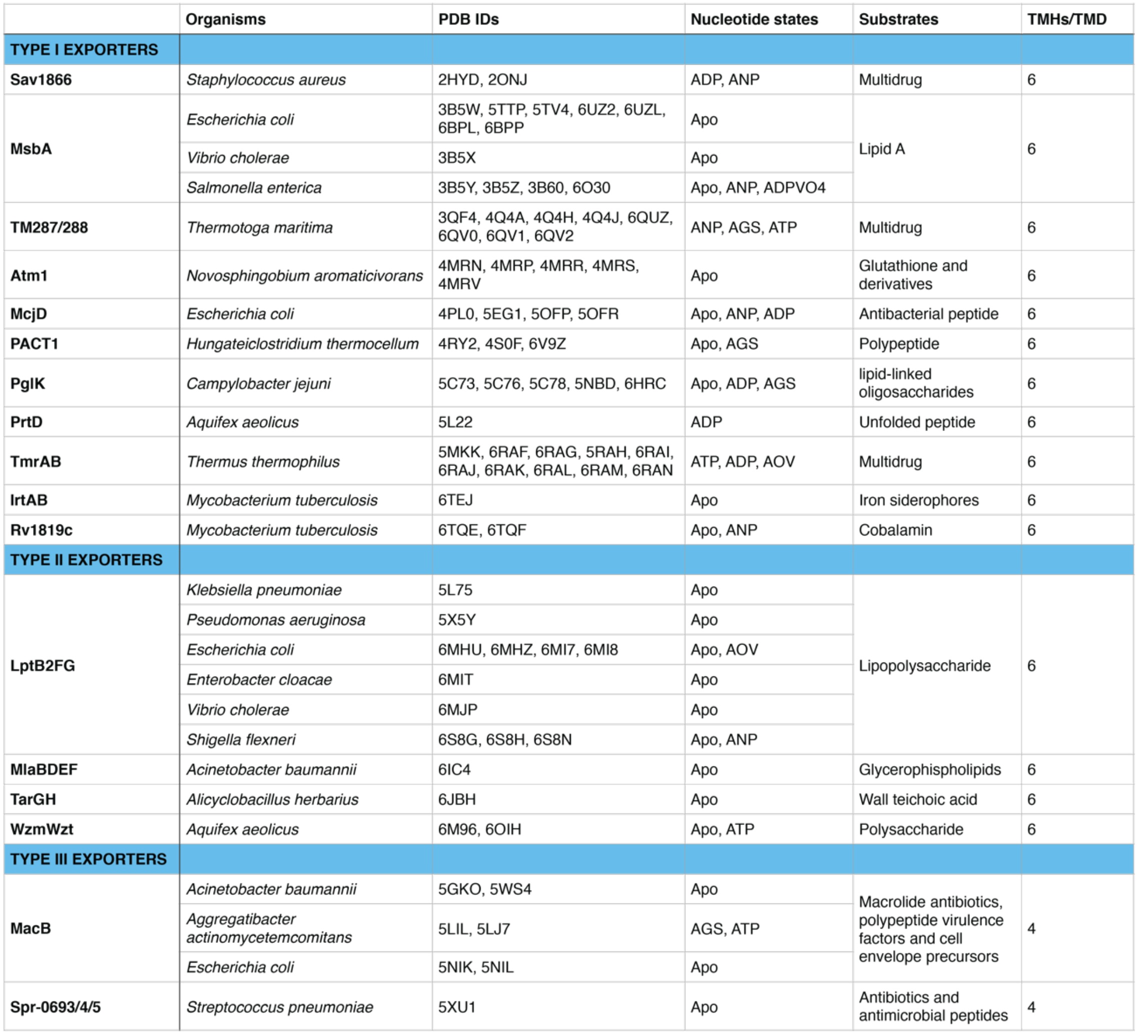

	Organisms	PDB IDs	Nucleotide states	Substrates	TMHs/TMD
TYPE I EXPORTERS					
Sav1866	*Staphylococcus aureus*	2HYD, 2ONJ	ADP, ANP	Multidrug	6
MsbA	*Escherichia coli*	3B5W, 5TTP, 5TV4, 6UZ2, 6UZL, 6BPL, 6BPP	Apo	Lipid A	6
	Vibrio cholerae	3B5X	Apo		
	Salmonella enterica	3B5Y, 3B5Z, 3B60, 6O30	Apo, ANP, ADPVO4		
TM287/288	*Thermotoga maritima*	3QF4, 4Q4A, 4Q4H, 4Q4J, 6QUZ, 6QV0, 6QV1, 6QV2	ANP, AGS, ATP	Multidrug	6
Atm1	*Novosphingobium aromaticivorans*	4MRN, 4MRP, 4MRR, 4MRS, 4MRV	Apo	Glutathione and derivatives	6
McjD	*Escherichia coli*	4PL0, 5EG1, 5OFP, 5OFR	Apo, ANP, ADP	Antibacterial peptide	6
PACT1	*Hungateiclostridium thermocellum*	4RY2, 4S0F, 6V9Z	Apo, AGS	Polypeptide	6
PglK	*Campylobacter jejuni*	5C73, 5C76, 5C78, 5NBD, 6HRC	Apo, ADP, AGS	lipid-linked oligosaccharides	6
PrtD	*Aquifex aeolicus*	5L22	ADP	Unfolded peptide	6
TmrAB	*Thermus thermophilus*	5MKK, 6RAF, 6RAG, 5RAH, 6RAI, 6RAJ, 6RAK, 6RAL, 6RAM, 6RAN	ATP, ADP, AOV	Multidrug	6
IrtAB	*Mycobacterium tuberculosis*	6TEJ	Apo	Iron siderophores	6
Rv1819c	*Mycobacterium tuberculosis*	6TQE, 6TQF	Apo, ANP	Cobalamin	6
TYPE II EXPORTERS					
LptB2FG	*Klebsiella pneumoniae*	5L75	Apo	Lipopolysaccharide	6
	Pseudomonas aeruginosa	5X5Y	Apo		
	Escherichia coli	6MHU, 6MHZ, 6MI7, 6MI8	Apo, AOV		
	Enterobacter cloacae	6MIT	Apo		
	Vibrio cholerae	6MJP	Apo		
	Shigella flexneri	6S8G, 6S8H, 6S8N	Apo, ANP		
MlaBDEF	*Acinetobacter baumannii*	6IC4	Apo	Glycerophospholipids	6
TarGH	*Alicyclobacillus herbarius*	6JBH	Apo	Wall teichoic acid	6
WzmWzt	*Aquifex aeolicus*	6M96, 6OIH	Apo, ATP	Polysaccharide	6
TYPE III EXPORTERS					
MacB	*Acinetobacter baumannii*	5GKO, 5WS4	Apo	Macrolide antibiotics, polypeptide virulence factors and cell envelope precursors	4
	Aggregatibacter actinomycetemcomitans	5LIL, 5LJ7	AGS, ATP		
	Escherichia coli	5NIK, 5NIL	Apo		
Spr-0693/4/5	*Streptococcus pneumoniae*	5XU1	Apo	Antibiotics and antimicrobial peptides	4

Table 3. Summary of eukaryotic ABC exporter structures.

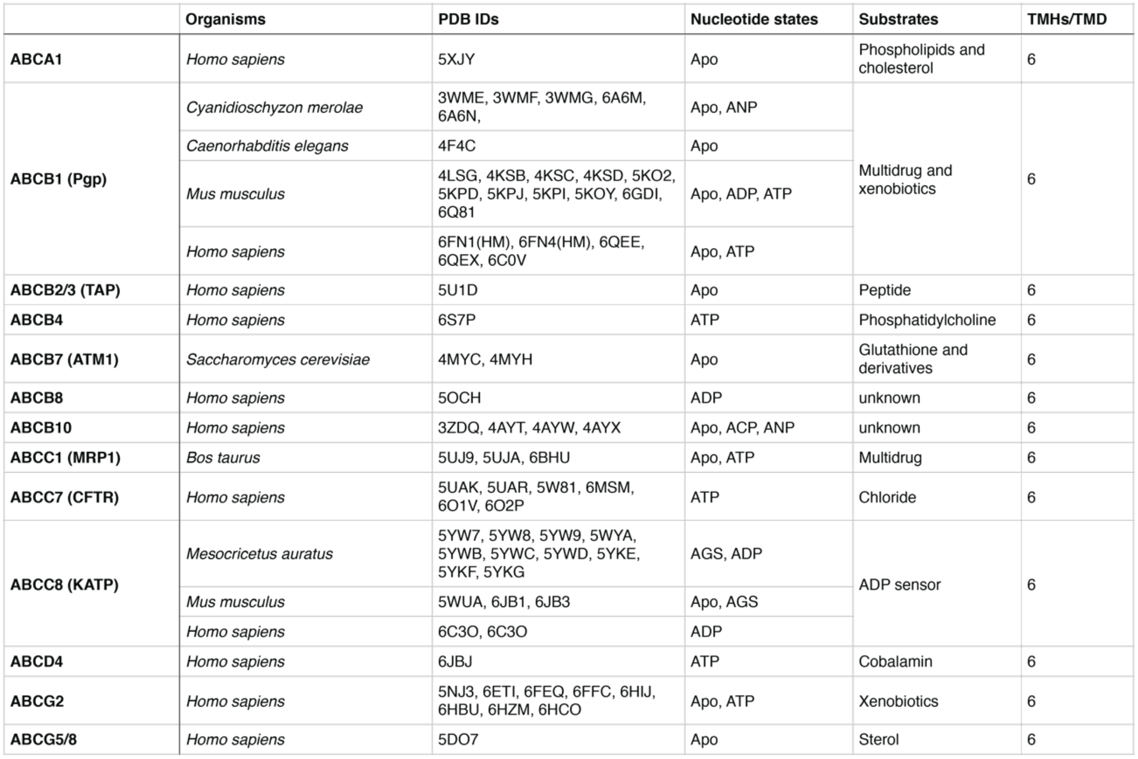

	Organisms	PDB IDs	Nucleotide states	Substrates	TMHs/TMD
ABCA1	*Homo sapiens*	5XJY	Apo	Phospholipids and cholesterol	6
ABCB1 (Pgp)	*Cyanidioschyzon merolae*	3WME, 3WMF, 3WMG, 6A6M, 6A6N,	Apo, ANP	Multidrug and xenobiotics	6
	Caenorhabditis elegans	4F4C	Apo		
	Mus musculus	4LSG, 4KSB, 4KSC, 4KSD, 5KO2, 5KPD, 5KPJ, 5KPI, 5KOY, 6GDI, 6Q81	Apo, ADP, ATP		
	Homo sapiens	6FN1(HM), 6FN4(HM), 6QEE, 6QEX, 6C0V	Apo, ATP		
ABCB2/3 (TAP)	*Homo sapiens*	5U1D	Apo	Peptide	6
ABCB4	*Homo sapiens*	6S7P	ATP	Phosphatidylcholine	6
ABCB7 (ATM1)	*Saccharomyces cerevisiae*	4MYC, 4MYH	Apo	Glutathione and derivatives	6
ABCB8	*Homo sapiens*	5OCH	ADP	unknown	6
ABCB10	*Homo sapiens*	3ZDQ, 4AYT, 4AYW, 4AYX	Apo, ACP, ANP	unknown	6
ABCC1 (MRP1)	*Bos taurus*	5UJ9, 5UJA, 6BHU	Apo, ATP	Multidrug	6
ABCC7 (CFTR)	*Homo sapiens*	5UAK, 5UAR, 5W81, 6MSM, 6O1V, 6O2P	ATP	Chloride	6
ABCC8 (KATP)	*Mesocricetus auratus*	5YW7, 5YW8, 5YW9, 5WYA, 5YWB, 5YWC, 5YWD, 5YKE, 5YKF, 5YKG	AGS, ADP	ADP sensor	6
	Mus musculus	5WUA, 6JB1, 6JB3	Apo, AGS		
	Homo sapiens	6C3O, 6C3O	ADP		
ABCD4	*Homo sapiens*	6JBJ	ATP	Cobalamin	6
ABCG2	*Homo sapiens*	5NJ3, 6ETI, 6FEQ, 6FFC, 6HIJ, 6HBU, 6HZM, 6HCO	Apo, ATP	Xenobiotics	6
ABCG5/8	*Homo sapiens*	5DO7	Apo	Sterol	6

Table 4. Summary of coupling efficiencies.*

Transporters	ATPase activity (nmol/min/mg)	Transport activity (nmol/min/mg)	Coupling efficiency	References
ABCC3	200	1,200	0.17	Zehnpfennig et al (2009)
MalFGK	~3	~2	1.4 - 17	Davidson et al (1990)
OpuA	~80 - 120	~30 - 70	1.7 - 4	Patzlaff et al (2003)
GlnPQ	15 (min^{-1})	8.5 (min^{-1})	1.8	Lycklama et al (2018)
Pgp	~750 - 1,300	~500	2	Eytan et al (1996)
ABCG5/8	110	50	2.2	Wang et al (2006)
MalFGK	~1.2 - 8	~0.3 - 2	4 - 10	Dean et al (1989)
Pgp	~110	~6	18	Dong et al (1996)
HisP	580	19	31	Nikaido and Ames (1999)
ABCG2	~750	~22	34	Manolaridis et al (2018)
TmrAB	~1,100 (MSP)	~30 (PLS)	37	Hofmann et al (2019)
BtuCDF	~400	~4	100	Borths et al (2005)
HmuUV	~130	~1.1	120	Woo et al (2012)
MalFGK	4,000	1.2	3,300	Chen et al (2001)
ABCB6	610	0.03	20,000	Chavan et al (2013)

*References: Zehnpfennig, Urbatsch, and Galla 2009, Davidson and Nikaido 1990, Patzlaff, van der Heide, and Poolman 2003, Lycklama et al. 2018, Eytan, Regev, and Assaraf 1996, Wang et al. 2006, Dean, Davidson, and Nikaido 1989, Dong, Penin, and Baggetto 1996, Nikaido and Ames 1999, Manolaridis et al. 2018, Hofmann et al. 2019, Borths et al. 2005, Woo et al. 2012, Chen et al. 2001, Chavan et al. 2013.

1.10 References

Aktas, M., K. A. Jost, C. Fritz, and F. Narberhaus. 2011. “Choline uptake in *Agrobacterium tumefaciens* by the high-affinity ChoXWV transporter.” *Journal of Bacteriology* 193 (19):5119-29. doi: 10.1128/JB.05421-11.

Aller, S. G., J. Yu, A. Ward, Y. Weng, S. Chittaboina, R. Zhuo, P. M. Harrell, Y. T. Trinh, Q. Zhang, I. L. Urbatsch, and G. Chang. 2009. “Structure of P-glycoprotein reveals a molecular basis for poly-specific drug binding.” *Science* 323 (5922):1718-22. doi: 10.1126/science.1168750.

Babenko, A. P., and J. Bryan. 2003. “Sur domains that associate with and gate KATP pores define a novel gatekeeper.” *Journal of Biological Chemistry* 278 (43):41577-80. doi: 10.1074/jbc.C300363200.

Bao, Z., X. Qi, S. Hong, K. Xu, F. He, M. Zhang, J. Chen, D. Chao, W. Zhao, D. Li, J. Wang, and P. Zhang. 2017. “Structure and mechanism of a group-I cobalt energy coupling factor transporter.” *Cell Research* 27 (5):675-687. doi: 10.1038/cr.2017.38.

Bekri, S., G. Kispal, H. Lange, E. Fitzsimons, J. Tolmie, R. Lill, and D. F. Bishop. 2000. “Human ABC7 transporter: Gene structure and mutation causing X-linked sideroblastic anemia with ataxia with disruption of cytosolic iron-sulfur protein maturation.” *Blood* 96 (9):3256-64.

Berger, E. A., and L. A. Heppel. 1974. “Different mechanisms of energy coupling for the shock-sensitive and shock-resistant amino acid permeases of *Escherichia coli*.” *Journal of Biological Chemistry* 249 (24):7747-55.

Bernard, D. G., Y. Cheng, Y. Zhao, and J. Balk. 2009. “An allelic mutant series of ATM3 reveals its key role in the biogenesis of cytosolic iron-sulfur proteins in *Arabidopsis*.” *Plant Physiology* 151 (2):590-602. doi: 10.1104/pp.109.143651.

Berntsson, R. P., S. H. Smits, L. Schmitt, D. J. Slotboom, and B. Poolman. 2010. “A structural classification of substrate-binding proteins.” *FEBS Letters* 584 (12):2606-17. doi: 10.1016/j.febslet.2010.04.043.

Bi, Y., E. Mann, C. Whitfield, and J. Zimmer. 2018. “Architecture of a channel-forming O-antigen polysaccharide ABC transporter.” *Nature* 553 (7688):361-365. doi: 10.1038/nature25190.

Biemans-Oldehinkel, E., M. K. Doeven, and B. Poolman. 2006. “ABC transporter architecture and regulatory roles of accessory domains.” *FEBS Letters* 580 (4):1023-35. doi: 10.1016/j.febslet.2005.11.079.

Bjorkman, A. J., R. A. Binnie, H. Zhang, L. B. Cole, M. A. Hermodson, and S. L. Mowbray. 1994. “Probing protein-protein interactions: The ribose-binding protein in bacterial transport and chemotaxis.” *Journal of Biological Chemistry* 269 (48):30206-11.

Borst, P., and A. H. Schinkel. 2013. “P-glycoprotein ABCB1: A major player in drug handling by mammals.” *Journal of Clinical Investigation* 123 (10):4131-3. doi: 10.1172/JCI70430.

Borths, E. L., K. P. Locher, A. T. Lee, and D. C. Rees. 2002. “The structure of *Escherichia coli* BtuF and binding to its cognate ATP binding cassette transporter.” *Proceedings of the National Academy of Sciences of the United States of America* 99 (26):16642-7. doi: 10.1073/pnas.262659699.

Borths, E. L., B. Poolman, R. N. Hvorup, K. P. Locher, and D. C. Rees. 2005. “*In vitro* functional characterization of BtuCD-F, the *Escherichia coli* ABC transporter for vitamin B_{12} uptake.” *Biochemistry* 44 (49):16301-9. doi: 10.1021/bi0513103.

Brahm, J. 1977. “Temperature-dependent changes of chloride transport kinetics in human red cells.” *Journal of General Physiology* 70 (3):283-306. doi: 10.1085/jgp.70.3.283.

Chavan, H., M. M. Khan, G. Tegos, and P. Krishnamurthy. 2013. “Efficient purification and reconstitution of ATP binding cassette transporter B6 (ABCB6) for functional and structural studies.” *Journal of Biological Chemistry* 288 (31):22658-69. doi: 10.1074/jbc.M113.485284.

Chavan, H., M. Oruganti, and P. Krishnamurthy. 2011. “The ATP-binding cassette transporter ABCB6 is induced by arsenic and protects against arsenic cytotoxicity.” *Toxicological Science* 120 (2):519-28. doi: 10.1093/toxsci/kfr008.

Chen, C. J., J. E. Chin, K. Ueda, D. P. Clark, I. Pastan, M. M. Gottesman, and I. B. Roninson. 1986. “Internal duplication and homology with bacterial transport proteins in the *mdr1* (P-glycoprotein) gene from multidrug-resistant human cells.” *Cell* 47 (3):381-9. doi: 10.1016/0092-8674(86)90595-7.

Chen, J., S. Sharma, F. A. Quiocho, and A. L. Davidson. 2001. “Trapping the transition state of an ATP-binding cassette transporter: Evidence for a concerted mechanism of maltose transport.” *Proceedings of the National Academy of Sciences of the United States of America* 98 (4):1525-30. doi: 10.1073/pnas.041542498.

Chen, L., W. T. Hou, T. Fan, B. Liu, T. Pan, Y. H. Li, Y. L. Jiang, W. Wen, Z. P. Chen, L. Sun, C. Z. Zhou, and Y. Chen. 2020. “Cryo-electron microscopy structure and transport mechanism of a wall teichoic acid ABC transporter.” *MBio* 11 (2). doi: 10.1128/mBio.02749-19.

Cole, S. P. 2014. “Multidrug resistance protein 1 (MRP1, ABCC1), a "multitasking" ATP-binding cassette (ABC) transporter.” *Journal of Biological Chemistry* 289 (45):30880-8. doi: 10.1074/jbc.R114.609248.

Covitz, K. M., C. H. Panagiotidis, L. I. Hor, M. Reyes, N. A. Treptow, and H. A. Shuman. 1994. “Mutations that alter the transmembrane signalling pathway in an ATP binding cassette (ABC) transporter.” *EMBO Journal* 13 (7):1752-9.

Davidson, A. L., E. Dassa, C. Orelle, and J. Chen. 2008. “Structure, function, and evolution of bacterial ATP-binding cassette systems.” *Microbiology and Molecular Biology Reviews* 72 (2):317-64. doi: 10.1128/MMBR.00031-07.

Davidson, A. L., and H. Nikaido. 1990. “Overproduction, solubilization, and reconstitution of the maltose transport system from *Escherichia coli*.” *Journal of Biological Chemistry* 265 (8):4254-60.

Dawson, R. J., and K. P. Locher. 2006. “Structure of a bacterial multidrug ABC transporter.” *Nature* 443 (7108):180-5. doi: 10.1038/nature05155.

Dean, D. A., A. L. Davidson, and H. Nikaido. 1989. “Maltose transport in membrane vesicles of *Escherichia coli* is linked to ATP hydrolysis.” *Proceedings of the National Academy of Sciences of the United States of America* 86 (23):9134-8. doi: 10.1073/pnas.86.23.9134.

Dong, M., F. Penin, and L. G. Baggetto. 1996. “Efficient purification and reconstitution of P-glycoprotein for functional and structural studies.” *Journal of Biological Chemistry* 271 (46):28875-83. doi: 10.1074/jbc.271.46.28875.

Eytan, G. D., R. Regev, and Y. G. Assaraf. 1996. “Functional reconstitution of P-glycoprotein reveals an apparent near stoichiometric drug transport to ATP hydrolysis.” *Journal of Biological Chemistry* 271 (6):3172-8. doi: 10.1074/jbc.271.6.3172.

Felder, C. B., R. C. Graul, A. Y. Lee, H. P. Merkle, and W. Sadee. 1999. “The Venus flytrap of periplasmic binding proteins: an ancient protein module present in multiple drug receptors.” *AAPS PharmSci* 1 (2):E2. doi: 10.1208/ps010202.

Fitzpatrick, A. W. P., S. Llabres, A. Neuberger, J. N. Blaza, X. C. Bai, U. Okada, S. Murakami, H. W. van Veen, U. Zachariae, S. H. W. Scheres, B. F. Luisi, and D. Du. 2017. “Structure of the MacAB-TolC ABC-type tripartite multidrug efflux pump.” *Nature Microbiology* 2:17070. doi: 10.1038/nmicrobiol.2017.70.

Fukami-Kobayashi, K., Y. Tateno, and K. Nishikawa. 1999. “Domain dislocation: A change of core structure in periplasmic binding proteins in their evolutionary history.” *Journal of Molecular Biology* 286 (1):279-90. doi: 10.1006/jmbi.1998.2454.

Geertsma, E. R., N. A. Nik Mahmood, G. K. Schuurman-Wolters, and B. Poolman. 2008. “Membrane reconstitution of ABC transporters and assays of translocator function.” *Nature Protocols* 3 (2):256-66. doi: 10.1038/nprot.2007.519.

George, A. M., and P. M. Jones. 2012. “Perspectives on the structure-function of ABC transporters: the switch and constant contact models.” *Progress in Biophysics and Molecular Biology* 109 (3):95-107. doi: 10.1016/j.pbiomolbio.2012.06.003.

Glavinas, H., D. Mehn, M. Jani, B. Oosterhuis, K. Heredi-Szabo, and P. Krajcsi. 2008. “Utilization of membrane vesicle preparations to study drug-ABC transporter interactions.” *Expert Opinion on Drug Metabolism and Toxicology* 4 (6):721-32. doi: 10.1517/17425255.4.6.721.

Gonin, S., P. Arnoux, B. Pierru, J. Lavergne, B. Alonso, M. Sabaty, and D. Pignol. 2007. “Crystal structures of an extracytoplasmic solute receptor from a TRAP transporter in its open and closed forms reveal a helix-swapped dimer requiring a cation for alpha-keto acid binding.” *BMC Structural Biology* 7:11. doi: 10.1186/1472-6807-7-11.

He, J. J., and F. A. Quiocho. 1993. “Dominant role of local dipoles in stabilizing uncompensated charges on a sulfate sequestered in a periplasmic active transport protein.” *Protein Science* 2 (10):1643-7. doi: 10.1002/pro.5560021010.

Higgins, C. F. 1992. "ABC transporters: From microorganisms to man." *Annual Review of Cell Biology* 8:67-113. doi: 10.1146/annurev.cb.08.110192.000435.

Higgins, C. F., I. D. Hiles, G. P. Salmond, D. R. Gill, J. A. Downie, I. J. Evans, I. B. Holland, L. Gray, S. D. Buckel, A. W. Bell, and et al. 1986. "A family of related ATP-binding subunits coupled to many distinct biological processes in bacteria." *Nature* 323 (6087):448-50. doi: 10.1038/323448a0.

Higgins, C. F., and K. J. Linton. 2004. "The ATP switch model for ABC transporters." *Nature Structural & Molecular Biology* 11 (10):918-926. doi: 10.1038/nsmb836.

Hlavac, V., and P. Soucek. 2015. "Role of family D ATP-binding cassette transporters (ABCD) in cancer." *Biochemical Society Transactions* 43 (5):937-42. doi: 10.1042/BST20150114.

Hofmann, S., D. Januliene, A. R. Mehdipour, C. Thomas, E. Stefan, S. Bruchert, B. T. Kuhn, E. R. Geertsma, G. Hummer, R. Tampe, and A. Moeller. 2019. "Conformation space of a heterodimeric ABC exporter under turnover conditions." *Nature* 571 (7766):580-583. doi: 10.1038/s41586-019-1391-0.

Hollenstein, K., D. C. Frei, and K. P. Locher. 2007. "Structure of an ABC transporter in complex with its binding protein." *Nature* 446 (7132):213-6. doi: 10.1038/nature05626.

Hsu, K. 2018. "Exploring the potential roles of band 3 and aquaporin-1 in blood CO_2 transport-inspired by comparative studies of glycophorin B-A-B hybrid protein GP.Mur." *Frontiers in Physiology* 9:733. doi: 10.3389/fphys.2018.00733.

Hu, Y., S. Rech, R. P. Gunsalus, and D. C. Rees. 1997. "Crystal structure of the molybdate binding protein ModA." *Nature Structural Biology* 4 (9):703-7. doi: 10.1038/nsb0997-703.

Hvorup, R. N., B. A. Goetz, M. Niederer, K. Hollenstein, E. Perozo, and K. P. Locher. 2007. "Asymmetry in the structure of the ABC transporter-binding protein complex BtuCD-BtuF." *Science* 317 (5843):1387-90. doi: 10.1126/science.1145950.

Hyde, S. C., P. Emsley, M. J. Hartshorn, M. M. Mimmack, U. Gileadi, S. R. Pearce, M. P. Gallagher, D. R. Gill, R. E. Hubbard, and C. F. Higgins. 1990. "Structural model of ATP-binding proteins associated with cystic fibrosis, multidrug resistance and bacterial transport." *Nature* 346 (6282):362-5. doi: 10.1038/346362a0.

Jardetzky, O. 1966. “Simple allosteric model for membrane pumps.” *Nature* 211 (5052):969-70.

Jayaram, H., A. Accardi, F. Wu, C. Williams, and C. Miller. 2008. “Ion permeation through a Cl^--selective channel designed from a CLC Cl^-/H^+ exchanger.” *Proceedings of the National Academy of Sciences of the United States of America* 105 (32):11194-9. doi: 10.1073/pnas.0804503105.

Johnson, Z. L., and J. Chen. 2017. “Structural basis of substrate recognition by the multidrug resistance protein MRP1.” *Cell* 168 (6):1075-1085 e9. doi: 10.1016/j.cell.2017.01.041.

Jones, P. M., and A. M. George. 2014. “A reciprocating twin-channel model for ABC transporters.” *Quarterly Reviews of Biophysics* 47 (3):189-220. doi: 10.1017/S0033583514000031.

Kadaba, N. S., J. T. Kaiser, E. Johnson, A. Lee, and D. C. Rees. 2008. “The high-affinity *E. coli* methionine ABC transporter: Structure and allosteric regulation.” *Science* 321 (5886):250-3. doi: 10.1126/science.1157987.

Kamischke, C., J. Fan, J. Bergeron, H. D. Kulasekara, Z. D. Dalebroux, A. Burrell, J. M. Kollman, and S. I. Miller. 2019. “The *Acinetobacter baumannii* Mla system and glycerophospholipid transport to the outer membrane.” *Elife* 8. doi: 10.7554/eLife.40171.

Kandt, C., Z. Xu, and D. P. Tieleman. 2006. “Opening and closing motions in the periplasmic vitamin B_{12} binding protein BtuF.” *Biochemistry* 45 (44):13284-92. doi: 10.1021/bi061280j.

Khare, D., M. L. Oldham, C. Orelle, A. L. Davidson, and J. Chen. 2009. “Alternating access in maltose transporter mediated by rigid-body rotations.” *Molecular Cell* 33 (4):528-36. doi: 10.1016/j.molcel.2009.01.035.

Kim, Y., and J. Chen. 2018. “Molecular structure of human P-glycoprotein in the ATP-bound, outward-facing conformation.” *Science* 359 (6378):915-919. doi: 10.1126/science.aar7389.

Kispal, G., P. Csere, B. Guiard, and R. Lill. 1997. “The ABC transporter Atm1p is required for mitochondrial iron homeostasis.” *FEBS Letters* 418 (3):346-50.

Kiss, K., A. Brozik, N. Kucsma, A. Toth, M. Gera, L. Berry, A. Vallentin, H. Vial, M. Vidal, and G. Szakacs. 2012. “Shifting the paradigm: The putative mitochondrial protein ABCB6 resides in the lysosomes of cells and in the plasma membrane of erythrocytes.” *PLoS One* 7 (5):e37378. doi: 10.1371/journal.pone.0037378.

Kleizen, B., J. F. Hunt, I. Callebaut, T. C. Hwang, I. Sermet-Gaudelus, S. Hafkemeyer, and D. N. Sheppard. 2020. “CFTR: New insights into structure and function and implications for modulation by small molecules.” *Journal of Cystic Fibrosis* 19 Suppl 1:S19-S24. doi: 10.1016/j.jcf.2019.10.021.

Korkhov, V. M., S. A. Mireku, and K. P. Locher. 2012. “Structure of AMP-PNP-bound vitamin B_{12} transporter BtuCD-F.” *Nature* 490 (7420):367-72. doi: 10.1038/nature11442.

Koropatkin, N., A. M. Randich, M. Bhattacharyya-Pakrasi, H. B. Pakrasi, and T. J. Smith. 2007. “The structure of the iron-binding protein, FutA1, from *Synechocystis* 6803.” *Journal of Biological Chemistry* 282 (37):27468-77. doi: 10.1074/jbc.M704136200.

Krishnamurthy, P. C., G. Du, Y. Fukuda, D. Sun, J. Sampath, K. E. Mercer, J. Wang, B. Sosa-Pineda, K. G. Murti, and J. D. Schuetz. 2006. “Identification of a mammalian mitochondrial porphyrin transporter.” *Nature* 443 (7111):586-9. doi: 10.1038/nature05125.

Kuhnke, G., K. Neumann, U. Muhlenhoff, and R. Lill. 2006. “Stimulation of the ATPase activity of the yeast mitochondrial ABC transporter Atm1p by thiol compounds.” *Molecular Membrane Biology* 23 (2):173-184.

Lecher, J., M. Pittelkow, S. Zobel, J. Bursy, T. Bonig, S. H. Smits, L. Schmitt, and E. Bremer. 2009. “The crystal structure of UehA in complex with ectoine-A comparison with other TRAP-T binding proteins.” *Journal of Molecular Biology* 389 (1):58-73. doi: 10.1016/j.jmb.2009.03.077.

Ledvina, P. S., A. L. Tsai, Z. Wang, E. Koehl, and F. A. Quiocho. 1998. “Dominant role of local dipolar interactions in phosphate binding to a receptor cleft with an electronegative charge surface: Equilibrium, kinetic, and crystallographic studies.” *Protein Science* 7 (12):2550-9. doi: 10.1002/pro.5560071208.

Lee, J. Y., L. N. Kinch, D. M. Borek, J. Wang, J. Wang, I. L. Urbatsch, X. S. Xie, N. V. Grishin, J. C. Cohen, Z. Otwinowski, H. H. Hobbs, and D. M. Rosenbaum. 2016. “Crystal structure of the human sterol transporter ABCG5/ABCG8." *Nature* 533 (7604):561-4. doi: 10.1038/nature17666.

Lee, J. Y., J. G. Yang, D. Zhitnitsky, O. Lewinson, and D. C. Rees. 2014. "Structural basis for heavy metal detoxification by an Atm1-type ABC exporter." *Science* 343 (6175):1133-6. doi: 10.1126/science.1246489.

Lee, K. P. K., J. Chen, and R. MacKinnon. 2017. "Molecular structure of human KATP in complex with ATP and ADP." *Elife* 6. doi: 10.7554/eLife.32481.

Lee, Y. H., R. K. Deka, M. V. Norgard, J. D. Radolf, and C. A. Hasemann. 1999. "*Treponema pallidum* TroA is a periplasmic zinc-binding protein with a helical backbone." *Nature Structural Biology* 6 (7):628-33. doi: 10.1038/10677.

Lerebours, A., V. V. To, and J. P. Bourdineaud. 2016. "*Danio rerio* ABC transporter genes *abcb3* and *abcb7* play a protecting role against metal contamination." *Journal of Applied Toxicology* 36 (12):1551-1557. doi: 10.1002/jat.3313.

Levdikov, V. M., E. V. Blagova, J. A. Brannigan, L. Wright, A. A. Vagin, and A. J. Wilkinson. 2005. "The structure of the oligopeptide-binding protein, AppA, from *Bacillus subtilis* in complex with a nonapeptide." *Journal of Molecular Biology* 345 (4):879-92. doi: 10.1016/j.jmb.2004.10.089.

Lewinson, O., and N. Livnat-Levanon. 2017. "Mechanism of action of ABC importers: conservation, divergence, and physiological adaptations." *Journal of Biological Chemistry* 429 (5):606-619. doi: 10.1016/j.jmb.2017.01.010.

Li, Y., B. J. Orlando, and M. Liao. 2019. "Structural basis of lipopolysaccharide extraction by the LptB$_2$FGC complex." *Nature* 567 (7749):486-490. doi: 10.1038/s41586-019-1025-6.

Lill, R., and G. Kispal. 2001. "Mitochondrial ABC transporters." *Research in Microbiology* 152 (3-4):331-40.

Lin, D. Y., S. Huang, and J. Chen. 2015. "Crystal structures of a polypeptide processing and secretion transporter." *Nature* 523 (7561):425-30. doi: 10.1038/nature14623.

Livnat-Levanon, N., I. Gilson A, N. Ben-Tal, and O. Lewinson. 2016. "The uncoupled ATPase activity of the ABC transporter BtuC$_2$D$_2$ leads to a hysteretic conformational change, conformational memory, and improved activity." *Science Reports* 6:21696. doi: 10.1038/srep21696.

Locher, K. P. 2016. “Mechanistic diversity in ATP-binding cassette (ABC) transporters.” *Nature Structural & Molecular Biology* 23 (6):487-93. doi: 10.1038/nsmb.3216.

Locher, K. P., A. T. Lee, and D. C. Rees. 2002. “The *E. coli* BtuCD structure: A framework for ABC transporter architecture and mechanism.” *Science* 296 (5570):1091-8. doi: 10.1126/science.1071142.

Lycklama, A. Nijeholt J. A., R. Vietrov, G. K. Schuurman-Wolters, and B. Poolman. 2018. “Energy coupling efficiency in the type I ABC transporter GlnPQ.” *Journal of Molecular Biology* 430 (6):853-866. doi: 10.1016/j.jmb.2018.02.001.

Manolaridis, I., S. M. Jackson, N. M. I. Taylor, J. Kowal, H. Stahlberg, and K. P. Locher. 2018. “Cryo-EM structures of a human ABCG2 mutant trapped in ATP-bound and substrate-bound states.” *Nature* 563 (7731):426-430. doi: 10.1038/s41586-018-0680-3.

Maruyama, Y., T. Itoh, A. Kaneko, Y. Nishitani, B. Mikami, W. Hashimoto, and K. Murata. 2015. “Structure of a bacterial ABC transporter involved in the import of an acidic polysaccharide alginate.” *Structure* 23 (9):1643-1654. doi: 10.1016/j.str.2015.06.021.

Mi, W., Y. Li, S. H. Yoon, R. K. Ernst, T. Walz, and M. Liao. 2017. “Structural basis of MsbA-mediated lipopolysaccharide transport.” *Nature* 549 (7671):233-237. doi: 10.1038/nature23649.

Miao, R., H. Kim, U.M.K. Koppolu, E.A. Ellis, R.A. Scott, and P.A. Lindahl. 2009. “Biophysical characterization of the iron in mitochondria from Atm1p-depleted *Saccharomyces cerevisiae*.” *Biochemistry* 48.

Moitra, K., L. Silverton, K. Limpert, K. Im, and M. Dean. 2011. “Moving out: From sterol transport to drug resistance - the ABCG subfamily of efflux pumps.” *Drug Metabolism and Drug Interactions* 26 (3):105-11. doi: 10.1515/DMDI.2011.015.

Mueckler, M., and B. Thorens. 2013. “The SLC2 (GLUT) family of membrane transporters.” *Molecular Aspects of Medicine* 34 (2-3):121-38. doi: 10.1016/j.mam.2012.07.001.

Muller, A., G. H. Thomas, R. Horler, J. A. Brannigan, E. Blagova, V. M. Levdikov, M. J. Fogg, K. S. Wilson, and A. J. Wilkinson. 2005. “An ATP-binding cassette-type cysteine transporter in *Campylobacter jejuni* inferred from the structure of an extracytoplasmic solute receptor protein.” *Mol Microbiol* 57 (1):143-55. doi: 10.1111/j.1365-2958.2005.04691.x.

Naoe, Y., N. Nakamura, A. Doi, M. Sawabe, H. Nakamura, Y. Shiro, and H. Sugimoto. 2016. "Crystal structure of bacterial haem importer complex in the inward-facing conformation." *Nature Communications* 7:13411. doi: 10.1038/ncomms13411.

Nguyen, P. T., J. Y. Lai, A. T. Lee, J. T. Kaiser, and D. C. Rees. 2018. "Noncanonical role for the binding protein in substrate uptake by the MetNI methionine ATP Binding Cassette (ABC) transporter." *Proceedings of the National Academy of Sciences of the United States of America* 115 (45):E10596-E10604. doi: 10.1073/pnas.1811003115.

Nguyen, P. T., Q. W. Li, N. S. Kadaba, J. Y. Lai, J. G. Yang, and D. C. Rees. 2015. "The contribution of methionine to the stability of the *Escherichia coli* MetNIQ ABC transporter-substrate binding protein complex." *Biological Chemistry* 396 (9-10):1127-34. doi: 10.1515/hsz-2015-0131.

Nikaido, K., and G. F. Ames. 1999. "One intact ATP-binding subunit is sufficient to support ATP hydrolysis and translocation in an ABC transporter, the histidine permease." *Journal of Biological Chemistry* 274 (38):26727-35. doi: 10.1074/jbc.274.38.26727.

Noll, A., C. Thomas, V. Herbring, T. Zollmann, K. Barth, A. R. Mehdipour, T. M. Tomasiak, S. Bruchert, B. Joseph, R. Abele, V. Olieric, M. Wang, K. Diederichs, G. Hummer, R. M. Stroud, K. M. Pos, and R. Tampe. 2017. "Crystal structure and mechanistic basis of a functional homolog of the antigen transporter TAP." *Proceedings of the National Academy of Sciences of the United States of America* 114 (4):E438-E447. doi: 10.1073/pnas.1620009114.

Oldham, M. L., N. Grigorieff, and J. Chen. 2016. "Structure of the transporter associated with antigen processing trapped by herpes simplex virus." *Elife* 5. doi: 10.7554/eLife.21829.

Oldham, M. L., D. Khare, F. A. Quiocho, A. L. Davidson, and J. Chen. 2007. "Crystal structure of a catalytic intermediate of the maltose transporter." *Nature* 450 (7169):515-21. doi: 10.1038/nature06264.

Olsen, J. A., A. Alam, J. Kowal, B. Stieger, and K. P. Locher. 2020. "Structure of the human lipid exporter ABCB4 in a lipid environment." *Nature Structural & Molecular Biology* 27 (1):62-70. doi: 10.1038/s41594-019-0354-3.

Owens, T. W., R. J. Taylor, K. S. Pahil, B. R. Bertani, N. Ruiz, A. C. Kruse, and D. Kahne. 2019. “Structural basis of unidirectional export of lipopolysaccharide to the cell surface.” *Nature* 567 (7749):550-553. doi: 10.1038/s41586-019-1039-0.

Paterson, J. K., S. Shukla, C. M. Black, T. Tachiwada, S. Garfield, S. Wincovitch, D. N. Ernst, A. Agadir, X. Li, S. V. Ambudkar, G. Szakacs, S. Akiyama, and M. M. Gottesman. 2007. “Human ABCB6 localizes to both the outer mitochondrial membrane and the plasma membrane.” *Biochemistry* 46 (33):9443-52. doi: 10.1021/bi700015m.

Patzlaff, J. S., T. van der Heide, and B. Poolman. 2003. “The ATP/substrate stoichiometry of the ATP-binding cassette (ABC) transporter OpuA.” *Journal of Biological Chemistry* 278 (32):29546-51. doi: 10.1074/jbc.M304796200.

Perez, C., S. Gerber, J. Boilevin, M. Bucher, T. Darbre, M. Aebi, J. L. Reymond, and K. P. Locher. 2015. “Structure and mechanism of an active lipid-linked oligosaccharide flippase.” *Nature* 524 (7566):433-8. doi: 10.1038/nature14953.

Pflugrath, J. W., and F. A. Quiocho. 1985. “Sulphate sequestered in the sulphate-binding protein of *Salmonella typhimurium* is bound solely by hydrogen bonds.” *Nature* 314 (6008):257-60. doi: 10.1038/314257a0.

Phillips, G. N., Jr., V. K. Mahajan, A. K. Siu, and F. A. Quiocho. 1976. “Structure of L-arabinose-binding protein from *Escherichia coli* at 5 Å resolution and preliminary results at 3.5 Å.” *Proceedings of the National Academy of Sciences of the United States of America* 73 (7):2186-90. doi: 10.1073/pnas.73.7.2186.

Pinkett, H. W., A. T. Lee, P. Lum, K. P. Locher, and D. C. Rees. 2007. “An inward-facing conformation of a putative metal-chelate-type ABC transporter.” *Science* 315 (5810):373-7. doi: 10.1126/science.1133488.

Pondarre, C., B. B. Antiochos, D. R. Campagna, S. L. Clarke, E. L. Greer, K. M. Deck, A. McDonald, A. P. Han, A. Medlock, J. L. Kutok, S. A. Anderson, R. S. Eisenstein, and M. D. Fleming. 2006. “The mitochondrial ATP-binding cassette transporter Abcb7 is essential in mice and participates in cytosolic iron-sulfur cluster biogenesis.” *Human Molecular Genetics* 15 (6):953-64. doi: 10.1093/hmg/ddl012.

Qi, W., J. Li, C. Y. Chain, G. A. Pasquevich, A. F. Pasquevich, and J. A. Cowan. 2012. "Glutathione complexed Fe-S centers." *Journal of the American Chemical Society* 134 (26):10745-8. doi: 10.1021/ja302186j.

Qian, H., X. Zhao, P. Cao, J. Lei, N. Yan, and X. Gong. 2017. "Structure of the human lipid exporter ABCA1." *Cell* 169 (7):1228-1239 e10. doi: 10.1016/j.cell.2017.05.020.

Quiocho, F. A., G. N. Phillips, Jr., R. G. Parsons, and R. W. Hogg. 1974. "Letter: Crystallographic data of an L-arabinose-binding protein from *Escherichia coli*." *Journal of Molecular Biology* 86 (2):491-3. doi: 10.1016/0022-2836(74)90032-1.

Quiocho, F. A., J. C. Spurlino, and L. E. Rodseth. 1997. "Extensive features of tight oligosaccharide binding revealed in high-resolution structures of the maltodextrin transport/chemosensory receptor." *Structure* 5 (8):997-1015. doi: 10.1016/s0969-2126(97)00253-0.

Quiocho, F. A., and N. K. Vyas. 1984. "Novel stereospecificity of the L-arabinose-binding protein." *Nature* 310 (5976):381-6. doi: 10.1038/310381a0.

Rakvacs, Z., N. Kucsma, M. Gera, B. Igriczi, K. Kiss, J. Barna, D. Kovacs, T. Vellai, L. Bencs, J. M. Reisecker, N. Szoboszlai, and G. Szakacs. 2019. "The human ABCB6 protein is the functional homologue of HMT-1 proteins mediating cadmium detoxification." *Cellular and Molecular Life Sciences* 76 (20):4131-4144. doi: 10.1007/s00018-019-03105-5.

Rees, D. C., E. Johnson, and O. Lewinson. 2009. "ABC transporters: The power to change." *Nature Reviews: Molecular Cell Biology* 10 (3):218-27. doi: 10.1038/nrm2646.

Riedel, S., B. Siemiatkowska, M. Watanabe, C. S. Muller, V. Schunemann, R. Hoefgen, and S. Leimkuhler. 2019. "The ABCB7-like transporter PexA in *Rhodobacter capsulatus* Is involved in the translocation of reactive sulfur species." *Front Microbiol* 10:406. doi: 10.3389/fmicb.2019.00406.

Sack, J. S., M. A. Saper, and F. A. Quiocho. 1989. "Periplasmic binding protein structure and function: Refined X-ray structures of the leucine/isoleucine/valine-binding protein and its complex with leucine." *Journal of Molecular Biology* 206 (1):171-91. doi: 10.1016/0022-2836(89)90531-7.

Santos, J. A., S. Rempel, S. T. Mous, C. T. Pereira, J. Ter Beek, J. W. de Gier, A. Guskov, and D. J. Slotboom. 2018. "Functional and structural characterization of an ECF-type ABC transporter for vitamin B_{12}." *Elife* 7. doi: 10.7554/eLife.35828.

Saper, M. A., and F. A. Quiocho. 1983. "Leucine, isoleucine, valine-binding protein from *Escherichia coli*: Structure at 3.0-Å resolution and location of the binding site." *Journal of Biological Chemistry* 258 (18):11057-62.

Schou, J., A. Tybjaerg-Hansen, H. J. Moller, B. G. Nordestgaard, and R. Frikke-Schmidt. 2012. "ABC transporter genes and risk of type 2 diabetes: A study of 40,000 individuals from the general population." *Diabetes Care* 35 (12):2600-6. doi: 10.2337/dc12-0082.

Shintre, C. A., A. C. Pike, Q. Li, J. I. Kim, A. J. Barr, S. Goubin, L. Shrestha, J. Yang, G. Berridge, J. Ross, P. J. Stansfeld, M. S. Sansom, A. M. Edwards, C. Bountra, B. D. Marsden, F. von Delft, A. N. Bullock, O. Gileadi, N. A. Burgess-Brown, and E. P. Carpenter. 2013. "Structures of ABCB10, a human ATP-binding cassette transporter in apo- and nucleotide-bound states." *Proceedings of the National Academy of Sciences of the United States of America* 110 (24):9710-5. doi: 10.1073/pnas.1217042110.

Skou, J. C. 1998. "The identification of the sodium-potassium pump (Nobel Lecture)." *Angewandte Chemie International Edition in English* 37 (17):2320-2328. doi: 10.1002/(SICI)1521-3773(19980918)37:17<2320::AID-ANIE2320>3.0.CO;2-2.

Srinivasan, V., A. J. Pierik, and R. Lill. 2014. "Crystal structures of nucleotide-free and glutathione-bound mitochondrial ABC transporter Atm1." *Science* 343 (6175):1137-40. doi: 10.1126/science.1246729.

Teschner, J., N. Lachmann, J. Schulze, M. Geisler, K. Selbach, J. Santamaria-Araujo, J. Balk, R. R. Mendel, and F. Bittner. 2010. "A novel role for *Arabidopsis* mitochondrial ABC transporter ATM3 in molybdenum cofactor biosynthesis." *Plant Cell* 22 (2):468-80. doi: 10.1105/tpc.109.068478.

Theodoulou, F. L., and I. D. Kerr. 2015. "ABC transporter research: Going strong 40 years on." *Biochemical Society Transactions* 43 (5):1033-40. doi: 10.1042/BST20150139.

Trakhanov, S., N. K. Vyas, H. Luecke, D. M. Kristensen, J. Ma, and F. A. Quiocho. 2005. "Ligand-free and -bound structures of the binding protein (LivJ) of the *Escherichia coli* ABC leucine/isoleucine/valine transport system: trajectory and dynamics of the interdomain rotation and ligand specificity." *Biochemistry* 44 (17):6597-608. doi: 10.1021/bi047302o.

Tsuchida, M., Y. Emi, Y. Kida, and M. Sakaguchi. 2008. "Human ABC transporter isoform B6 (ABCB6) localizes primarily in the Golgi apparatus." *Biochemical and Biophysical Research Communications* 369 (2):369-75. doi: 10.1016/j.bbrc.2008.02.027.

Vasiliou, V., K. Vasiliou, and D. W. Nebert. 2009. "Human ATP-binding cassette (ABC) transporter family." *Human Genomics* 3 (3):281-90.

Viitanen, P., M. L. Garcia, and H. R. Kaback. 1984. "Purified reconstituted lac carrier protein from *Escherichia coli* is fully functional." *Proceedings of the National Academy of Sciences of the United States of America* 81 (6):1629-33. doi: 10.1073/pnas.81.6.1629.

Wang, J., F. Sun, D. W. Zhang, Y. Ma, F. Xu, J. D. Belani, J. C. Cohen, H. H. Hobbs, and X. S. Xie. 2006. "Sterol transfer by ABCG5 and ABCG8: *In vitro* assay and reconstitution." *Journal of Biological Chemistry* 281 (38):27894-904. doi: 10.1074/jbc.M605603200.

Wang, T., G. Fu, X. Pan, J. Wu, X. Gong, J. Wang, and Y. Shi. 2013. "Structure of a bacterial energy-coupling factor transporter." *Nature* 497 (7448):272-6. doi: 10.1038/nature12045.

Wang, Zhiming, Wenxin Hu, and Hongjin Zheng. 2020. "Pathogenic siderophore ABC importer YbtPQ adopts a surprising fold of exporter." *Science Advances* 6 (6). doi: 10.1126/sciadv.aay7997.

Ward, A., C. L. Reyes, J. Yu, C. B. Roth, and G. Chang. 2007. "Flexibility in the ABC transporter MsbA: Alternating access with a twist." *Proceedings of the National Academy of Sciences of the United States of America* 104 (48):19005-10. doi: 10.1073/pnas.0709388104.

Woo, J. S., A. Zeltina, B. A. Goetz, and K. P. Locher. 2012. "X-ray structure of the *Yersinia pestis* heme transporter HmuUV." *Nature Structural & Molecular Biology* 19 (12):1310-5. doi: 10.1038/nsmb.2417.

Xu, D., Z. Feng, W. T. Hou, Y. L. Jiang, L. Wang, L. Sun, C. Z. Zhou, and Y. Chen. 2019. "Cryo-EM structure of human lysosomal cobalamin exporter ABCD4." *Cell Research* 29 (12):1039-1041. doi: 10.1038/s41422-019-0222-z.

Yang, H. B., W. T. Hou, M. T. Cheng, Y. L. Jiang, Y. Chen, and C. Z. Zhou. 2018. "Structure of a MacAB-like efflux pump from *Streptococcus pneumoniae*." *Nature Communications* 9 (1):196. doi: 10.1038/s41467-017-02741-4.

Yao, N., S. Trakhanov, and F. A. Quiocho. 1994. "Refined 1.89-Å structure of the histidine-binding protein complexed with histidine and its relationship with many other active transport/chemosensory proteins." *Biochemistry* 33 (16):4769-79. doi: 10.1021/bi00182a004.

Yoo, E. G. 2016. "Sitosterolemia: A review and update of pathophysiology, clinical spectrum, diagnosis, and management." *Annals of Pediatric Endocrinology & Metabolism* 21 (1):7-14. doi: 10.6065/apem.2016.21.1.7.

Yu, J., J. Ge, J. Heuveling, E. Schneider, and M. Yang. 2015. "Structural basis for substrate specificity of an amino acid ABC transporter." *Proceedings of the National Academy of Sciences of the United States of America* 112 (16):5243-8. doi: 10.1073/pnas.1415037112.

Zehnpfennig, B., I. L. Urbatsch, and H. J. Galla. 2009. "Functional reconstitution of human ABCC3 into proteoliposomes reveals a transport mechanism with positive cooperativity." *Biochemistry* 48 (20):4423-30. doi: 10.1021/bi9001908.

Zhang, Z., F. Liu, and J. Chen. 2018. "Molecular structure of the ATP-bound, phosphorylated human CFTR." *Proceedings of the National Academy of Sciences of the United States of America* 115 (50):12757-12762. doi: 10.1073/pnas.1815287115.

Zuo, J., Z. Wu, Y. Li, Z. Shen, X. Feng, M. Zhang, and H. Ye. 2017. "Mitochondrial ABC transporter ATM3 is essential for cytosolic iron-sulfur cluster assembly." *Plant Physiology* 173 (4):2096-2109. doi: 10.1104/pp.16.01760.

Chapter 2

A STRUCTURAL FRAMEWORK FOR THE UNIDIRECTIONAL TRANSPORT OF A BACTERIAL ABC EXPORTER

This chapter is adapted from:

> Fan, C., Kaiser, J.T. and Rees, D.C. “A structural framework for the unidirectional transport by a bacterial ABC exporter.” *In revision*.

2.1 Abstract

The ATP-binding cassette (ABC) transporter of mitochondria (Atm1) mediates iron homeostasis in eukaryotes, while the prokaryotic homolog from *Novosphingobium aromaticivorans* (*Na*Atm1) can export glutathione derivatives and confer protection against heavy metal toxicity. To establish the structural framework underlying the *Na*Atm1 transport mechanism, we determined eight structures by X-ray crystallography and single particle cryo-EM in distinct conformational states, stabilized by individual disulfide crosslinks and nucleotides. As *Na*Atm1 progresses through the transport cycle, conformational changes in transmembrane helix 6 (TM6) alter the glutathione binding site and the associated substrate binding cavity. Significantly, kinking of TM6 in the post-ATP hydrolysis state stabilized by $MgADPVO_4$ eliminates this cavity, precluding uptake of glutathione derivatives. The presence of this cavity during the transition from the inward-facing to outward-facing conformational states, and its absence in the reverse direction, thereby provides an elegant and conceptually simple mechanism for enforcing the export directionality of transport by *Na*Atm1. One of the disulfide crosslinked *Na*Atm1 variants characterized in this work retains significant glutathione transport activity, suggesting ATP hydrolysis and substrate transport by Atm1 may involve a limited set of conformational states with minimal separation of the nucleotide binding domains in the inward-facing conformation.

2.2 Significance Statement

ATP Binding Cassette (ABC) transporters are generally viewed to function as either exporters or importers, but in principle they could transport substrates in either direction across the membrane. Structural studies of the prokaryotic ABC exporter *Na*Atm1 demonstrate that progression through the transport cycle is accompanied by changes in transmembrane helix 6 (TM6) that modulate the binding cavity for transported substrate. Significantly, kinking of TM6 in a post-ATP hydrolysis state stabilized by $MgADPVO_4$ eliminates the substrate binding cavity. The presence of this cavity during the transition from the inward-facing to outward-facing conformational states, and its absence in the reverse direction, thereby provides an elegant and conceptually simple mechanism for enforcing the export directionality of transport.

2.3 Introduction

The translocation mechanism of ATP Binding Cassette (ABC) transporters is generally described in terms of the alternating access model involving inward-facing, occluded and outward-facing states, with the transitions between states coupled to the binding and hydrolysis of ATP, along with product release (Higgins 1992, Davidson et al. 2008, Rees, Johnson, and Lewinson 2009, Locher 2016, Thomas and Tampe 2018). ABC exporters constitute an important branch of ABC transporters found in all forms of life, exhibiting a broad range of activities from exporting macromolecular building blocks to serving as multidrug efflux pumps. Despite the name, it has generally not been experimentally demonstrated that exporters have a unique transport directionality, or how this directionality is maintained. An informative example is provided by the recent studies of mycobacterial ABC transporters with an exporter fold that mediates the uptake of cobalamin and other hydrophilic compounds (Rempel et al. 2020, Arnold et al. 2020). The structural characterization of ABC exporters in distinct conformational states has been primarily achieved by controlling the nucleotide state, often in combination with the ATPase deficient "E to Q" mutant in the Walker-B motif (Moody et al. 2002). Other approaches to stabilizing specific conformational states include introduction of disulfide crosslinks between the nucleotide binding domains (NBDs) (Korkhov, Mireku, and Locher 2012, Alam et al. 2018), or through the binding of state-specific nanobodies (Alam et al. 2019), inhibitors (Alam et al. 2018), or substrate (Johnson and Chen 2017). Detailed structural frameworks are now available for addressing the transport mechanism of different ABC exporter systems, including CFTR (Liu et al. 2017, Zhang, Liu, and Chen 2017, Liu et al. 2019), MsbA (Ward et al. 2007, Mi et al. 2017), TmrAB (Hofmann et al. 2019), PglK (Perez et al. 2019), and P-glycoprotein (Aller et al. 2009, Jin et al. 2012, Kim and Chen 2018, Alam et al. 2018) in distinct conformational states. These studies reinforce the view that significant conformational variability exists between different members of the ABC exporter family.

The ABC-transporter of mitochondria (Atm1) is a homodimeric transporter that was first shown to be involved in iron-sulfur cluster biogenesis in yeast (Kispal et al. 1997); it is also a homolog to the human ABCB6 and ABCB7 transporters and plant atm3 transporter that were all found to play a role in iron homeostasis (Lill and Kispal 2001, Pondarre et al. 2006, Cavadini et al. 2007, Zuo et al. 2017). Previous analysis of the bacterial homolog from *Novosphingobium aromaticivorans* (*Na*Atm1) revealed a role in heavy metal detoxification, plausibly by exporting metallated glutathione species (Lee et al. 2014). The initial characterization of *Na*Atm1 established the structure in an inward-facing conformation and defined the binding interactions for glutathione derivatives (Lee et al. 2014). To stabilize *Na*Atm1 in different conformations states, we introduced disulfide crosslinks at multiple positions within the NBD dimerization interface. In this work, we report the structures and functions of disulfide crosslinking variants, together with the "E to Q" ATP-hydrolysis deficient mutant and wild type *Na*Atm1, in distinct conformational states. From these structures, a framework for the transport cycle of *Na*Atm1 is delineated. Unexpectedly, one of the crosslinked variants retained significant GSSG transport activity and further exhibited improved coupling efficiency between ATP hydrolysis and GSSG transport relative to wild type protein, highlighting the role of conformational dynamics in the coupling mechanism. A prominent feature of the transport cycle is the coupling between the conformation of transmembrane helix 6 (TM6) and the glutathione binding site. During the transition from inward to outward conformation, a large binding cavity exists, but in the return process, as trapped by $MgADPVO_4$ in a post-ATP hydrolysis state, kinking of TM6 eliminates this cavity. The net effect would be to restrict glutathione transport to the export direction, providing a mechanism for enforcing directionality of the transport mechanism.

2.4 Results

Disulfide crosslinking

To stabilize *Na*Atm1 in distinct conformational states, we introduced cysteine mutations at the dimerization interface between the NBDs of the natively cysteine-less homodimeric *Na*Atm1. Three residues identified through sequence alignments of *Na*Atm1 to other transporters with dimerized NBDs (Dawson and Locher 2006, Korkhov, Mireku, and Locher 2012, Alam et al. 2018) are T525, S526, and A527, positioned near the Walker-B motif where disulfide bonds could potentially form between the two equivalent residues (Figure S1a). These residues were separately mutated to cysteine to generate three single-site variants: *Na*T525C, *Na*S526C, and *Na*A527C. Initial crosslinking tests with purified protein revealed that similar crosslinking yields at ~70% (Figure

S1b). We crystallized and solved the structures of all three variants to assess the consequences of the disulfide crosslinks on the conformational states of *Na*Atm1.

Crystal structures of inward-facing occluded conformations

*Na*A527C crystallized in a MgADP bound state with four transporters in the asymmetric unit. Despite the moderate anisotropic diffraction to 3.7 Å resolution, two distinguishable inward-facing occluded states, designated state #1 (Figure 1a) and state #2 (Figure 1b), were evident. The presence of two conformational states was confirmed from the positions of the selenium sites in selenomethionine substituted protein crystals (Figure S2a). Clear electron density was observed for the disulfide bridges and the nucleotides in all four transporters (Figure S2bc). A structural alignment of the two states revealed that while the transmembrane domains (TMDs) are structurally similar, sharing an overall RMSD of 1.7 Å (Figure S3a), the α-helical subdomains of the NBDs differ by a small rotation (~10°) about the molecular two-fold axis of the transporter (Figure S3b). These two states also differ from the previous *Na*Atm1 inward-facing conformation with RMSDs of 2.1 Å and 4.4 Å for state #1 and state #2, respectively (Figure S3cd); the primary differences are in the separation of the NBDs and changes near the coupling helices of the TMDs that interact with the NBDs.

Crystals of *Na*A527C were prepared either with or without 5 mM GSSG. While weak density in the substrate binding pocket was observed for crystals grown in the presence of GSSG, the moderate resolution was insufficient to unambiguously establish the presence of GSSG. To crystallographically assess the substrate binding capability of *Na*A527C, we co-crystallized *Na*A527C with a glutathione-mercury complex (GS-Hg) and collected data at the Hg absorption edge. Anomalous electron density peaks identifying Hg sites were found in all GSSG binding sites (Lee et al. 2014) and were strongest in the two best resolved transporters in the asymmetric unit (Figure S4). These sites were not observed in control studies using mercury compounds in the absence of glutathione, supporting the presence of GS-Hg and the substrate binding capability of *Na*A527C.

Crystal structures of the pre-hydrolysis occluded conformations

Crystals of *Na*S526C diffracted anisotropically to 3.4 Å resolution, and the transporter adopted an occluded conformation with bound ATP and a fully resolved disulfide bridge (Figure 1c, S5ab). Even though GSSG or GS-Hg were included during crystallization, the binding of substrate was not detected in the electron density maps. The periplasmic regions of the transporter (residues 60-82 and 284-300) were not well resolved in the electron density maps, possibly due to the lack of stabilizing crystal contacts. These regions were accordingly modeled based on the previously determined high-resolution crystal structure and refined with reduced occupancies.

Surprisingly, crystals of *Na*T525C were nearly isomorphous to those of *Na*S526C, and the structures were found to be quite similar (Figure 1d). In contrast to the *Na*A527C and *Na*S526C structures, however, no disulfide bridge was observed between the two T525C residues (Figure 1d, S5cd). Instead, the two T525C residues were 13 Å apart, calculated from the corresponding Cα positions. Since no reductant was present, presumably crystallization of the crosslinked protein was not favored in this condition and instead the uncrosslinked population crystallized.

Crystals of the ATP-hydrolysis deficient *Na*E523Q diffracted anisotropically to 3.3 Å resolution and the structure revealed the occluded conformation with ATP bound (Figure 1e, S5e). While the overall structure of *Na*E523Q was similar to that observed for *Na*S526C and *Na*T525C, including the flexible periplasmic loops, the crystal form was distinct. Overall, the three occluded structures are similar with RMSDs in the range of 0.5 - 0.7 Å (Figure S5fgh).

Wild type *Na*Atm1 was crystallized in an occluded state with bound MgAMPPNP (Figure 1f, S6a). This occluded structure shared a similar overall architecture with the other three mutant occluded structures with alignment RMSDs of ~1 Å (Figure S6bcd); the major conformational differences are in the resolved periplasmic loop regions and the partially resolved elbow helices. Although GSSG was present in the crystallization conditions, bound substrate was not evident in the crystal structure, which is the same outcome observed for the other occluded structures.

Single-particle cryo-EM structure of the post-hydrolysis closed conformation

To capture the post-hydrolysis state of the transporter, we utilized the post-hydrolysis ATP analog MgADPVO$_4$ (Goodno 1982) and determined a single-particle cryo-EM structure of *Na*Atm1 in a closed conformation at 3.0 Å resolution (Figure 1g, S7abc). For this analysis, *Na*Atm1 was reconstituted in nanodiscs formed by the membrane scaffolding protein MSP1D1 (Ritchie et al. 2009). The overall architecture of this single particle structure has RMSDs in the range of 1.7 - 2.1 Å with the crystal structures in the pre-hydrolysis occluded state (Figure S7defg). These structures all adopt similarly dimerized NBDs, but with pronounced differences in the TMDs. The kinked TM6 observed in the post-hydrolysis MgADPVO$_4$ occluded structure contrasts with the straightened conformation observed in the pre-hydrolysis occluded states; as a consequence of this structural change, the GSSG binding cavity is eliminated and so this form is designated as a "closed" state.

Single-particle structure of the inward-facing conformation

We determined an inward-facing conformation of *Na*Atm1 reconstituted into nanodiscs by single particle cryo-EM in the absence of ligands. This reconstruction was obtained at 3.9 Å resolution (Figure 1h, S8ab) where large side chains are well resolved (Figure S8c). This structure is designated as a "wide-open" inward-facing conformation, since the NBDs are significantly further apart in comparison to the original crystal structures of *Na*Atm1. The RMSDs between this structure and other inward-facing conformation (Lee et al. 2014) and the inward-facing occluded structures are in 5.8 - 9.3 Å, with the major difference in the separation of the two half-transporters (Figure S8def).

ATPase activities, transport activities and coupling efficiencies of all variants

To establish the functional competence of the disulfide crosslinked variants and wild type *Na*Atm1, their ATPase and transport activities were characterized (Figure 2). ATPase activities were measured in both detergent and proteoliposomes (PLS) with 10 mM ATP and 2.5 mM GSSG, concentrations approximating those measured physiologically (Bennett et al. 2009) (Figure 2ab). Wild type *Na*Atm1 in detergent showed a basal ATPase activity of 115 ± 15 nmol Pi min^{-1} mg^{-1} transporter, and the addition of 2.5 mM GSSG stimulated the ATPase activity by nearly 2-fold to 206 ± 8 nmol Pi min^{-1} mg^{-1} transporter. *Na*Atm1 reconstituted in PLS showed an ATPase activity of 66 ± 13 nmol Pi min^{-1} mg^{-1} transporter, again with ~2-fold stimulation in the presence of 2.5 mM GSSG to 152 ± 31 nmol Pi min^{-1} mg^{-1} transporter. Based on the *Na*Atm1 molecular weight of 133 kDa (with 1 mg

≈ 7.5 nmole), neglecting orientation effects and assuming all the transporters are functionally active, an ATPase rate of 152 nmol Pi min^{-1} mg^{-1} corresponds to a turnover rate of ~20 ATP min^{-1}. Unexpectedly, *Na*S526C had a similar basal ATPase activity to the wild type protein, with no stimulation by GSSG in detergent, but a slight stimulation by GSSG in PLS. *Na*T525C exhibited reduced ATPase activities in detergent and PLS. The *Na*A527C and *Na*E523Q constructs exhibited little ATPase activity in either detergent or PLS.

The transport activity was by necessity measured only in PLS, again using 10 mM MgATP and 2.5 mM GSSG (Figure 2cd). Control experiments indicated that low levels of GSSG may stick to liposomes, complicating the measurement of very low levels of transport activities. For wild type *Na*Atm1, the uptake of GSSG was linear with time, corresponding to a rate of 1.52 ± 0.03 nmol GSSG min^{-1} mg^{-1} transporter, equivalent to ~0.2 GSSG translocated per minute per transporter (Figure 2c). Interestingly, *Na*S526C exhibited ~ 60% of wild type transport activity at a rate of 0.9 ± 0.1 nmol GSSG min^{-1} mg^{-1} transporter (Figure 2d), while *Na*T525C retained about 30% of the transport activity of wild type *Na*Atm1. *Na*A527C and *Na*E523Q exhibited GSSG uptake rates ~10% of the wild type protein transport activity (Figure 2d). A complicating feature in the interpretation of these results is that since disulfide bond formation in these variants was not quantitative, we cannot eliminate some contribution by the uncrosslinked material to the observed ATPase and transport activities. If the uncrosslinked material exhibits the same activity as wild type protein, then in the absence of transport activity by the crosslinked protein, a residual ~30% transport activity would be anticipated based on the estimate of 70% disulfide bond formation. As the transport activity measured for the *Na*S526C variant exceeds this threshold, *Na*Atm1 with a disulfide crosslink between the two Cys 526 residues is competent for GSSG transport. In contrast, the transport activity *Na*T525C variant is at the 30% threshold value, and hence the transport competence of the crosslinked variant cannot be confidently established.

From the ATPase and transport activities, the coupling efficiency - the number of ATP hydrolyzed per GSSG translocated - can be computed. For this calculation, we defined the coupling efficiency as the ratio of the total ATPase rate to the transport rate measured under the same conditions (in the presence of 2.5 mM substrate). For the wild type protein, the coupling efficiency is measured to be

100 ± 20, compared to 76 ± 6 for the *Na*S526C variant. Although these coupling efficiencies may seem high relative to the canonical value of 2 typically envisioned for ABC transporters (Patzlaff, van der Heide, and Poolman 2003), they are in the range reported for other transporters (Table S1), reflecting the generally high basal ATPase activity and coupling inefficiencies of ABC transporters.

Volumes of substrate binding cavities

The volumes of the substrate binding cavities in different structures were calculated using the program CastP with a 2.5 Å probe radius (Tian et al. 2018). For reference, the volume of a GSSG molecule (molecular weight 612.6 g mol^{-1}) is estimated to be ~740 Å^3, assuming a partial specific volume for GSSG typical of globular proteins (~0.73 cm^3 g^{-1}) (Erickson 2009). With the exception of the MgADPVO$_4$ stabilized state, the binding pockets in the various *Na*Atm1 structures are all found to be of sufficient size to accommodate GSSG (Figure 3). Significantly, the binding pocket is no longer present in the "post-hydrolysis" MgADPVO$_4$ stabilized state (Figure 3i). For reference, the outward-facing conformation of Sav1866 (Dawson and Locher 2006) has a cavity volume of ~3,400 Å^3 (Figure 3j). As GSSG was not experimentally found to be present in the pre-hydrolysis occluded conformations, the absence of substrate in these structures suggests that they may represent lower affinity, post-translocational states of the transporter when the empty transporter is transitioning back to the inward-facing conformation. The comparison with the post-hydrolysis occluded structure suggests that a key conformational change after ATP hydrolysis is the generation of kinked TM6 helices, which eliminates the central cavity.

2.5 Discussion

We have expanded the structurally characterized conformations of the ABC exporter *Na*Atm1 from the previously determined inward-facing conformation (Lee et al. 2014) to multiple occluded conformations, through introduction of disulfide bridges and the use of nucleotide analogs. From all available *Na*Atm1 structures, we have observed the inward-facing conformations (including the inward-facing occluded conformation) in either nucleotide-free or MgADP-bound forms, while the occluded conformations are stabilized by ATP or analogs (Figure 1). Substrates have only been observed to bind to the inward-facing conformations, even though substrate binding cavities of sufficient size to accommodate GSSG are present in the occluded conformations (Figure 4). The most striking changes between these different conformational states occur in the TMDs, most notably in the positioning of TM4-5 described previously (Lee et al. 2014), and the straightening and kinking of TM6s.

The conformation of TM6 is directly coupled to the binding of glutathione by *Na*Atm1 and hence to the directionality of transport. The kinking of TM6 observed in the inward-facing, inward-facing occluded and the post-hydrolysis occluded structures (Figure 4a), contrasts with the more subtly bent TM6 helices in the pre-hydrolysis occluded structures of *Na*Atm1 (Figure 4a). The TM6 kink present in the inward-facing conformation occurs adjacent to a turn of 310-helix at residues 314-317, such that the amide NH groups of residues 319 and 320 hydrogen bond to the α-carboxyl of the γ-Glu of GSSG, while the α-amino group of GSSG hydrogen bonds to the carbonyl oxygen of residue 316 (Lee et al. 2014) (Figure 4b). Upon transition to the occluded conformation of *Na*Atm1, TM6 adopts a regular α-helical structure (Figure 4c), accompanied by an increased separation between the symmetry related TM6s, so that these peptide bond groups are no longer available to hydrogen bond the transported substrate. As a consequence, as *Na*Atm1 transitions from the inward to outward-facing conformational states, the binding site for the transported substrate is restructured for substrate release, providing a mechanism for coupling protein conformation to the ligand binding affinity. As *Na*Atm1 resets to the inward-facing conformation, kinking of TM6 in the MgADPVO$_4$ stabilized form effectively closes the substrate binding cavity. The inability to bind glutathione in the post-hydrolysis state enforces the unidirectionality of the transport cycle, since the binding site only exists during the transition from the inward to outward facing conformations.

Other ABC transporter systems, such as the oligosaccharide flippase, PglK, the multidrug resistance protein, TmrAB, and the drug efflux pump ABCB1 (P-glycoprotein), also exhibit changes in TM6 kinking and binding between distinct conformational states (Figure S9). The detailed progression of changes in TM6 vary between the different transporters, however, and *Na*Atm1 is so far unique in the nearly straight TM6s present in the occluded structure. The coupling of TM6 to substrate binding observed with *Na*Atm1 has also been noted for other transporters. From the analysis of multiple TmrAB structures, TM6 of each subunit was identified as the gatekeeper controlling access to substrate binding cavities (Hofmann et al. 2019), while in ABCB1 (Alam et al. 2018), TM6 and TM12 (equivalent to TM6 in a full ABC transporter), were found to be important in substrate binding, along with TM4 and TM10. Rather than a universal set of structural changes associated with the transport cycle, however, each system will have its own distinct structural features. Thus, detailed characterizations of the different intermediate states of a specific transporter are essential for addressing its transport mechanism.

The structural and functional characterization of the disulfide crosslinked variants revealed several unanticipated findings that reflect the apparent the plasticity of the NBD-NBD interface. The structures of the two disulfide crosslinking variants, *Na*A527C and *Na*S526C, determined in this study included three different conformational states, the two inward-occluded conformations of *Na*A527C and the occluded conformation of *Na*S526C. Unexpectedly, the disulfide crosslinked *N*aS526C variant not only hydrolyzed ATP, but could also transport substrate (Figure 2). While the presence of a disulfide crosslink between the NBDs might be expected to inhibit the functionality by restricting relevant conformational changes, the observation that this variant is transport competent indicates that ATP hydrolysis and substrate transport involve a limited set of conformational states that do not require wide separation of the NBDs.

The characterization of *Na*Atm1 in multiple conformational states provides the opportunity to outline the structural changes that occur in the transport cycle. Since each structure represents a separate experiment determined under different conditions, it is not possible to unambiguously order the structures in a sequence along the transport cycle. With the introduction of several assumptions about the relationships between structures, however, a working model for a structure-based transport mechanism of *Na*Atm1 can be devised. These assumptions are: i) the available *Na*Atm1 structures approximate on-path intermediates, ii) the transported ligand binds preferentially to the inward-facing conformation (Lee et al. 2014, Srinivasan, Pierik, and Lill 2014) and iii) the outward-facing conformation is stabilized by ATP (see (Dawson and Locher 2006, Kim and Chen 2018, Stefan, Hofmann, and Tampe 2020)), with return to the inward-facing conformation accompanying Pi dissociation (Hofmann et al. 2019). A schematic mechanism for substrate-dependent transport by *Na*Atm1 is presented in Figure 5 (top), with the main features summarized as follows. Substrate and

MgATP can bind to the transporter in both the inward-facing and inward-facing occluded states. The transition from the inward-facing to outward-facing conformation through the occluded states is accompanied by ATP binding. The progression from the inward-facing to outward-facing conformations is reflected in the straightening of TM6, which alters the GSSG binding site, creating the larger cavity of the occluded conformation, and ultimately leading to dissociation from the outward-facing conformation. Although we were unable to capture an outward facing conformation by either x-ray crystallography or electron microscopy, it is possible that the flexibility of the periplasmic loops observed in the occluded conformation may transiently open an exit pathway for glutathione release. On resetting to the inward conformation, regeneration of kinked TM6 helices creates a closed conformation by eliminating the substrate binding cavity as trapped in the post-hydrolysis $MgADPVO_4$ trapped state. Although we have only observed symmetric *Na*Atm1 structures, we cannot exclude the presence of asymmetric states as observed for TmrAB (Hofmann et al. 2019). Upon Pi dissociation, the transporter returns to the inward-facing and/or the inward-facing occluded states, and the transporter is ready for the next transport cycle.

A key question for ABC exporters centers on the role of the substrate in the transport cycle; given the observed basal ATPase activities, there is not an obligatory coupling between the ATPase activity and substrate binding/transport. This is a surprising situation given what is known for the transport cycles of well-coupled transporters such as lac permease (Kaback 2015) and P-type ATPases (Palmgren and Nissen 2011), where both the transported substrate and the energy source (H^+ or ATP, respectively) must be present for translocation to proceed. As depicted in Figure 5 (bottom), the uncoupled activity could reflect the operation of a parallel, but distinct, pathway for ATP hydrolysis that occurs in the absence of the transported substrate, as proposed for certain ABC importers (Lewinson and Livnat-Levanon 2017) and ABC exporters (Hofmann et al. 2019). A key intermediate for understanding the coupling mechanism of an ABC exporter is the occluded state with both substrate and ATP bound (Figure 5); this state has not been captured for *Na*Atm1 or, to our knowledge, for any other ABC exporter. This particular species perhaps exists only transiently before the substrate dissociates from the outward-facing conformation (also likely a transiently occurring state (Hofmann et al. 2019, Grossmann et al. 2014)), even in the transport-competent form with the disulfide linked NBDs. Engineering a construct adopting an occluded conformation with both substrate and ATP bound will be a priority for future investigations to address the coupling mechanism of *Na*Atm1.

2.6 Material and Methods

Mutagenesis and protein expression

The gene encoding *Na*Atm1 (with GenBank accession code ABD27067) was previously cloned into a pJL-H6 ligation independent vector with 6-His tag on the carboxy-terminus (Lee et al. 2014), and deposited in Addgene with catalog #78308. All mutants were generated using Q5 Site-Directed Mutagenesis Kit (New England Biolabs). All native proteins were overexpressed in *Escherichia coli* BL21-gold (DE3) cells (Agilent Technologies) using ZYM-5052 autoinduction media and all the selenomethionine substituted proteins were overexpressed in *Escherichia coli* B834 (DE3) cells (Novagen) using PASM-5052 autoinduction media as described previously (Lee et al. 2014). Cells were collected by centrifugation and stored at -80 ˚C until use.

Purification and crosslinking

Frozen cell pellets of cysteine mutants were resuspended in lysis buffer containing 100 mM NaCl, 20 mM Tris, pH 7.5, 40 mM imidazole, pH 7.5, 5 mM β-mercaptoethanol (BME), 10 mM $MgCl_2$, 0.5% (w/v) n-dodecyl-β-D-maltopyranoside (DDM) (Anatrace), 0.5% (w/v) octaethylene glycol monododecyl ether (C12E8) (Anatrace), lysozyme, DNase, and protease inhibitor tablet. The resuspended cells were lysed either by solubilizing by stirring for 3 hours at 4 ˚C, or by using a M-110L pneumatic microfluidizer (Microfluidics). Unlysed cells and cell debris were removed by ultracentrifugation at ~113,000x g for 45 minutes at 4 ˚C. The supernatant was collected and loaded onto a prewashed NiNTA column with NiNTA wash buffer at 4 ˚C. NiNTA wash buffer contained 100 mM NaCl, 20 mM Tris, pH 7.5, 50 mM imidazole, pH 7.5, 5 mM BME, 0.05% DDM and 0.05% C12E8. Elution was achieved using the same buffer containing 350 mM imidazole instead. The eluted protein was then buffer exchanged to 100 mM NaCl, 20 mM Tris, pH 7.5, 0.05% DDM and 0.05% C12E8 (SEC buffer). Oxidation of engineered cysteines to form disulfide bonds was achieved by incubating buffer exchanged protein with 1 mM Cu (II) $(1,10\text{-phenanthroline})_3$ for 1 hour at 4 ˚C. Crosslinked sample was buffer exchanged into SEC buffer to remove the oxidant, and further purified by size exclusion chromatography (SEC) using HiLoad 16/60 Superdex 200 (GE Healthcare). Fractions were pooled and concentrated to 20-35 mg/mL using an Amicon Ultra 15 concentrator (Millipore) with a molecular weight cutoff of 100 kDa. Wild type *Na*Atm1 was solubilized in lysis buffer containing 1% DDM and purified in NiNTA and SEC buffers containing 0.1% DDM for crystallization in the occluded conformation with MgAMPPNP.

Crystallizations

*Na*A527C was crystallized in MemGold (Molecular Dimensions) condition #68. Upon optimization of the crystallization conditions, including the use of additive screens (Hampton Research), the best crystals were grown from 100 mM NaCl, 100 mM Tris, pH 8.3, 25 mM $MgCl_2$, and 28% polyethylene glycol 2,000 monomethyl ether (PEG 2,000 MME) with 20 mM ATP, pH 7.5 at 20 ˚C. *Na*A527C crystallization sample was prepared at 20 mg/mL with 1 mM ATP, pH 7.5, 5 mM EDTA, pH 7.5 and with or without 5 mM GSSG, pH 7.5. Crystals appeared in about 2 weeks and lasted for about a month. Crystals were harvested in cryoprotectant solutions containing 100 mM NaCl, 100 mM Tris, pH 8.3, 25 mM $MgCl_2$, 28% PEG 2,000 MME with PEG 400 at 10%, 15%, and 20% before flash-freezing in liquid nitrogen.

*Na*S526C, *Na*T525C and *Na*E523Q crystals were prepared in the same condition as *Na*A527C except the removal of $MgCl_2$ in the crystallization well solution. All crystallization samples were prepared with 1 mM ATP, pH 7.5 and 5 mM EDTA, pH 7.5. The crystallization condition of *Na*T525C was further optimized with 200 mM of NDSB-221 using the Additive Screen (Hampton Research). The crystallization condition of *Na*E523Q was further optimized with 10 mM dithiothreitol but without 20 mM ATP, pH 7.5 in the crystallization conditions. Crystals of all three constructs were harvested in cryoprotectant solutions containing 100 mM NaCl, 100 mM Tris, pH 8.3, 28% PEG 2,000 MME with PEG 400 at 10%, 15%, and 20% before flash-freezing in liquid nitrogen.

*Na*Atm1 purified in DDM was crystallized in MemChannel (Molecular Dimensions) condition #29. The crystallization sample was prepared with 1 mM AMPPNP, pH 7.5, 2 mM $MgCl_2$, and either with or without 5 mM GSSG, pH 7.5. The condition was further optimized to 50 mM ADA, pH 7.1, 8-10% PEG 1000 and 8-10% PEG 1500 at 20˚C with protein at 8 mg/ml. Crystals appeared within a week and were harvested in cryoprotectant solutions containing 50 mM ADA, pH 7.1, 10% PEG 1000 and 10% PEG 1500 with PEG400 at 10%, 15%, and 20% before flash-freezing in liquid nitrogen.

X-ray data collection and structure determinations

X-ray datasets were collected at the Stanford Synchrotron Radiation Laboratory beamline 12-2 using a Pilatus 6M detector with Blu-Ice interface (McPhillips et al. 2002) and Advanced Photon Source GM/CA beamline 23ID-B using an Eiger 16M detector with JBluIce-EPICS interface (Stepanov et al. 2011). All datasets were processed and integrated with XDS (Kabsch 2010) and scaled with Aimless (Winn et al. 2011). For the *Na*A527C crystal structure, the first three transporters in the asymmetric unit were identified by searching for multiple copies of the TMDs and NBDs using the inward-facing structure (PDB ID: 4MRN) with Phaser in Phenix (Adams et al. 2010). Due to the relatively poor electron density for the fourth transporter, the helices of the TMDs were first built using Find Helices and Strands in Phenix (Adams et al. 2010), then a full transporter from the previously identified partial model was superposed onto the built helices in Coot (Emsley et al. 2010), which resulted in the misplacement of one NBD. The misplaced NBD was removed from the model and was subsequently correctly placed using Molrep in CCP4 (Winn et al. 2011). For the *Na*S526C structure, molecular replacement was carried out using Sav1866 (PDB ID: 2HYD) with superposed *Na*Atm1 sequence as the input model for Phaser in Phenix (Adams et al. 2010). For the *Na*T525C, *Na*E523Q and *Na*Atm1 structures, molecular replacement was carried out using the *Na*S526C structure as the input model for Phaser in Phenix (Adams et al. 2010). For all structures, experimental phase information was derived from SeMet datasets by MR-SAD using AutoSol in Phenix (Adams et al. 2010). Iterative refinement and model building cycles were carried out with phenix.refine in Phenix (Adams et al. 2010), Refmac in CCP4 (Winn et al. 2011) and Coot (Emsley et al. 2010). The final refinements were performed with phenix.refine in Phenix (Adams et al. 2010).

Single particle sample and grid preparation

The expression plasmid for the membrane scaffolding protein (MSP1D1) was purchased from Addgene (plasmid #20061) and its expression and purification were carried out using published protocols (Ritchie et al. 2009). The reconstitutions were performed with 1-palmitoyl-2-oleoyl-glycero-3-phosphocholine (POPC) (Avanti Lipids) at a ratio of *Na*Atm1: MSP1D1: POPC = 1:(2-4):130. For the structure with MgADPVO$_4$ bound, MSP1D1 and POPC were added after incubating detergent purified protein with 4 mM MgCl$_2$, 4 mM ATP, pH 7.5, and 4 mM VO$_4^{3-}$ for 4hrs to allow for ATP hydrolysis at 4˚C. VO$_4^{3-}$ was prepared from sodium orthovanadate following a published protocol (Oldham and Chen 2011). The reconstituted samples were incubated overnight at 4 ˚C with BioBeads addition at 400 mg/ml for detergent removal. The samples were subjected to size exclusion chromatography with Superdex 200 Increase 10/300 (GE Healthcare). Peak fractions were either pooled and concentrated or directly used for grid preparation. Grids were prepared with protein concentrations between 0.6 to 4 mg/mL. Briefly, 3 μL of protein solution was applied to freshly glow discharged UltrAuFoil 2/2 200 mesh grids (MgADPVO$_4$ stabilized closed conformation) and QuantiFoil Au R1.2/1.3 200 mesh grids (inward-facing conformation), blotted for 4 seconds with 0 blot force and 100% humidity at room temperature using Vitrobot Mark IV (FEI).

Single-particle data collection, processing and refinement

For the MgADPVO$_4$ stabilized closed conformation, two datasets were collected with a Gatan K3 direct electron detector on a 300 keV Titan Krios in the super-resolution mode using SerialEM. For data collection, a total dosage of 60 $e^-/Å^2$ was utilized, with a defocus range between -1.5 to -3.5 μm at the Caltech CryoEM facility, and a total dosage of 48.6 $e^-/Å^2$ with a defocus range between -1.7 to -2.4 μm at the Stanford-SLAC Cryo-EM Center (S2C2). The two datasets were processed separately. For the inward-facing conformation, data was collected with a Gatan K2 Summit direct electron detector on a 300 keV Titan Krios in the super-resolution mode using EPU with a total dosage of 36 $e^-/Å^2$ with a defocus range between -1.0 to -3.5 μm at the Caltech CryoEM facility.

Processing of all single particle datasets was performed with cryoSPARC 2 (Punjani et al. 2017), using patch-motion for motion correction and estimating the CTF parameters with CTFFIND (Rohou and Grigorieff 2015). Particles were picked using either a previous reconstruction of *Na*Atm1 or a blob as template, and then extracted. Rounds of 2D classifications were performed, leaving ~170K particles for the MgADPVO$_4$ stabilized closed conformation using data from the S2C2 collection and ~100K particles for the inward-facing conformation for the 3D reconstruction.

The resulting 3D reconstructions were then refined with homogeneous and non-uniform refinements in cryoSPARC 2 (Punjani et al. 2017). For the $MgADPVO_4$ stabilized closed structure, local CTF refinement was carried out to refine per-particle defocus, and the final local refinement was performed using symmetry expanded (C2) particles in cryoSPARC 2 (Punjani et al. 2017) along with a mask generated in Chimera (Pettersen et al. 2004) based on a fitted model.

Initial model fitting was carried out with phenix.dock_in_map in Phenix (Adams et al. 2010) using a single chain of the MgAMPPNP bound occluded structure (PDB ID: 6PAR) as the starting model for the $MgADPVO_4$ bound closed structure, and a single chain of the inward-facing conformation (PDB ID: 4MRN) for the wide open inward-facing conformation. Model building and ligand fitting were manually carried out in Coot (Emsley et al. 2010) and the structures were iteratively refined using phenix.real_space_refine in Phenix (Adams et al. 2010).

Proteoliposome preparation and transport assay

Proteoliposomes (PLS) were prepared by following the published protocol for ABC transporter PLS reconstitution using *Escherichia coli* polar lipid extract and 1,2-dioleoyl-sn-glycero-3-phosphocholine (DOPC) (Avanti Lipids) (Geertsma et al. 2008), with an additional step of Biobeads addition at 40 mg/ml to ensure the complete removal of detergents. The transport assay was conducted with *Na*Atm1 reconstituted in PLS in a 1 mL format at 37 °C. The reaction mixture contained PLS at 5 mg/mL, 10 mM MgATP, pH 7.5, 2.5 mM GSSG, pH 7.5, and transport buffer at 85 mM NaCl, and 17 mM Tris, pH 7.5. The different controls were also prepared in a similar fashion. 150 µL aliquots of the reaction mixture were taken every 15 minutes, added to 1 ml cold transport buffer, and then ultracentrifuged at ~203,000g in a TLA 100.3 rotor in a Beckman Ultima benchtop ultracentrifuge for 10 minutes at 4 °C. The pellets were washed 10 times with cold transport buffer, and then resuspended to 100 µl with solubilization buffer (85 mM NaCl, 17 mM Tris, pH 7.5 and 2% sodium dodecanoyl sarcosine (Anatrace)). The samples were solubilized for 2 hours until the solution clarified before spinning down in the TLA 100 rotor to remove bubbles. 10 µL samples were taken for GSSG quantification using the Glutathione Quantification Assay (Sigma-Aldrich). Reactions were done in triplicates and the rates were not corrected for orientation effects of *Na*Atm1 in PLS.

ATPase assay

The ATPase activity was determined by the molybdate-based phosphate quantification method (Chifflet et al. 1988). All reactions were performed in a 250 µL scale with a final protein concentration of 0.05 mg/ml for both PLS and detergent, at various concentrations of MgATP and GSSG, pH 7.5 at 37 °C. 50 µL of reaction were taken every 5 minutes for 4 times, mixed with 50 µL of 12% SDS in a 96-well plate at room temperature. 100 µL of ascorbic acid/molybdate mix was added, incubated for 5 minutes before the addition of 150 µL of citric acid/arsenite/acetic acid solution. The reaction was then incubated for 20 minutes at room temperature before reading at 850 nm with a Tecan plate reader. Reactions were done in triplicates, the measurements were plotted against time, and the final linear rates were fitted with nonlinear regression fit using Prism 8. The rates were not corrected for orientation of *Na*Atm1 in PLS.

2.7 Acknowledgments

We thank the staffs of the Stanford Synchrotron Radiation Lightsource beamline 12-2 and of the Advanced Photon Source GM/CA beamline for support during X-ray diffraction data collection. Discussions with Paul Adams, Kaspar Locher, Oded Lewinson, Gabriele Meloni, William Clemons, the organizers and speakers at the Cold Spring Harbor X-ray Method in Structural Biology Course (2018), the CCP4/APS School for Macromolecular Crystallography (2017), and the SBGrid/NE-CAT Phenix Workshop (2016) are gratefully acknowledged. We thank Haoqing Wang, Andrey Malyutin, Songye Chen and Megan Meyer for their support during single-particle cryo-EM data collections. We also thank the Gordon and Betty Moore Foundation and the Beckman Institute for their generous support of the Molecular Observatory at Caltech. Use of the Stanford Synchrotron Radiation Lightsource, SLAC National Accelerator Laboratory, is supported by the U.S. Department of Energy, Office of Science, Office of Basic Energy Sciences under Contract No. DE-AC02-76SF00515. The SSRL Structural Molecular Biology Program is supported by the DOE Office of Biological and Environmental Research, and by the National Institutes of Health, National Institute of General Medical Sciences (including P41GM103393). GM/CA@APS has been funded in whole or in part with Federal funds from the National Cancer Institute (ACB-12002) and the National

Institute of General Medical Sciences (AGM-12006). This research used resources of the Advanced Photon Source, a U.S. Department of Energy (DOE) Office of Science User Facility operated for the DOE Office of Science by Argonne National Laboratory under Contract No. DE-AC02-06CH11357. The Eiger 16M detector was funded by an NIH–Office of Research Infrastructure Programs, High-End Instrumentation Grant (1S10OD012289-01A1). Cryo-electron microscopy was performed in the Beckman Institute Resource Center for Transmission Electron Microscopy at Caltech, and at the Stanford SLAC Cryo-EM Center (S2C2). The S2C2 is supported by the National Institutes of Health Common Fund Transformative High Resolution Cryo-Electron Microscopy program. The crystallographic atomic coordinates and structure factors have been deposited in the Protein Data Bank (PDB) with accession codes 6PAM (*Na*A527C-MgADP), 6PAN (*Na*S526C-ATP), 6PAO (*Na*T525C-ATP), 6PAQ (*Na*E523Q-ATP) and 6PAR (*Na*Atm1-MgAMPPNP). The two single particle structures have also been deposited in the PDB with accession codes 6VQT (*Na*Atm1-MgADPVO$_4$) and 6VQU (*Na*Atm1), and in the Electron Microscopy Data Bank (EMDB) with accession codes EMD-21356 (*Na*Atm1-MgADPVO$_4$) and EMD-21357 (*Na*Atm1).

2.8 Figures

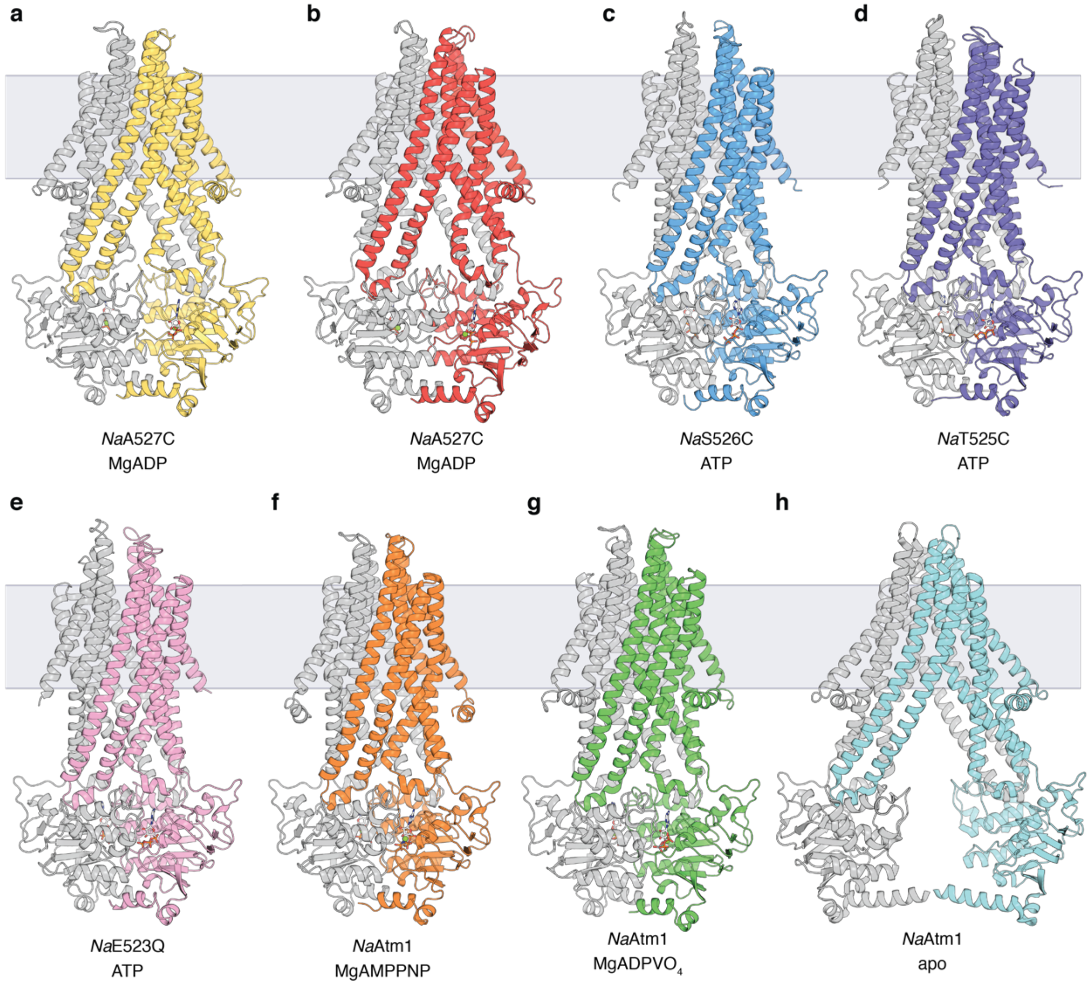

Figure 1. *Na*Atm1 structure overview.

Crystal structures of *Na*A527C in the inward-facing occluded conformation in (**a**) state #1, and (**b**) state #2, both with MgADP bound. Crystal structures of (**c**) *Na*S526C, (**d**) *Na*T525C and (**e**) *Na*E523Q in the occluded conformation, all with ATP bound. (**f**) Crystal structure of *Na*Atm1 in an occluded conformation with MgAMPPNP bound. (**g**) Single particle cryo-EM structure of *Na*Atm1 in a closed conformation with $MgADPVO_4$ bound. (**h**) Single particle cryo-EM structure of *Na*Atm1 in a wide-open inward-facing conformation. All structures are colored with one chain in grey and the second chain in yellow, red, blue, purple, pink, orange, green, and cyan, respectively. Nucleotides are shown in sticks with Mg^{2+} shown as green spheres.

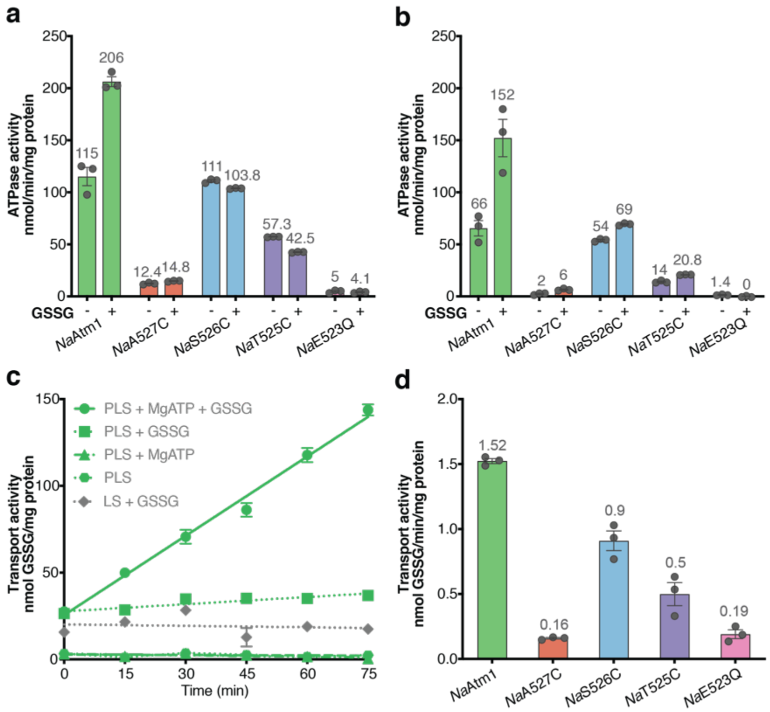

Figure 2. *Na*Atm1 transport and ATPase activities.

ATPase activities of *Na*Atm1 and its variants at 10 mM MgATP in the absence and presence of 2.5 mM GSSG, in (**a**) detergent and (**b**) PLS. (**c**) Wild type *Na*Atm1 transport activities with various controls at 10 mM MgATP and 2.5 mM GSSG. (**d**) Transport activities of *Na*Atm1 and its variants with 10 mM MgATP and 2.5 mM GSSG. Error bars represent the standard errors of the means and circles represent the results of individual measurements. All measurements shown were done in triplicate. The individual rate measurements for the ATPase and transport activities are presented in Tables S2 and S3.

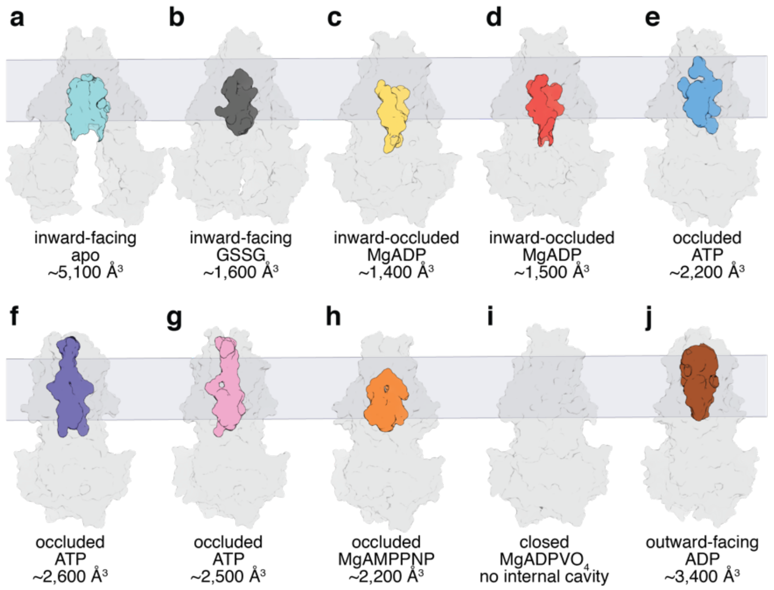

Figure 3. **Comparison of the central cavities for the *Na*Atm1 structures**.

Surface representations of the overall structures and internal binding cavities for (**a**) *Na*Atm1 wide-open inward-facing conformation, (**b**) *Na*Atm1 inward-facing conformation (PDB ID: 4MRN), (**c**) *Na*A527C inward-facing occluded state #1, (**d**) *Na*A527C inward-facing occluded state #2, (**e**) *Na*S526C occluded conformation, (**f**) *Na*T525C occluded conformation, (**g**) *Na*E523Q occluded conformation, (**h**) *Na*Atm1 MgAMPPNP bound occluded structure, and (**i**) *Na*Atm1 MgADPVO4 bound closed structure. (**j**) Surface representation of the overall structure and central binding cavity of Sav1866 in the outward-facing conformation (PDB ID: 2HYD). The cavity of *Na*Atm1 wide-open inward-facing structure is shown in cyan, *Na*Atm1 inward-facing structure is shown in gray, *Na*A527C inward-occluded structure #1 in yellow, *Na*A527C inward-occluded structure #2 in red, *Na*S526C occluded structure in blue, *Na*T525C occluded structure in purple, *Na*E523Q occluded structure in pink, *Na*Atm1 MgAMPPNP occluded structure in orange, and Sav1866 outward-facing structure in brown. The volumes of the cavities were all calculated by CastP (Tian et al. 2018) with a probe radius of 2.5 Å.

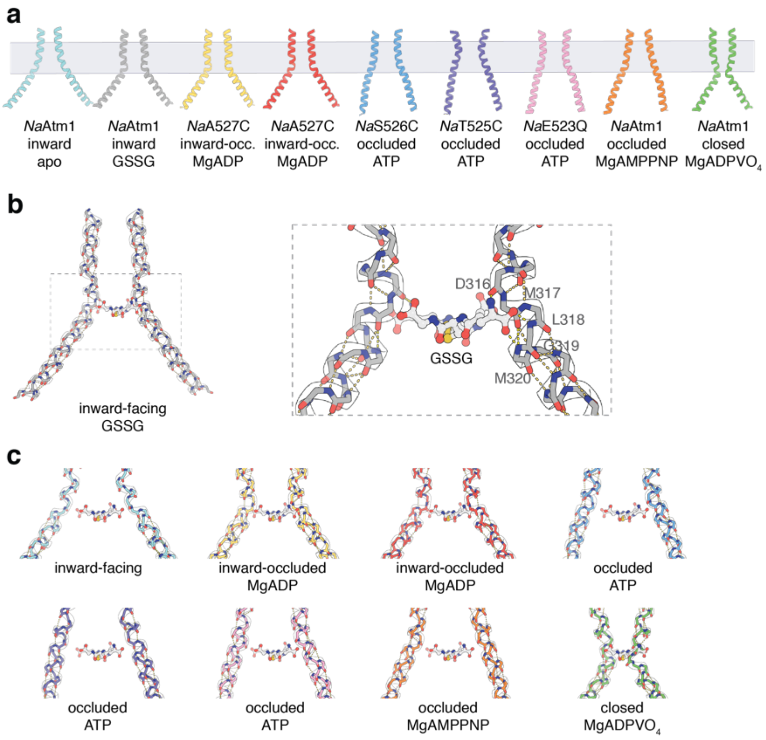

Figure 4. **TM6 comparisons of *Na*Atm1.**

(**a**) TM6 (residues 300-340) conformations observed in different *Na*Atm1 structures. (**b**) Hydrogen bonding interactions between GSSG and TM6 main chain groups from residues in the kink region of the primary binding site (residues 316-320; (PDB ID: 4MRS)). Hydrogen bonding interactions are shown in yellow dashes and GSSG is shown in ball and sticks. (**c**) Potential interactions between GSSG and residues 316-320 in other *Na*Atm1 structures. The approximate location of GSSG is obtained from the structural alignments of TM6s in different structures to the TM6 of the inward-facing conformation of *Na*Atm1 (PDB ID: 4MRS). TM6s in the *Na*Atm1 wide-open inward-facing structure are shown in cyan, *Na*A527C inward-occluded structure #1 in yellow, *Na*A527C inward-occluded structure #2 in red, *Na*S526C occluded structure in blue, *Na*T525C occluded structure in purple, *Na*E523Q occluded structure in pink, *Na*Atm1 MgAMPPNP bound occluded structure in orange, and *Na*Atm1 $MgADPVO_4$ bound closed structure in green.

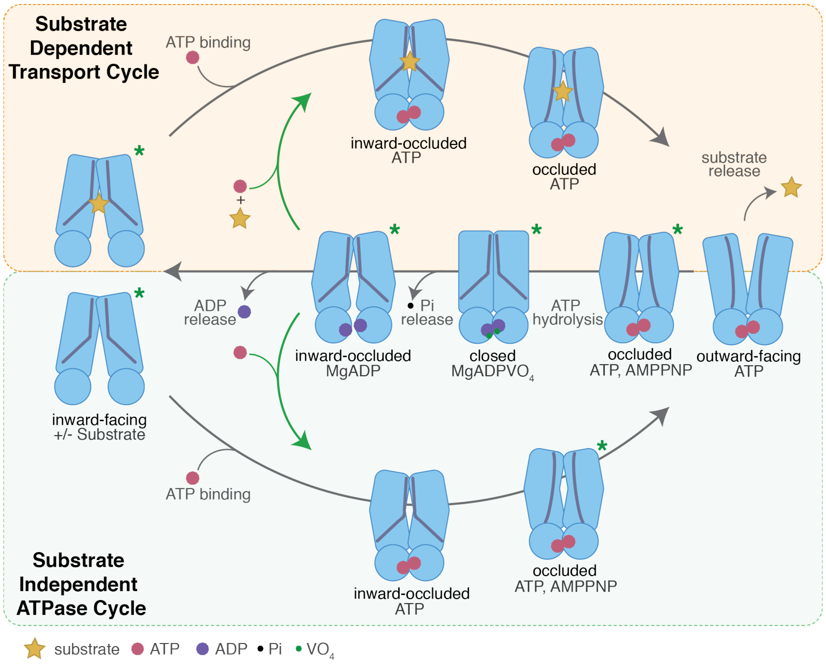

Figure 5. Schematic representation of a structure-based transport mechanism for *Na*Atm1. The substrate-dependent (transport, top cycle) and substrate-independent (bottom cycle) ATPase pathways differ by the presence or absence of bound substrate, respectively, during the transition from the inward- to outward-facing conformation. Resetting the outward-facing to the inward-facing conformation involves a set of intermediates common to both pathways, including the closed, post-hydrolysis conformation lacking a substrate binding site. Ligand binding to disulfide crosslinked variants may occur in the inward-occluded conformations (green arrows), without accessing the fully inward-facing conformations. Inward-facing and inward-facing occluded structures have been determined in both apo and substrate bound states (PDB IDs: 6VQU (wide-open), 4MRN (apo), 4MRS (GSSG bound), 4MRP (GSH bound), 4MRV (GS-Hg bound) and 6PAM (MgADP bound)). The inward-occluded state with both substrate and ATP present is modeled on the crystal structure of the inward-facing occluded structure with MgADP bound (PDB ID: 6PAM). The ATP bound occluded state has been determined for the disulfide crosslinking mutants (*Na*S526C and *Na*T525C with PDB IDs: 6PAN and 6PAO, separately), the ATP hydrolysis deficient mutant (*Na*E523Q with PDB ID: 6PAQ) and the wild type transporter with MgAMPPNP bound (PDB ID: 6PAR). The outward-facing conformation of *Na*Atm1 has not been structurally characterized, but its presence is essential for substrate release. The post-hydrolysis closed state has been characterized with

$MgADPVO_4$ bound (PDB ID: 6VQT), while the ADP bound occluded state after ATP hydrolysis has been solved with *Na*A527C (PDB ID: 6PAM). Asterisks denote the structurally characterized structures to date for *Na*Atm1.

2.9 Supplemental Information

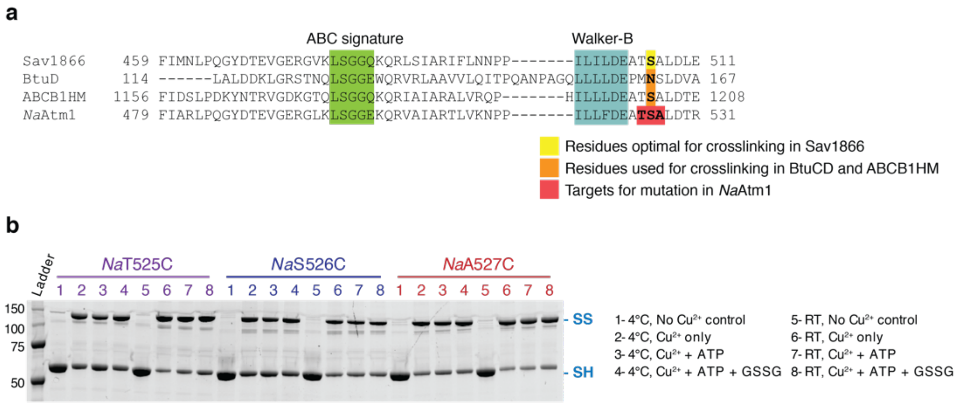

Figure S1. Screening candidate residues in *Na*Atm1 for disulfide crosslinking.

(**a**) Partial sequence alignments of NBDs of various ABC transporters. (**b**) SDS-PAGE of the products of crosslinking with Cu (II) (1,10-phenanthroline)$_3$ under different conditions for the three cysteine variants in this report. RT = room temperature, SS = crosslinked species, SH = uncrosslinked (disulfide reduced) species.

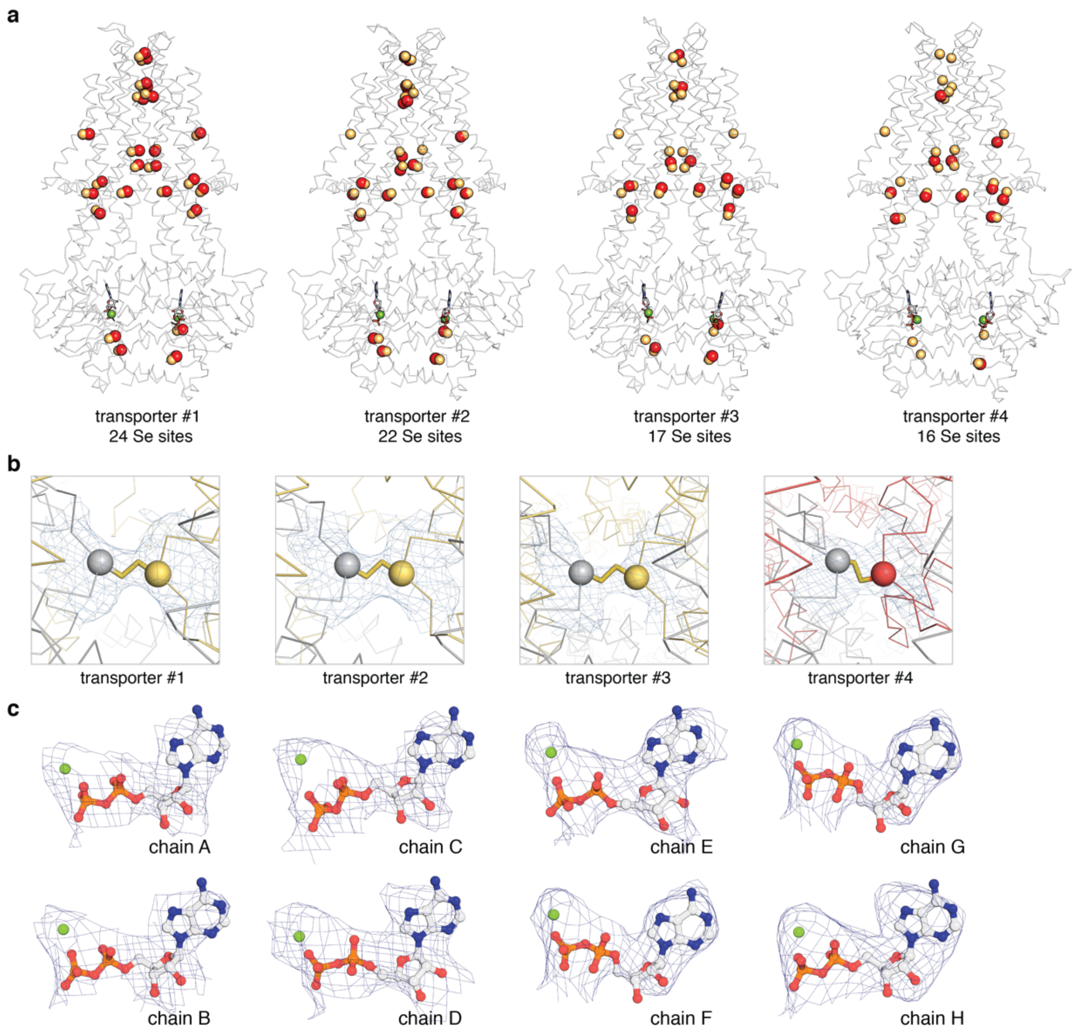

Figure S2. ***Na*****A527C inward-facing occluded structures.**

(**a**) Location of selenium sites in the four transporters present in the selenomethionine-substituted *Na*A527C asymmetric unit. The selenium sites identified in AutoSol of Phenix (Adams et al. 2010) are shown in red spheres, the sulfur atoms of methionine residues from the refined model are shown in yellow spheres, and nucleotides are shown in sticks with Mg^{2+} shown in green spheres. (**b**) Disulfide bridges in the four transporters in the asymmetric unit. The Cα positions corresponding to C527 in the two chains are depicted as grey and yellow spheres for transporters #1-3, and grey and red spheres for transporter #4, separately. (**c**) Composite omit map calculated from Phenix (Adams et al. 2010) showing the electron density for the bound MgADP in different chains of *Na*A527C in the asymmetric unit. Nucleotides are shown in sticks with Mg^{2+} shown as green spheres.

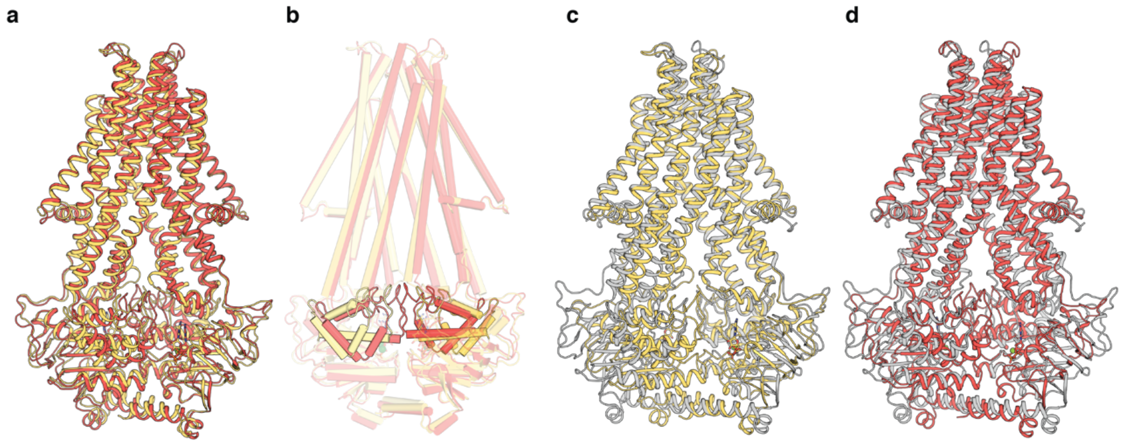

Figure S3. Structural alignments of *Na*A527C in the inward-facing occluded conformations. (**a**) Alignment of *Na*A527C inward-facing occluded conformation #1 (yellow) to *Na*A527C inward-facing occluded conformation #2 (red) with an overall RMSD of 1.7 Å. The relative rotation of the α-helical domains in the NBDs between the two states is shown in (**b**). (**c**) Alignment of *Na*A527C inward-facing occluded conformation #1 to *Na*Atm1 inward-facing conformation (PDB ID: 4MRN) (grey) with an overall RMSD of 2.1 Å. (**d**) Alignment of *Na*A527C inward-facing occluded conformation #2 (red) to *Na*Atm1 inward-facing conformation (PDB ID: 4MRN) (grey) with an overall RMSD of 4.4 Å. Nucleotides are shown in sticks with Mg^{2+} shown as green spheres.

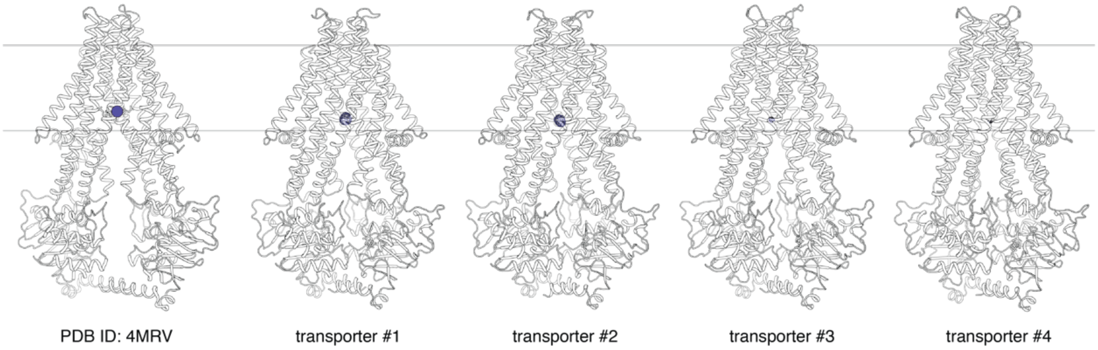

Figure S4. Binding of GS-Hg to *Na*A527C inward-facing occluded structures.
Anomalous electron density maps calculated from data collected at the Hg edge, contoured at the 5 σ levels (dark blue) for *Na*A527C crystallized in the presence of GS-Hg. For comparison, the structure of *Na*Atm1 with GS-Hg bound (PDB ID: 4MRV) is indicated (left) with mercury shown in purple sphere.

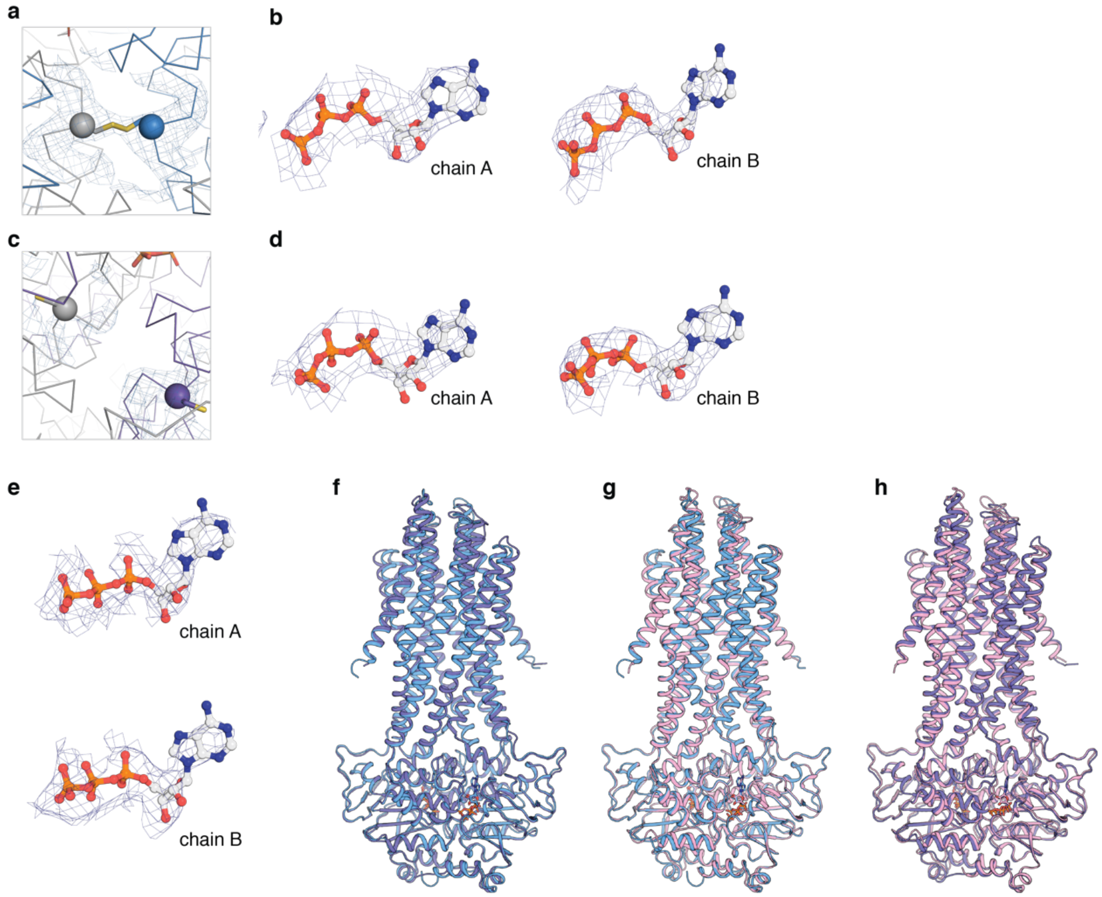

Figure S5. *Na*Atm1 in the occluded conformations.

(**a**) Disulfide bridge formed by S526C in the *Na*S526C structure with the Cα positions shown as grey and blue spheres. (**b**) Composite omit map calculated from Phenix (Adams et al. 2010) showing the electron density for the bound ATP in the dimeric *Na*S526C structure. (**c**) T525C residues in the *Na*T525C occluded structure with the Cα positions shown as grey and purple spheres. (**d**) Composite omit map showing the electron density for the bound ATP in the dimeric *Na*T525C structure. (**e**) Composite omit map calculated from Phenix (Adams et al. 2010) showing the electron density for the bound ATP in the dimeric *Na*E523Q structure. (**f**) *Na*T525C overall structural alignment to *Na*S526C with an RMSD of 0.5 Å. (**g**) *Na*E523Q overall structural alignment to *Na*S526C with an RMSD of 0.5 Å. (**h**) *Na*E523Q overall structural alignment to *Na*T525C with an RMSD of 0.7 Å. *Na*S526C is colored in blue, *Na*T525C in purple, and *Na*E523Q in pink. Nucleotides are shown in sticks.

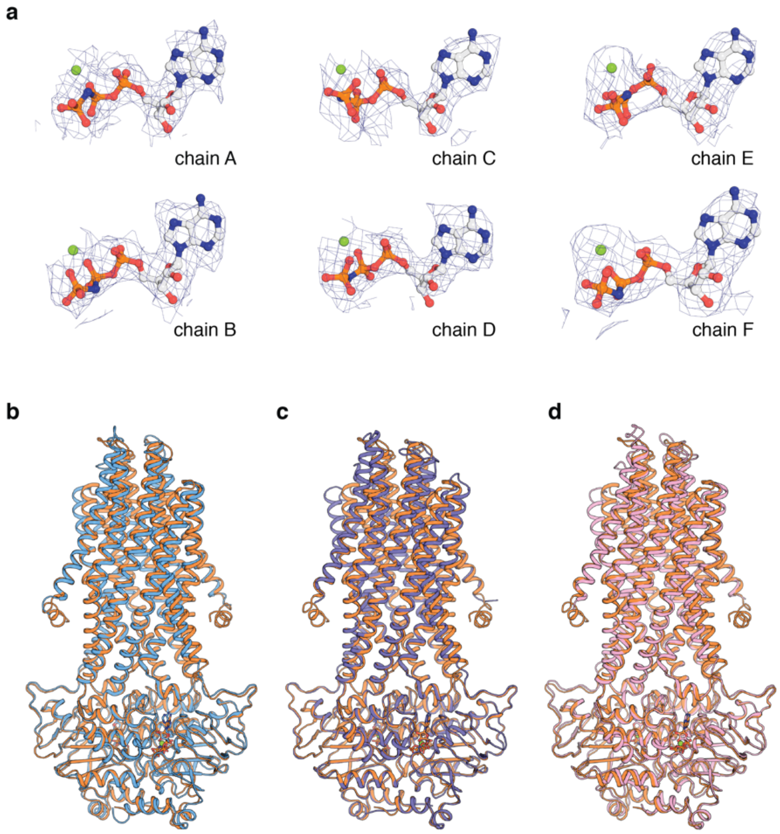

Figure S6. Structural alignments of *Na*Atm1 with MgAMPPNP bound in the occluded conformation.

(**a**) Composite omit map calculated from Phenix (Adams et al. 2010) showing the electron density for the bound MgAMPPNP in the three copies of *Na*Atm1 in the asymmetric unit. *Na*Atm1 occluded structure alignments to (**b**) *Na*S526C with an overall RMSD of 1.1 Å, (**c**) *Na*T525C with an overall RMSD of 0.9 Å, and (**d**) *Na*E523Q with an overall RMSD of 1.1 Å. *Na*Atm1 occluded structure colored in orange, *Na*S526C in blue, *Na*T525C in purple and *Na*E523Q in pink. Nucleotides are shown in sticks with Mg^{2+} shown as green spheres.

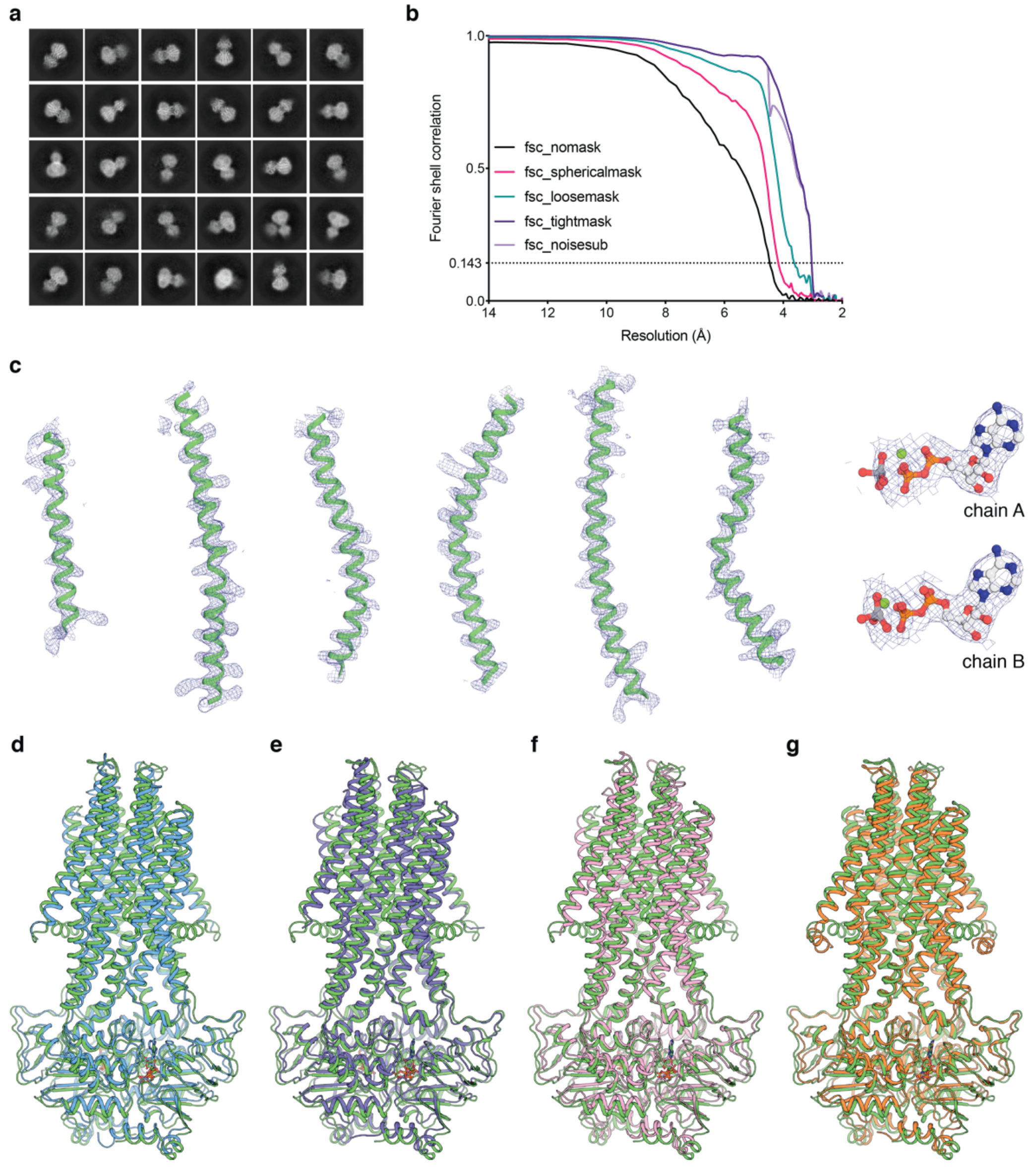

Figure S7. Single particle cryo-EM structure of *Na*Atm1 in the closed conformation stabilized with MgADPVO$_4$.

(**a**) Examples of 2D classes. (**b**) Fourier shell correlation (FSC) curve showing the resolution estimate for the final reconstruction, generated from the final refinement in cryoSPARC 2 (Punjani et al. 2017). (**c**) Density fitting for different TM helices and nucleotides (MgADPVO$_4$). Overall structural alignments to the occluded structures of (**d**) *Na*S526C, (**e**) *Na*T525C, (**f**) *Na*E523Q and (**g**) *Na*Atm1 occluded crystal structures with RMSDs of 2.0 Å, 2,1 Å, 2.0 Å and 1.7 Å, respectively. Nucleotides are shown in sticks with Mg^{2+} shown as green spheres.

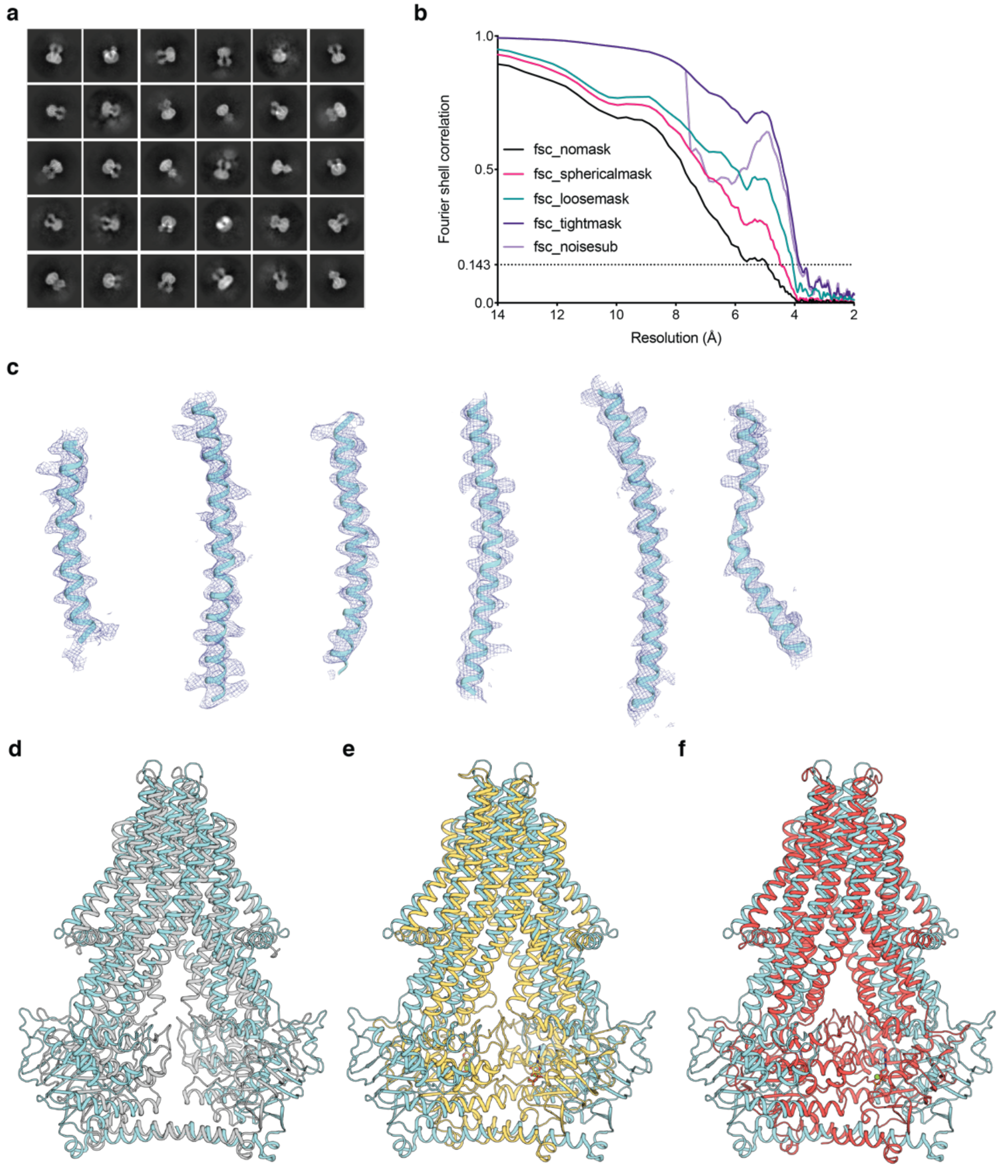

Figure S8. Single particle cryo-EM structure of *Na*Atm1 in the wide-open inward-facing conformation.

(**a**) Examples of 2D classes. (**b**) FSC curve showing the resolution estimate for the final reconstruction, generated from the final refinement in cryoSPARC 2 (Punjani et al. 2017). (**c**) Density fitting for different TM helices. Overall structural alignments to (**d**) *Na*Atm1 inward-facing conformation (PDB ID 4MRN), (**e**) *Na*A527C inward-facing occluded state #1, and (**f**) *Na*A527C inward-facing occluded state #2 crystal structures with RMSDs of 5.8 Å, 8.9 Å, and 9.3 Å, respectively. Nucleotides are shown in sticks with Mg^{2+} shown as green spheres.

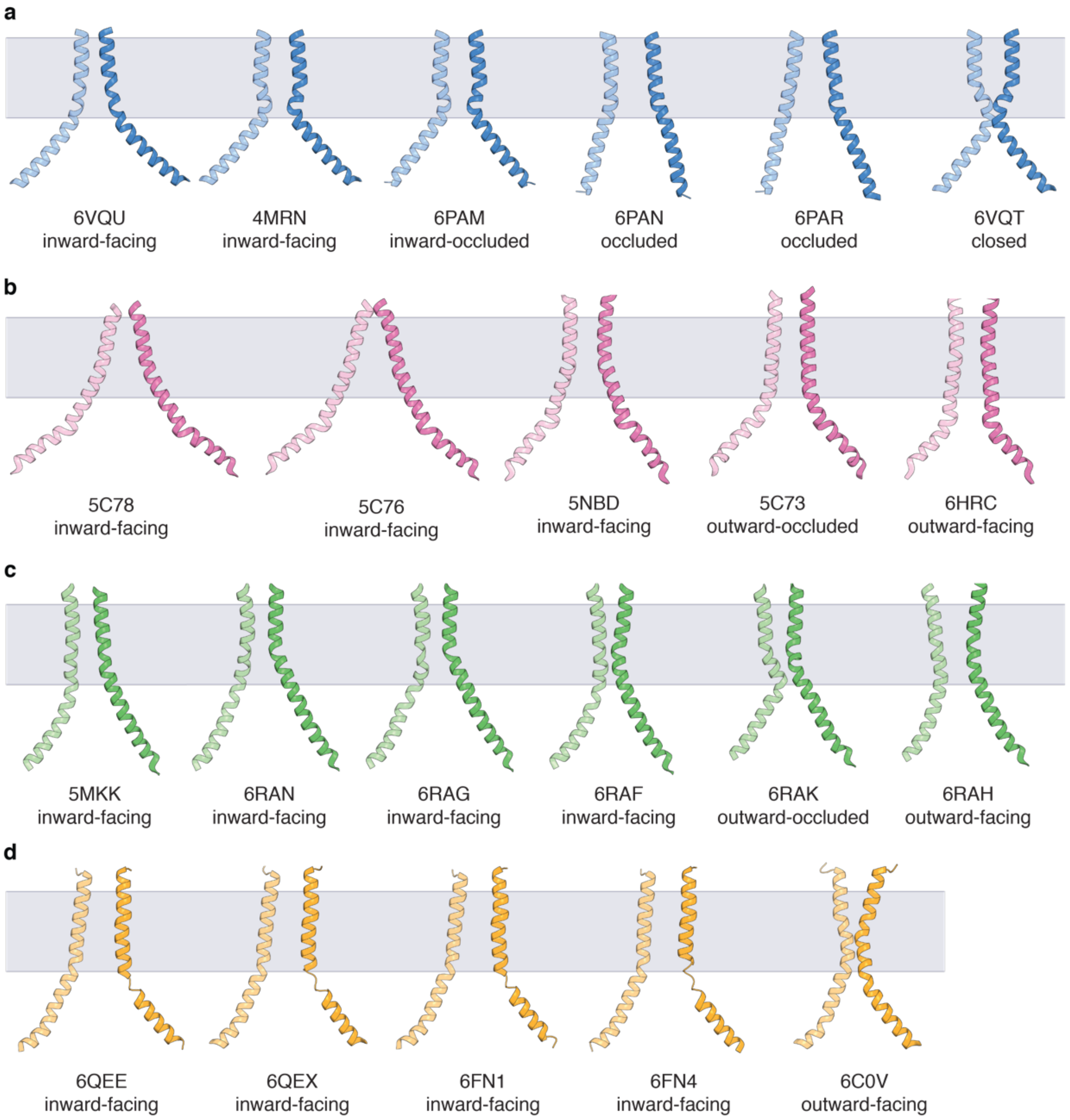

Figure S9. **TM6 comparisons for different ABC transporter systems.**

(**a**) TM6 (residues 300-340) arrangements of representative *Na*Atm1 structures. (**b**) TM6 (residues 288-335) arrangements of representative PglK structures. (**c**) TM6 (residues 290-333 of chain A and residues 275-319 of chain B) arrangements of representative TmrAB structures. (**d**) TM6 (residues 324-370 and residues 968-1013) arrangements of representative ABCB1 structures. The corresponding PDB IDs and the conformational states are labeled below the structures.

Table S1. Coupling efficiencies between ATP hydrolysis and substrate translocation for ABC transporters.

Coupling efficiencies for different transport systems (Zehnpfennig, Urbatsch, and Galla 2009, Davidson and Nikaido 1990, Patzlaff, van der Heide, and Poolman 2003, Lycklama et al. 2018, Eytan, Regev, and Assaraf 1996, Wang et al. 2006, Dean, Davidson, and Nikaido 1989, Dong, Penin, and Baggetto 1996, Nikaido and Ames 1999, Manolaridis et al. 2018, Hofmann et al. 2019, Borths et al. 2005, Woo et al. 2012, Chen et al. 2001, Chavan et al. 2013). Coupling efficiencies are either presented in the corresponding reference or calculated based on the reported ATPase and transport activities of the transporter. Coupling efficiency = ATPase activity/transport activity.

Transporters	ATPase activity (nmol/min/mg)	Transport Activity (nmol/min/mg)	Coupling efficiency	References
ABCC3	200	1,200	0.17	Zehnpfennig et al (2009)
MalFGK	~3	~2	1.4 - 17	Davidson et al (1990)
OpuA	~80 - 120	~30 - 70	1.7 - 4	Patzlaff et al (2003)
GlnPQ	15 (min^{-1})	8.5 (min^{-1})	1.8	Lycklama et al (2018)
Pgp	~750 - 1,300	~500	2	Eytan et al (1996)
ABCG5/8	110	50	2.2	Wang et al (2006)
MalFGK	~1.2 - 8	~0.3 - 2	4 - 10	Dean et al (1989)
Pgp	~110	~6	18	Dong et al (1996)
HisP	580	19	31	Nikaido and Ames (1999)
ABCG2	~750	~22	34	Manolaridis et al (2018)
TmrAB	~1,100	~30	37	Hofmann et al (2019)
BtuCDF	~400	~4	100	Borths et al (2005)
HmuUV	~130	~1.1	120	Woo et al (2012)
***Na*Atm1**	150	1.5	100	This study
MalFGK	4,000	1.2	3,300	Chen et al (2001)
ABCB6	610	0.03	20,000	Chavan et al (2013)

Table S2. Raw ATPase activities of *Na*Atm1 and variants in both proteoliposomes and detergent.

The ATPase activities were measured in triplicate at 10 mM MgATP and 2.5 mM GSSG at 37 °C.

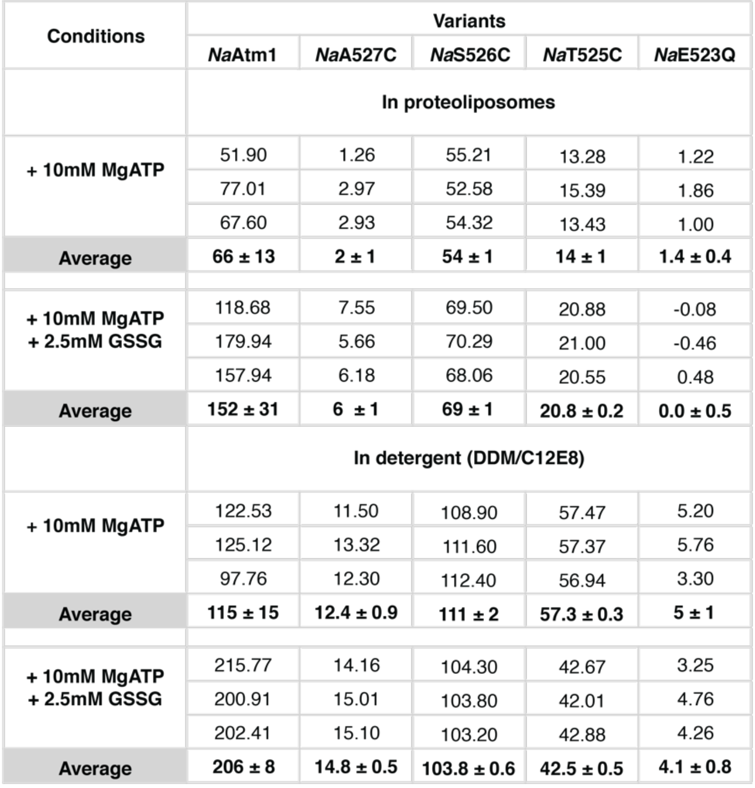

Conditions	Variants				
	***Na*Atm1**	***Na*A527C**	***Na*S526C**	***Na*T525C**	***Na*E523Q**
	In proteoliposomes				
+ 10mM MgATP	51.90	1.26	55.21	13.28	1.22
	77.01	2.97	52.58	15.39	1.86
	67.60	2.93	54.32	13.43	1.00
Average	**66 ± 13**	**2 ± 1**	**54 ± 1**	**14 ± 1**	**1.4 ± 0.4**
+ 10mM MgATP + 2.5mM GSSG	118.68	7.55	69.50	20.88	-0.08
	179.94	5.66	70.29	21.00	-0.46
	157.94	6.18	68.06	20.55	0.48
Average	**152 ± 31**	**6 ± 1**	**69 ± 1**	**20.8 ± 0.2**	**0.0 ± 0.5**
	In detergent (DDM/C12E8)				
+ 10mM MgATP	122.53	11.50	108.90	57.47	5.20
	125.12	13.32	111.60	57.37	5.76
	97.76	12.30	112.40	56.94	3.30
Average	**115 ± 15**	**12.4 ± 0.9**	**111 ± 2**	**57.3 ± 0.3**	**5 ± 1**
+ 10mM MgATP + 2.5mM GSSG	215.77	14.16	104.30	42.67	3.25
	200.91	15.01	103.80	42.01	4.76
	202.41	15.10	103.20	42.88	4.26
Average	**206 ± 8**	**14.8 ± 0.5**	**103.8 ± 0.6**	**42.5 ± 0.5**	**4.1 ± 0.8**

Table S3. Raw transport activities of *Na*Atm1 and variants.

The transport activities for various controls and the different *Na*Atm1 variants were measured in triplicate at 10 mM MgATP and 2.5 mM GSSG at 37 °C.

Samples	**Transport rate (nmol/mg protein) at various time points (min)**						**Transport rates (nmole/min/mg)**
	0	**15**	**30**	**45**	**60**	**75**	
***Na*Atm1 PLS +MgATP +GSSG**	28.17	45.49	69.95	81.08	113.06	141.67	1.488
	28.05	49.95	64.09	94.01	125.89	139.62	1.554
	26.57	54.53	77.96	83.45	114.33	149.99	1.528
Average	**27.6 ± 0.9**	**50 ± 5**	**71 ± 7**	**86 ± 7**	**118 ± 7**	**144 ± 5**	**1.52 ± 0.03**
***Na*Atm1 PLS +GSSG**	26.69	26.22	30.82	34.07	34.73	39.73	0.179
	26.08	28.78	37.44	36.06	38.74	32.31	0.1137
	26.59	30.69	36.27	35.48	31.99	38.69	0.1211
Average	**26.5 ± 0.3**	**29 ± 2**	**35 ± 4**	**35 ± 1**	**35 ± 3**	**37 ± 4**	**0.14 ± 0.04**
***Na*Atm1 PLS +MgATP**	2.84	1.03	2.95	2.98	1.13	1.48	-0.01235
	3.39	1.59	3.58	2.29	2.17	1.83	-0.01406
	3.39	2.54	4.10	2.08	1.65	-1.82	-0.05857
Average	**3.2 ± 0.3**	**1.7 ± 0.7**	**3.5 ± 0.6**	**2.5 ± 0.5**	**1.7 ± 0.5**	**0 ± 2**	**-0.03 ± 0.03**
***Na*Atm1 PLS**	3.30	1.80	3.34	2.64	1.48	1.76	-0.01782
	3.39	1.76	3.75	2.18	1.31	1.59	-0.02279
	3.39	0.16	4.03	3.30	2.04	3.95	0.01463
Average	**3.4 ± 0.1**	**1.2 ± 0.9**	**3.7 ± 0.3**	**2.7 ± 0.6**	**1.6 ± 0.4**	**2 ± 1**	**-0.01 ± 0.02**
Liposomes +GSSG	20.25	22.67	29.57	17.30	20.47	16.88	-0.06808
	14.00	21.70	25.88	18.91	16.76	16.41	-0.01854
	12.87	20.42	29.74	2.07	19.66	19.29	0.004169
Average	**16 ± 4**	**22 ± 1**	**28 ± 2**	**13 ± 9**	**19 ± 2**	**18 ± 2**	**-0.03 ± 0.04**
***Na*A527C PLS +MgATP +GSSG**	23.88	19.64	31.19	30.18	26.25	37.11	0.1618
	24.36	26.97	32.05	31.50	33.88	35.79	0.1473
	19.28	26.69	33.64	31.78	29.64	35.41	0.1669
Average	**23 ± 3**	**24 ± 4**	**32 ± 1**	**31.2 ± 0.9**	**30 ± 4**	**36.1 ± 0.9**	**0.16 ± 0.01**
***Na*S526C PLS +MgATP +GSSG**	22.86	42.06	53.21	66.26	77.55	79.59	0.7679
	21.26	41.68	59.75	61.69	84.84	92.92	0.9328
	22.58	37.91	61.09	64.64	82.63	103.12	1.029
Average	**22.2 ± 0.9**	**41 ± 2**	**58 ± 4**	**64 ± 2**	**82 ± 4**	**92 ± 12**	**0.9 ± 0.1**
***Na*T525C PLS +MgATP +GSSG**	23.32	25.75	15.61	49.92	58.39	63.36	0.6332
	20.60	26.69	40.53	51.72	52.88	37.39	0.3309
	21.82	25.94	39.12	42.16	59.62	57.18	0.535
Average	**22 ± 1**	**26.1 ± 0.5**	**32 ± 14**	**48 ± 5**	**57 ± 4**	**53 ± 14**	**0.5 ± 0.2**
***Na*E523Q PLS +MgATP +GSSG**	21.82	26.31	30.16	31.69	32.19	32.12	0.1345
	16.01	24.62	30.91	8.99	35.00	33.71	0.1862
	17.88	21.80	23.30	32.07	35.00	34.47	0.2501
Average	**19 ± 3**	**24 ± 2**	**28 ± 4**	**24 ± 13**	**34 ± 2**	**33 ± 1**	**0.19 ± 0.06**

Table S4. Data collection and refinement statistics of *Na*A527C

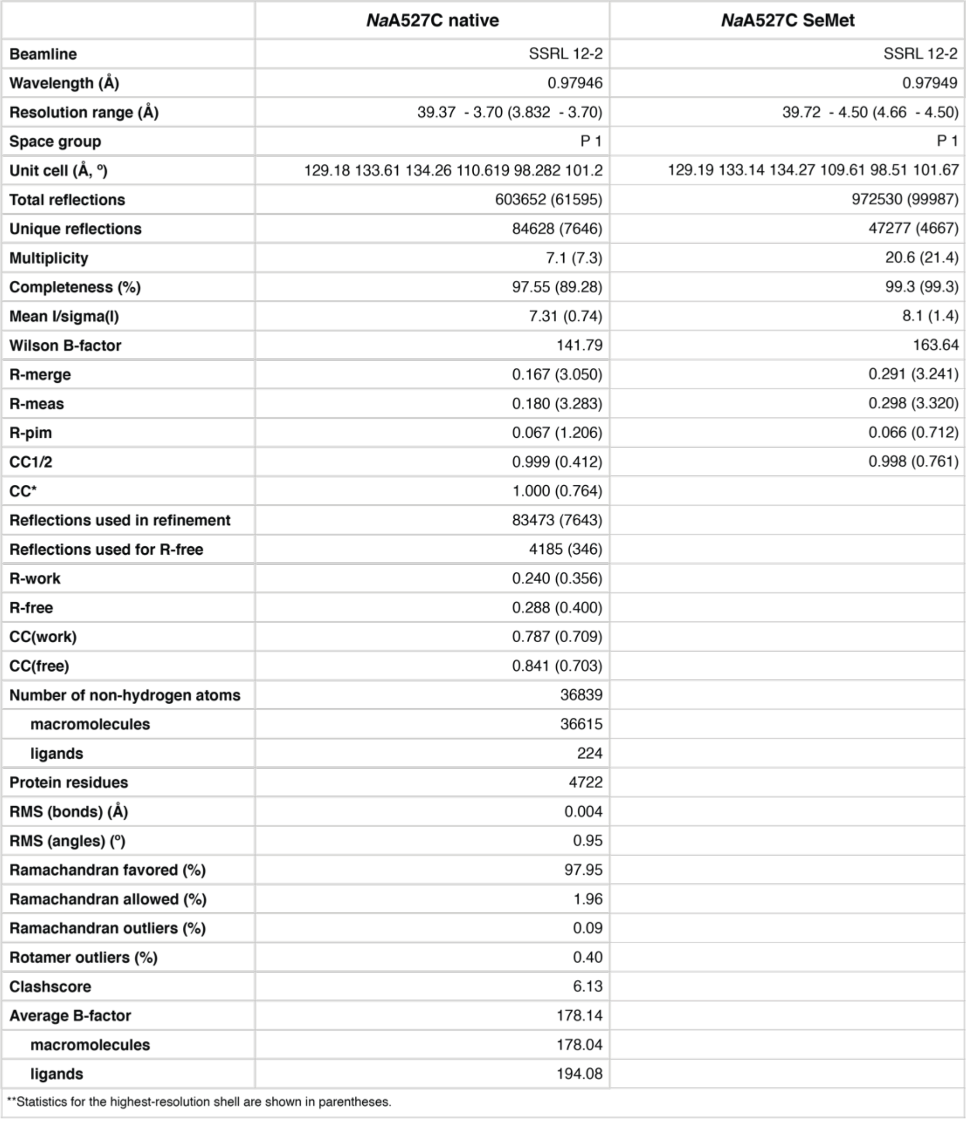

	***Na*A527C native**	***Na*A527C SeMet**
Beamline	SSRL 12-2	SSRL 12-2
Wavelength (Å)	0.97946	0.97949
Resolution range (Å)	39.37 - 3.70 (3.832 - 3.70)	39.72 - 4.50 (4.66 - 4.50)
Space group	P 1	P 1
Unit cell (Å, º)	129.18 133.61 134.26 110.619 98.282 101.2	129.19 133.14 134.27 109.61 98.51 101.67
Total reflections	603652 (61595)	972530 (99987)
Unique reflections	84628 (7646)	47277 (4667)
Multiplicity	7.1 (7.3)	20.6 (21.4)
Completeness (%)	97.55 (89.28)	99.3 (99.3)
Mean I/sigma(I)	7.31 (0.74)	8.1 (1.4)
Wilson B-factor	141.79	163.64
R-merge	0.167 (3.050)	0.291 (3.241)
R-meas	0.180 (3.283)	0.298 (3.320)
R-pim	0.067 (1.206)	0.066 (0.712)
CC1/2	0.999 (0.412)	0.998 (0.761)
CC*	1.000 (0.764)	
Reflections used in refinement	83473 (7643)	
Reflections used for R-free	4185 (346)	
R-work	0.240 (0.356)	
R-free	0.288 (0.400)	
CC(work)	0.787 (0.709)	
CC(free)	0.841 (0.703)	
Number of non-hydrogen atoms	36839	
macromolecules	36615	
ligands	224	
Protein residues	4722	
RMS (bonds) (Å)	0.004	
RMS (angles) (º)	0.95	
Ramachandran favored (%)	97.95	
Ramachandran allowed (%)	1.96	
Ramachandran outliers (%)	0.09	
Rotamer outliers (%)	0.40	
Clashscore	6.13	
Average B-factor	178.14	
macromolecules	178.04	
ligands	194.08	

**Statistics for the highest-resolution shell are shown in parentheses.

Table S5. Data collection and refinement statistics of *Na*S526C

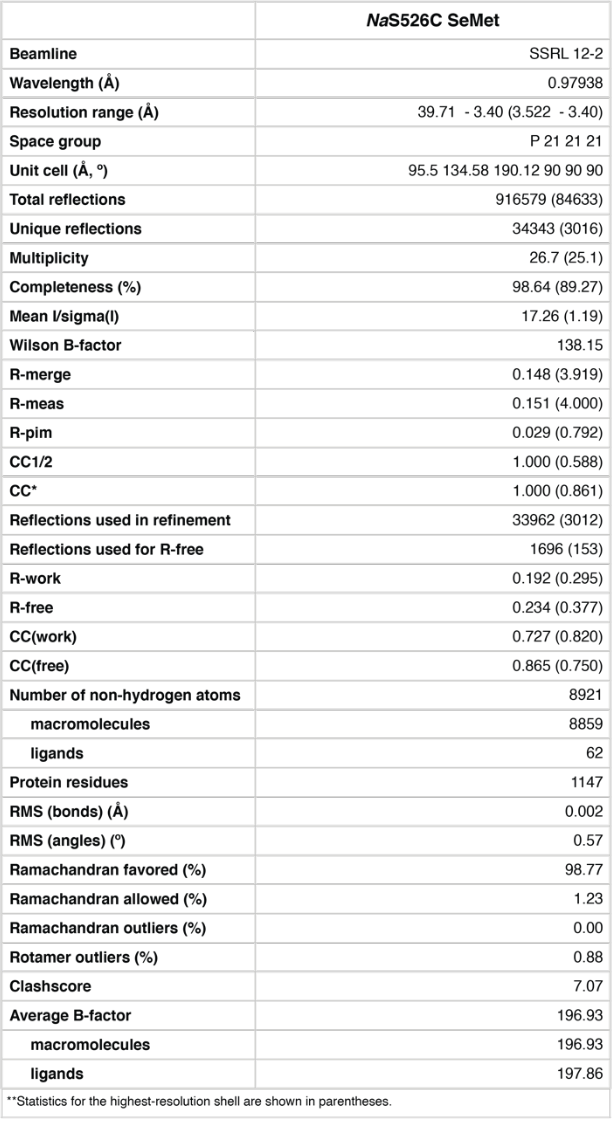

	***Na*S526C SeMet**
Beamline	SSRL 12-2
Wavelength (Å)	0.97938
Resolution range (Å)	39.71 - 3.40 (3.522 - 3.40)
Space group	P 21 21 21
Unit cell (Å, °)	95.5 134.58 190.12 90 90 90
Total reflections	916579 (84633)
Unique reflections	34343 (3016)
Multiplicity	26.7 (25.1)
Completeness (%)	98.64 (89.27)
Mean I/sigma(I)	17.26 (1.19)
Wilson B-factor	138.15
R-merge	0.148 (3.919)
R-meas	0.151 (4.000)
R-pim	0.029 (0.792)
CC1/2	1.000 (0.588)
CC*	1.000 (0.861)
Reflections used in refinement	33962 (3012)
Reflections used for R-free	1696 (153)
R-work	0.192 (0.295)
R-free	0.234 (0.377)
CC(work)	0.727 (0.820)
CC(free)	0.865 (0.750)
Number of non-hydrogen atoms	8921
macromolecules	8859
ligands	62
Protein residues	1147
RMS (bonds) (Å)	0.002
RMS (angles) (º)	0.57
Ramachandran favored (%)	98.77
Ramachandran allowed (%)	1.23
Ramachandran outliers (%)	0.00
Rotamer outliers (%)	0.88
Clashscore	7.07
Average B-factor	196.93
macromolecules	196.93
ligands	197.86

**Statistics for the highest-resolution shell are shown in parentheses.

Table S6. Data collection and refinement statistics of *Na*T525C

	***Na*T525C native**	***Na*T525C SeMet**
Beamline	APS GM/CA 23-IDB	APS GM/CA 23-IDB
Wavelength (Å)	1.033202	0.979338
Resolution range (Å)	39.1 - 3.65 (3.78 - 3.65)	39.31 - 3.90 (4.21 - 3.90)
Space group	P 21 21 21	P 21 21 21
Unit cell (Å, °)	94.164 135.415 191.592 90 90 90	93.78 136.37 192.48 90 90 90
Total reflections	246061 (22321)	237126 (49769)
Unique reflections	27912 (2712)	23170 (4675)
Multiplicity	8.8 (8.1)	10.2 (10.6)
Completeness (%)	97.77 (97.54)	99.9 (99.9)
Mean I/sigma(I)	14.33 (1.11)	12.1 (1.6)
Wilson B-factor	172.32	180.32
R-merge	0.076 (2.002)	0.100 (1.852)
R-meas	0.080 (2.146)	0.106 (1.945)
R-pim	0.027 (0.758)	0.033 (0.590)
CC1/2	0.999 (0.634)	1.000 (0.586)
CC*	1.000 (0.881)	
Reflections used in refinement	27348 (2699)	
Reflections used for R-free	1356 (126)	
R-work	0.251 (0.430)	
R-free	0.285 (0.475)	
CC(work)	0.713 (0.364)	
CC(free)	0.877 (0.304)	
Number of non-hydrogen atoms	8835	
macromolecules	8773	
ligands	62	
Protein residues	1135	
RMS (bonds) (Å)	0.003	
RMS (angles) (°)	0.63	
Ramachandran favored (%)	97.70	
Ramachandran allowed (%)	2.30	
Ramachandran outliers (%)	0.00	
Rotamer outliers (%)	0.22	
Clashscore	7.07	
Average B-factor	214.38	
macromolecules	214.56	
ligands	189.06	

**Statistics for the highest-resolution shell are shown in parentheses.

Table S7. Data collection and refinement statistics of *Na*E523Q

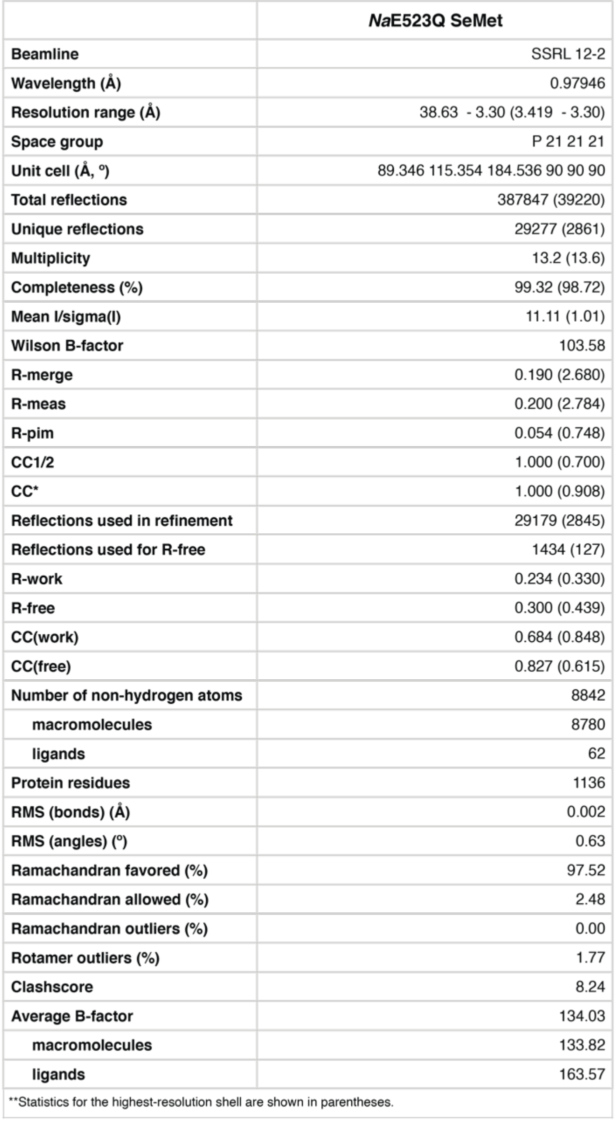

	***Na*E523Q SeMet**
Beamline	SSRL 12-2
Wavelength (Å)	0.97946
Resolution range (Å)	38.63 - 3.30 (3.419 - 3.30)
Space group	P 21 21 21
Unit cell (Å, º)	89.346 115.354 184.536 90 90 90
Total reflections	387847 (39220)
Unique reflections	29277 (2861)
Multiplicity	13.2 (13.6)
Completeness (%)	99.32 (98.72)
Mean I/sigma(I)	11.11 (1.01)
Wilson B-factor	103.58
R-merge	0.190 (2.680)
R-meas	0.200 (2.784)
R-pim	0.054 (0.748)
CC1/2	1.000 (0.700)
CC*	1.000 (0.908)
Reflections used in refinement	29179 (2845)
Reflections used for R-free	1434 (127)
R-work	0.234 (0.330)
R-free	0.300 (0.439)
CC(work)	0.684 (0.848)
CC(free)	0.827 (0.615)
Number of non-hydrogen atoms	8842
macromolecules	8780
ligands	62
Protein residues	1136
RMS (bonds) (Å)	0.002
RMS (angles) (º)	0.63
Ramachandran favored (%)	97.52
Ramachandran allowed (%)	2.48
Ramachandran outliers (%)	0.00
Rotamer outliers (%)	1.77
Clashscore	8.24
Average B-factor	134.03
macromolecules	133.82
ligands	163.57

**Statistics for the highest-resolution shell are shown in parentheses.

Table S8. Data collection and refinement statistics of *Na*Atm1

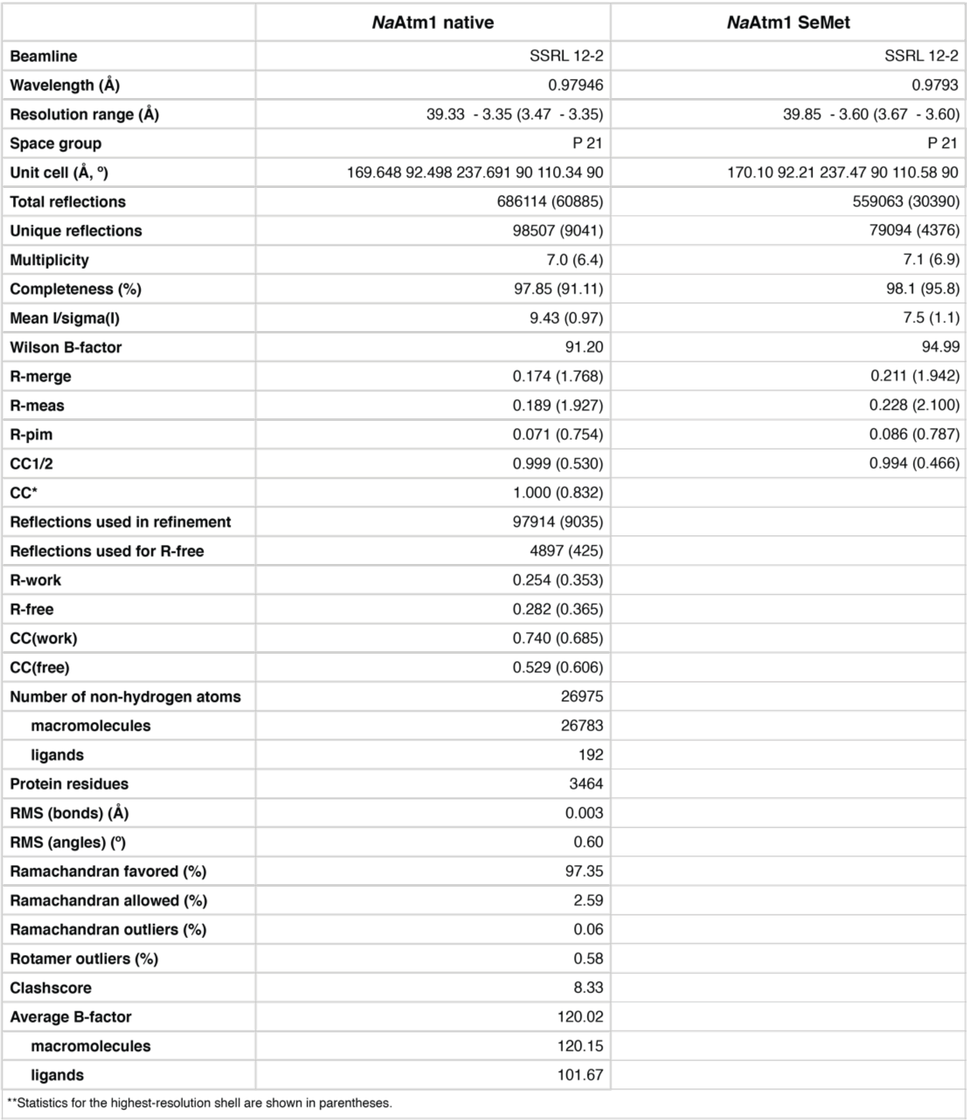

	***Na*Atm1 native**	***Na*Atm1 SeMet**
Beamline	SSRL 12-2	SSRL 12-2
Wavelength (Å)	0.97946	0.9793
Resolution range (Å)	39.33 - 3.35 (3.47 - 3.35)	39.85 - 3.60 (3.67 - 3.60)
Space group	P 21	P 21
Unit cell (Å, º)	169.648 92.498 237.691 90 110.34 90	170.10 92.21 237.47 90 110.58 90
Total reflections	686114 (60885)	559063 (30390)
Unique reflections	98507 (9041)	79094 (4376)
Multiplicity	7.0 (6.4)	7.1 (6.9)
Completeness (%)	97.85 (91.11)	98.1 (95.8)
Mean I/sigma(I)	9.43 (0.97)	7.5 (1.1)
Wilson B-factor	91.20	94.99
R-merge	0.174 (1.768)	0.211 (1.942)
R-meas	0.189 (1.927)	0.228 (2.100)
R-pim	0.071 (0.754)	0.086 (0.787)
CC1/2	0.999 (0.530)	0.994 (0.466)
CC*	1.000 (0.832)	
Reflections used in refinement	97914 (9035)	
Reflections used for R-free	4897 (425)	
R-work	0.254 (0.353)	
R-free	0.282 (0.365)	
CC(work)	0.740 (0.685)	
CC(free)	0.529 (0.606)	
Number of non-hydrogen atoms	26975	
macromolecules	26783	
ligands	192	
Protein residues	3464	
RMS (bonds) (Å)	0.003	
RMS (angles) (º)	0.60	
Ramachandran favored (%)	97.35	
Ramachandran allowed (%)	2.59	
Ramachandran outliers (%)	0.06	
Rotamer outliers (%)	0.58	
Clashscore	8.33	
Average B-factor	120.02	
macromolecules	120.15	
ligands	101.67	

**Statistics for the highest-resolution shell are shown in parentheses.

Table S9. Cryo-EM data collection, refinement and validation statistics

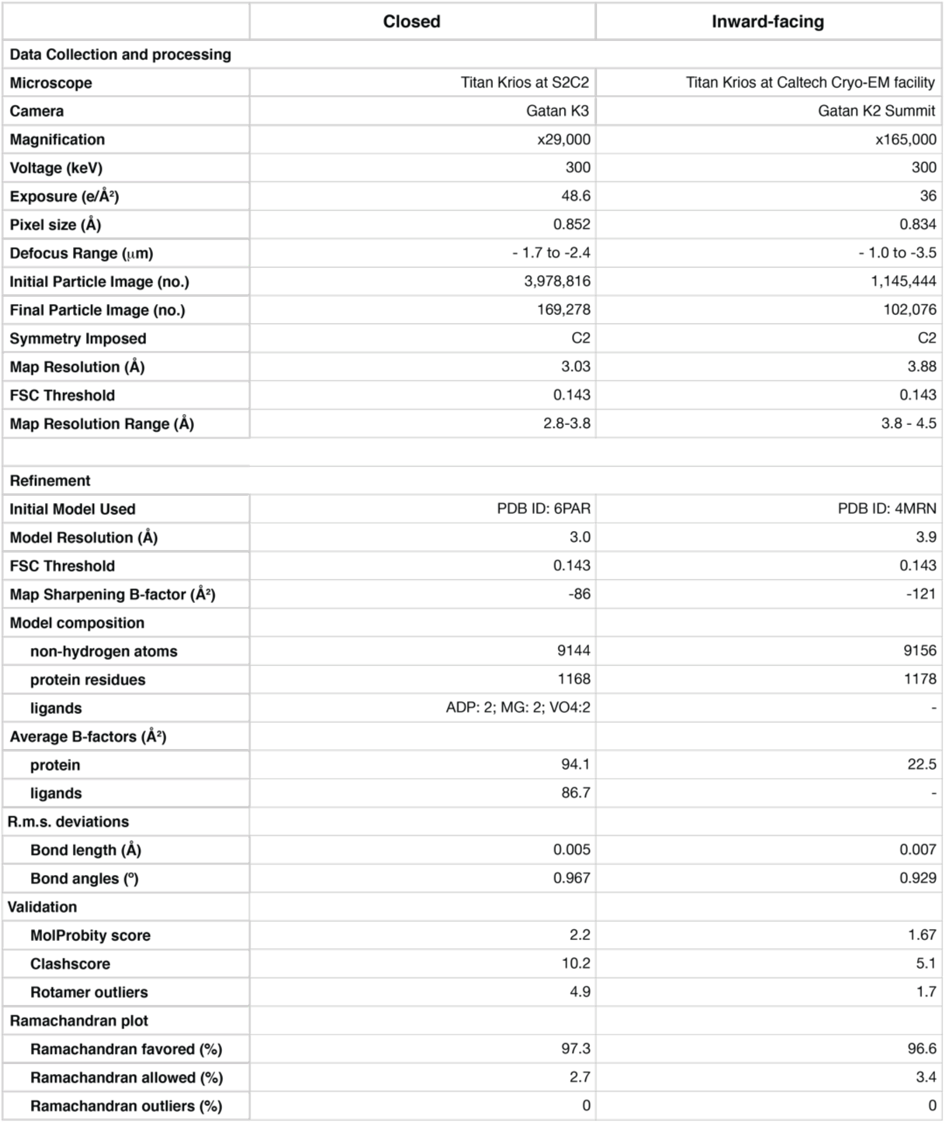

	Closed	Inward-facing
Data Collection and processing		
Microscope	Titan Krios at S2C2	Titan Krios at Caltech Cryo-EM facility
Camera	Gatan K3	Gatan K2 Summit
Magnification	x29,000	x165,000
Voltage (keV)	300	300
Exposure (e/Å^2)	48.6	36
Pixel size (Å)	0.852	0.834
Defocus Range (μm)	- 1.7 to -2.4	- 1.0 to -3.5
Initial Particle Image (no.)	3,978,816	1,145,444
Final Particle Image (no.)	169,278	102,076
Symmetry Imposed	C2	C2
Map Resolution (Å)	3.03	3.88
FSC Threshold	0.143	0.143
Map Resolution Range (Å)	2.8-3.8	3.8 - 4.5
Refinement		
Initial Model Used	PDB ID: 6PAR	PDB ID: 4MRN
Model Resolution (Å)	3.0	3.9
FSC Threshold	0.143	0.143
Map Sharpening B-factor (Å^2)	-86	-121
Model composition		
non-hydrogen atoms	9144	9156
protein residues	1168	1178
ligands	ADP: 2; MG: 2; VO4:2	-
Average B-factors (Å^2)		
protein	94.1	22.5
ligands	86.7	-
R.m.s. deviations		
Bond length (Å)	0.005	0.007
Bond angles (º)	0.967	0.929
Validation		
MolProbity score	2.2	1.67
Clashscore	10.2	5.1
Rotamer outliers	4.9	1.7
Ramachandran plot		
Ramachandran favored (%)	97.3	96.6
Ramachandran allowed (%)	2.7	3.4
Ramachandran outliers (%)	0	0

2.10 References

Adams, P. D., P. V. Afonine, G. Bunkoczi, V. B. Chen, I. W. Davis, N. Echols, J. J. Headd, L. W. Hung, G. J. Kapral, R. W. Grosse-Kunstleve, A. J. McCoy, N. W. Moriarty, R. Oeffner, R. J. Read, D. C. Richardson, J. S. Richardson, T. C. Terwilliger, and P. H. Zwart. 2010. "PHENIX: A comprehensive Python-based system for macromolecular structure solution." *Acta Crystallographica D Biological Crystallography* 66 (Pt 2):213-21. doi: 10.1107/S0907444909052925.

Alam, A., J. Kowal, E. Broude, I. Roninson, and K. P. Locher. 2019. "Structural insight into substrate and inhibitor discrimination by human P-glycoprotein." *Science* 363 (6428):753-756. doi: 10.1126/science.aav7102.

Alam, A., R. Kung, J. Kowal, R. A. McLeod, N. Tremp, E. V. Broude, I. B. Roninson, H. Stahlberg, and K. P. Locher. 2018. "Structure of a zosuquidar and UIC2-bound human-mouse chimeric ABCB1." *Proceedings of the National Academy of Sciences of the United States of America* 115 (9):E1973-E1982. doi: 10.1073/pnas.1717044115.

Aller, S. G., J. Yu, A. Ward, Y. Weng, S. Chittaboina, R. Zhuo, P. M. Harrell, Y. T. Trinh, Q. Zhang, I. L. Urbatsch, and G. Chang. 2009. "Structure of P-glycoprotein reveals a molecular basis for poly-specific drug binding." *Science* 323 (5922):1718-22. doi: 10.1126/science.1168750.

Arnold, F. M., M. S. Weber, I. Gonda, M. J. Gallenito, S. Adenau, P. Egloff, I. Zimmermann, C. A. J. Hutter, L. M. Hurlimann, E. E. Peters, J. Piel, G. Meloni, O. Medalia, and M. A. Seeger. 2020. "The ABC exporter IrtAB imports and reduces mycobacterial siderophores." *Nature* 580 (7803):413-417. doi: 10.1038/s41586-020-2136-9.

Bennett, B. D., E. H. Kimball, M. Gao, R. Osterhout, S. J. Van Dien, and J. D. Rabinowitz. 2009. "Absolute metabolite concentrations and implied enzyme active site occupancy in *Escherichia coli*." *Nature Chemical Biology* 5 (8):593-9. doi: 10.1038/nchembio.186.

Borths, E. L., B. Poolman, R. N. Hvorup, K. P. Locher, and D. C. Rees. 2005. "*In vitro* functional characterization of BtuCD-F, the *Escherichia coli* ABC transporter for vitamin B_{12} uptake." *Biochemistry* 44 (49):16301-9. doi: 10.1021/bi0513103.

Cavadini, P., G. Biasiotto, M. Poli, S. Levi, R. Verardi, I. Zanella, M. Derosas, R. Ingrassia, M. Corrado, and P. Arosio. 2007. "RNA silencing of the mitochondrial ABCB7 transporter in HeLa cells causes an iron-deficient phenotype with mitochondrial iron overload." *Blood* 109 (8):3552-9. doi: 10.1182/blood-2006-08-041632.

Chavan, H., M. M. Khan, G. Tegos, and P. Krishnamurthy. 2013. "Efficient purification and reconstitution of ATP binding cassette transporter B6 (ABCB6) for functional and structural studies." *Journal of Biological Chemistry* 288 (31):22658-69. doi: 10.1074/jbc.M113.485284.

Chen, J., S. Sharma, F. A. Quiocho, and A. L. Davidson. 2001. "Trapping the transition state of an ATP-binding cassette transporter: Evidence for a concerted mechanism of maltose transport." *Proceedings of the National Academy of Sciences of the United States of America* 98 (4):1525-30. doi: 10.1073/pnas.041542498.

Chifflet, S., A. Torriglia, R. Chiesa, and S. Tolosa. 1988. "A method for the determination of inorganic phosphate in the presence of labile organic phosphate and high concentrations of protein: application to lens ATPases." *Analytical Biochemistry* 168 (1):1-4.

Davidson, A. L., E. Dassa, C. Orelle, and J. Chen. 2008. "Structure, function, and evolution of bacterial ATP-binding cassette systems." *Microbiology and Molecular Biology Reviews* 72 (2):317-64. doi: 10.1128/MMBR.00031-07.

Davidson, A. L., and H. Nikaido. 1990. "Overproduction, solubilization, and reconstitution of the maltose transport system from *Escherichia coli*." *Journal of Biological Chemistry* 265 (8):4254-60.

Dawson, R. J., and K. P. Locher. 2006. "Structure of a bacterial multidrug ABC transporter." *Nature* 443 (7108):180-5. doi: 10.1038/nature05155.

Dean, D. A., A. L. Davidson, and H. Nikaido. 1989. "Maltose transport in membrane vesicles of *Escherichia coli* is linked to ATP hydrolysis." *Proceedings of the National Academy of Sciences of the United States of America* 86 (23):9134-8. doi: 10.1073/pnas.86.23.9134.

Dong, M., F. Penin, and L. G. Baggetto. 1996. "Efficient purification and reconstitution of P-glycoprotein for functional and structural studies." *Journal of Biological Chemistry* 271 (46):28875-83. doi: 10.1074/jbc.271.46.28875.

Emsley, P., B. Lohkamp, W. G. Scott, and K. Cowtan. 2010. "Features and development of Coot." *Acta Crystallographica D Biological Crystallography* 66 (Pt 4):486-501. doi: 10.1107/S0907444910007493.

Erickson, H. P. 2009. “Size and shape of protein molecules at the nanometer level determined by sedimentation, gel filtration, and electron microscopy.” *Biological Procedures Online* 11:32-51. doi: 10.1007/s12575-009-9008-x.

Eytan, G. D., R. Regev, and Y. G. Assaraf. 1996. “Functional reconstitution of P-glycoprotein reveals an apparent near stoichiometric drug transport to ATP hydrolysis.” *Journal of Biological Chemistry* 271 (6):3172-8. doi: 10.1074/jbc.271.6.3172.

Geertsma, E. R., N. A. Nik Mahmood, G. K. Schuurman-Wolters, and B. Poolman. 2008. “Membrane reconstitution of ABC transporters and assays of translocator function.” *Nature Protocols* 3 (2):256-66. doi: 10.1038/nprot.2007.519.

Goodno, C. C. 1982. “Myosin active-site trapping with vanadate ion.” *Methods in Enzymology* 85 Pt B:116-23. doi: 10.1016/0076-6879(82)85014-3.

Grossmann, N., A. S. Vakkasoglu, S. Hulpke, R. Abele, R. Gaudet, and R. Tampe. 2014. “Mechanistic determinants of the directionality and energetics of active export by a heterodimeric ABC transporter.” *Nature Communications* 5:5419. doi: 10.1038/ncomms6419.

Higgins, C. F. 1992. “ABC transporters: From microorganisms to man.” *Annual Review of Cell Biology* 8:67-113. doi: 10.1146/annurev.cb.08.110192.000435.

Hofmann, S., D. Januliene, A. R. Mehdipour, C. Thomas, E. Stefan, S. Bruchert, B. T. Kuhn, E. R. Geertsma, G. Hummer, R. Tampe, and A. Moeller. 2019. “Conformation space of a heterodimeric ABC exporter under turnover conditions.” *Nature* 571 (7766):580-583. doi: 10.1038/s41586-019-1391-0.

Jin, M. S., M. L. Oldham, Q. Zhang, and J. Chen. 2012. “Crystal structure of the multidrug transporter P-glycoprotein from *Caenorhabditis elegans*.” *Nature* 490 (7421):566-9. doi: 10.1038/nature11448.

Johnson, Z. L., and J. Chen. 2017. “Structural basis of substrate recognition by the multidrug resistance protein MRP1.” *Cell* 168 (6):1075-1085 e9. doi: 10.1016/j.cell.2017.01.041.

Kaback, H. R. 2015. “A chemiosmotic mechanism of symport.” *Proceedings of the National Academy of Sciences of the United States of America* 112 (5):1259-64. doi: 10.1073/pnas.1419325112.

Kabsch, W. 2010. “Xds.” *Acta Crystallographica D Biological Crystallography* 66 (Pt 2):125-32. doi: 10.1107/S0907444909047337.

Kim, Y., and J. Chen. 2018. “Molecular structure of human P-glycoprotein in the ATP-bound, outward-facing conformation.” *Science* 359 (6378):915-919. doi: 10.1126/science.aar7389.

Kispal, G., P. Csere, B. Guiard, and R. Lill. 1997. “The ABC transporter Atm1p is required for mitochondrial iron homeostasis.” *FEBS Letters* 418 (3):346-50.

Korkhov, V. M., S. A. Mireku, and K. P. Locher. 2012. “Structure of AMP-PNP-bound vitamin B_{12} transporter BtuCD-F.” *Nature* 490 (7420):367-72. doi: 10.1038/nature11442.

Lee, J. Y., J. G. Yang, D. Zhitnitsky, O. Lewinson, and D. C. Rees. 2014. “Structural basis for heavy metal detoxification by an Atm1-type ABC exporter.” *Science* 343 (6175):1133-6. doi: 10.1126/science.1246489.

Lewinson, O., and N. Livnat-Levanon. 2017. “Mechanism of action of ABC importers: conservation, divergence, and physiological adaptations.” *Journal of Biological Chemistry* 429 (5):606-619. doi: 10.1016/j.jmb.2017.01.010.

Lill, R., and G. Kispal. 2001. “Mitochondrial ABC transporters.” *Research in Microbiology* 152 (3-4):331-40.

Liu, F., Z. Zhang, L. Csanady, D. C. Gadsby, and J. Chen. 2017. “Molecular structure of the human CFTR ion channel.” *Cell* 169 (1):85-95 e8. doi: 10.1016/j.cell.2017.02.024.

Liu, F., Z. Zhang, A. Levit, J. Levring, K. K. Touhara, B. K. Shoichet, and J. Chen. 2019. “Structural identification of a hotspot on CFTR for potentiation.” *Science* 364 (6446):1184-1188. doi: 10.1126/science.aaw7611.

Locher, K. P. 2016. “Mechanistic diversity in ATP-binding cassette (ABC) transporters.” *Nature Structural & Molecular Biology* 23 (6):487-93. doi: 10.1038/nsmb.3216.

Lycklama, A. Nijeholt J. A., R. Vietrov, G. K. Schuurman-Wolters, and B. Poolman. 2018. “Energy coupling efficiency in the type I ABC transporter GlnPQ.” *Journal of Molecular Biology* 430 (6):853-866. doi: 10.1016/j.jmb.2018.02.001.

Manolaridis, I., S. M. Jackson, N. M. I. Taylor, J. Kowal, H. Stahlberg, and K. P. Locher. 2018. “Cryo-EM structures of a human ABCG2 mutant trapped in ATP-bound and substrate-bound states.” *Nature* 563 (7731):426-430. doi: 10.1038/s41586-018-0680-3.

McPhillips, T. M., S. E. McPhillips, H. J. Chiu, A. E. Cohen, A. M. Deacon, P. J. Ellis, E. Garman, A. Gonzalez, N. K. Sauter, R. P. Phizackerley, S. M. Soltis, and P. Kuhn. 2002. "Blu-Ice and the distributed control system: Software for data acquisition and instrument control at macromolecular crystallography beamlines." *Journal of Synchrotron Radiation* 9 (Pt 6):401-6. doi: 10.1107/s0909049502015170.

Mi, W., Y. Li, S. H. Yoon, R. K. Ernst, T. Walz, and M. Liao. 2017. "Structural basis of MsbA-mediated lipopolysaccharide transport." *Nature* 549 (7671):233-237. doi: 10.1038/nature23649.

Moody, J. E., L. Millen, D. Binns, J. F. Hunt, and P. J. Thomas. 2002. "Cooperative, ATP-dependent association of the nucleotide binding cassettes during the catalytic cycle of ATP-binding cassette transporters." *Journal of Biological Chemistry* 277 (24):21111-4. doi: 10.1074/jbc.C200228200.

Nikaido, K., and G. F. Ames. 1999. "One intact ATP-binding subunit is sufficient to support ATP hydrolysis and translocation in an ABC transporter, the histidine permease." *Journal of Biological Chemistry* 274 (38):26727-35. doi: 10.1074/jbc.274.38.26727.

Oldham, M. L., and J. Chen. 2011. "Snapshots of the maltose transporter during ATP hydrolysis." *Proceedings of the National Academy of Sciences of the United States of America* 108 (37):15152-6. doi: 10.1073/pnas.1108858108.

Palmgren, M. G., and P. Nissen. 2011. "P-type ATPases." *Annual Review of Biophysics* 40:243-66. doi: 10.1146/annurev.biophys.093008.131331.

Patzlaff, J. S., T. van der Heide, and B. Poolman. 2003. "The ATP/substrate stoichiometry of the ATP-binding cassette (ABC) transporter OpuA." *Journal of Biological Chemistry* 278 (32):29546-51. doi: 10.1074/jbc.M304796200.

Perez, C., A. R. Mehdipour, G. Hummer, and K. P. Locher. 2019. "Structure of outward-facing PglK and molecular dynamics of lipid-linked oligosaccharide recognition and translocation." *Structure* 27 (4):669-678 e5. doi: 10.1016/j.str.2019.01.013.

Pettersen, E. F., T. D. Goddard, C. C. Huang, G. S. Couch, D. M. Greenblatt, E. C. Meng, and T. E. Ferrin. 2004. "UCSF Chimera--a visualization system for exploratory research and analysis." *Journal of Computational Chemistry* 25 (13):1605-12. doi: 10.1002/jcc.20084.

Pondarre, C., B. B. Antiochos, D. R. Campagna, S. L. Clarke, E. L. Greer, K. M. Deck, A. McDonald, A. P. Han, A. Medlock, J. L. Kutok, S. A. Anderson, R. S. Eisenstein, and M. D. Fleming. 2006. “The mitochondrial ATP-binding cassette transporter Abcb7 is essential in mice and participates in cytosolic iron-sulfur cluster biogenesis.” *Human Molecular Genetics* 15 (6):953-64. doi: 10.1093/hmg/ddl012.

Punjani, A., J. L. Rubinstein, D. J. Fleet, and M. A. Brubaker. 2017. “cryoSPARC: Algorithms for rapid unsupervised cryo-EM structure determination.” *Nature Methods* 14 (3):290-296. doi: 10.1038/nmeth.4169.

Rees, D. C., E. Johnson, and O. Lewinson. 2009. “ABC transporters: The power to change.” *Nature Reviews: Molecular Cell Biology* 10 (3):218-27. doi: 10.1038/nrm2646.

Rempel, S., C. Gati, M. Nijland, C. Thangaratnarajah, A. Karyolaimos, J. W. de Gier, A. Guskov, and D. J. Slotboom. 2020. “A mycobacterial ABC transporter mediates the uptake of hydrophilic compounds.” *Nature*. doi: 10.1038/s41586-020-2072-8.

Ritchie, T. K., Y. V. Grinkova, T. H. Bayburt, I. G. Denisov, J. K. Zolnerciks, W. M. Atkins, and S. G. Sligar. 2009. “Reconstitution of membrane proteins in phospholipid bilayer nanodiscs.” In *Methods in Enzymology*, 211-231.

Rohou, A., and N. Grigorieff. 2015. “CTFFIND4: Fast and accurate defocus estimation from electron micrographs.” *Journal of Structural Biology* 192 (2):216-21. doi: 10.1016/j.jsb.2015.08.008.

Srinivasan, V., A. J. Pierik, and R. Lill. 2014. “Crystal structures of nucleotide-free and glutathione-bound mitochondrial ABC transporter Atm1.” *Science* 343 (6175):1137-40. doi: 10.1126/science.1246729.

Stefan, E., S. Hofmann, and R. Tampe. 2020. “A single power stroke by ATP binding drives substrate translocation in a heterodimeric ABC transporter.” *Elife* 9. doi: 10.7554/eLife.55943.

Stepanov, S., O. Makarov, M. Hilgart, S. B. Pothineni, A. Urakhchin, S. Devarapalli, D. Yoder, M. Becker, C. Ogata, R. Sanishvili, N. Venugopalan, J. L. Smith, and R. F. Fischetti. 2011. “JBluIce-EPICS control system for macromolecular crystallography.” *Acta Crystallographica D Biological Crystallography* 67 (Pt 3):176-88. doi: 10.1107/S0907444910053916.

Thomas, C., and R. Tampe. 2018. “Multifaceted structures and mechanisms of ABC transport systems in health and disease.” *Current Opinion in Structural Biology* 51:116-128. doi: 10.1016/j.sbi.2018.03.016.

Tian, W., C. Chen, X. Lei, J. Zhao, and J. Liang. 2018. “CASTp 3.0: Computed atlas of surface topography of proteins.” *Nucleic Acids Research* 46 (W1):W363-W367. doi: 10.1093/nar/gky473.

Wang, J., F. Sun, D. W. Zhang, Y. Ma, F. Xu, J. D. Belani, J. C. Cohen, H. H. Hobbs, and X. S. Xie. 2006. “Sterol transfer by ABCG5 and ABCG8: *In vitro* assay and reconstitution.” *Journal of Biological Chemistry* 281 (38):27894-904. doi: 10.1074/jbc.M605603200.

Ward, A., C. L. Reyes, J. Yu, C. B. Roth, and G. Chang. 2007. “Flexibility in the ABC transporter MsbA: Alternating access with a twist.” *Proceedings of the National Academy of Sciences of the United States of America* 104 (48):19005-10. doi: 10.1073/pnas.0709388104.

Winn, M. D., C. C. Ballard, K. D. Cowtan, E. J. Dodson, P. Emsley, P. R. Evans, R. M. Keegan, E. B. Krissinel, A. G. Leslie, A. McCoy, S. J. McNicholas, G. N. Murshudov, N. S. Pannu, E. A. Potterton, H. R. Powell, R. J. Read, A. Vagin, and K. S. Wilson. 2011. “Overview of the CCP4 suite and current developments.” *Acta Crystallographica D Biological Crystallography* 67 (Pt 4):235-42. doi: 10.1107/S0907444910045749.

Woo, J. S., A. Zeltina, B. A. Goetz, and K. P. Locher. 2012. “X-ray structure of the *Yersinia pestis* heme transporter HmuUV.” *Nature Structural & Molecular Biology* 19 (12):1310-5. doi: 10.1038/nsmb.2417.

Zehnpfennig, B., I. L. Urbatsch, and H. J. Galla. 2009. “Functional reconstitution of human ABCC3 into proteoliposomes reveals a transport mechanism with positive cooperativity.” *Biochemistry* 48 (20):4423-30. doi: 10.1021/bi9001908.

Zhang, Z., F. Liu, and J. Chen. 2017. “Conformational changes of CFTR upon phosphorylation and ATP binding.” *Cell* 170 (3):483-491 e8. doi: 10.1016/j.cell.2017.06.041.

Zuo, J., Z. Wu, Y. Li, Z. Shen, X. Feng, M. Zhang, and H. Ye. 2017. “Mitochondrial ABC transporter ATM3 is essential for cytosolic iron-sulfur cluster assembly.” *Plant Physiology* 173 (4):2096-2109. doi: 10.1104/pp.16.01760.

Chapter 3

A KINETIC MODEL FOR THE ATPASE STIMULATION OF THE ABC EXPORTER *NA*ATM1 BY THE TRANSPORTED SUBSTRATE GSSG

This chapter is adapted from:

Fan, C., and Rees, D.C. “A kinetic model for the ATPase stimulation of the ABC exporter *Na*Atm1 by the transported substrate GSSG.” *In preparation*.

3.1 Abstract

Previous structural analysis on a bacterial homolog of the eukaryotic ABC transporter of mitochondria from *Novosphingohium aromaticivorans* (*Na*Atm1) outlined a conformational framework for both the substrate-dependent transport cycle and the substrate-independent ATPase cycle. Here, we report the characterization of the ATPase activities of *Na*Atm1 in the absence and presence of a transported substrate, oxidized glutathione (GSSG), in detergent, nanodiscs and proteoliposomes. The basal ATPase activities of *Na*Atm1 were significantly stimulated by increasing concentrations of GSSG, although the details varied between the different samples, highlighting the importance of the detailed lipid environment for *Na*Atm1 function. Changes in the apparent Michaelis-Menten constant K_M for MgATP with changes in GSSG concentration were also observed. The kinetic data were fit to the "non-essential activator model" where the basal ATPase rate of the transporter is stimulated by the transported substrate, which consequently functions as an ATPase activator. An expanded non-essential activator kinetic model with two GSSG binding sites recapitulated the dependence of the turnover rate and apparent MgATP binding affinity on GSSG concentration.

3.2 Introduction

Membrane transporters couple the translocation of ligands to a thermodynamically favorable driving force. A key feature of the transport mechanism is that these two processes - ligand transport and the driving force - must be linked to minimize "short circuiting" of the transduction process (Tanford 1983, Hill 1989). In essence, transporters kinetically facilitate the coupled reaction while disfavoring the individual uncoupled reactions. One way to achieve coupling between the favored and unfavored reactions is when both processes proceed through a common set of conformational states so that they can only be accessed when the relevant components are both present (Rees and Howard 1999). Structure based mechanisms defining these coupling processes have been advanced for several transporters, including lactose permease (Kaback 2015) and P-type ATPases (Palmgren and Nissen 2011).

ATP Binding Cassette (ABC) transporters form a large family where substrate translocation is coupled to the ATPase activity (Higgins 1992, Rees, Johnson, and Lewinson 2009, Locher 2016). Of note, they typically exhibit significant basal ATPase activity in the absence of transported substrates (i.e. uncoupled ATPase activity). The presence of transported substrates stimulates the ATPase activity and indeed, putative substrates for ABC exporters are commonly identified as ATPase activators, although these molecules may not necessarily be the transported substrate (Lefevre and Boutry 2018). Our previous structural analyses on a bacterial ABC exporter from *Novosphingobium aromaticavorans* (*Na*Atm1) identified multiple conformational states, including the inward-facing, outward-facing and various occluded states in the presence of different nucleotides. In addition to the substrate-dependent transport cycle, there also exists a substrate independent ATPase cycle responsible for the basal activity of the transporter. To gain more insights into the substrate dependent transport cycle, we measured the substrate dependent ATPase activities of *Na*Atm1 in detergent, nanodiscs (ND), and proteoliposomes (PLS). The reconstructed equilibrium kinetic model revealed interesting findings for the ATP dependent substrate translocation.

3.3 Results

Michaelis-Menten kinetics

To measure the ATPase activities of *Na*Atm1 in different membrane-like environments, we reconstituted detergent purified protein into both nanodiscs (ND) formed by membrane scaffolding proteins and proteoliposomes (PLS), using previously described protocols. The ATPase rates were measured under varying concentrations of MgATP and GSSG, by quantifying the amount of inorganic phosphate (Pi) released upon ATP hydrolysis using a molybdate-based colorimetric assay (Chifflet et al. 1988). In contrast to *Na*Atm1 solubilized in detergent (Figure 1a) or reconstituted into ND (Figure 1b), *Na*Atm1 in PLS presents an orientational issue, with the NBDs either positioned outside the PLS (and accessible to the assay) or positioned inside the PLS (and inaccessible to the assay). If there is no orientational preference in the reconstitution process, then 50% of the transporters will adopt each orientation. As this effect was not experimentally investigated, we do not have independent confirmation of the orientation factor and so the measured ATPase activities in PLS for *Na*Atm1 are not corrected for this effect.

The measured ATPase activities of *Na*Atm1 in the presence of a fixed concentration of GSSG were fit to the Michaelis-Menten equation (Figure 2). From these fits, values for the observed turnover rate k_{obs} and the apparent binding constant for MgATP binding K_T (K_M for MgATP) were obtained at various concentrations of GSSG, summarized in Table 1. In all three environments (detergent, ND and PLS), the ATPase activities exhibit dependence on the concentration of GSSG in a dose-dependent manner. In the absence of GSSG, the maximal rates (V_{max}) of ATP hydrolysis were extrapolated to 135, 170 and 70 nmol Pi min^{-1} mg^{-1} transporter in detergent, ND and PLS, corresponding to turnover rates of 18.0, 22.6, and 9.5 min^{-1} per dimeric *Na*Atm1, respectively. (Figure 2, Table 1a). At the highest concentration of GSSG that the ATPase activities were measured (20 mM), about eight times of the physiological GSSG concentration (Bennett et al. 2009), the maximum extrapolated ATPase activity for *Na*Atm1 in detergent was ~700 nmol Pi min^{-1} mg^{-1}, by stimulating its corresponding basal activity to ~5 times, 2400 nmol Pi min^{-1} mg^{-1} for *Na*Atm1 in ND with ~14 times of basal activity stimulation, and 800 nmol Pi min^{-1} mg^{-1} for *Na*Atm1 in PLS with ~11 times of basal activity stimulation (Figure 2). As the orientation effect in PLS was not taken into account, the actual ATPase rate in PLS may be ~2 times of the measured activity.

Basic non-essential activator kinetic model

Both k_{obs}, the observed turnover rate, and K_T, the Michaelis-Menten constant for MgATP, depend on the concentration of the transported substrate GSSG. To model this data, we used a non-essential activator model (Figure 3a) where the transported substrate GSSG is an activator that stimulates the ATPase rate above the basal level (Segel 1975, Baici 2015). The key kinetic parameters in this model are: i) K_T, the binding constant for MgATP; ii) K_S, the binding constant for the transported substrate, GSSG, which is also an activator of the ATPase rate, iii) α, the interaction factor for how binding of MgATP influences the binding of GSSG (and vice versa). The convention is that $\alpha < 1$ or > 1 denotes positive and negative cooperativity, respectively; iv) k, the basal rate constant for MgATP hydrolysis in the absence of GSSG and v) β, the acceleration factor for MgATP hydrolysis with bound GSSG. In this model, the ATPase sites are treated as independent since the dependence of the ATPase rate on ATP does not exhibit positive cooperativity. E_T stands for the total concentration of enzymes. For this scheme, expressions for the overall velocity, k_{obs} and K_T^{app}, may be derived.

$$\text{Equation 1: } v = \frac{E_T k \left\{ \frac{[T]}{K_T} + \beta \left(\frac{[S][T]}{\alpha K_S K_T} \right) \right\}}{1 + \frac{[T]}{K_T} + \frac{[S]}{K_S} + \frac{[S][T]}{\alpha K_S K_T}}$$

$$\text{Equation 2: } k_{obs} = k \frac{\left(1 + \beta \frac{[S]}{\alpha K_S}\right)}{\left(1 + \frac{[S]}{\alpha K_S}\right)}$$

$$\text{Equation 3: } K_T^{app} = K_T \frac{\left(1 + \frac{[S]}{K_S}\right)}{\left(1 + \frac{[S]}{\alpha K_S}\right)}$$

From the fit of the non-essential activator model with all of the kinetic data (Equation 1, Table 2), the ATPase activities were fitted reasonably well (Figure S1), similar to that of the Michaelis-Menten kinetics (Figure 2) with minor changes in the extrapolated V_{max} (Figure S1). The goodness of fit in all three membrane conditions are also shown in Table S1. In addition, we were able to obtain the different kinetic parameters, k_{obs}, K_T, K_S, α and β (Table 2). The observed turnover rates are 17.6 min^{-1} in detergent, 23.3 min^{-1} in ND, and 9 min^{-1} in PLS (Table 2), similar to that in the Michaelis-Menten kinetics in the absence of GSSG (Table 1a), and the observed binding affinities of MgATP are 0.82 mM in detergent, 1.41 mM in ND, and 1.6 mM in PLS, also close to those of the Michaelis-Menten kinetics (Table 1b). Yet, this fitting resulted in K_S, binding affinity of GSSG, to about 10 mM in detergent, ND, and PLS, which is inconsistent with the previously published data of a binding affinity that's less than 1 mM for GSSG to the transporter in detergent (Lee et al. 2014). Additionally, the α value in detergent was about 1, suggesting no cooperativity between the MgATP and GSSG binding. In comparison, the values of α are 10 in ND and 3 in PLS, suggestive of negative cooperativity between GSSG and MgATP binding. In all conditions, the acceleration factors β value are 8.3, 77, and 29 in detergent, ND, and PLS, respectively (Table 2).

When using the non-essential activator model to model the GSSG concentration dependence of the turnover rates by fitting the observed values of the turnover rates from Michaelis-Menten kinetics (Table 1a) at various GSSG concentration using Equation 2, we observed that non-essential activator model could well captured the dependence of the turnover rate, k_{obs} on the GSSG concentration in detergent, ND, and PLS, which is also reflected in the R^2 values (Figure 3b). But this model failed to capture the effect of the substrate activator GSSG on K_T at low GSSG concentrations for the detergent and ND conditions (Figure 3c) when fitted using Equation 3, again reflected in the R^2.

Expanded non-essential activator kinetic model

To address this deficiency, an expanded activator model was developed with two additional parameters (Figure 4a) to accommodate two GSSG binding sites as observed crystallographically (Lee et al. 2014). The first GSSG binding is hypothesized to stabilize the ET state responsible for the basal ATPase rate, while the second GSSG binding stabilizes a conformation with a different affinity for MgATP (interaction factor γ) and a significantly higher ATPase activity. For γ, the convention is similar to that of α, in which $\gamma < 1$ or > 1 separately denotes positive and negative cooperativity. Like the non-essential activator model, the non-linear fit in expanded non-essential activator using Equation 4 was also able to recapitulate the hyperbolic curves (Figure S2) observed in the Michaelis-Mention kinetics (Figure 1, Table S1) with small changes in the extrapolated values of the maximum velocities in all three membrane conditions.

$$\text{Equation 4: } v = \frac{E_T k\left\{\left(\frac{[T]}{K_T} + \frac{[T][S]}{\alpha K_T K_{S1}}\right) + \beta\left(\frac{[T][S]^2}{\gamma K_T K_{S1} K_{S2}}\right)\right\}}{1 + \frac{[T]}{K_T} + \frac{[S]}{K_{S1}} + \frac{[T][S]}{\alpha K_T K_{S1}} + \frac{[S]^2}{K_{S1}K_{S2}} + \frac{[T][S]^2}{\gamma K_T K_{S1} K_{S2}}}$$

$$\text{Equation 5: } k_{obs} = k\frac{\left(1 + \frac{[S]}{\alpha K_{S1}} + \beta\frac{[S]^2}{\gamma K_{S1} K_{S2}}\right)}{\left(1 + \frac{[S]}{\alpha K_{S1}} + \frac{[S]^2}{\gamma K_{S1} K_{S2}}\right)}$$

$$\text{Equation 6: } K_T^{app} = K_T \frac{\left(1+\frac{[S]}{K_{S1}}+\frac{[S]^2}{K_{S1}K_{S2}}\right)}{\left(1+\frac{[S]}{\alpha K_{S1}}+\frac{[S]^2}{\gamma K_{S1}K_{S2}}\right)}$$

This expanded non-essential activator model could not only capture the dependence of k_{obs} on the GSSG concentration (Figure 4b, Equation 5), but it could also fit the K_T dependence on GSSG concentration in detergent, ND and PLS (Figure 4c, Equation 6). Within the framework of the expanded activator model, the MgATP binding constants in different membrane conditions, K_T, are all about to 1 mM, while the first GSSG binds to the transporter with refined K_{S1} of ~0.3 mM in detergent and ~0.1 mM in ND and PLS, and the second GSSG binding to the transporter with a K_{S2} of ~10 mM in detergent, ND and PLS (Table 3). In detergent, the α value is 0.76, suggestive of small positive cooperativity between the binding of MgATP and GSSG. In contrast, the α values are 1.07 and 1.2 in ND and PLS, respectively, corresponding to little or slight negative cooperativity. In contrast to the α values, the γ values are 0.8 in detergent, 11 in ND, and 3.1 in PLS, respectively. The γ values in ND and PLS are suggestive of negative cooperativity in ND and PLS, but the effects of MgATP binding on the first and second GSSG binding are different. Further, the binding of GSSG stimulates the ATPase activities as reflected in the acceleration factor β of 8 in detergent, 79 in ND, and 27 in PLS.

3.4 Discussion

The effects of the transported substrate GSSG of the ATPase activity of *Na*Atm1 were measured under three different conditions: 1) purified in a detergent mixture composed of 0.05% n-dodecyl-β-D-maltopyranoside (DDM) and 0.5% octaethylene glycol monododecyl ether (C12E8) used in the structural studies, 2) reconstituted into nanodiscs (ND) composed of the MSP1D1 and 1-palmitoyl-2-oleoyl-sn-glycero-3-phosphocholine (POPC), and 3) reconstituted into proteoliposomes (PLS) composed of *Escherichia coli* polar lipid extract and 1,2-dioleoyl-sn-glycero-3-phosphocholine (DOPC). For a given GSSG concentration, the dependence of the ATPase activity on ATP could be modeled by a Michaelis-Menten (hyperbolic) equation, yielding the k_{cat} and K_M for ATP hydrolysis as a function of GSSG concentration (Table 1). In the absence of GSSG, the k_{cat} characterizing the basal ATPase rate was 18.0 ± 0.4, 22.6 ± 0.5, and 9.5 ± 0.4 min^{-1} in detergent, ND and PLS, respectively. In each system, GSSG was observed to stimulate the ATPase activity of *Na*Atm1 in a concentration dependent fashion (Figure 2, Table 1), although the magnitude of the stimulation was dependent on the conditions; the k_{cat}'s were increased above the basal rate by factors of ~5, 14, and 11, in detergent, ND and PLS, respectively. Less pronounced changes, but statistically significant changes in K_M were also observed, corresponding to a decrease of ~20% in detergent, and increases of 2.7 and 1.9 times in ND and PLS, respectively.

An important aspect of this analysis is the opportunity to explore the binding interactions between ATP and GSSG, which are reflected in the cooperativity parameters α and γ. In detergent, little cooperativity is evident, with $\alpha \sim 1$ for the basic model, and α and $\gamma \sim 0.8$ for the expanded (suggests of slight positive cooperativity). In contrast, in ND and PLS, evidence for negative cooperativity is evident with $\alpha \sim 10$ and 3 respectively in the basic model; comparable values are observed for γ in the expanded model, with $\alpha \sim 1$ for the binding of the first GSSG molecule. The acceleration factor β is significantly larger in ND and PLS (79 and 27, respectively), compared to $\beta \sim 8$ in detergent (Table 3). Reflecting large value of γ observed in ND, however, the maximal activity in the presence of GSSG occurs at concentrations much higher than were used in this study (Fig 3b, 4b).

While our previously determined structural models help define the ligand dependence of the *Na*Atm1 conformational state, the kinetic models presented in this study define the ligand dependence of the ATPase activity. Integration of the structural and kinetic models remains challenging, however. An important open question concerns the conformational states of the various species in the kinetic models (Figures 3a and 4a). The structural studies are consistent with the free transporter and the transporter-GSSG complex (E and ES species, respectively) primarily adopting inward-facing conformations, while transporter-ATP states (ET) primarily exhibit occluded or outward-facing conformations. The preference for GSSG and ATP to stabilize distinct conformational states is consistent with the observed negative cooperativity in the binding of these ligands in ND and PLS (although curiously, not in detergent). Of course, each kinetic state exists as a distribution of multiple states; for example, while ATP stabilizes outward-facing conformations, it must initially bind to the inward-facing conformation, and indeed ABC exporters complexed with ATP analogues have been observed in the inward-facing conformation (Shintre et al. 2013). The stimulation of the ATPase rate by GSSG requires that the transported ligand should stabilize *Na*Atm1 in the state competent for ATP hydrolysis. However, the structural studies of the individual ligands bound to the transporter suggest that ATP and GSSG preferentially bind to distinct conformations. Nevertheless, the ternary complex has an accelerated ATPase rate - understanding how this species promotes ATP hydrolysis is at the heart of the coupling mechanism and emphasizes the importance of characterizing the structure and dynamics of this elusive transporter-ATP-substrate state.

3.5 Materials and Methods

Protein expression, purification and reconstitution

*Na*Atm1 was previously deposited in Addgene (plasmid # 78308). The over-expression of *Na*Atm1 was carried with *Escherichia coli* BL21-gold (DE3) cells (Agilent Technologies) using ZYM-5052 autoinduction media as described previously (Lee et al. 2014). Cells were harvested by centrifugation and stored at -80 ˚C until use.

Protein purification was carried out as follows. Frozen cell pellets were resuspended in lysis buffer containing 100 mM NaCl, 20 mM Tris, pH 7.5, 40 mM imidazole, pH 7.5, 10 mM $MgCl_2$, 0.5% (w/v) n-dodecyl-β-D-maltopyranoside (DDM) (Anatrace), and 0.5% (w/v) octaethylene glycol monododecyl ether (C12E8) (Anatrace) in the presence of lysozyme, DNase, and protease inhibitor tablet. Resuspended cells were solubilized by stirring for 3 hrs at 4 ˚C. The lysate was ultracentrifuged at ~113,000x g for 45 minutes at 4 ˚C to remove unlysed cells and cell debris. The supernatant was loaded onto a prewashed NiNTA column. NiNTA wash buffer contained 100 mM NaCl, 20 mM Tris, pH 7.5, 50 mM imidazole, pH 7.5, 0.05% DDM and 0.05% C12E8 and the elution buffer contained 350 mM imidazole instead. The eluted sample was then subjected to size exclusion chromatography using HiLoad 16/60 Superdex 200 (GE Healthcare) with buffer containing 100 mM NaCl, 20 mM Tris, pH 7.5, 0.05% DDM and 0.05% C12E8. Peak fractions were collected and concentrated with Amicon Ultra 15 concentrator (Millipore) (MW 100 kDa cutoff) to ~20 mg/ml.

*Na*Atm1 nanodiscs in membrane scaffolding protein was reconstituted in membrane scaffolding protein (MSP1D1) with 1-palmitoyl-2-oleoyl-glycero-3-phosphocholine (POPC). MSP1D1 was purchased from Addgene (plasmid # 20061) and its expression and purification were carried out by following published protocol (Ritchie et al. 2009). The detailed experimental protocol is described in Chapter 2. *Na*Atm1 in proteoliposomes was prepared by reconstituting detergent purified *Na*Atm1 into liposomes containing *Escherichia coli* polar lipid extract and 1,2-dioleoyl-sn-glycero-3-phosphocholine (DOPC) by following published protocol (Geertsma et al. 2008). The detailed experimental procedures are described in Chapter 2.

ATPase assay

The ATPase activities were measured by the molybdate-based phosphate quantification method (Chifflet et al. 1988). All reactions were carried out at 37 °C in 250 µL scale. The reaction mixture contains a final *Na*Atm1 concentration of 0.05 mg/ml, various concentrations of MgATP, pH 7.5, various concentrations of GSSG, pH 7.5, and buffer (100 mM NaCl and 20 mM Tris, pH 7.5). For each reaction, 50 µL of reaction mixture was taken every 5 minutes for 4 times and subsequently mixed with 50 µL of 12% SDS, 100 µL of ascorbic acid/molybdate mix, and 150 µL of citric acid/arsenite/acetic acid solution before reading with Tecan plate reader at 850 nm. Reactions in detergent and proteoliposomes were done in sextuplicates and reactions in nanodiscs were done in triplicates. The measurements were plotted against time to obtain the ATPase activities. The final rates were fitted into Michaelis-Menten kinetics or the non-essential activator models in Prism 8.

3.6 Figures

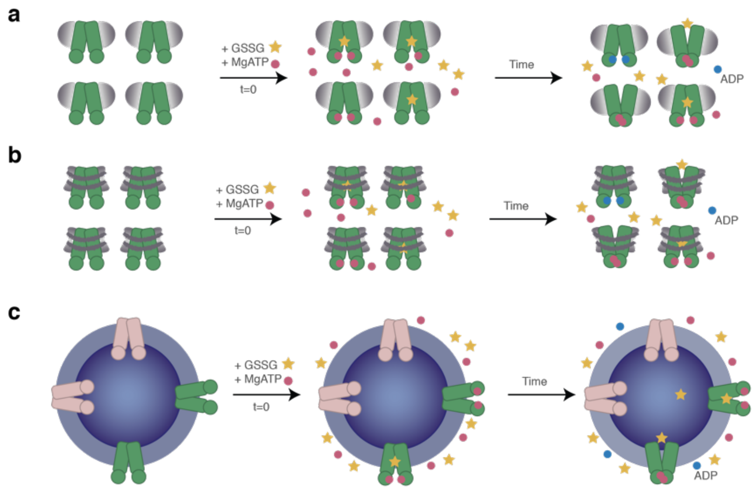

Figure 1. ATPase assay setups.

Schematics showing the ATPase reactions with (**a**) *Na*Atm1 purified in detergent, (**b**) *Na*Atm1 reconstituted in nanodiscs and (**c**) *Na*Atm1 reconstituted in proteoliposomes.

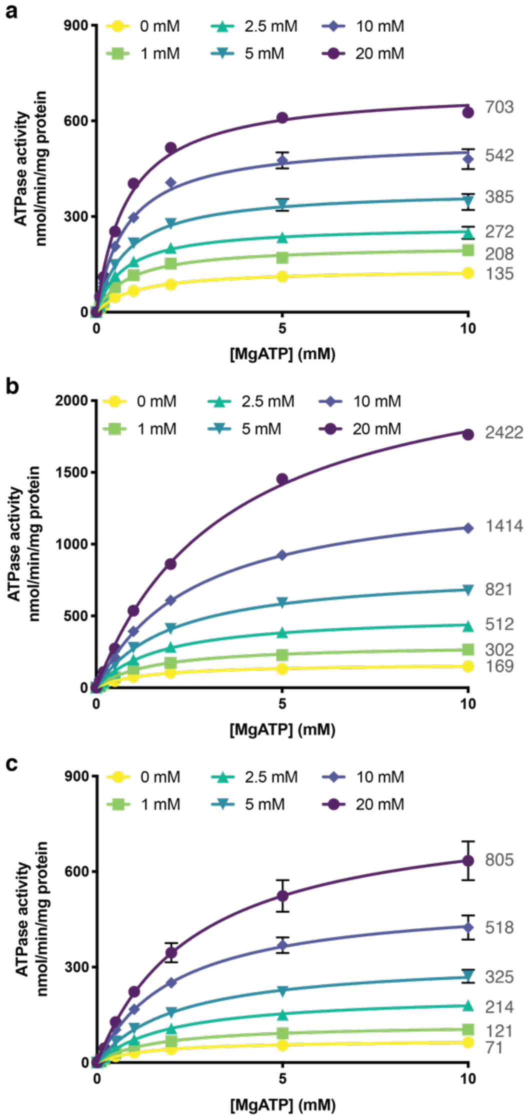

Figure 2. ATPase activities of *Na*Atm1 fitted to Michaelis-Menten kinetics.

ATPase activities of *Na*Atm1 in (**a**) detergent (DDM/C12E8), (**b**) nanodiscs (ND), and (**c**) proteoliposomes (PLS) with stimulations by GSSG at various concentrations. ATPase activities of *Na*Atm1 in detergent and PLS were measured six times, and three times in ND, all with distinct samples. All of the extrapolated V_{max} values are shown next to each GSSG concentration curve. Error bars represent the standard error of the mean for the replicates.

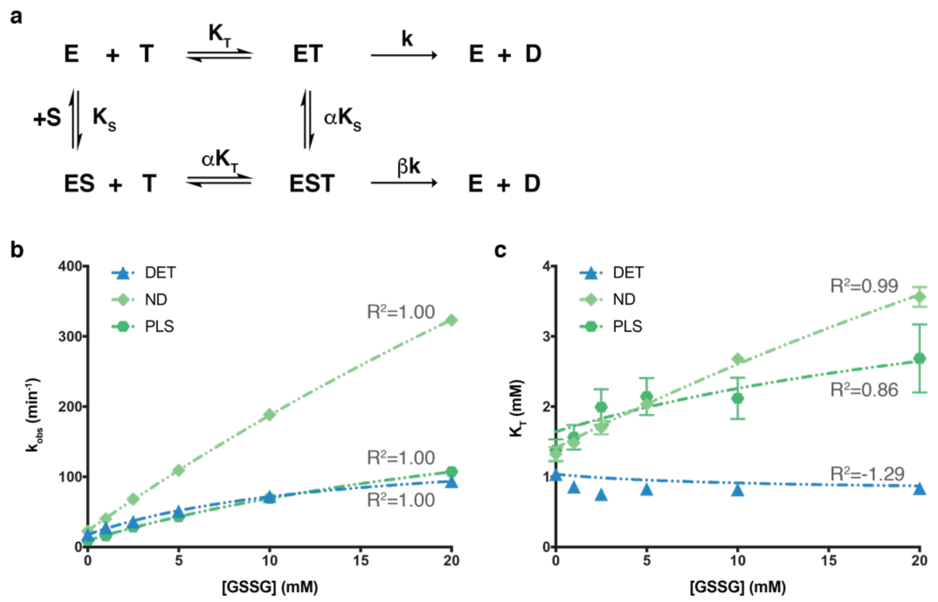

Figure 3. **Non-essential activator model of *Na*Atm1 ATPase kinetics**.

(**a**) Expanded activator model for the ATPase activities of *Na*Atm1. (**b**) Michaelis-Menten constant, K_T, of MgATP binding, and (**c**) apparent rate constant, k_{obs}, of ATP hydrolysis fittings based on the expanded activator model for *Na*Atm1 in detergent, nanodiscs, and proteoliposomes, respectively. In these schemes, E = *Na*Atm1, T = MgATP, D = ADP, S = GSSG, K_T = binding constant for MgATP, K_S = binding constant for GSSG, k = rate constant for MgATP hydrolysis, α = interaction factor of how ATP binding influences GSSG binding and vice versa, and β = acceleration factor for ATP hydrolysis with bound GSSG. Corresponding R^2 values from non-linear regressions are labeled. Error bars represent the calculated standard deviations.

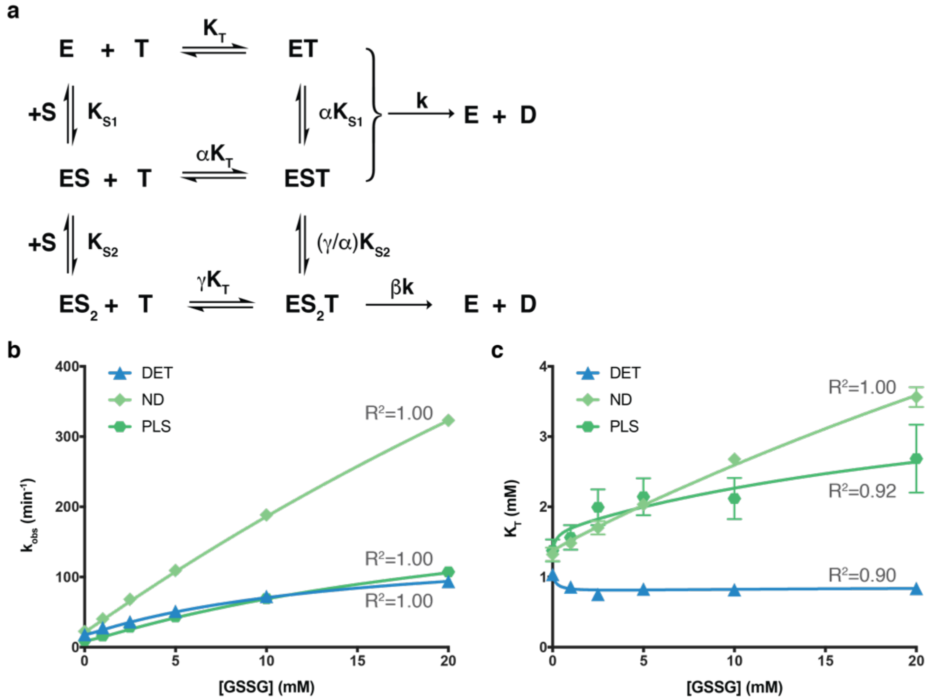

Figure 4. **Expanded non-essential activator model of *Na*Atm1 ATPase kinetics**.

(**a**) Expanded activator model for the ATPase activities of *Na*Atm1. (**b**) Michaelis-Menten constant, K_T, of MgATP binding, and (**c**) apparent rate constant, k_{obs}, of ATP hydrolysis fittings based on the expanded activator model for *Na*Atm1 in detergent, nanodiscs, and proteoliposomes, respectively. In these schemes, E = *Na*Atm1, T = MgATP, D = ADP, S = GSSG, K_T = binding constant for MgATP, K_{S1} and K_{S2} = binding constants for the first and second molecules of GSSG, respectively, k = rate constant for MgATP hydrolysis, α = interaction factor of how ATP binding influences first GSSG binding and vice versa, β = acceleration factor for ATP hydrolysis with bound GSSG, and γ = interaction factor of how ATP binding influences the binding of second GSSG binding and vice versa. Corresponding R^2 values from non-linear regressions are labeled. Error bars represent the calculated standard deviations.

3.7 Tables

Table 1. Calculated Michaelis-Menten parameters.

(**a**) Apparent rate constants for ATP hydrolysis and (**b**) apparent binding affinity of MgATP at different concentration of GSSG.

Table 1a. Observed turnover rate, k_{obs} (min $^{-1}$) in Michaelis-Menten kinetics.

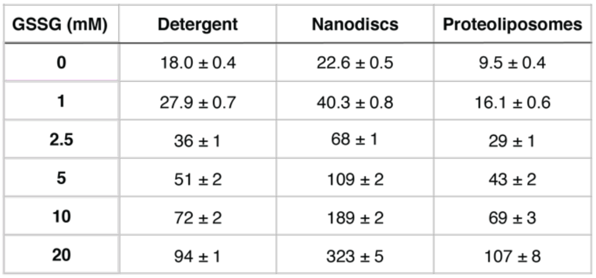

GSSG (mM)	Detergent	Nanodiscs	Proteoliposomes
0	18.0 ± 0.4	22.6 ± 0.5	9.5 ± 0.4
1	27.9 ± 0.7	40.3 ± 0.8	16.1 ± 0.6
2.5	36 ± 1	68 ± 1	29 ± 1
5	51 ± 2	109 ± 2	43 ± 2
10	72 ± 2	189 ± 2	69 ± 3
20	94 ± 1	323 ± 5	107 ± 8

Table 1b. Observed binding constant, K_T (K_M for MgATP) (mM) in Michaelis-Menten kinetics.

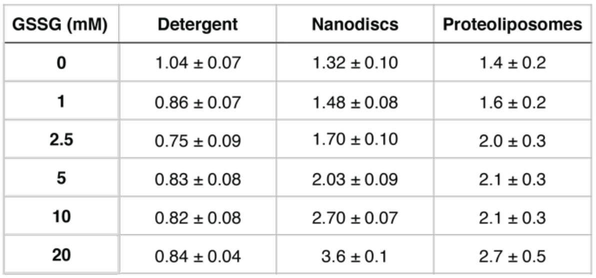

GSSG (mM)	Detergent	Nanodiscs	Proteoliposomes
0	1.04 ± 0.07	1.32 ± 0.10	1.4 ± 0.2
1	0.86 ± 0.07	1.48 ± 0.08	1.6 ± 0.2
2.5	0.75 ± 0.09	1.70 ± 0.10	2.0 ± 0.3
5	0.83 ± 0.08	2.03 ± 0.09	2.1 ± 0.3
10	0.82 ± 0.08	2.70 ± 0.07	2.1 ± 0.3
20	0.84 ± 0.04	3.6 ± 0.1	2.7 ± 0.5

Table 2. Kinetic parameters of the non-essential activator model.

Parameters calculated with the expanded activator model shown in Figure 3 and S1 for the ATPase activities of *Na*Atm1 in detergent, nanodiscs, and proteoliposomes.

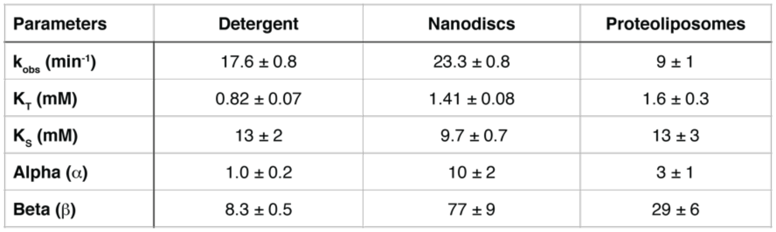

Parameters	Detergent	Nanodiscs	Proteoliposomes
k_{obs} (min^{-1})	17.6 ± 0.8	23.3 ± 0.8	9 ± 1
K_T (mM)	0.82 ± 0.07	1.41 ± 0.08	1.6 ± 0.3
K_S (mM)	13 ± 2	9.7 ± 0.7	13 ± 3
Alpha (α)	1.0 ± 0.2	10 ± 2	3 ± 1
Beta (β)	8.3 ± 0.5	77 ± 9	29 ± 6

Table 3. Kinetic parameters of the expanded non-essential activator model. Parameters calculated with the expanded activator model shown in Figure 4 and S2 for the ATPase activities of *Na*Atm1 in detergent, nanodiscs, and proteoliposomes.

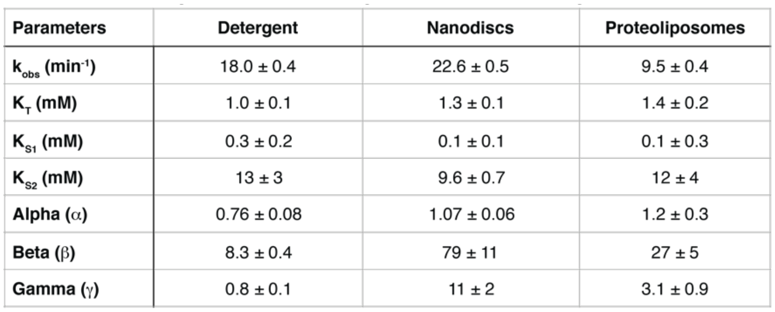

Parameters	**Detergent**	**Nanodiscs**	**Proteoliposomes**
k_{obs} (min^{-1})	18.0 ± 0.4	22.6 ± 0.5	9.5 ± 0.4
K_T (mM)	1.0 ± 0.1	1.3 ± 0.1	1.4 ± 0.2
K_{S1} (mM)	0.3 ± 0.2	0.1 ± 0.1	0.1 ± 0.3
K_{S2} (mM)	13 ± 3	9.6 ± 0.7	12 ± 4
Alpha (α)	0.76 ± 0.08	1.07 ± 0.06	1.2 ± 0.3
Beta (β)	8.3 ± 0.4	79 ± 11	27 ± 5
Gamma (γ)	0.8 ± 0.1	11 ± 2	3.1 ± 0.9

3.8 Supplemental Information

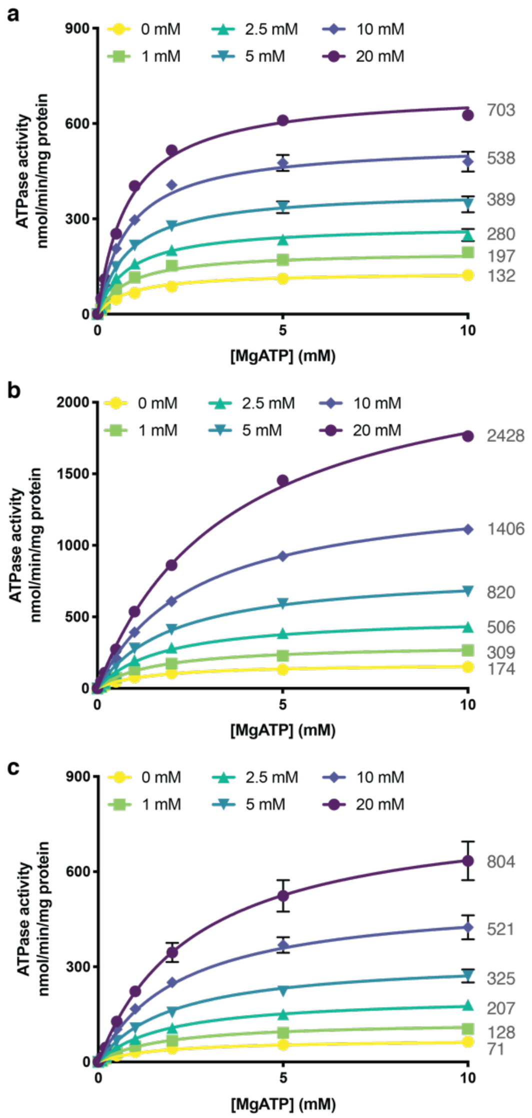

Figure S1. ATPase activities of *Na*Atm1 fitted to non-essential activator model.

ATPase activities of *Na*Atm1 in (**a**) detergent (DDM/C12E8), (**b**) nanodiscs, and (**c**) proteoliposomes (PLS) with stimulations by GSSG at various concentrations. ATPase activities of *Na*Atm1 in detergent and PLS were measured six times, and three times in ND, all with distinct samples. All of the extrapolated V_{max} values are shown next to each GSSG concentration curve. Error bars represent the standard error of the mean for the replicates.

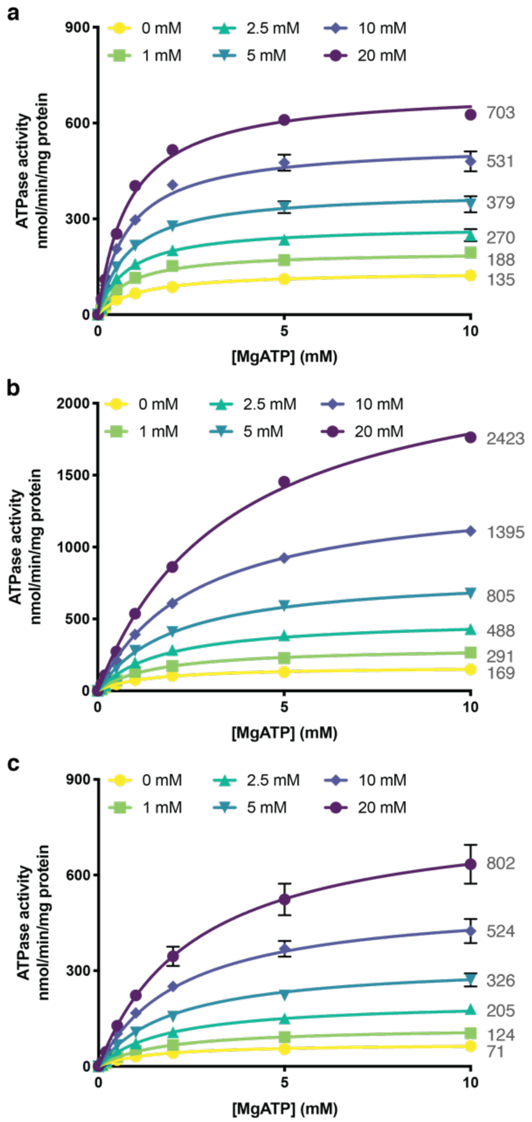

Figure S2. ATPase activities of *Na*Atm1 fitted to expanded non-essential activator model. ATPase activities of *Na*Atm1 in (**a**) detergent (DDM/C12E8), (**b**) nanodiscs, and (**c**) proteoliposomes (PLS) with stimulations by GSSG at various concentrations. ATPase activities of *Na*Atm1 in detergent and PLS were measured six times, and three times in ND, all with distinct samples. All of the extrapolated V_{max} values are shown next to each GSSG concentration curve. Error bars represent the standard error of the mean for the replicates.

Table S1. Goodness of fit comparison.

Table S1a. Goodness of fit (R^2) in detergent

[GSSG] (mM)	0	1	2.5	5	10	20
Michaelis-Menten	0.9814	0.9694	0.9408	0.9579	0.9615	0.9908
Basic non-essential	0.9734	0.9633	0.9396	0.9574	0.9612	0.9908
Expanded non-essential	0.9814	0.9654	0.9399	0.9576	0.9611	0.9908

Table S1b. Goodness of fit (R^2) in nanodiscs

[GSSG] (mM)	0	1	2.5	5	10	20
Michaelis-Menten	0.9907	0.9945	0.9949	0.9967	0.9990	0.9981
Basic non-essential	0.9899	0.9941	0.9942	0.9966	0.9989	0.9981
Expanded non-essential	0.9907	0.9943	0.9934	0.9966	0.9989	0.9981

Table S1c. Goodness of fit (R^2) in proteoliposomes

[GSSG] (mM)	0	1	2.5	5	10	20
Michaelis-Menten	0.9536	0.9565	0.9477	0.9527	0.9414	0.9137
Basic non-essential	0.9451	0.9537	0.9470	0.9512	0.9406	0.9137
Expanded non-essential	0.9536	0.9559	0.9466	0.9510	0.9408	0.9137

3.9 References

Baici, Antonio. 2015. *Kinetics of enzyme-modifier interactions : Selected topics in the theory and diagnosis of inhibition and activation mechanisms*. New York, NY: Springer Berlin Heidelberg.

Bennett, B. D., E. H. Kimball, M. Gao, R. Osterhout, S. J. Van Dien, and J. D. Rabinowitz. 2009. "Absolute metabolite concentrations and implied enzyme active site occupancy in *Escherichia coli*." *Nature Chemical Biology* 5 (8):593-9. doi: 10.1038/nchembio.186.

Chifflet, S., A. Torriglia, R. Chiesa, and S. Tolosa. 1988. "A method for the determination of inorganic phosphate in the presence of labile organic phosphate and high concentrations of protein: application to lens ATPases." *Analytical Biochemistry* 168 (1):1-4.

Geertsma, E. R., N. A. Nik Mahmood, G. K. Schuurman-Wolters, and B. Poolman. 2008. "Membrane reconstitution of ABC transporters and assays of translocator function." *Nature Protocols* 3 (2):256-66. doi: 10.1038/nprot.2007.519.

Higgins, C. F. 1992. "ABC transporters: From microorganisms to man." *Annual Review of Cell Biology* 8:67-113. doi: 10.1146/annurev.cb.08.110192.000435.

Hill, Terrell L. 1989. *Free energy transduction and ciochemical cycle kinetics*: Springer, New York, NY.

Kaback, H. R. 2015. "A chemiosmotic mechanism of symport." *Proceedings of the National Academy of Sciences of the United States of America* 112 (5):1259-64. doi: 10.1073/pnas.1419325112.

Lee, J. Y., J. G. Yang, D. Zhitnitsky, O. Lewinson, and D. C. Rees. 2014. "Structural basis for heavy metal detoxification by an Atm1-type ABC exporter." *Science* 343 (6175):1133-6. doi: 10.1126/science.1246489.

Lefevre, F., and M. Boutry. 2018. "Towards identification of the substrates of ATP-binding cassette transporters." *Plant Physiology* 178 (1):18-39. doi: 10.1104/pp.18.00325.

Locher, K. P. 2016. "Mechanistic diversity in ATP-binding cassette (ABC) transporters." *Nature Structural & Molecular Biology* 23 (6):487-93. doi: 10.1038/nsmb.3216.

Palmgren, M. G., and P. Nissen. 2011. "P-type ATPases." *Annual Review of Biophysics* 40:243-66. doi: 10.1146/annurev.biophys.093008.131331.

Rees, D. C., and J. B. Howard. 1999. "Structural bioenergetics and energy transduction mechanisms." *Journal of Molecular Biology* 293 (2):343-50. doi: 10.1006/jmbi.1999.3005.

Rees, D. C., E. Johnson, and O. Lewinson. 2009. "ABC transporters: The power to change." *Nature Reviews: Molecular Cell Biology* 10 (3):218-27. doi: 10.1038/nrm2646.

Ritchie, T. K., Y. V. Grinkova, T. H. Bayburt, I. G. Denisov, J. K. Zolnerciks, W. M. Atkins, and S. G. Sligar. 2009. "Reconstitution of membrane proteins in phospholipid bilayer nanodiscs." In *Methods in Enzymology*, 211-231.

Segel, Irwin H. 1975. *Enzyme kinetics : Behavior and analysis of rapid equilibrium and steady state enzyme systems*. New York: Wiley.

Shintre, C. A., A. C. Pike, Q. Li, J. I. Kim, A. J. Barr, S. Goubin, L. Shrestha, J. Yang, G. Berridge, J. Ross, P. J. Stansfeld, M. S. Sansom, A. M. Edwards, C. Bountra, B. D. Marsden, F. von Delft, A. N. Bullock, O. Gileadi, N. A. Burgess-Brown, and E. P. Carpenter. 2013. "Structures of ABCB10, a human ATP-binding cassette transporter in apo- and nucleotide-bound states." *Proceedings of the National Academy of Sciences of the United States of America* 110 (24):9710-5. doi: 10.1073/pnas.1217042110.

Tanford, C. 1983. "Mechanism of free energy coupling in active transport." *Annual Review of Biochemistry* 52:379-409. doi: 10.1146/annurev.bi.52.070183.002115.

Chapter 4

CRYSTAL STRUCTURE OF THE *ESCHERICHIA COLI* TRANSCRIPTION TERMINATION FACTOR RHO

This chapter is adapted from:

> Fan, C. and Rees, D.C. “Crystal structure of the *Escherichia coli* transcription termination factor Rho.” *Submitted*.

4.1 Abstract

During the crystal structure analysis of an ATP-Binding Cassette (ABC) transporter overexpressed in *Escherichia coli*, we crystallized a contaminant protein. The identity of the contaminant was revealed by mass spectrometry to be the *Escherichia coli* transcription terminator factor Rho, whose structures had been previously determined in different conformational states. Although Rho was present at only ~1% of the target protein (a bacterial homolog of the eukaryotic ABC transporter of mitochondria (Atm1) from *Novosphingobium aromaticivorans* (*Na*Atm1)), it preferentially crystallized in space group C2 as thin plates that diffracted to 3.3 Å resolution. The structure of Rho in this crystal form exhibits a hexameric open-ring staircase conformation with bound ATP; this characteristic structure was also observed on electron microscopy grids of the *Na*Atm1 preparation.

4.2 Introduction

Among the challenges in the crystallography of membrane proteins are the typically low expression levels, which necessitate a significant degree of purification to separate the protein of interest from all other cellular proteins. This can consequently lead to inadvertent purification of contaminant proteins that might otherwise be at negligible levels when the target protein expresses at high levels. In unfortunate cases, these impurities may crystallize more readily than the target protein, leading to misplaced enthusiasm until the contaminant is recognized. As examples, the multi-drug efflux pump AcrB is a well-known crystallization contaminant in membrane protein preparations due to its relatively high expression levels during recombinant protein expressions with antibiotic selection, and its nonspecific binding to NiNTA columns (Veesler et al. 2008, Das et al. 2007). Bacterioferritin has also been crystallized as a contaminant in preparations of cytochrome cbb3 oxidase (Nam et al. 2010). In addition, exogenous proteins such as DNase, lysozyme and various proteases used in the target protein purification have also been shown as crystallization contaminants (Niedzialkowska et al. 2016). Compilations facilitate the identification of crystals of contaminant proteins (Hungler et al. 2016, Simpkin et al. 2018), but crystallization of "novel" impurities is still a concern. In this work, we report the crystal structure of a previously unreported contaminating protein, the transcription termination factor Rho from *Escherichia coli*, obtained during the structural analysis of a bacterial ATP-Binding Cassette (ABC) transporter.

Rho is a hexameric RNA helicase that functions in transcription termination in *Escherichia coli*. The six subunits together form a ring-like structure, and the structure switches between an open-ring staircase conformation to a closed-ring conformation coupled to the binding and hydrolysis of ATP (Skordalakes and Berger 2003, Thomsen and Berger 2009). Here, we present the crystal structure of Rho in a broken staircase conformation at 3.30 Å resolution with ATP bound.

4.3 Results and Discussion

Crystals of Rho were unexpectedly obtained during studies of the bacterial ABC transporter *Na*Atm1 from *Novosphingobium aromaticivorans*. *Na*Atm1 was recombinantly expressed in *Escherichia coli* BL21(DE3)-gold cells with a C-terminal 6xHis-tag following a previously established protocol (Lee et al. 2014). After solubilization of the *Escherichia coli* cells in n-dodecyl-β-D-maltopyranoside (DDM) and octaethylene glycol monododecyl ether (C12E8), the protein purification proceeded by NiNTA affinity purification followed by size exclusion chromatography (Figure 1a). SDS-PAGE gels indicated a high degree of purity, although in subsequent analysis of overloaded gels, a small amount of another protein was present at molecular weight of ~40 kDa (Figure 1b).

Crystals obtained during a crystallization optimization were in space group C2 with cell dimensions: a = 161.8 Å, b = 101.9 Å, c = 184.0 Å, and β = 107.8˚. The asymmetric unit volume was of sufficient size to accommodate a *Na*Atm1 dimer (molecular weight 133 kDa). Analysis of the self-rotation function calculated from diffraction data revealed a non-crystallographic symmetry (NCS) 6-fold axis offset ~3-4˚ from the crystallographic a-axis. Interaction of the perpendicular 2-fold and 6-fold axes generates a set of non-crystallographic two-fold rotation operations separated by 60˚ in the plane perpendicular to the NCS 6-fold axis (Figure 1c). Given the unit cell dimensions, this apparent NCS was incompatible with dimeric *Na*Atm1, which raised the possibility that a contaminant was crystallized. With an estimated molecular weight of ~40 kDa based on the observation of a faint impurity band in SDS-PAGE and a Matthews coefficient analysis, we then performed molecular replacements with the known crystallization contaminants (Hungler et al. 2016, Simpkin et al. 2018), which all failed to yield a molecular replacement solution.

Identification of Rho (molecular weight 47 kDa) was established by a mass spectrometry analysis of the peptides prepared by trypsin digestion of protein in the SDS-PAGE bands. With this information, we were able to obtain a molecular replacement solution using Rho in the AMPPNP bound state (PDB ID: 1PVO; (Skordalakes and Berger 2003)) as input model. The molecular replacement results established that in these crystals, Rho adopts a six-membered broken staircase conformation. The structure was refined to R_{work} and R_{free} of 25.2% and 29.6%, respectively (Table 4). The electron density map also revealed ATP bound at all six subunits (Figure 2a). The individual Rho subunits are structurally similar overall, except for the terminal subunit at the “break” in the staircase, where the first 50 residues at the N-terminus exhibited a shift of 2 to 8 Å relative to the other monomers (Figure 2b). The overall RMSD between the present structure and the molecular replacement input model (PDB ID: 1PVO) is 2.5 Å, with the present structure exhibiting a more closed ring in comparison to the original broken staircase structure (Figure 3ab).

How did Rho end up in our crystallization conditions? Our hypothesis is that during protein overexpression, the *Escherichia coli* transcription and translation machineries are highly expressed for the production of mRNAs and recombinant proteins, respectively. Rho, as the termination factor, would plausibly be overexpressed as part of the transcription termination process. The fact that Rho eluted from the NiNTA column along with His-tagged *Na*Atm1 suggests that there is nonspecific binding to the Ni^{2+} resin by the histidine residues distributed throughout the whole protein (Figure 3c). The open ring conformation that Rho adopts in solution (Thomsen et al. 2016) with a molecular weight of 282 kDa for the hexamer apparently has a comparable hydrodynamic radius to *Na*Atm1with a dimer molecular weight of 133 kDa in addition to the detergent micelle. Given the low abundance, the presence of Rho in the SEC fractions was only detected in hindsight.

We have also observed Rho in single particle cryoEM studies of *Na*Atm1 reconstituted in membrane scaffolding protein (MSP) nanodiscs. The *Na*Atm1 nanodiscs sample was prepared by incubating detergent purified *Na*Atm1 with MSPs and lipids, and further purified by size exclusion chromatography. Similar to the purification in detergent, the peak fractions were collected for single particle cryo-EM sample preparation (Figure 4a). The 2D classification reported one class of Rho in the broken hexameric state (Figure 4b), again suggesting that Rho has a similar hydrodynamic radius and plausibly similar molecular weight to our reconstituted *Na*Atm1 in nanodiscs.

In a structural analysis of a prokaryotic chloride channel, a single peptide of Rho was identified in a mass spectrometry analysis of the gel band (Abeyrathne and Grigorieff 2017), representing for the first time, to our knowledge, that Rho was identified as a possible contaminant during membrane protein expression. As demonstrated in this report, Rho can crystallize even in the presence of a large excess of other proteins, and thus it should be added to the list of the known crystallography contaminant proteins.

4.4 Materials and Methods

Protein expression and purification

Rho co-purified with the bacterial ABC exporter *Na*Atm1, a homolog of the ABC transporter of mitochondria (Atm1) from *Novosphingobium aromaticivorans*, using an *Escherichia coli* expression system and a modified version of previously published protocols (Lee et al. 2014). Briefly, frozen *Escherichia coli* cell pellets containing overexpressed *Na*Atm1 (and Rho) were lysed in lysis buffer containing 100 mM NaCl, 20 mM Tris, pH 7.5, 40 mM imidazole, pH 7.5, 10 mM $MgCl_2$, 0.5% (w/v) n-dodecyl-β-D-maltopyranoside (DDM) (Anatrace), 0.5% (w/v) octaethylene glycol monododecyl ether (C12E8) (Anatrace) with the addition of lysozyme, DNase, and protease inhibitor. After stirring for 3 hours at 4 ˚C, the lysate was subjected to ultracentrifugation at ~113,000x g for 45 minutes at 4 ˚C. The supernatant was collected and loaded onto a pre-washed NiNTA column in buffer containing 100 mM NaCl, 20 mM Tris, pH 7.5, 50 mM imidazole, pH 7.5, 0.05% DDM and 0.05% C12E8 and eluted with the same buffer containing 350 mM imidazole, pH 7.5. The protein was further purified by size exclusion chromatography (SEC) using a HiLoad 16/60 Superdex 200 column (GE Healthcare) with SEC buffer containing 100 mM NaCl, 20 mM Tris, pH 7.5, 0.05% DDM and 0.05% C12E8. Peak fractions were collected and concentrated to ~20 mg/mL using a 100 kDa cutoff Amicon Ultra 15 concentrator (Millipore).

Crystallization

Rho crystallized during the crystallization trials of *Na*Atm1 under the optimized conditions of MemGold (Molecular Dimensions) condition #68 at 20 ˚C. The final crystallization condition contains 100 mM NaCl, 100 mM Tris, pH 8.3, and 28% polyethylene glycol 2,000 monomethyl ether (PEG 2,000 MME), 0.2 M non-detergent sulfo-betaine (NDSB)-221 and 20 mM ATP, pH 7.5. The crystallization sample was prepared with 1 mM ATP, pH 7.5 and 5 mM EDTA, pH 7.5 in the presence and absence of 5 mM oxidized glutathione (GSSG), pH 7.5, a transport ligand for *Na*Atm1. Thin plate crystals appeared in about 2 weeks. Crystals were harvested in cryoprotectant solutions containing 100 mM NaCl, 100 mM Tris, pH 8.3, 28% PEG 2,000 MME with PEG 400 at 10%, 15%, and 20% before flash-freezing in liquid nitrogen.

Data collection and processing

Crystals were screened at the Advanced Photon Source GM/CA beamline 23ID-B and the Stanford Synchrotron Radiation Laboratory beamline 12-2. The final dataset was collected at the GM/CA beamline 23-IDB with an Eiger 16M detector (Dectris) with JBluIce-EPICS (Stepanov et al. 2011), processed and integrated with XDS (Kabsch 2010), and scaled with Aimless (Evans and Murshudov 2013). The crystals of Rho diffracted to about 3.30 Å resolution in space group C2 with unit cell constants: a = 161.8 Å, b =101.9 Å, c =184.0 Å, and β =107.8°.

Structure solution and refinement

The self-rotation function was calculated with the CCP4 program molrep (Winn et al. 2011). Molecular replacement was performed with Phaser in Phenix (Adams et al. 2010) using a monomeric subunit of a previous structure of Rho with PDB ID: 1PVO. Initial jelly-body refinements were carried out with Refmac5 in CCP4 (Winn et al. 2011). Subsequent iterative refinement and model building runs were separately conducted with phenix.refine (Adams et al. 2010) and Coot (Emsley et al. 2010).

Electron microscopy sample preparation

The expression plasmid for the membrane scaffolding protein MSP1D1 was purchased from Addgene (plasmid #20061). The expression and purification of MSP1D1 were carried out using published protocols with minor modifications (Ritchie et al. 2009). Reconstitution of *Na*Atm1 (and the Rho contaminant) with MSP1D1 was carried out with 1-palmitoyl-2-oleoyl-glycero-3-phosphocholine (POPC) at a molar ratio of *Na*Atm1: MSP1D1: POPC = 1:2:130. This reconstituted sample was incubated overnight at 4˚C. BioBeads were added after two hours of incubation at 200 mg/ml for detergent removal. The sample was then subjected to size exclusion chromatography with Superdex 200 Increase 10/300 (GE Healthcare). The peak fractions were then pooled and concentrated to ~8 mg/ml.

EM grids were prepared with a protein concentration of 4 mg/ml in the presence of 5 mM GSSG and 5 mM AMPPNP. 3 µl of protein sample was applied to freshly glow discharged QuantiFoil Cu R2/2 300 mesh grids and blotted for 4 seconds with blot force of 0 and 100% humidity at room temperature using Vitrobot MarkIV (FEI). The data was collected on a 200 keV Talos Arctica with a Falcon III detector at a magnification of 92,000x and a total dosage of 81 $e^{-}/Å^{2}$ at the Caltech CryoEM Facility.

The data processing was performed with cryoSPARC 2 (Punjani et al. 2017), following motion corrected with full-frame motion, and estimation of the contrast transfer function (CTF) with CTFFIND (Rohou and Grigorieff 2015). Particles were picked using a reconstruction of NaAtm1 as template and extracted in cryoSPARC 2. The initial 2D classification revealed a single class of Rho with ~2,500 particles. The particles were then 2D-classed again into five classes with four good classes with a total of ~2,200 particles shown in Figure 4b.

4.5 Acknowledgments

We thank Jens T. Kaiser and the beamline staff at the Advanced Photon Source GM/CA 23ID-B and the Stanford Synchrotron Radiation Lightsource (SSRL) beamline 12-2 for their support during crystallographic data collection; Mona Shahgholi at the Caltech CCE Multiuser Mass Spectrometry Laboratory for Rho identification; Andrey Malyutin at the Caltech CryoEM facility for their support during electron microscopy data collection. We gratefully acknowledge the Gordon and Betty Moore Foundation and the Beckman Institute at Caltech for their generous support of the Molecular Observatory at Caltech. Cryo-electron microscopy was performed in the Beckman Institute Resource Center for Transmission Electron Microscopy at Caltech. GM/CA@APS has been funded in whole or in part with Federal funds from the National Cancer Institute (ACB-12002) and the National Institute of General Medical Sciences (AGM-12006). This research used resources of the Advanced Photon Source, a U.S. Department of Energy (DOE) Office of Science User Facility operated for the DOE Office of Science by Argonne National Laboratory under Contract No. DE-AC02-06CH11357. The Eiger 16M detector was funded by an NIH–Office of Research Infrastructure Programs, High-End Instrumentation Grant (1S10OD012289-01A1). Use of the Stanford Synchrotron Radiation Lightsource, SLAC National Accelerator Laboratory, is supported by the U.S. Department of Energy, Office of Science, Office of Basic Energy Sciences under Contract No. DE-AC02-76SF00515. The SSRL Structural Molecular Biology Program is supported by the DOE Office of Biological and Environmental Research, and by the National Institutes of Health, National Institute of General Medical Sciences (including P41GM103393).

4.6 Figures

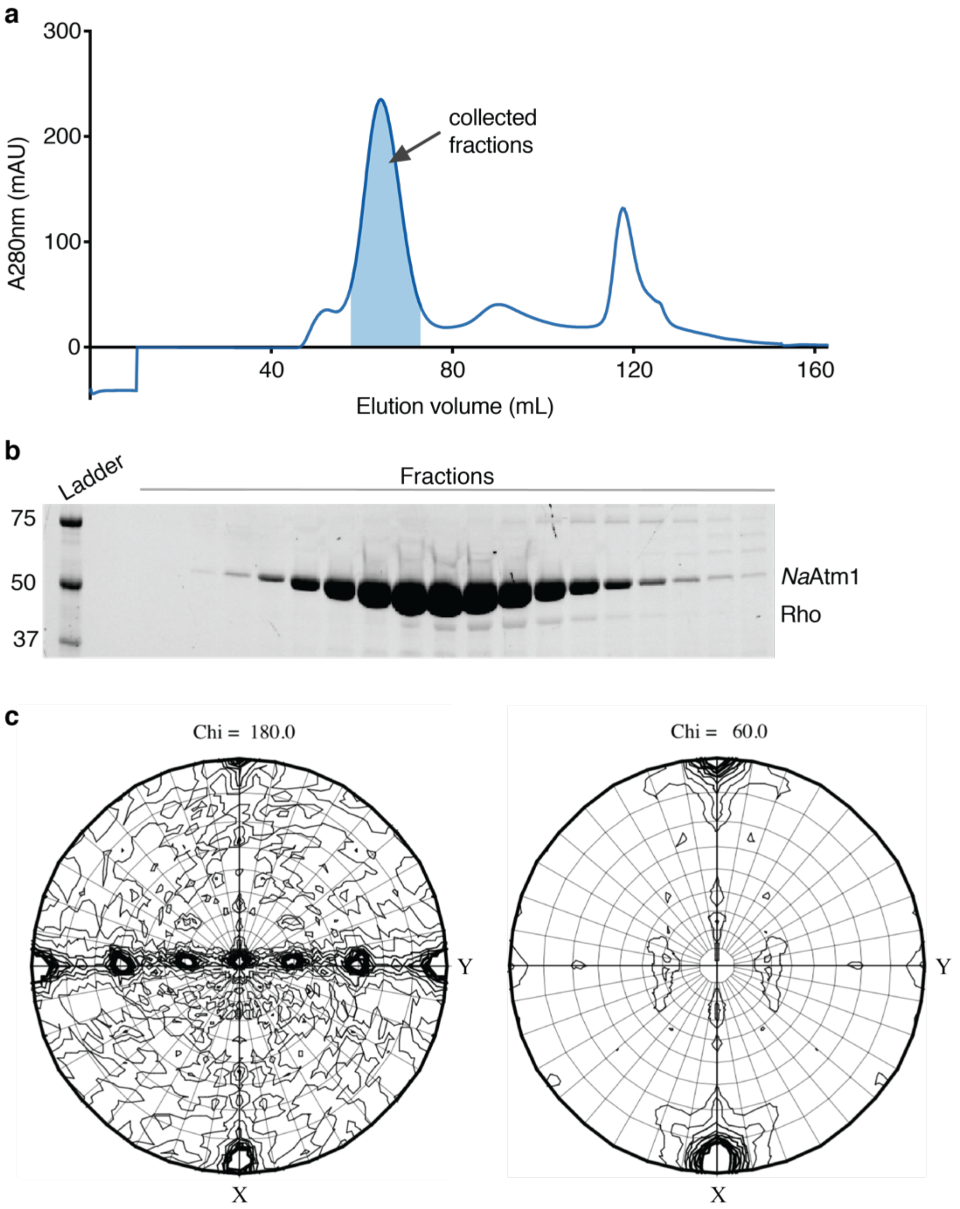

Figure 1. Purification and self-rotation function analysis of Rho.

(**a**) Size exclusion chromatograph of *Na*Atm1 purification using a HiLoad Superdex 200 16/60 column. (**b**) SDS-PAGE of the peak fractions of SEC purification from (**a**). (**c**) The Chi = 180° and 60° sections of the self-rotation function calculated using molrep in CCP4 with an integration radius of 51 Å using diffraction data between 3.3 to 40 Å resolution.

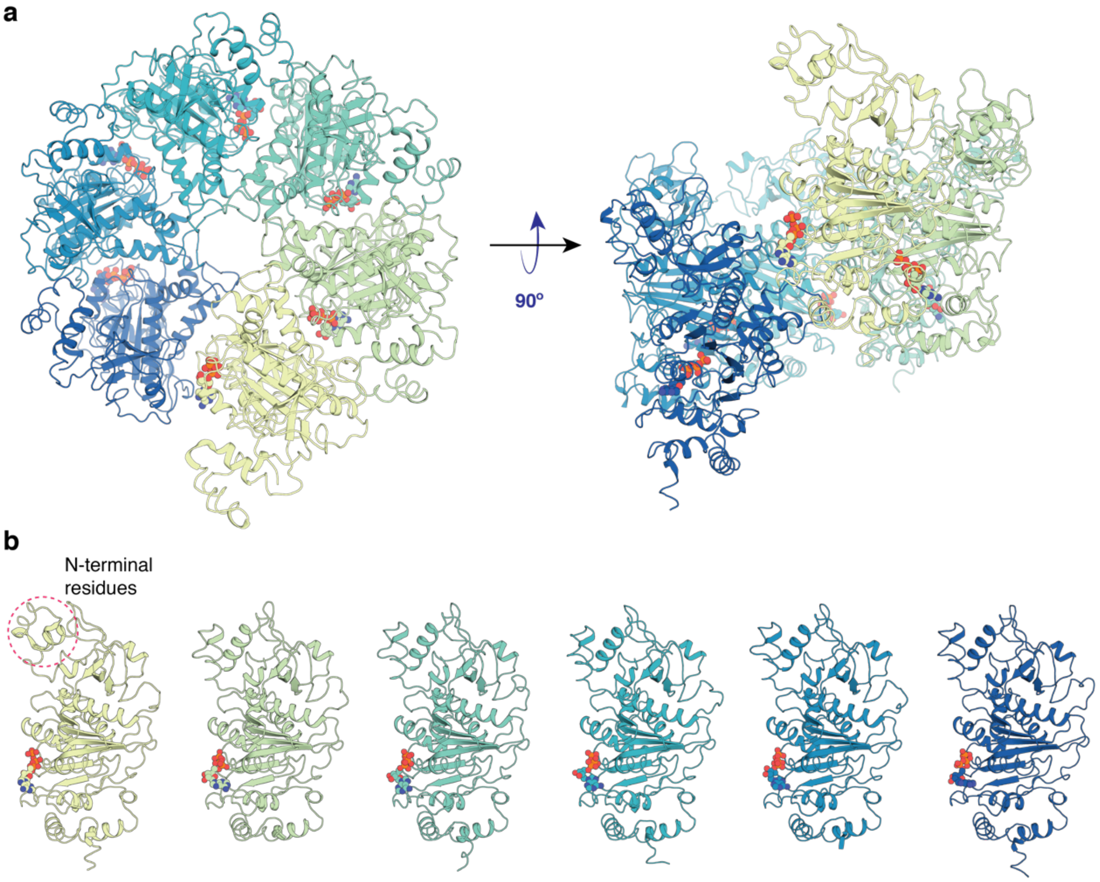

Figure 2. Crystal structure of Rho.

(**a**) Overall view of Rho in broken staircase conformation with ATP bound. (**b**) Single subunit of Rho with ATP bound. The six subunits are shown separately, and ATP is shown in red spheres. The dashed circle identifies the N-terminal ~50 residues of the Rho subunit positioned at the break in the hexameric staircase arrangement; this region has rearranged in this subunit relative to the conformation exhibited in the other five subunits.

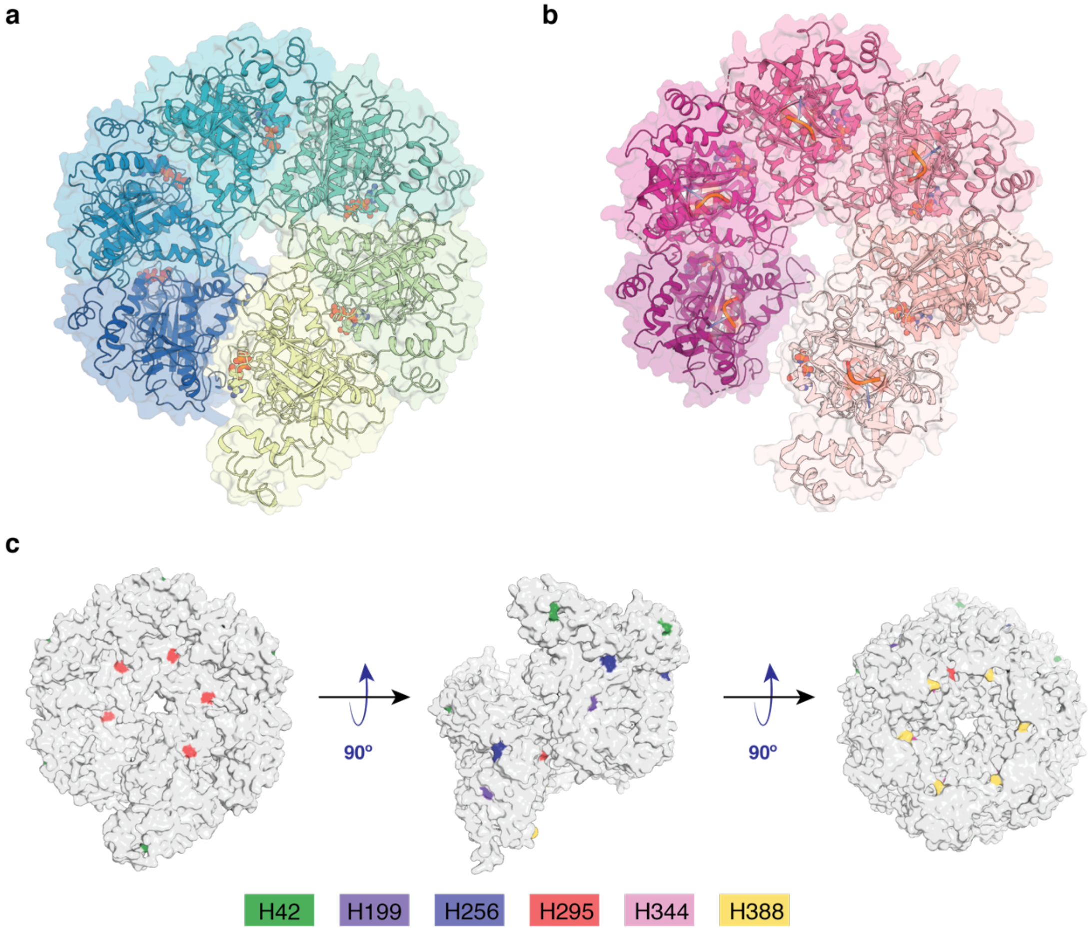

Figure 3. Overall architecture of Rho.

Overall structural representations of (**a**) ATP bound Rho (this study) and (**b**) AMPPNP bound structure of Rho (PDB ID: 1PVO; (Skordalakes and Berger 2003)). (**c**) Distribution of surface histidine residues (colored by residue number) in the ATP bound structure of Rho. The spacings between the surface exposed histidines are several nanometers, comparable to the loading density of His-tagged proteins bound to NiNTA beads (Hayworth and Hermanson 2014), which presumably allows multiple binding sites to NiNTA and contributes to the observed affinity of Rho for NiNTA resin.

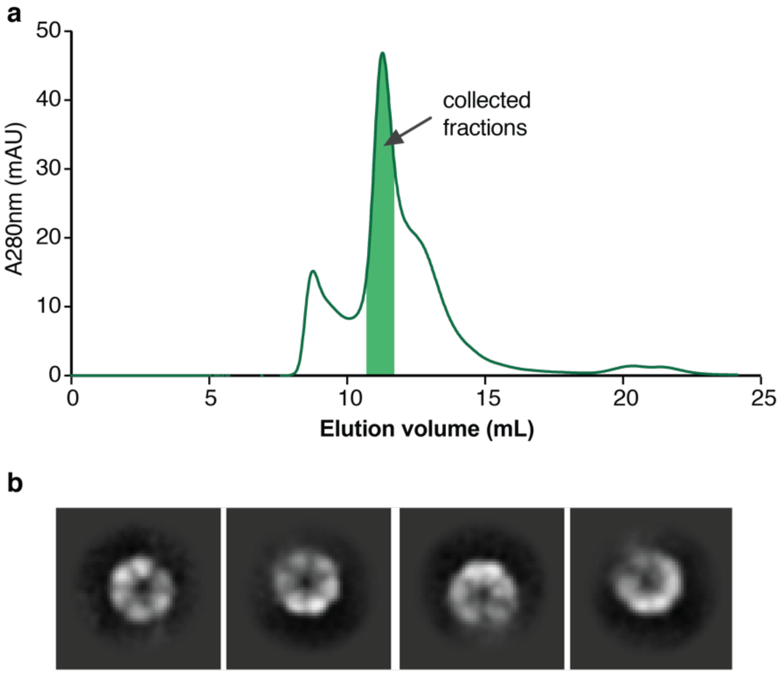

Figure 4. Single particle cryo-EM analysis of *Na*Atm1 samples containing Rho.

(**a**) Size exclusion chromatograph of the reconstituted *Na*Atm1 in MSP1D1 nanodiscs using Superdex 200 Increase 10/300. (**b**) 2D classes of Rho illustrating the hexameric arrangement with a diameter of ~100 Å.

4.7 Tables

Table 1. Macromolecule production information.

Source organism	*Escherichia coli*
DNA source	*Escherichia coli* genomic DNA
Expression host	*Escherichia coli* BL21-gold (DE3)

Complete amino acid sequence of the construct produced	`MNLTELKNTPVSELITLGENMGLENLARMRKQDIIFAILKQHAKSGEDIFGDGV`
	`LEILQDGFGFLRSADSSYLAGPDDIYVSPSQIRRFNLRTGDTISGKIRPPKEGE`
	`RYFALLKVNEVNFDKPENARNKILFENLTPLHANSRLRMERGNGSTEDLTARVL`
	`DLASPIGRGQRGLIVAPPKAGKTMLLQNIAQSIAYNHPDCVLMVLLIDERPEEV`
	`TEMQRLVKGEVVASTFDEPASRHVQVAEMVIEKAKRLVEHKKDVIILLDSITRL`
	`ARAYNTVVPASGKVLTGGVDANALHRPKRFFGAARNVEEGGSLTIIATALIDTG`
	`SKMDEVIYEEFKGTGNMELHLSRKIAEKRVFPAIDYNRSGTRKEELLTTQEELQ`
	`KMWILRKIIHPMGEIDAMEFLINKLAMTKTNDDFFEMMKRS`

The protein was expressed in *Escherichia coli* without the use of an expression plasmid.

Table 2. Crystallization.

Method	Vapor diffusion
Plate type	Hampton VDX
Temperature (K)	293 K
Protein concentration	< 1 mg/ml
Buffer composition of protein solution	100 mM NaCl, 20 mM Tris, pH 7.5
Composition of reservoir solution	100 mM NaCl, 100 mM Tris, pH 8.3, 20 mM ATP, 200 mM NDSB 221, and 28% PEG 2,000 MME
Volume and ratio of drop	1 μl protein solution + 1 μl reservoir solution
Volume of reservoir	500 μL

Table 3. Data collection and processing.

Values for the outer shell are given in parentheses.

Diffraction source	APS GM/CA 23ID-B
Wavelength (Å)	0.9793
Temperature (K)	100
Detector	DECTRIS EIGER 16M
Crystal-detector distance (mm)	400
Rotation range per image (°)	0.2
Total rotation range (°)	360
Exposure time per image (s)	0.2
Space group	C2
a, b, c (Å)	161.74, 101.90, 184.02
α, β, γ (°)	90, 107.8, 90
Mosaicity (°)	0.11
Resolution range (Å)	38.51 - 3.30 (3.42 - 3.30)
Total no. of reflections	304,610 (29,798)
No. of unique reflections	43,031 (4,465)
Completeness (%)	99.9 (99.7)
Redundancy	7.0 (6.7)
$\langle I/\sigma(I) \rangle$	6.6 (1.5) [#]
R_{pim}	0.103 (0.729)
Overall B factor from Wilson plot (Å^2)	79.1 [‡]

[#] Overall resolution cut-off determined by data completeness and $CC_{1/2} > 0.50$ in high resolution shell. $I/\sigma(I)$ falls below 2.0 past 3.46 Å resolution.

[‡] There were ice rings in the data.

Table 4. Structure solution and refinement

Values for the outer shell are given in parentheses.

Resolution range (Å)	38.51 - 3.30 (3.42 - 3.30)
Completeness (%)	99.6 (97.3)
σ cutoff	8.9 (1.3)
No. of reflections, working set	42,901 (4,145)
No. of reflections, test set	2,095 (217)
Final R_{cryst}	0.252 (0.320)
Final R_{free}	0.296 (0.364)
No. of non-H atoms	19,776
Protein	19,590
Ligand	186
Total	19,776
R.m.s. deviations	
Bonds (Å)	0.002
Angles (°)	0.58
Average B factors (Å^2)	
Protein	101.4
Ligand	143.2
Ramachandran plot	
Most favored (%)	95.5
Allowed (%)	4.2

4.8 References

Abeyrathne, P. D., and N. Grigorieff. 2017. “Expression, purification, and contaminant detection for structural studies of *Ralstonia metallidurance* ClC protein rm1.” *PLoS One* 12 (7):e0180163. doi: 10.1371/journal.pone.0180163.

Adams, P. D., P. V. Afonine, G. Bunkoczi, V. B. Chen, I. W. Davis, N. Echols, J. J. Headd, L. W. Hung, G. J. Kapral, R. W. Grosse-Kunstleve, A. J. McCoy, N. W. Moriarty, R. Oeffner, R. J. Read, D. C. Richardson, J. S. Richardson, T. C. Terwilliger, and P. H. Zwart. 2010. “PHENIX: A comprehensive Python-based system for macromolecular structure solution.” *Acta Crystallographica D Biological Crystallography* 66 (Pt 2):213-21. doi: 10.1107/S0907444909052925.

Das, D., Q. S. Xu, J. Y. Lee, I. Ankoudinova, C. Huang, Y. Lou, A. DeGiovanni, R. Kim, and S. H. Kim. 2007. “Crystal structure of the multidrug efflux transporter AcrB at 3.1Å resolution reveals the N-terminal region with conserved amino acids.” *Journal of Structural Biology* 158 (3):494-502. doi: 10.1016/j.jsb.2006.12.004.

Emsley, P., B. Lohkamp, W. G. Scott, and K. Cowtan. 2010. “Features and development of Coot.” *Acta Crystallographica D Biological Crystallography* 66 (Pt 4):486-501. doi: 10.1107/S0907444910007493.

Evans, P. R., and G. N. Murshudov. 2013. “How good are my data and what is the resolution?” *Acta Crystallographica D Biological Crystallography* 69 (Pt 7):1204-14. doi: 10.1107/S0907444913000061.

Hayworth, Douglas A. , and Greg T. Hermanson. 2014. “Calculate the number of immobilized proteins per bead of agarose affinity supports.” accessed April 5. https://www.thermofisher.com/us/en/home/life-science/protein-biology/protein-biology-learning-center/protein-biology-resource-library/protein-biology-application-notes/calculate-number-immobilized-proteins-per-bead-agarose-affinity-supports.html.

Hungler, A., A. Momin, K. Diederichs, and S. T. Arold. 2016. “ContaMiner and ContaBase: A webserver and database for early identification of unwantedly crystallized protein contaminants.” *Journal of Applied Crystallography* 49 (Pt 6):2252-2258. doi: 10.1107/S1600576716014965.

Kabsch, W. 2010. "Xds." *Acta Crystallographica D Biological Crystallography* 66 (Pt 2):125-32. doi: 10.1107/S0907444909047337.

Lee, J. Y., J. G. Yang, D. Zhitnitsky, O. Lewinson, and D. C. Rees. 2014. "Structural basis for heavy metal detoxification by an Atm1-type ABC exporter." *Science* 343 (6175):1133-6. doi: 10.1126/science.1246489.

Nam, K. H., Y. Xu, S. Piao, A. Priyadarshi, E. H. Lee, H. Y. Kim, Y. H. Jeon, N. C. Ha, and K. Y. Hwang. 2010. "Crystal structure of bacterioferritin from *Rhodobacter sphaeroides*." *Biochemical and Biophysical Research Communications* 391 (1):990-4. doi: 10.1016/j.bbrc.2009.12.003.

Niedzialkowska, E., O. Gasiorowska, K. B. Handing, K. A. Majorek, P. J. Porebski, I. G. Shabalin, E. Zasadzinska, M. Cymborowski, and W. Minor. 2016. "Protein purification and crystallization artifacts: The tale usually not told." *Protein Science* 25 (3):720-33. doi: 10.1002/pro.2861.

Punjani, A., J. L. Rubinstein, D. J. Fleet, and M. A. Brubaker. 2017. "cryoSPARC: Algorithms for rapid unsupervised cryo-EM structure determination." *Nature Methods* 14 (3):290-296. doi: 10.1038/nmeth.4169.

Ritchie, T. K., Y. V. Grinkova, T. H. Bayburt, I. G. Denisov, J. K. Zolnerciks, W. M. Atkins, and S. G. Sligar. 2009. "Reconstitution of membrane proteins in phospholipid bilayer nanodiscs." In *Methods in Enzymology*, 211-231.

Rohou, A., and N. Grigorieff. 2015. "CTFFIND4: Fast and accurate defocus estimation from electron micrographs." *Journal of Structural Biology* 192 (2):216-21. doi: 10.1016/j.jsb.2015.08.008.

Simpkin, A. J., F. Simkovic, J. M. H. Thomas, M. Savko, A. Lebedev, V. Uski, C. Ballard, M. Wojdyr, R. Wu, R. Sanishvili, Y. Xu, M. N. Lisa, A. Buschiazzo, W. Shepard, D. J. Rigden, and R. M. Keegan. 2018. "SIMBAD: A sequence-independent molecular-replacement pipeline." *Acta Crystallographica D Structural Biology* 74 (Pt 7):595-605. doi: 10.1107/S2059798318005752.

Skordalakes, Emmanuel, and James M. Berger. 2003. "Structure of the Rho transcription terminator." *Cell* 114 (1):135-146. doi: 10.1016/s0092-8674(03)00512-9.

Stepanov, S., O. Makarov, M. Hilgart, S. B. Pothineni, A. Urakhchin, S. Devarapalli, D. Yoder, M. Becker, C. Ogata, R. Sanishvili, N. Venugopalan, J. L. Smith, and R. F. Fischetti. 2011. “JBluIce-EPICS control system for macromolecular crystallography.” *Acta Crystallographica D Biological Crystallography* 67 (Pt 3):176-88. doi: 10.1107/S0907444910053916.

Thomsen, N. D., and J. M. Berger. 2009. “Running in reverse: The structural basis for translocation polarity in hexameric helicases.” *Cell* 139 (3):523-34. doi: 10.1016/j.cell.2009.08.043.

Thomsen, N. D., M. R. Lawson, L. B. Witkowsky, S. Qu, and J. M. Berger. 2016. “Molecular mechanisms of substrate-controlled ring dynamics and substepping in a nucleic acid-dependent hexameric motor.” *Proceedings of the National Academy of Sciences of the United States of America* 113 (48):E7691-E7700. doi: 10.1073/pnas.1616745113.

Veesler, D., S. Blangy, C. Cambillau, and G. Sciara. 2008. “There is a baby in the bath water: AcrB contamination is a major problem in membrane-protein crystallization.” *Acta Crystallographica F Structural Biology and Crystallization Communications* 64 (Pt 10):880-5. doi: 10.1107/S1744309108028248.

Winn, M. D., C. C. Ballard, K. D. Cowtan, E. J. Dodson, P. Emsley, P. R. Evans, R. M. Keegan, E. B. Krissinel, A. G. Leslie, A. McCoy, S. J. McNicholas, G. N. Murshudov, N. S. Pannu, E. A. Potterton, H. R. Powell, R. J. Read, A. Vagin, and K. S. Wilson. 2011. “Overview of the CCP4 suite and current developments.” *Acta Crystallographica D Biological Crystallography* 67 (Pt 4):235-42. doi: 10.1107/S0907444910045749.

Chapter 5

STRUCTURAL ANALYSIS OF PERIPLASMIC BINDING PROTEIN-DERIVED BIOSENSORS

This chapter contributed to work published in:

> Fan, C.*, Nichols, A.*, Muthusamy, A., Bera, K., Shivange, A.V., Luebbert, L., Gao, F., Beatty Z., Unger, E., Marvin, J.S., Tian, L., Looger, L.L, Rees, D.C., and Lester, H.A. “A family of iDrugSnFRs, nearly modular fusion of evolved periplasmic binding proteins and circularly permutated GFP for subcellular and supercellular dynamical measurements of drugs.” *In preparation*.
>
> Borden, P.M., Zhang, P., Shivange, A.V., Marvin, J.S., Cichon, J., Dan, C., Podgorski, K., Figueiredo, A., Novak, O., Tanimoto, M., Shigetomi, E., Lobas, M.A., Kim, H., Zhu, P.K., Zhang, Y., Zheng, W.S., Fan, C., Wang, G., Xiang, B., Gan, L., Zhang, G., Guo, K., Lin, L., Cai, Y., Yee, A.G, Aggarwal, A., Ford, C.P., Rees, D.C., Dietrich, D, Khakh, B.S., Dittman, J.S., Gan, W., Koyama, M., Jayaraman, V., Cheer, J.F., Lester, H.A., Zhu, J.J. and Looger, L.L. “A fast genetically encoded fluorescent sensor for faithful *in vivo* acetylcholine detection in mice, fish, worms, and flies.” *In review*.

5.1 Introduction

There has been significant interest in probing the intracellular concentrations of neurotransmitters over the past decade. One of the first genetically engineered biosensors for this purpose was a Ca^{2+} sensitive probe based on calmodulin and green fluorescent protein (GFP), named G-CaMP. G-CaMP could sense Ca^{2+} concentration in the nanomolar range with large fluorescence changes (Yamaguchi et al. 2001). G-CaMP was designed by genetically engineering a fusion protein of a circular permutated enhanced green fluorescent protein (cpEGFP), a Ca^{2+} binding calmodulin (CaM), and a M13 peptide from myosin light chain kinase (Nakai, Ohkura, and Imoto 2001). The same general strategy was later adopted in designing biosensors for maltose (Marvin et al. 2011), neurotransmitters (Marvin et al. 2013, Marvin et al. 2018), and smoking sensation drugs (Shivange et al. 2019). The basic design of these subsequent biosensors employed a periplasmic binding protein (PBP) from a bacterial ATP-Binding Cassette (ABC) transporter system and a circular-permutated green fluorescent protein (cpGFP). The cpGFP moiety is inserted between the N and C-terminal lobes of the PBP via two separate linkers. These linkers are thought to be important in sensing the apo and liganded conformational states of the PBP. Upon ligand binding to apo PBP, conformational changes of the linkers promote the last folding step of the cpGFP, resulting in a fluorescence increase.

The Lester group has pioneered the development of a family of genetically encoded nicotine sensing fluorescent reporters, known as the iNicSnFRs, and a family of the genetically encoded acetylcholine sensing fluorescent reporters, known as the iAChSnFRs. These two families were designed from the same bacterial PBP, through modification and evolution of the protein sequence to optimize ligand binding affinity, ligand binding specificity, fluorescent effective range, and pH sensitivity. Following the initial screening of acetylcholine and choline binding proteins from different organisms, the PBP used in designing the iNicSnFRs and iAChSnFRs is the betaine/choline-binding protein OpuBC from *Thermoanaerobacter sp.* X513 (Shivange et al. 2019, Borden et al. 2020). These OpuBC based biosensors are designed like the early PBP based biosensors with the cpGFP inserted in the middle of the PBP via two linkers (Figure 1a). In addition, epitope tags were also included, with an HA-tag on the N-terminus and a MYC-tag on the C-terminus of the biosensor. For purification purposes, a 6xHis tag is placed on the N-terminus of the fusion protein before the HA-tag (Figure 1a). Currently, iNicSnFRs have apparent binding affinities of ~10 μM for nicotine (Shivange et al. 2019), and iAChSnFRs has apparent binding affinity of ~1 μM for acetylcholine (Borden et al. 2020). Missing from the characterization of these biosensors has been direct structural characterization of the liganded states, which is necessary for understanding the specificity of ligand binding. Here, we have determined high X-ray structures of iNicSnFRs and iAChSnFRs in both the apo and liganded states.

5.2 Results

Crystallization construct design

Initial crystallization studies were carried out with full length iNicSnFR3 with about 20 different commercial crystallization screens in the presence of 10 mM nicotine, pH 7.5. Unfortunately, none of the crystal hits yielded any structures with nicotine bound, albeit they all diffracted to the 2 to 3 Å resolution range without any optimization. To improve the crystallizability of the biosensors in the liganded states, we removed the potentially floppy HA and MYC epitope tags for crystallization purposes; these constructs are referred to as "dt" constructs where dt stands for Δ (delta) tags (Figure 1b). Furthermore, to help crystallization and determination of high-resolution structures, we removed the cpGFP and the linkers of iNicSnFR3dt and other dt constructs, leaving only the His-tagged PBP of the biosensors (Figure 1c). These cpGFP-less constructs are referred as the "dtbp" constructs where dtbp stands for delta binding protein. This strategy is applied for all the biosensor structures discussed in this Chapter, including the iNicSnFR3, iNicSnFR4, and iAChSnFR.

Crystal structures of the nicotine and varenicline bound iNicSnFR3dt

Crystals of iNicSnFR3dt in the presence of 10 mM nicotine diffracted to 2.95 Å resolution in space group $P6_1$ with unit cell constants: a = b = 192.3 Å, c = 49.7 Å, $\alpha = \beta = 90°$, and $\gamma = 120°$. Overall, the PBP domain of iNicSnFR3dt adopts a closed conformation (Figure 2a). In the binding pocket between the top and bottom lobes of the PBP (Figure 2a), we have observed an "avocado" shaped electron density in the nicotine binding site. This density blob is enclosed by a number of different aromatic residues, including phenylalanine, tyrosine and tryptophan (Figure 2b). Further map calculation using polder map in Phenix (Adams et al. 2010) suggested the presence of nicotine in the binding pocket between the two lobes. Based on the molecular geometry of nicotine, the distorted pyrrolidine should be placed on the electron-heavier side of the electron density blob and the flat pyridine ring should be placed on the thinner side of the electron density blob. Yet, nicotine could adopt both *cis* and *trans* conformations in response to deprotonation and protonation of the nitrogen in the pyrrolidine ring and the pyridine ring is also associated with rotation (Figure 2c) (Elmore and Dougherty 2000). These conformational dynamics of nicotine make it difficult to unambiguously place it in the binding pocket.

To obtain a liganded biosensor structure, we tried different ligands and were successful in crystallizing iNicSnFR3dt in the presence of 10 mM varenicline in the same crystallization condition. Varenicline is a smoking cessation drug used to treat nicotine addiction. Crystals of iNicSnFR3dt with varenicline bound were isomorphous to those of the nicotine bound crystals and diffracted to 3.2 Å resolution. While the protein structure (Figure 3a) is identical to that of the nicotine bound structure (Figure 2a), we were able to unambiguously place varenicline in the same binding pocket. Similar to the avocado blob observed in the nicotine bound structure, varenicline is also enclosed by the same aromatic residues, forming an extensive amount of hydrophobic interactions with the pocket residues (Figure 3b).

Crystal structures of the apo iNicSnFR3dt

iNicSnFR3dt also crystallized in the apo state in space group P1, diffracting to 2.5 Å resolution with unit cell constants of $a = 81.2$ Å, $b = 86.0$ Å, $c = 91.8$ Å, $\alpha = 75.7°$, $\beta = 85.6°$, and $\gamma = 85.3°$. Although there are four copies of iNicSnFR3dt in the asymmetric unit, they all share the same overall open conformation (Figure 4a). In comparison to the varenicline bound structure, this open conformation has the two lobes of the PBP separated from each other (Figure 4a). Structural alignment based on the N-terminal 70 residues revealed the main conformational difference of the open and closed states is the hinge-bending motion of the PBP about the hinge helix connecting the two lobes. This conformational change is also referred to as the Venus-flytrap mechanism (Figure 4b). In addition, there’s a slight rotation of the cpGFP about the linker region between the two conformational states (Figure 4b).

The chromophore CRO in cpGFP moiety of the biosensors is formed by three consecutive residues, threonine, tyrosine and glycine. The resulting π-resonance systems accounts for the absorbance of GFP (Tsien 1998, Ormo et al. 1996). The fluorescence of the chromophore is known to be highly dependent on the surrounding water molecules and side chains (Brejc et al. 1997, Tsien 1998). In understanding the conformation associated fluorescence changes, we've observed that a glutamate residue (E78) from the linker 1 region changes its orientation in which it interacts with two positively charged residues (K97 and R99) on the surface of the cpGFP in the liganded state, and this same glutamate residue forms a hydrogen bonding interaction with the chromophore of cpGFP in the unliganded apo state of iNicSnFR3dt. Presumably the liganded state of iNicSnFR3dt allows for a water molecule to hydrogen bond with the hydroxy group of the chromophore, promoting its fluorescence, but this water molecule was replaced by E78 in the unliganded state, which leads to the dark state of cpGFP.

Crystal structures of the PBP domains of iNicSnFR and iAChSnFR

By eliminating both the epitope tags and cpGFP, we were able to crystallize the PBP domains to high resolution. iNicSnFR3dtbp crystals diffracted to 1.1 Å resolution in an open conformation without substrate present (Figure 5a). In this structure, we observed a peptide bound in the binding pocket; after rounds of refinement, the identity of this peptide was revealed to be the N-terminal His-tag with MHHH sequence bound such that with one histidine residue was inserted in between a tyrosine and a tryptophan residue. This observation suggests to us that these designed hydrophobic pockets for nicotine or other smoking cessation drugs also favor molecules with rings for binding. In addition, the binding protein domain of the iNicSnFR4, named as iNicSnFR4dtbp, was crystallized in both the apo and ligand states (Figure 5bc). The iNicSnFR4dtbp apo structure solved at 1.4 Å resolution (Figure 5b) with overall structure similar to that of the iNicSnFR3dtbp (Figure 5a), sharing an overall RMSD of 0.4 Å. The structure of the varenicline bound iNicSnFR4dtbp was solved at 1.7 Å resolution (Figure 5c); it is also structurally similar to that of the iNicSnFR3dt PBP domain with an overall RMSD of 0.5Å (Figure 3).

Besides the iNicSnFRs, iAChSnFRdtbp also crystallized in liganded and apo states (Figure 5def). The first structure was of choline bound iAChSnFRdtbp at 1.55 Å resolution (Figure 5d). Choline was not used in the crystallization, instead the initial crystallization condition contained 10 mM acetylcholine. The presence of choline was presumably due to the hydrolysis of acetylcholine during the crystallization. We thus closely monitored the crystallization conditions to shorten the crystallization period to obtain acetylcholine bound iAChSnFRdtbp crystals, diffracting to 1.65 Å resolution (Figure 5e). These two liganded structures of iAChSnFRdtbp are structurally similar with an overall RMSD of 0.1 Å. Furthermore, the apo structure of iAChSnFRdtbp solved at 1.4 Å resolution is similar to the apo structures of iNicSnFR3dtbp and iNicSnFR4dtbp with overall RMSDs of 0.2 - 0.3 Å.

Overall structural comparison

Despite the different ligands, the binding protein domains of the liganded conformations of iNicSnFRs and iAChSnFR are structurally similar, and their corresponding ligands all bind in the binding pocket between the two PBP lobes as seen in the overall structural alignment (Figure 6a). Similarly, the open conformations of the "dtbp" constructs are also structurally similar to the open conformation of the binding protein domain of the iNicSnFR3dt (Figure 6b). This is suggestive that the removal of the cpGFP in the "dtbp" constructs does not alter the liganded and unliganded conformation of the PBP domain of the biosensors.

In the binding pockets of the liganded structures for iNicSnFR3dt, iNicSnFR4dtbp, and iAChSnFRdtbp, the ligands, varenicline and acetylcholine are enclosed by the same set of residues (Figure 7). In the varenicline bound structure of iNicSnFR3dt (Figure 7a), varenicline forms cation-π interactions with two of the tyrosine residues (Y65 and Y357) in the binding pocket and a secondary amine of varenicline forms a hydrogen bonding interaction with the carbonyl group of asparagine (N355) with a distance of 3.2 Å (Figure 7a). The same kind of cation-π and hydrogen bonding interaction are also observed in the iNicSnFR4dtbp varenicline bound structure with residues Y65, Y111, and N209 (Figure 7b). The residues numbers in the dtbp constructs are offset by a residue count of 246 after residue 78 in comparison to the full length and the "dt" construct due to the removal of the two linkers and the cpGFP moiety. The interacting residues are slightly different in the acetylcholine bound iAChSnFRdtbp structure, where acetylcholine forms only cation- π interactions with the nearby tyrosine residues, Y65, Y111, and Y214 (Figure 7c). This is suggestive that there might be different binding interactions with different ligands.

5.3 Discussion

As these biosensors are all modified from the *Thermoanaerobacter sp.* X513 choline/betaine binding protein, one question is whether the design process for different ligands has affected the actual conformational changes between the open and closed conformation. We thus performed principal component analysis to characterize the major conformational changes. This analysis demonstrated that component 1 accounts for 75% of the total conformational change, which is associated with the hinge motion. Component 2 accounts for 17% of the total conformational change, which is associated with the overall conformational difference between the PBPs of biosensors and the other published betaine and choline binding proteins. With this analysis, the liganded and apo biosensor structures are separated into two groups (Figure 8a) with the main difference in component 1, which accounts for the Venus-flytrap type of conformational change and this conformational change is best represented by the structural alignment of varenicline bound iNicSnFR3dt and the apo iNicSnFR3dtbp (Figure 8b). As seen in the other betaine or choline binding protein structures in the Protein Data Bank, the liganded conformations differ little from each other, and the conformational change between liganded and unliganded states are also related by the Venus-flytrap mechanism (Figure 8c). Component 2 only accounts for a small fraction of the conformational differences between the native structures and the genetically optimized biosensor. This small difference is also observed in the structural alignment between a choline bound iASnFRdtbp and a choline bound *Bacillus subtilis* with overall RMSD of 1 Å.

In conclusion, we have structurally characterized apo and liganded states for nicotine and acetylcholine biosensors that are genetically engineered from the bacterial periplasmic binding protein of a choline/betaine ABC transporter system and a circular permutated green fluorescent protein. We further showed that the removal of the cpGFP for crystallization purposes had little impact on the open or closed conformation of the biosensor, suggesting that in the intact sensor, the presence of cpGFP did not perturb the conformational changes in the PBP domain of the biosensor. Analysis of the binding pocket residues revealed that the key residues in forming the cation- π interactions with nicotine in iNicSnFR and acetylcholine in iAChSnFR are two tyrosine residues, Y65 and Y357. In addition, the binding pockets are filled with aromatic residues that favor binding of hydrophobic molecules, with some polar, non-aromatic residues present to form hydrogen bonding interactions with the bound ligand. Lastly, principal component analysis with other binding proteins revealed similar conformational changes following the Venus-flytrap mechanism of ABC transporter periplasmic binding proteins. The structural analysis presented details for the first time liganded states of the engineered biosensors for smoking cessation drugs and neurotransmitters, revealing the binding specificity of ligands to the biosensor. This work sets the foundation for future work on biosensor design and optimization.

5.4 Materials and Methods

Cloning, protein expression, and purification

The gene encoding full length biosensor (iNicSnFR3) was previously cloned into a bacterial expression vector as described with a N-terminal 6x His tag (Shivange et al. 2019). The removal of HA-tag, MYC-tag, and cpGFP were separately carried out with the Q5 Site-Directed Mutagenesis Kit (New England Biolabs). All proteins were overexpressed in *Escherichia coli* BL21-gold (DE3) cells (Agilent Technologies) using ZYM-5052 autoinduction media (Studier 2005). Cells were collected by centrifugation and stored at -80 ˚C until use.

For purification, frozen cell pellets were resuspended in lysis buffer containing 100 mM NaCl, 20 mM Tris, pH 7.5, 20 mM imidazole, pH 7.5, 5 mM β-mercaptoethanol (BME), lysozyme, DNase, and protease inhibitor tablet. The resuspended cells were lysed by freezing and thawing using liquid nitrogen and room temperature water bath for 3 cycles. Unlysed cells and cell debris were removed by centrifugation at ~20,000x g for 40 minutes at 4 ˚C. The supernatant was collected and loaded onto a prewashed NiNTA column with wash buffer at 4 ˚C. NiNTA wash buffer contains 100 mM NaCl, 20 mM Tris, pH 7.5, 30 mM imidazole, pH 7.5, and 5 mM BME. Elution was achieved using the same buffer containing 300 mM imidazole, pH 7.5. The eluted sample was further purified by size exclusion chromatography (SEC) using HiLoad 16/60 Superdex 200 in the same buffer without imidazole and BME. Peak fractions were collected and concentrated to ~50 mg/ml with Amicon Ultra 15 concentrator (Millipore) with 10kDa cutoff.

Crystallization

For all constructs, initial crystallization screening was carried out with 40 mg/ml protein in the presence and absence of 10 mM nicotine or varenicline. iNicSnFR3dt crystallized separately with 10 mM nicotine and varenicline in PACT premier, condition #96 with 0.2 M sodium malonate dibasic monohydrate, 0.1 M Bis-Tris Propane pH 8.5, and 20% polyethylene glycol (PEG) 3,350 at 20 °C. Crystals of iNicSnFR3dt grew within two weeks of crystallization in a hexagonal rod shape with dimensions of ~ 80 μm x 80 μm x 300 μm. Crystals were harvested and cryo-protected in 25% ethylene glycol, 0.2 M sodium malonate dibasic monohydrate, 0.1 M BisTrisPropane pH 8.5, and 20% PEG 3350. Phase information was obtained through soaking with potassium iodide before cryo-protection. The unliganded iNicSnFR3dt crystallized in Morpheus (Molecular Dimensions), condition #92 with 2.5% PEG 1,000, 12.5% PEG 3,350, 12.5% 2-methyl-2,4-pentanediol, 0.02 M of each amino acid and 0.1 M MOPS/HEPES-Na, pH 7.5 at 23 °C with no further optimization.

The unliganded iNicSnFR3dtbp crystallized in Index (Hampton Research), condition # 79 with 0.2 M ammonium acetate, 0.1 M Bis-Tris, pH 6.5, 25% PEG 3,350 at 23 °C. iNicSnFR4dtbp with bound varenicline crystallized in Wizard 1 (Molecular Dimensions), condition #1 with 20% PEG 8,000 and 0.1 M CHES, pH 9.5 and the condition was further optimized with Additive screen (Hampton Research) with the final condition containing an additional 10 mM spermidine. The unliganded iNicSnFR4dtbp crystallized in Wizard 4 (Molecular Dimensions), condition #39 with 0.1 M imidazole, pH 6.5, 3% 2-methyl-2,4-pentanediol, 20% PEG 8,000 at 23 °C with no further optimization. These crystals were harvested directly with well solution before flash-freezing in liquid nitrogen.

The initial crystallization screening for iAchSnFRdtbp was carried out with 40 mg/ml protein in the presence and absence of 10 mM acetylcholine at 23 °C. The acetylcholine and choline bound iAchSnFRdtbp were crystallized in Wizard 1 (Molecular Dimensions), condition #1 with 20% PEG 8,000 and 0.1 M CHES, pH 9.5. The unliganded iAchSnFRdtbp crystallized in Wizard 4 (Molecular Dimensions), condition #21 with 25% PEG 8,000 and 0.1M MIB (malonate, imidazole, and boric acid), pH 5.0. The crystals were harvested directly with well solution before flash-freezing in liquid nitrogen.

Data collection, data processing and structural determination

X-ray datasets were collected at Stanford Synchrotron Radiation Laboratory beamline 12-2 and Advanced Light Source beamline 5.0.2 using Pilatus 6M detectors. All datasets were processed and integrated with XDS (Kabsch 2010) and scaled with Aimless (Winn et al. 2011). For iNicSnFR3dt, molecular replacement was carried out using domains of the unliganded structure (PDB ID: 6EFR) with Phaser in Phenix (Adams et al. 2010). The experimental phase information of KI-soaked crystals of iNicSnFR3dt was obtained with MR-SAD using AutoSol in Phenix (Adams et al. 2010). Molecular replacements of the remaining structures were carried out with the refined model of iNicSnFR3dt. Iterative refinement and model building cycles for all structures were carried out separately with phenix.refine in Phenix (Adams et al. 2010) and Coot (Emsley et al. 2010).

5.5 Acknowledgments

We thank Jens T. Kaiser, Silvia Russi and the beamline staffs of the Stanford Synchrotron Radiation Lightsource beamline 12-2 and of the Advanced Light Source beamline 5.0.2 for their support during data collection. We also gratefully acknowledge the Gordon and Betty Moore Foundation and the Beckman Institute for their generous support of the Molecular Observatory at Caltech. Use of the Stanford Synchrotron Radiation Lightsource, SLAC National Accelerator Laboratory, is supported by the U.S. Department of Energy, Office of Science, Office of Basic Energy Sciences under Contract No. DE-AC02-76SF00515. Beamline 5.0.2 of the Advanced Light Source, a DOE Office of Science User Facility under Contract No. DE-AC02-05CH11231, is supported in part by the ALS-ENABLE program funded by the National Institutes of Health, National Institute of General Medical Sciences, grant P30 GM124169-01.

5.6 Figures

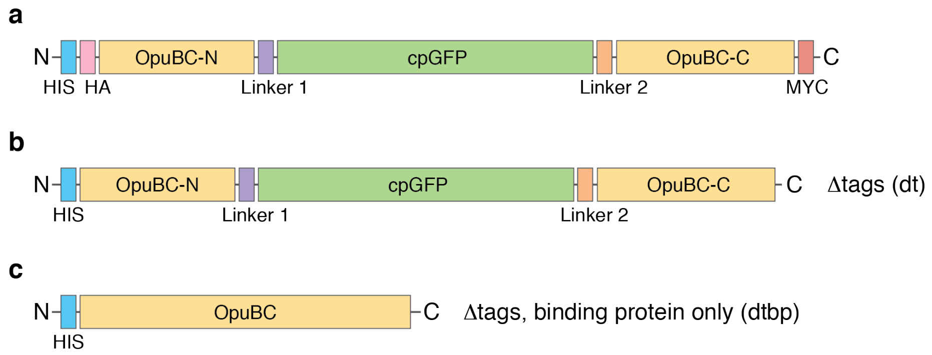

Figure 1. Construct design.

(**a**) Full length biosensor. (**b**) Biosensors with epitope tags removed. (**c**) PBP domain-only constructs.

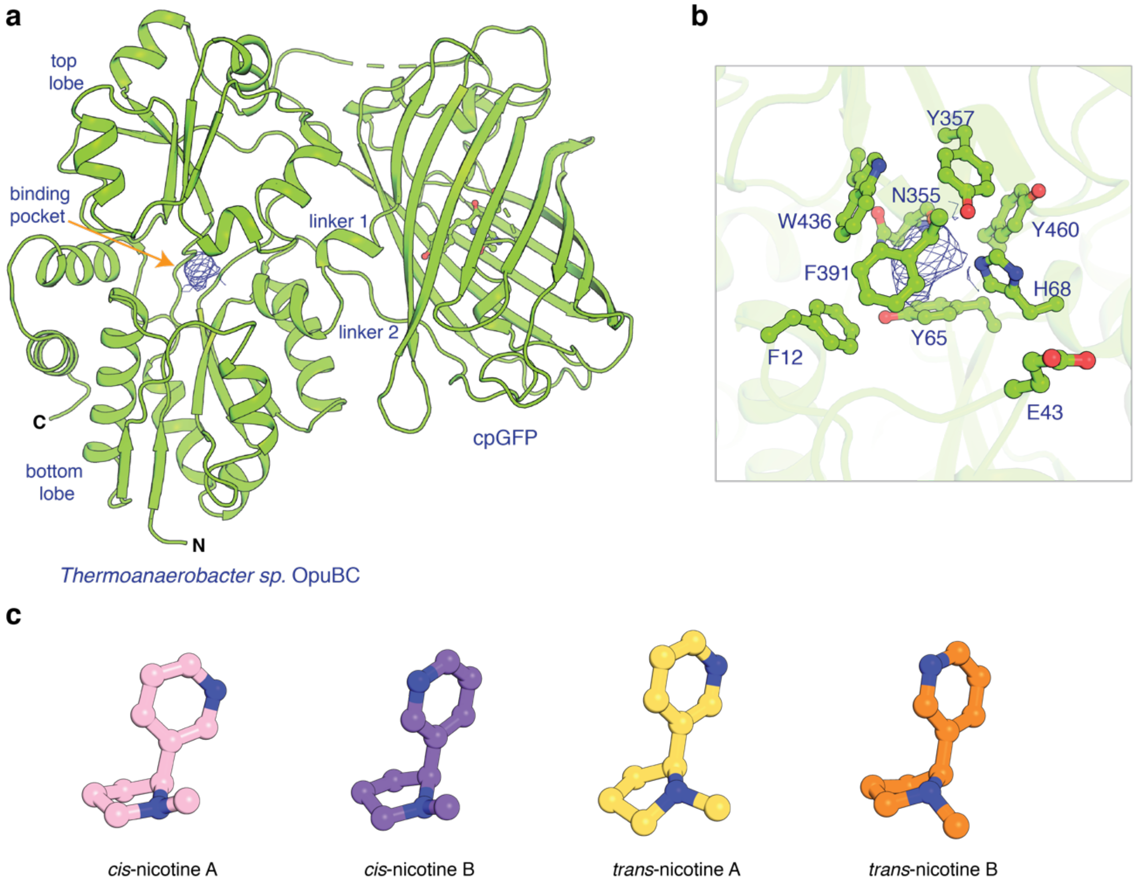

Figure 2. Nicotine bound structure of iNicSnFR3dt.

(**a**) Overall conformation of iNicSnFR3dt with an electron density blob at the nicotine binding site. (**b**) iNicSnFR3dt binding site residues. (**c**) Possible *cis* and *trans* conformers of nicotine.

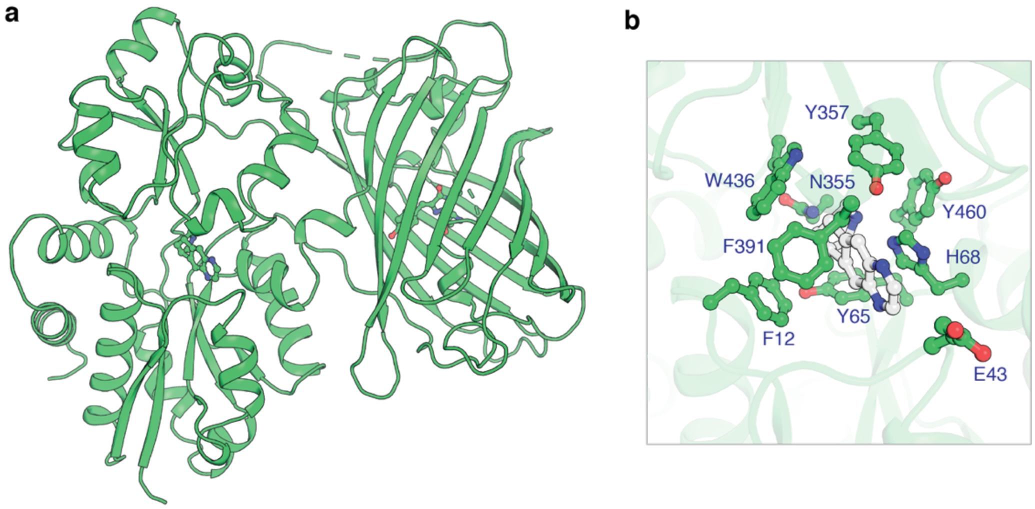

Figure 3. Varenicline bound structure of iNicSnFR3dt.

(**a**) Overall conformation of iNicSnFR3dt with varenicline bound. (**b**) iNicSnFR3dt binding site with varenicline present.

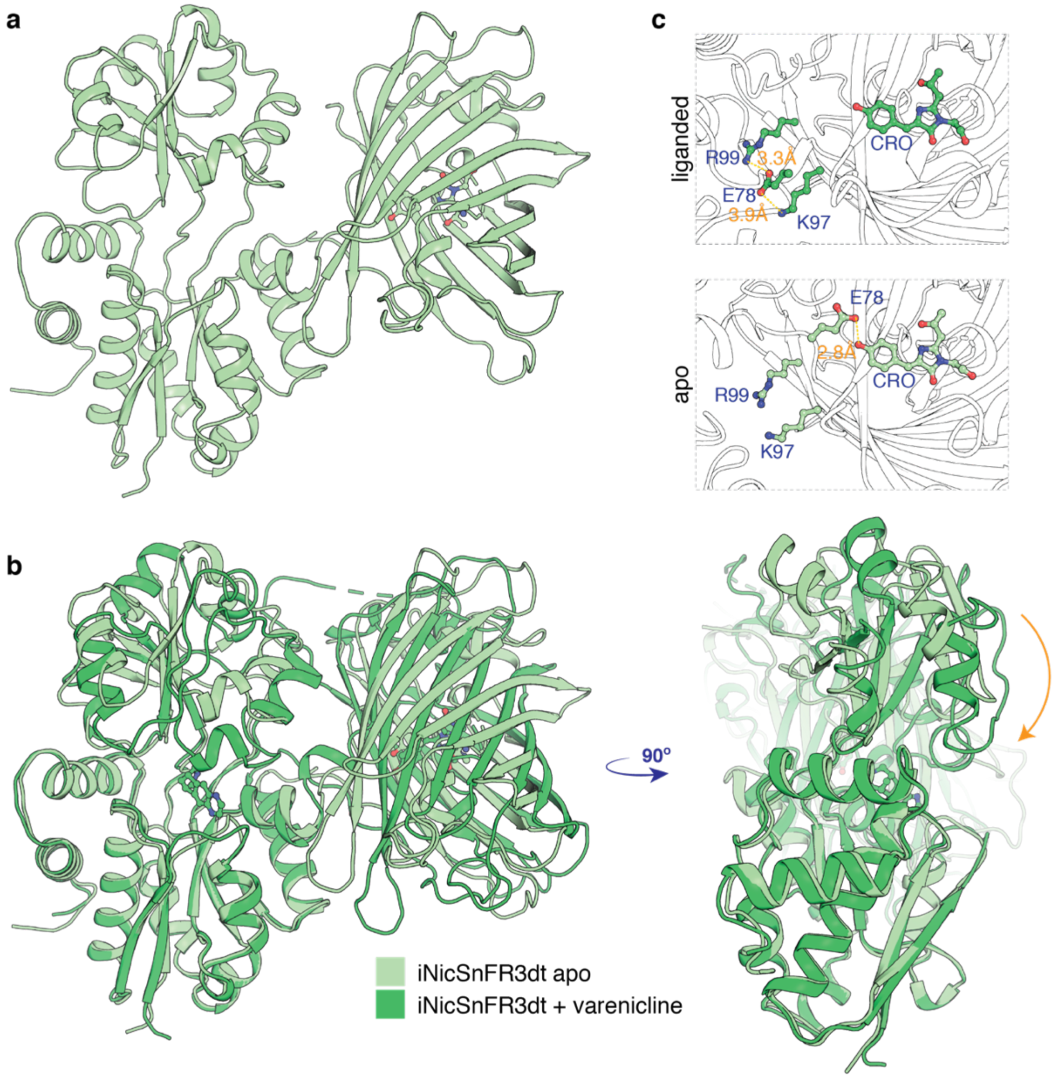

Figure 4. Apo structure of iNicSnFR3dt.

(**a**) Overall conformation of the apo iNicSnFR3dt. (**b**) Structural alignment of iNicSnFR3dt in apo and varenicline bound conformations. The arrow represents the conformational change of the top lobe, resembling the Venus-flytrap mechanism. (**c**) Orientation differences of E78 in liganded and apo structures of iNicSnFR3dt.

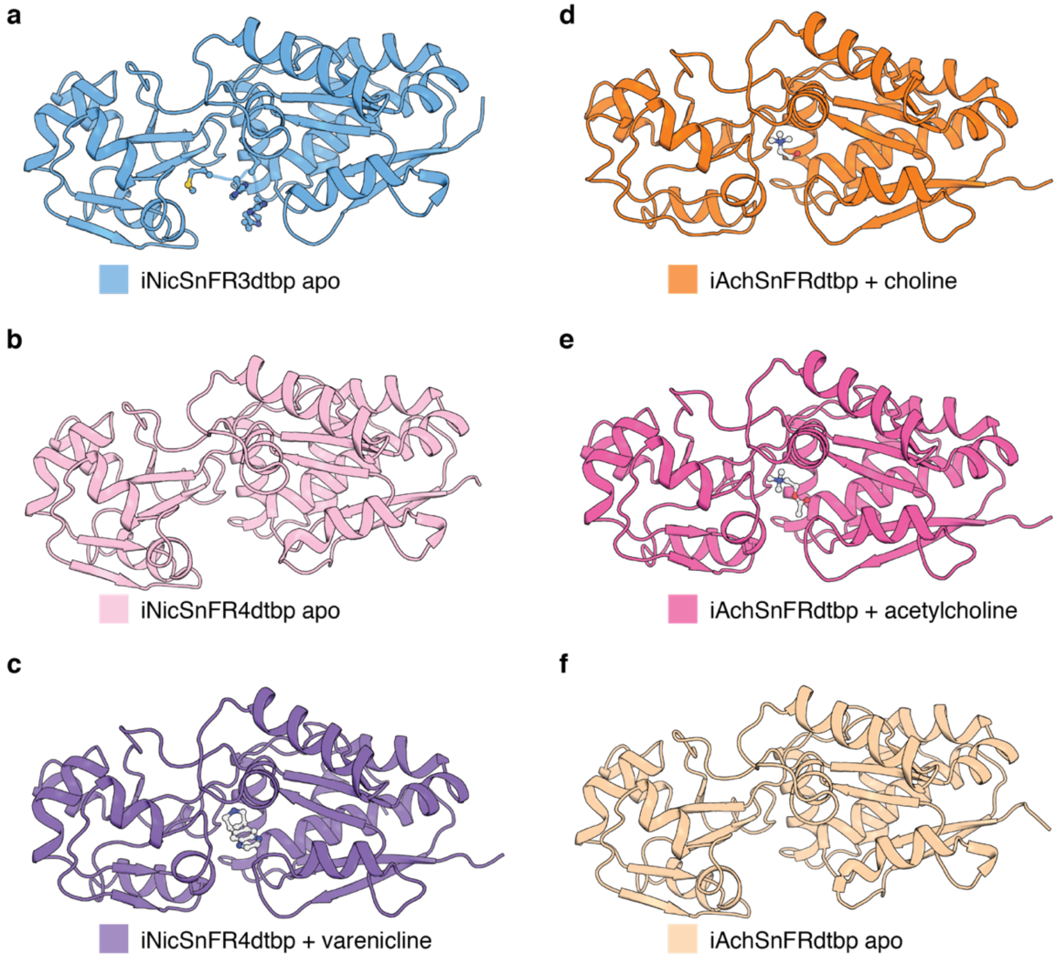

Figure 5. Structures of PBP domains of iNicSnFR and iAChSnFR.

(**a**) iNicSnFR3dtbp in the apo conformation. (**b**) iNicSnFR4dtbp in the apo conformation. **c**) iNicSnFR3dtbp in the varenicline bound conformation. (**d**) iAChSnFRdtbp in the choline bound conformation. (**e**) iAChSnFRdtbp in the acetylcholine bound conformation. (**f**) iAChSnFRdtbp in the apo conformation.

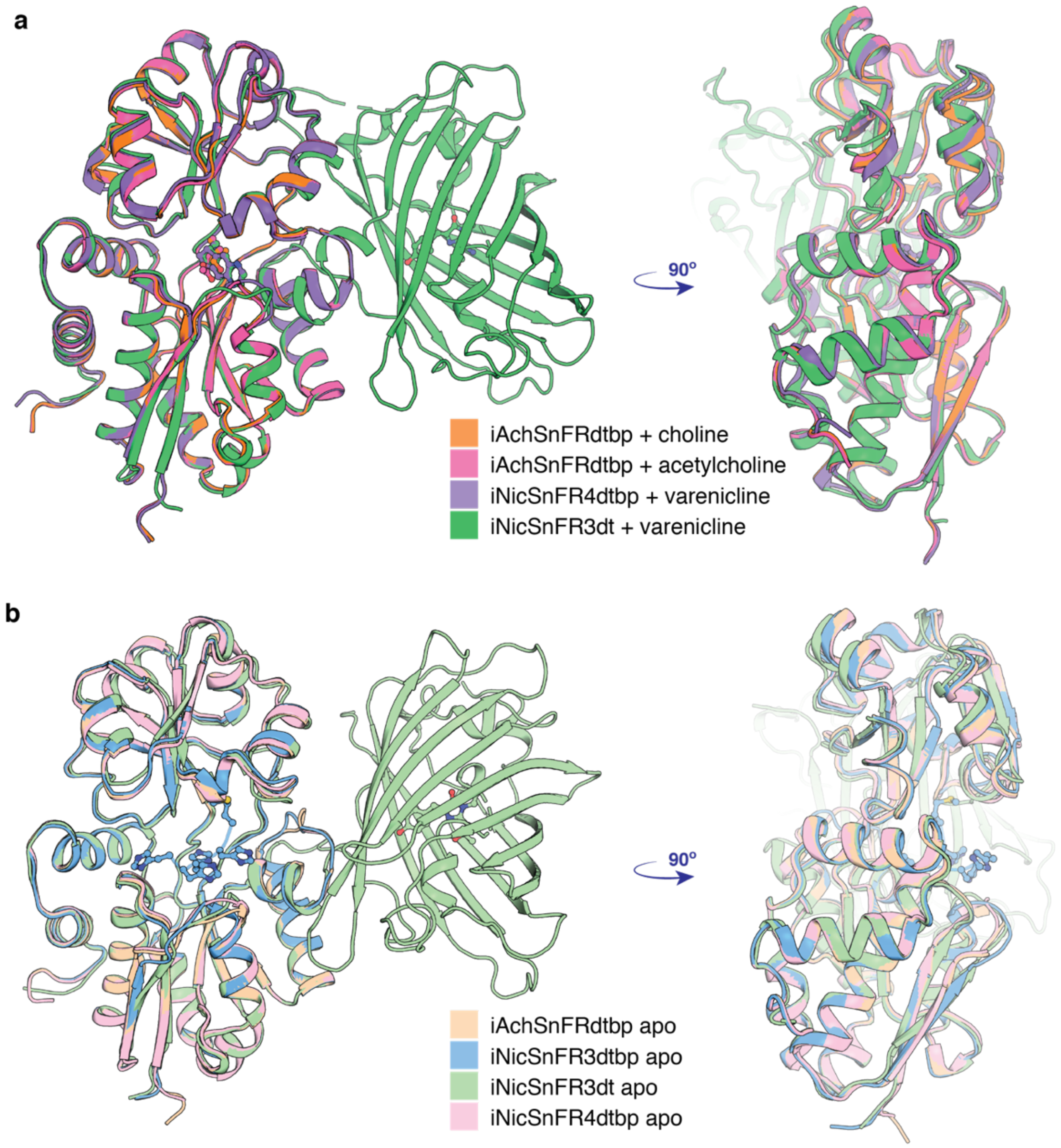

Figure 6. Structural alignments of iNicSnFR and iAChSnFR.

(**a**) Structural alignments of the liganded PBP domain structures of iNicSnFR3, iNicSnFR4, and iAChSnFR to the varenicline bound conformation of iNicSnFR3dt. (**b**) Structural alignments of the apo PBP domain structures of iNicSnFR3, iNicSnFR4, and iAChSnFR to the apo conformation of iNicSnFR3dt.

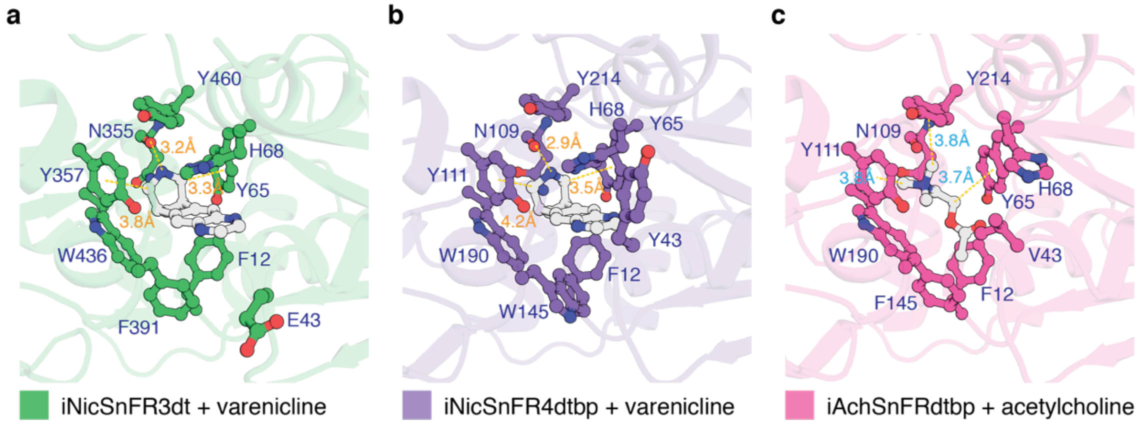

Figure 7. Binding pocket residues.

Ligand binding pocket residues in (**a**) iNicSnFR3dt with varenicline bound, (**b**) iNicSnFR4dtbp with varenicline bound, and (**c**) iAChSnFR3dt with acetylcholine bound.

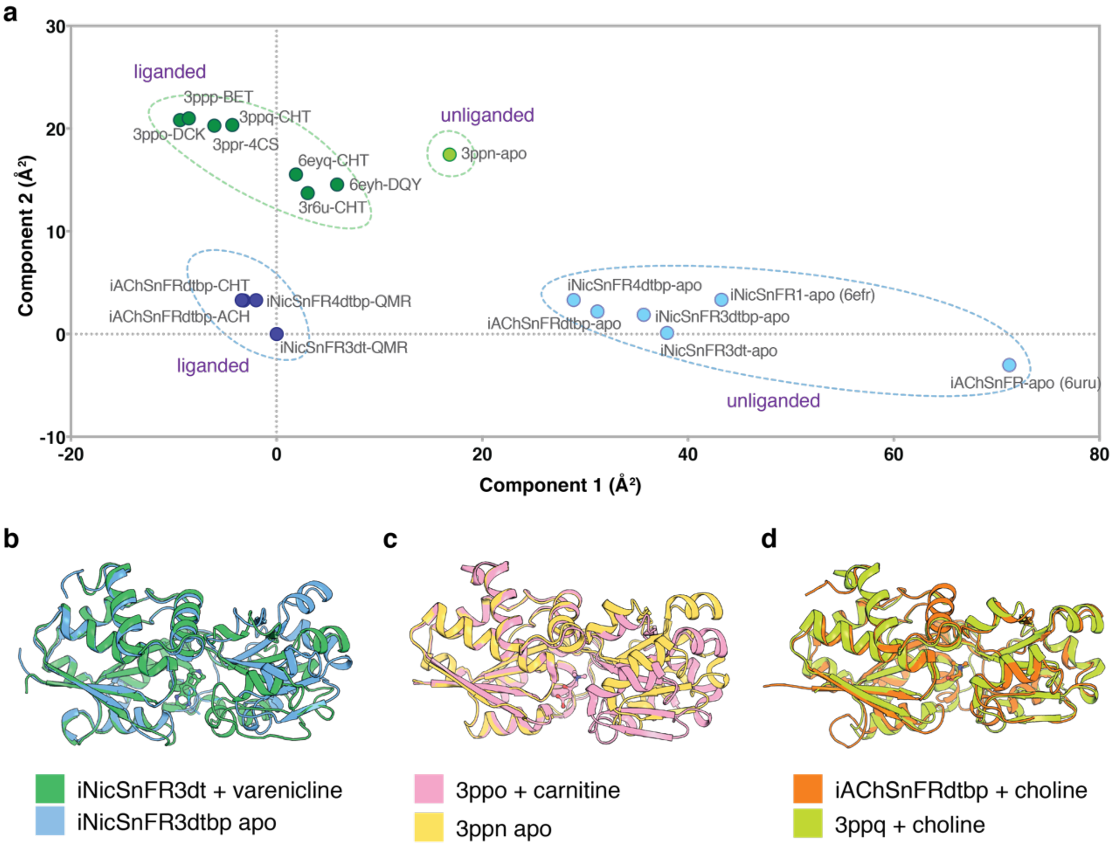

Figure 8. Principal component analysis.

(**a**) Principal component analysis of the available structures of the biosensors and other betaine/choline binding protein structures in the Protein Data Bank. Component 1 accounts for 75% and component 2 accounts for 17% of total conformational change. Structural alignment of (**b**) the varenicline bound iNicSnFR3dt and apo iNicSnFR3dtbp conformation, (**c**) the apo structure (PDB ID: 3PPN) to the carnitine bound structure (PDB ID: 3PPO) of OpuCC, and (**d**) the choline bound iAchSnFRdtbp to the choline bound OpuCC (PDB ID: 3PPQ). The PDB IDs for the structures published in the Protein Data Bank are labeled in the figure.

5.7 Tables

Table 1. Data collection and refinement statistics for iNicSnFR3dt with nicotine bound

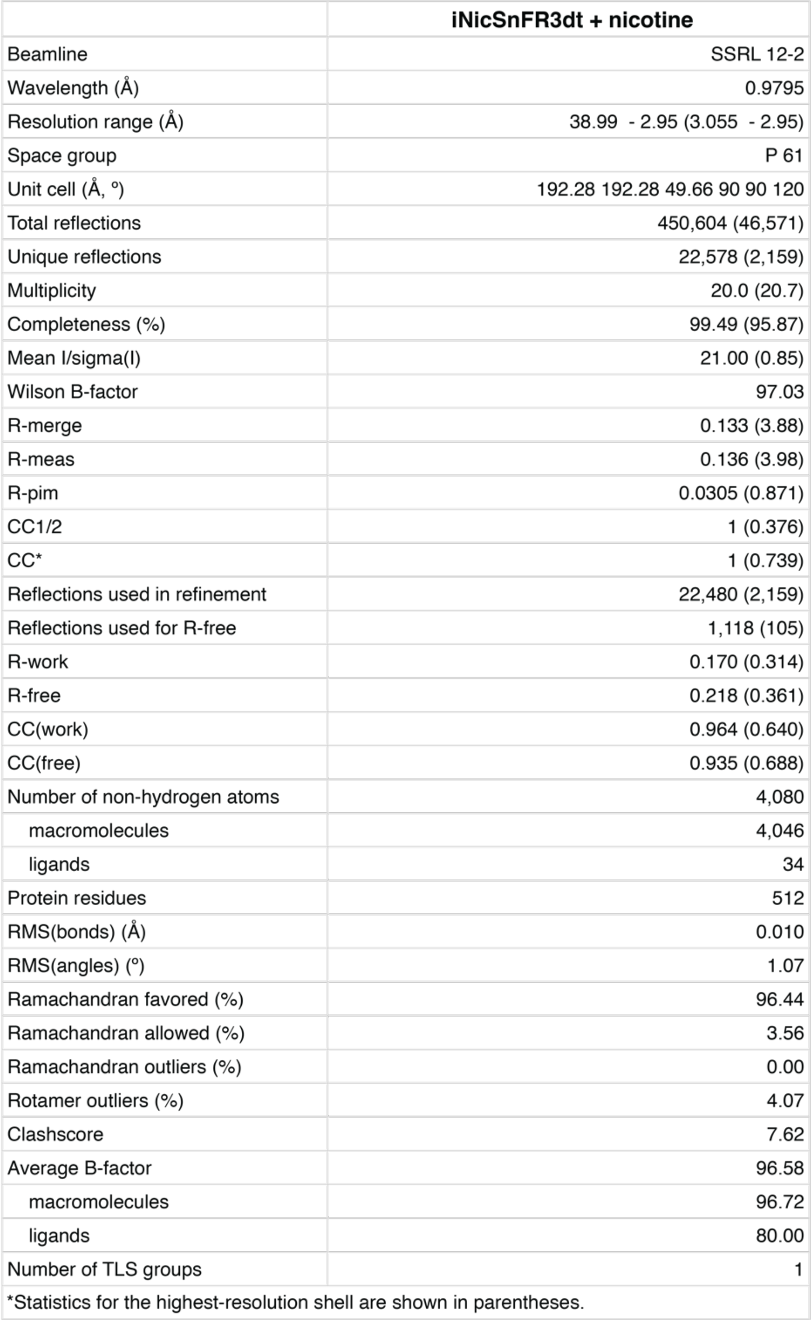

	iNicSnFR3dt + nicotine
Beamline	SSRL 12-2
Wavelength (Å)	0.9795
Resolution range (Å)	38.99 - 2.95 (3.055 - 2.95)
Space group	P 61
Unit cell (Å, °)	192.28 192.28 49.66 90 90 120
Total reflections	450,604 (46,571)
Unique reflections	22,578 (2,159)
Multiplicity	20.0 (20.7)
Completeness (%)	99.49 (95.87)
Mean I/sigma(I)	21.00 (0.85)
Wilson B-factor	97.03
R-merge	0.133 (3.88)
R-meas	0.136 (3.98)
R-pim	0.0305 (0.871)
CC1/2	1 (0.376)
CC*	1 (0.739)
Reflections used in refinement	22,480 (2,159)
Reflections used for R-free	1,118 (105)
R-work	0.170 (0.314)
R-free	0.218 (0.361)
CC(work)	0.964 (0.640)
CC(free)	0.935 (0.688)
Number of non-hydrogen atoms	4,080
macromolecules	4,046
ligands	34
Protein residues	512
RMS(bonds) (Å)	0.010
RMS(angles) (°)	1.07
Ramachandran favored (%)	96.44
Ramachandran allowed (%)	3.56
Ramachandran outliers (%)	0.00
Rotamer outliers (%)	4.07
Clashscore	7.62
Average B-factor	96.58
macromolecules	96.72
ligands	80.00
Number of TLS groups	1

*Statistics for the highest-resolution shell are shown in parentheses.

Table 2. Data collection and refinement statistics for iNicSnFR3dt with varenicline bound

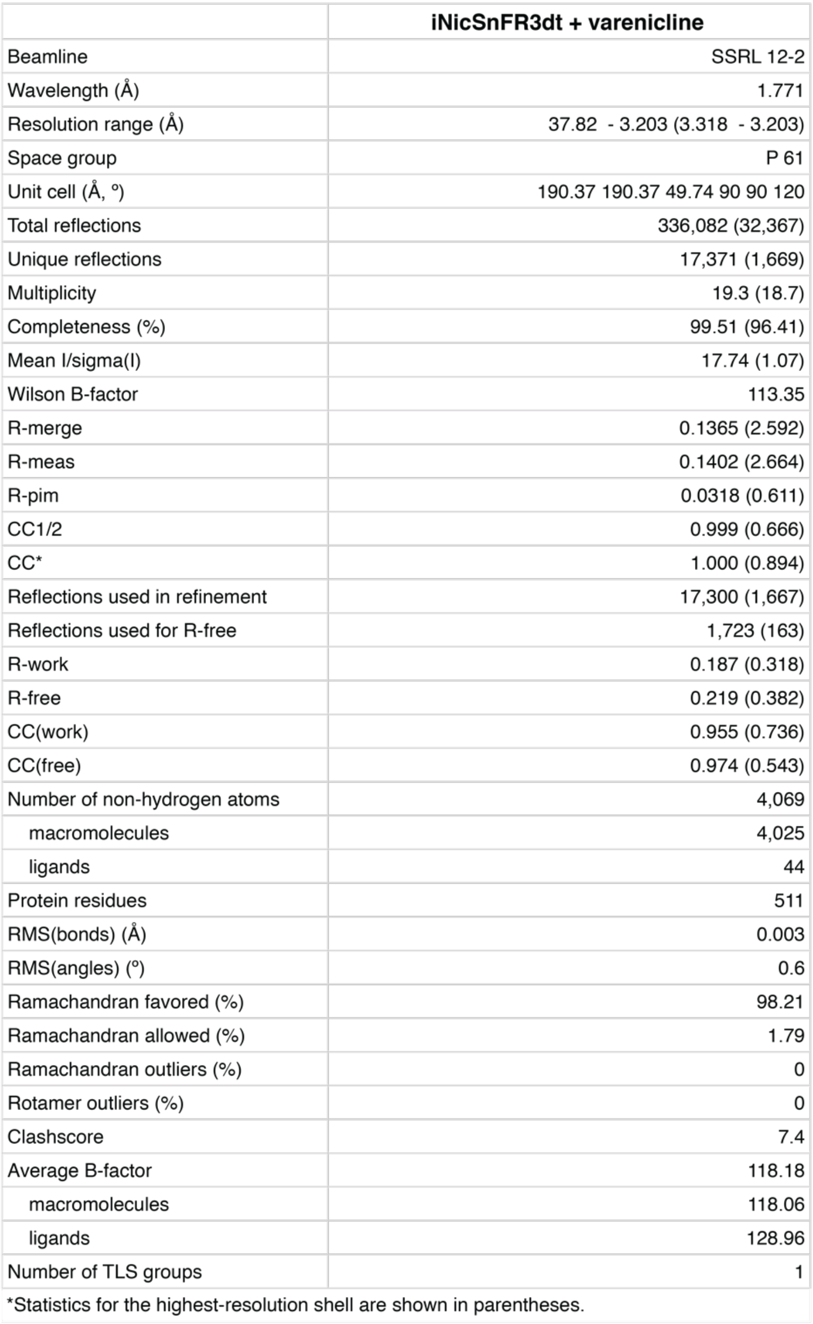

	iNicSnFR3dt + varenicline
Beamline	SSRL 12-2
Wavelength (Å)	1.771
Resolution range (Å)	37.82 - 3.203 (3.318 - 3.203)
Space group	P 61
Unit cell (Å, °)	190.37 190.37 49.74 90 90 120
Total reflections	336,082 (32,367)
Unique reflections	17,371 (1,669)
Multiplicity	19.3 (18.7)
Completeness (%)	99.51 (96.41)
Mean I/sigma(I)	17.74 (1.07)
Wilson B-factor	113.35
R-merge	0.1365 (2.592)
R-meas	0.1402 (2.664)
R-pim	0.0318 (0.611)
CC1/2	0.999 (0.666)
CC*	1.000 (0.894)
Reflections used in refinement	17,300 (1,667)
Reflections used for R-free	1,723 (163)
R-work	0.187 (0.318)
R-free	0.219 (0.382)
CC(work)	0.955 (0.736)
CC(free)	0.974 (0.543)
Number of non-hydrogen atoms	4,069
macromolecules	4,025
ligands	44
Protein residues	511
RMS(bonds) (Å)	0.003
RMS(angles) (°)	0.6
Ramachandran favored (%)	98.21
Ramachandran allowed (%)	1.79
Ramachandran outliers (%)	0
Rotamer outliers (%)	0
Clashscore	7.4
Average B-factor	118.18
macromolecules	118.06
ligands	128.96
Number of TLS groups	1

*Statistics for the highest-resolution shell are shown in parentheses.

Table 3. Data collection and refinement statistics for iNicSnFR3dt apo structure

	iNicSnFR3dt apo
Beamline	ALS 5.0.2
Wavelength (Å)	0.9848
Resolution range (Å)	40.39 - 2.5 (2.589 - 2.5)
Space group	P 1
Unit cell (Å, º)	81.19 86.87 91.83 75.72 85.56 85.28
Total reflections	283,541 (27,520)
Unique reflections	81,831 (8,190)
Multiplicity	3.5 (3.4)
Completeness (%)	98.53 (97.83)
Mean I/sigma(I)	10.69 (1.72)
Wilson B-factor	40.02
R-merge	0.0827 (0.601)
R-meas	0.0985 (0.716)
R-pim	0.0527 (0.384)
CC1/2	0.995 (0.665)
CC*	0.999 (0.894)
Reflections used in refinement	82,497 (8,190)
Reflections used for R-free	2,003 (185)
R-work	0.232 (0.308)
R-free	0.274 (0.340)
CC(work)	0.908 (0.724)
CC(free)	0.889 (0.586)
Number of non-hydrogen atoms	16,649
macromolecules	16,049
ligands	88
solvent	512
Protein residues	2,034
RMS(bonds) (Å)	0.004
RMS(angles) (º)	0.81
Ramachandran favored (%)	98.06
Ramachandran allowed (%)	1.69
Ramachandran outliers (%)	0.25
Rotamer outliers (%)	1.88
Clashscore	9.66
Average B-factor	39.86
macromolecules	40.03
ligands	31.05
solvent	36.31

*Statistics for the highest-resolution shell are shown in parentheses.

Table 4. Data collection and refinement statistics for iNicSnFR3dtbp apo structure

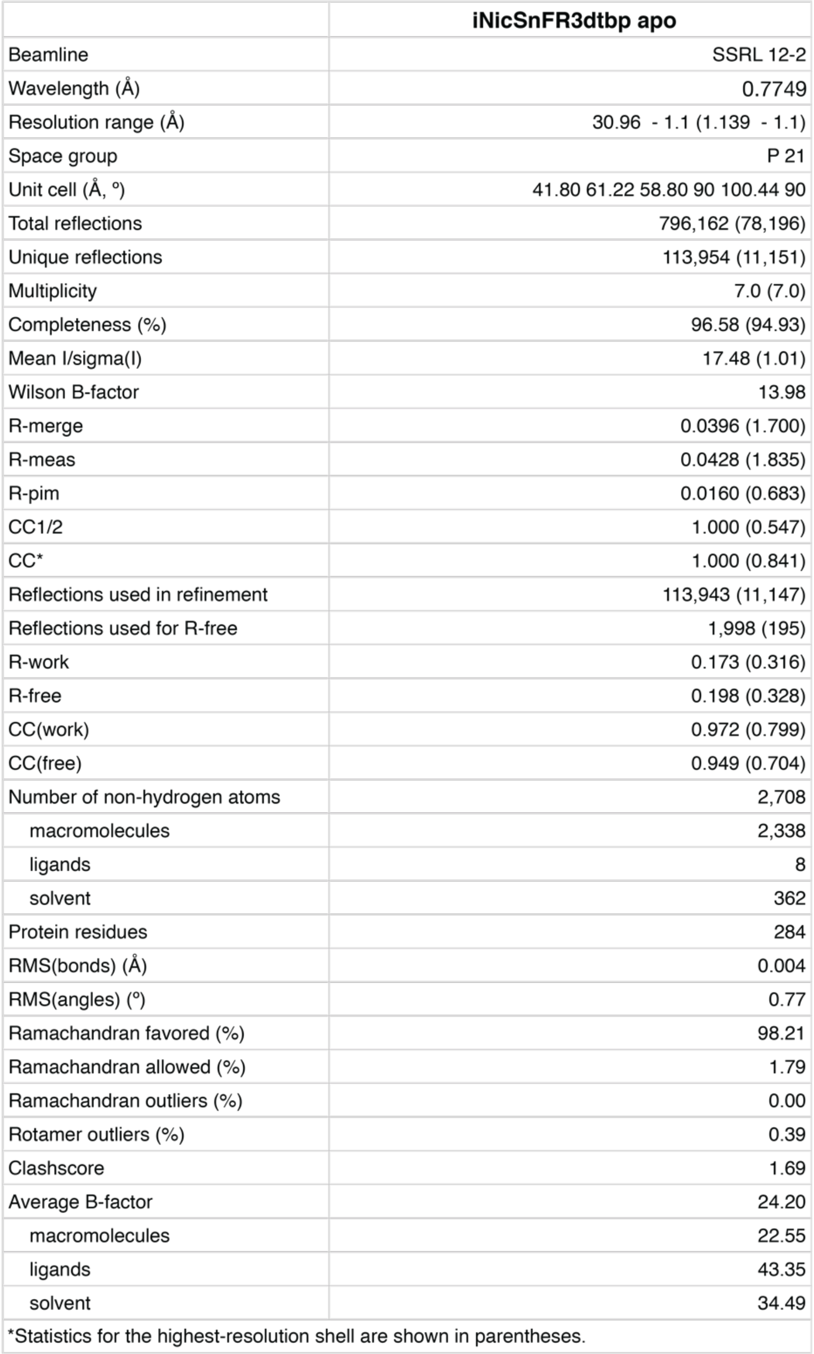

	iNicSnFR3dtbp apo
Beamline	SSRL 12-2
Wavelength (Å)	0.7749
Resolution range (Å)	30.96 - 1.1 (1.139 - 1.1)
Space group	P 21
Unit cell (Å, º)	41.80 61.22 58.80 90 100.44 90
Total reflections	796,162 (78,196)
Unique reflections	113,954 (11,151)
Multiplicity	7.0 (7.0)
Completeness (%)	96.58 (94.93)
Mean I/sigma(I)	17.48 (1.01)
Wilson B-factor	13.98
R-merge	0.0396 (1.700)
R-meas	0.0428 (1.835)
R-pim	0.0160 (0.683)
CC1/2	1.000 (0.547)
CC*	1.000 (0.841)
Reflections used in refinement	113,943 (11,147)
Reflections used for R-free	1,998 (195)
R-work	0.173 (0.316)
R-free	0.198 (0.328)
CC(work)	0.972 (0.799)
CC(free)	0.949 (0.704)
Number of non-hydrogen atoms	2,708
macromolecules	2,338
ligands	8
solvent	362
Protein residues	284
RMS(bonds) (Å)	0.004
RMS(angles) (º)	0.77
Ramachandran favored (%)	98.21
Ramachandran allowed (%)	1.79
Ramachandran outliers (%)	0.00
Rotamer outliers (%)	0.39
Clashscore	1.69
Average B-factor	24.20
macromolecules	22.55
ligands	43.35
solvent	34.49

*Statistics for the highest-resolution shell are shown in parentheses.

Table 5. Data collection and refinement statistics for iNicSnFR4dtbp with varenicline bound

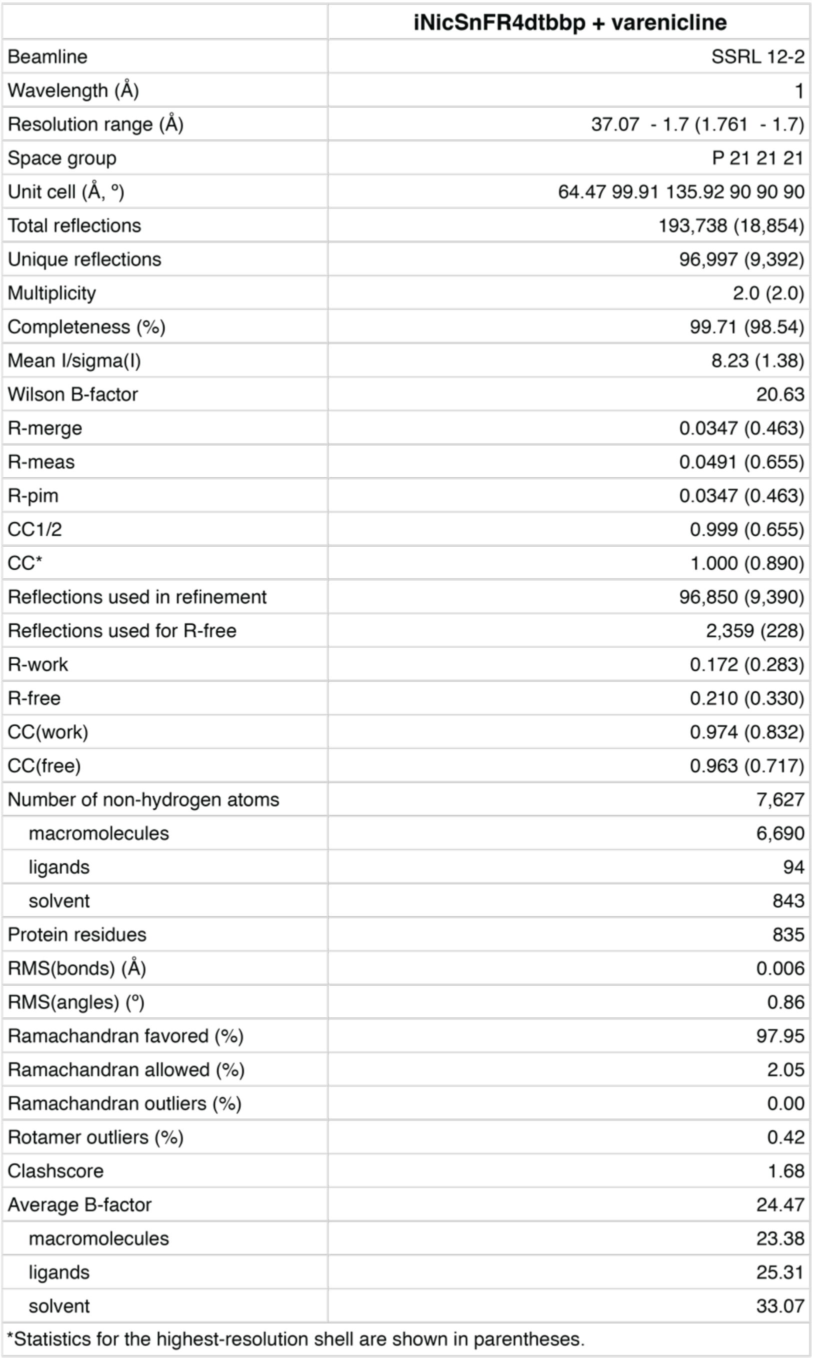

	iNicSnFR4dtbbp + varenicline
Beamline	SSRL 12-2
Wavelength (Å)	1
Resolution range (Å)	37.07 - 1.7 (1.761 - 1.7)
Space group	P 21 21 21
Unit cell (Å, °)	64.47 99.91 135.92 90 90 90
Total reflections	193,738 (18,854)
Unique reflections	96,997 (9,392)
Multiplicity	2.0 (2.0)
Completeness (%)	99.71 (98.54)
Mean I/sigma(I)	8.23 (1.38)
Wilson B-factor	20.63
R-merge	0.0347 (0.463)
R-meas	0.0491 (0.655)
R-pim	0.0347 (0.463)
CC1/2	0.999 (0.655)
CC*	1.000 (0.890)
Reflections used in refinement	96,850 (9,390)
Reflections used for R-free	2,359 (228)
R-work	0.172 (0.283)
R-free	0.210 (0.330)
CC(work)	0.974 (0.832)
CC(free)	0.963 (0.717)
Number of non-hydrogen atoms	7,627
macromolecules	6,690
ligands	94
solvent	843
Protein residues	835
RMS(bonds) (Å)	0.006
RMS(angles) (º)	0.86
Ramachandran favored (%)	97.95
Ramachandran allowed (%)	2.05
Ramachandran outliers (%)	0.00
Rotamer outliers (%)	0.42
Clashscore	1.68
Average B-factor	24.47
macromolecules	23.38
ligands	25.31
solvent	33.07

*Statistics for the highest-resolution shell are shown in parentheses.

Table 6. Data collection and refinement statistics for iNicSnFR4dtbp apo structure

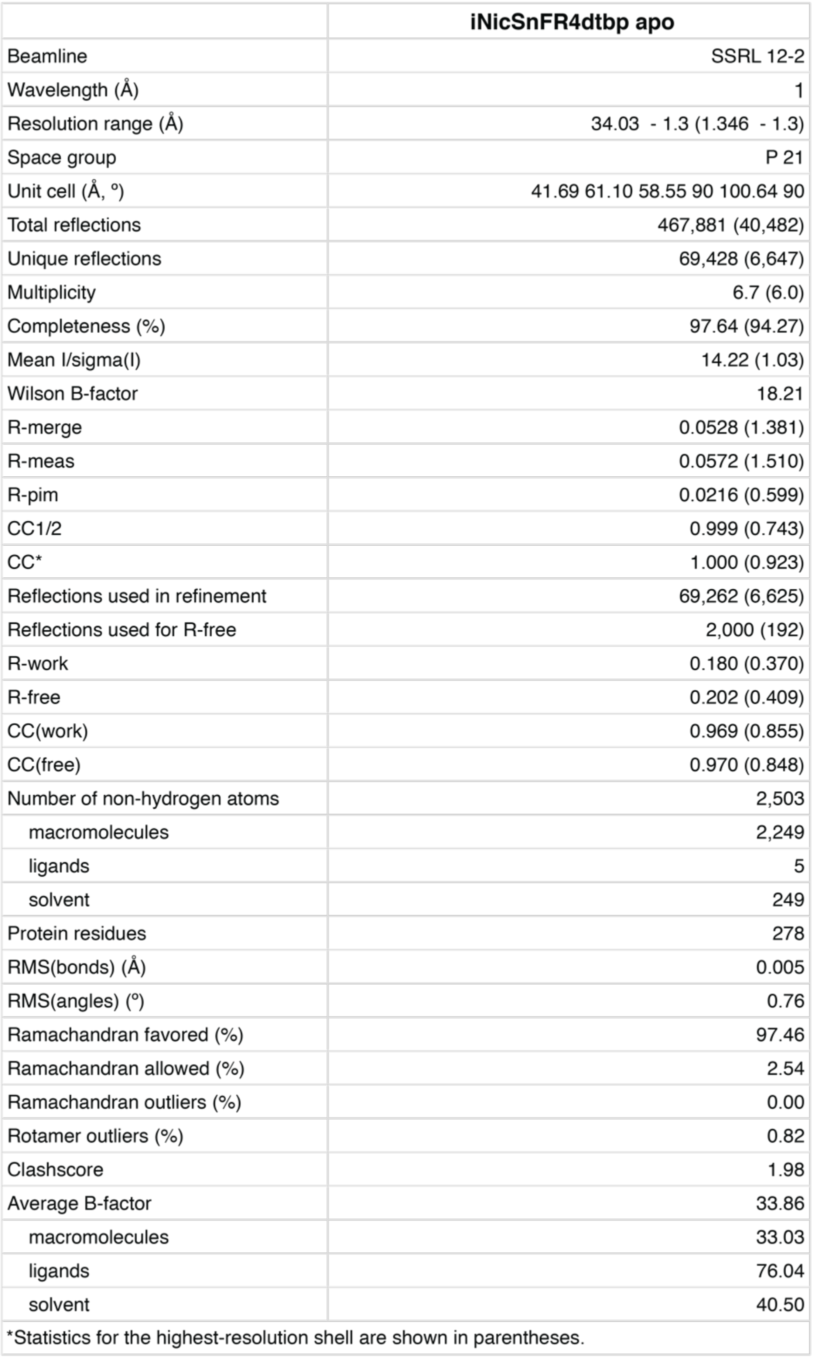

	iNicSnFR4dtbp apo
Beamline	SSRL 12-2
Wavelength (Å)	1
Resolution range (Å)	34.03 - 1.3 (1.346 - 1.3)
Space group	P 21
Unit cell (Å, º)	41.69 61.10 58.55 90 100.64 90
Total reflections	467,881 (40,482)
Unique reflections	69,428 (6,647)
Multiplicity	6.7 (6.0)
Completeness (%)	97.64 (94.27)
Mean I/sigma(I)	14.22 (1.03)
Wilson B-factor	18.21
R-merge	0.0528 (1.381)
R-meas	0.0572 (1.510)
R-pim	0.0216 (0.599)
CC1/2	0.999 (0.743)
CC*	1.000 (0.923)
Reflections used in refinement	69,262 (6,625)
Reflections used for R-free	2,000 (192)
R-work	0.180 (0.370)
R-free	0.202 (0.409)
CC(work)	0.969 (0.855)
CC(free)	0.970 (0.848)
Number of non-hydrogen atoms	2,503
macromolecules	2,249
ligands	5
solvent	249
Protein residues	278
RMS(bonds) (Å)	0.005
RMS(angles) (º)	0.76
Ramachandran favored (%)	97.46
Ramachandran allowed (%)	2.54
Ramachandran outliers (%)	0.00
Rotamer outliers (%)	0.82
Clashscore	1.98
Average B-factor	33.86
macromolecules	33.03
ligands	76.04
solvent	40.50

*Statistics for the highest-resolution shell are shown in parentheses.

Table 7. Data collection and refinement statistics for iAChSnFRdtbp with choline bound

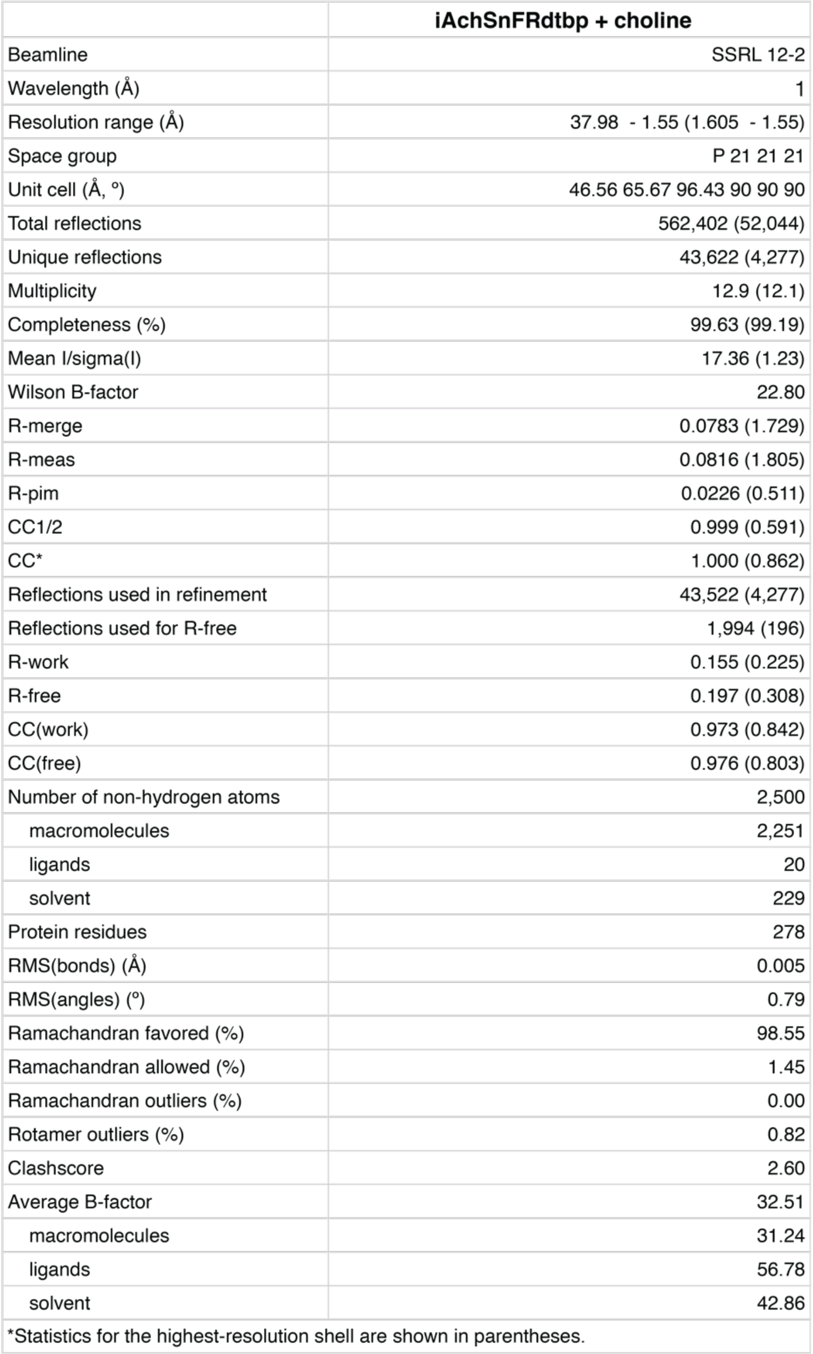

	iAchSnFRdtbp + choline
Beamline	SSRL 12-2
Wavelength (Å)	1
Resolution range (Å)	37.98 - 1.55 (1.605 - 1.55)
Space group	P 21 21 21
Unit cell (Å, °)	46.56 65.67 96.43 90 90 90
Total reflections	562,402 (52,044)
Unique reflections	43,622 (4,277)
Multiplicity	12.9 (12.1)
Completeness (%)	99.63 (99.19)
Mean I/sigma(I)	17.36 (1.23)
Wilson B-factor	22.80
R-merge	0.0783 (1.729)
R-meas	0.0816 (1.805)
R-pim	0.0226 (0.511)
CC1/2	0.999 (0.591)
CC*	1.000 (0.862)
Reflections used in refinement	43,522 (4,277)
Reflections used for R-free	1,994 (196)
R-work	0.155 (0.225)
R-free	0.197 (0.308)
CC(work)	0.973 (0.842)
CC(free)	0.976 (0.803)
Number of non-hydrogen atoms	2,500
macromolecules	2,251
ligands	20
solvent	229
Protein residues	278
RMS(bonds) (Å)	0.005
RMS(angles) (°)	0.79
Ramachandran favored (%)	98.55
Ramachandran allowed (%)	1.45
Ramachandran outliers (%)	0.00
Rotamer outliers (%)	0.82
Clashscore	2.60
Average B-factor	32.51
macromolecules	31.24
ligands	56.78
solvent	42.86
*Statistics for the highest-resolution shell are shown in parentheses.	

Table 8. Data collection and refinement statistics for iAChSnFRdtbp with acetylcholine bound

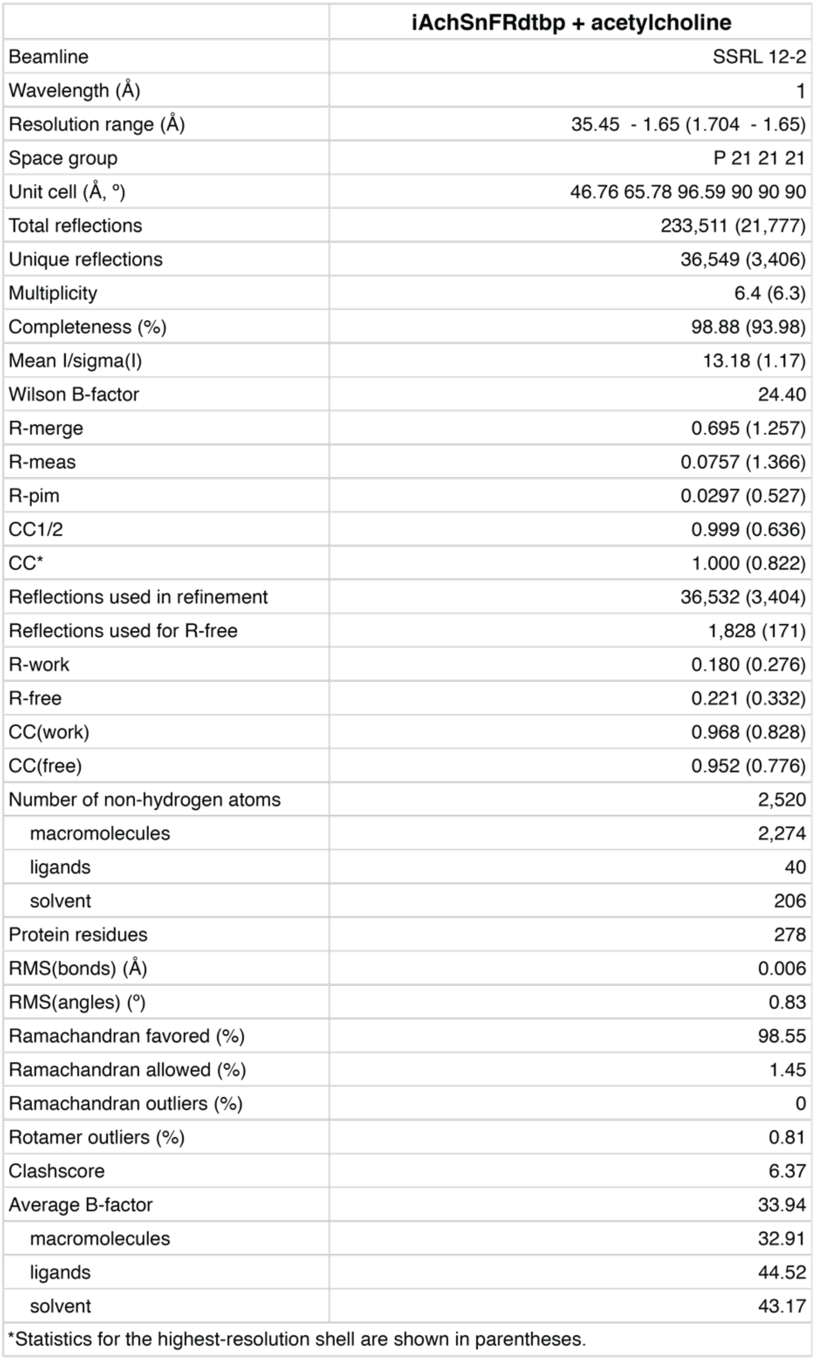

	iAchSnFRdtbp + acetylcholine
Beamline	SSRL 12-2
Wavelength (Å)	1
Resolution range (Å)	35.45 - 1.65 (1.704 - 1.65)
Space group	P 21 21 21
Unit cell (Å, °)	46.76 65.78 96.59 90 90 90
Total reflections	233,511 (21,777)
Unique reflections	36,549 (3,406)
Multiplicity	6.4 (6.3)
Completeness (%)	98.88 (93.98)
Mean I/sigma(I)	13.18 (1.17)
Wilson B-factor	24.40
R-merge	0.695 (1.257)
R-meas	0.0757 (1.366)
R-pim	0.0297 (0.527)
CC1/2	0.999 (0.636)
CC*	1.000 (0.822)
Reflections used in refinement	36,532 (3,404)
Reflections used for R-free	1,828 (171)
R-work	0.180 (0.276)
R-free	0.221 (0.332)
CC(work)	0.968 (0.828)
CC(free)	0.952 (0.776)
Number of non-hydrogen atoms	2,520
macromolecules	2,274
ligands	40
solvent	206
Protein residues	278
RMS(bonds) (Å)	0.006
RMS(angles) (°)	0.83
Ramachandran favored (%)	98.55
Ramachandran allowed (%)	1.45
Ramachandran outliers (%)	0
Rotamer outliers (%)	0.81
Clashscore	6.37
Average B-factor	33.94
macromolecules	32.91
ligands	44.52
solvent	43.17

*Statistics for the highest-resolution shell are shown in parentheses.

Table 9. Data collection and refinement statistics for iAChSnFRdtbp apo structure

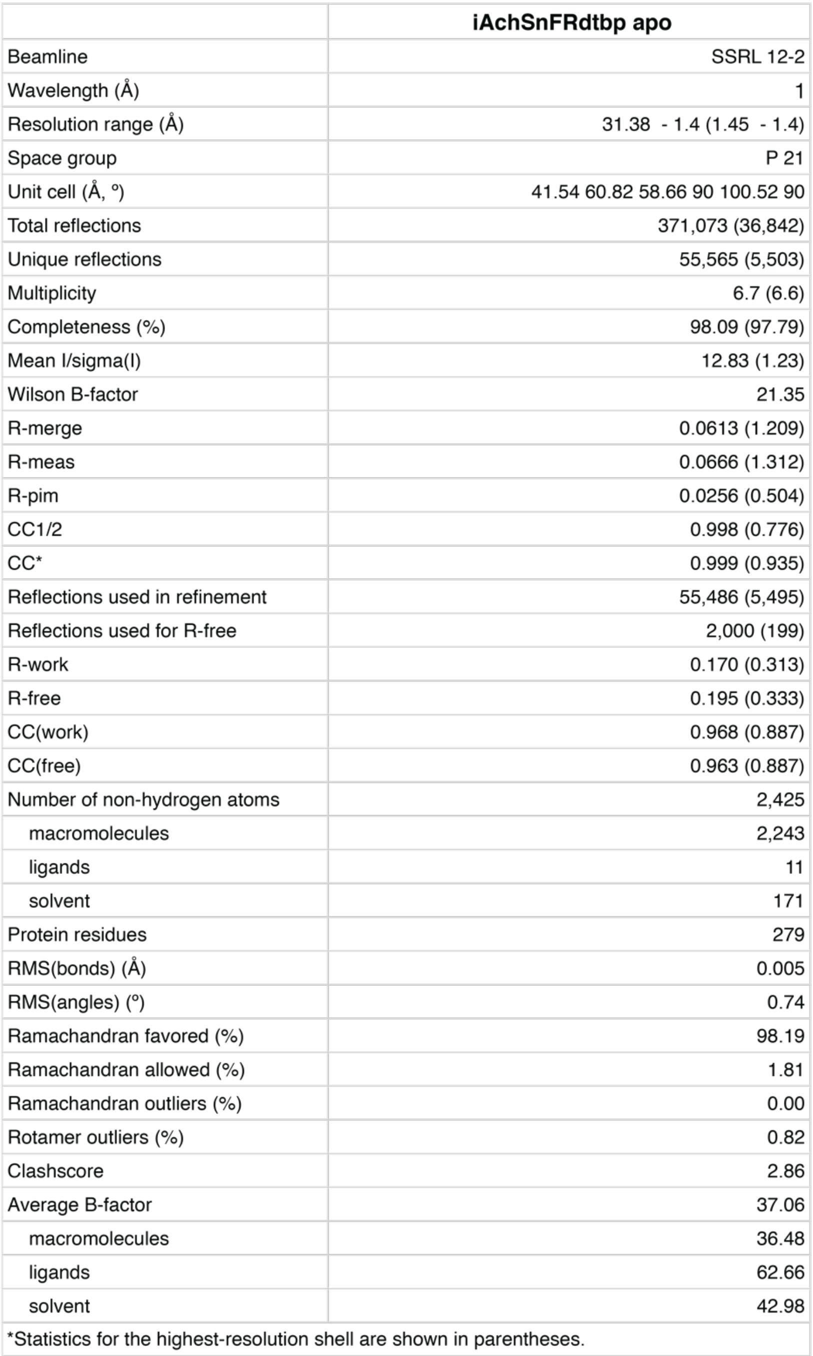

	iAchSnFRdtbp apo
Beamline	SSRL 12-2
Wavelength (Å)	1
Resolution range (Å)	31.38 - 1.4 (1.45 - 1.4)
Space group	P 21
Unit cell (Å, º)	41.54 60.82 58.66 90 100.52 90
Total reflections	371,073 (36,842)
Unique reflections	55,565 (5,503)
Multiplicity	6.7 (6.6)
Completeness (%)	98.09 (97.79)
Mean I/sigma(I)	12.83 (1.23)
Wilson B-factor	21.35
R-merge	0.0613 (1.209)
R-meas	0.0666 (1.312)
R-pim	0.0256 (0.504)
CC1/2	0.998 (0.776)
CC*	0.999 (0.935)
Reflections used in refinement	55,486 (5,495)
Reflections used for R-free	2,000 (199)
R-work	0.170 (0.313)
R-free	0.195 (0.333)
CC(work)	0.968 (0.887)
CC(free)	0.963 (0.887)
Number of non-hydrogen atoms	2,425
macromolecules	2,243
ligands	11
solvent	171
Protein residues	279
RMS(bonds) (Å)	0.005
RMS(angles) (º)	0.74
Ramachandran favored (%)	98.19
Ramachandran allowed (%)	1.81
Ramachandran outliers (%)	0.00
Rotamer outliers (%)	0.82
Clashscore	2.86
Average B-factor	37.06
macromolecules	36.48
ligands	62.66
solvent	42.98

*Statistics for the highest-resolution shell are shown in parentheses.

5.8 References

Adams, P. D., P. V. Afonine, G. Bunkoczi, V. B. Chen, I. W. Davis, N. Echols, J. J. Headd, L. W. Hung, G. J. Kapral, R. W. Grosse-Kunstleve, A. J. McCoy, N. W. Moriarty, R. Oeffner, R. J. Read, D. C. Richardson, J. S. Richardson, T. C. Terwilliger, and P. H. Zwart. 2010. “PHENIX: A comprehensive Python-based system for macromolecular structure solution.” *Acta Crystallographica D Biological Crystallography* 66 (Pt 2):213-21. doi: 10.1107/S0907444909052925.

Borden, Philip M., Peng Zhang, Amol V. Shivange, Jonathan S. Marvin, Joseph Cichon, Chuntao Dan, Kaspar Podgorski, Antonio Figueiredo, Ondrej Novak, Masashi Tanimoto, Eiji Shigetomi, Mark A. Lobas, Hyuntae Kim, Paula K. Zhu, Yajun Zhang, W. Sharon Zheng, ChengCheng Fan, Guangfu Wang, Bowen Xiang, Li Gan, Guang-Xian Zhang, Kaiming Guo, Li Lin, Yuan Cai, Andrew G. Yee, Abhi Aggarwal, Christopher P. Ford, Douglas C. Rees, Dirk Dietrich, Baljit S. Khakh, Jeremy S. Dittman, Wen-Biao Gan, Minoru Koyama, Vivek Jayaraman, Joseph F. Cheer, Henry A. Lester, J. Julius Zhu, and Loren L. Looger. 2020. “A fast genetically encoded fluorescent sensor for faithful *in vivo* acetylcholine detection in mice, fish, worms and flies.” doi: 10.1101/2020.02.07.939504.

Brejc, K., T. K. Sixma, P. A. Kitts, S. R. Kain, R. Y. Tsien, M. Ormo, and S. J. Remington. 1997. “Structural basis for dual excitation and photoisomerization of the *Aequorea victoria* green fluorescent protein.” *Proceedings of the National Academy of Sciences of the United States of America* 94 (6):2306-11.

Elmore, D. E., and D. A. Dougherty. 2000. “A computational study of nicotine conformations in the gas phase and in water.” *Journal of Organic Chemistry* 65 (3):742-7. doi: 10.1021/jo991383q.

Emsley, P., B. Lohkamp, W. G. Scott, and K. Cowtan. 2010. “Features and development of Coot.” *Acta Crystallographica D Biological Crystallography* 66 (Pt 4):486-501. doi: 10.1107/S0907444910007493.

Kabsch, W. 2010. “Xds.” *Acta Crystallographica D Biological Crystallography* 66 (Pt 2):125-32. doi: 10.1107/S0907444909047337.

Marvin, J. S., B. G. Borghuis, L. Tian, J. Cichon, M. T. Harnett, J. Akerboom, A. Gordus, S. L. Renninger, T. W. Chen, C. I. Bargmann, M. B. Orger, E. R. Schreiter, J. B. Demb, W. B.

Gan, S. A. Hires, and L. L. Looger. 2013. “An optimized fluorescent probe for visualizing glutamate neurotransmission.” *Nature Methods* 10 (2):162-70. doi: 10.1038/nmeth.2333.

Marvin, J. S., B. Scholl, D. E. Wilson, K. Podgorski, A. Kazemipour, J. A. Muller, S. Schoch, F. J. U. Quiroz, N. Rebola, H. Bao, J. P. Little, A. N. Tkachuk, E. Cai, A. W. Hantman, S. S. Wang, V. J. DePiero, B. G. Borghuis, E. R. Chapman, D. Dietrich, D. A. DiGregorio, D. Fitzpatrick, and L. L. Looger. 2018. “Stability, affinity, and chromatic variants of the glutamate sensor iGluSnFR.” *Nature Methods* 15 (11):936-939. doi: 10.1038/s41592-018-0171-3.

Marvin, J. S., E. R. Schreiter, I. M. Echevarria, and L. L. Looger. 2011. “A genetically encoded, high-signal-to-noise maltose sensor.” *Proteins* 79 (11):3025-36. doi: 10.1002/prot.23118.

Nakai, J., M. Ohkura, and K. Imoto. 2001. “A high signal-to-noise Ca$^{(2+)}$ probe composed of a single green fluorescent protein.” *Nature Biotechnology* 19 (2):137-41. doi: 10.1038/84397.

Ormo, M., A. B. Cubitt, K. Kallio, L. A. Gross, R. Y. Tsien, and S. J. Remington. 1996. “Crystal structure of the *Aequorea victoria* green fluorescent protein.” *Science* 273 (5280):1392-5.

Shivange, A. V., P. M. Borden, A. K. Muthusamy, A. L. Nichols, K. Bera, H. Bao, I. Bishara, J. Jeon, M. J. Mulcahy, B. Cohen, S. L. O'Riordan, C. Kim, D. A. Dougherty, E. R. Chapman, J. S. Marvin, L. L. Looger, and H. A. Lester. 2019. “Determining the pharmacokinetics of nicotinic drugs in the endoplasmic reticulum using biosensors.” *Journal of General Physiology* 151 (6):738-757. doi: 10.1085/jgp.201812201.

Studier, F. William. 2005. “Protein production by auto-induction in high-density shaking cultures.” *Protein Expression and Purification* 41 (1):207-234. doi: 10.1016/j.pep.2005.01.016.

Tsien, R. Y. 1998. “The green fluorescent protein.” *Annual Review of Biochemistry* 67:509-44. doi: 10.1146/annurev.biochem.67.1.509.

Winn, M. D., C. C. Ballard, K. D. Cowtan, E. J. Dodson, P. Emsley, P. R. Evans, R. M. Keegan, E. B. Krissinel, A. G. Leslie, A. McCoy, S. J. McNicholas, G. N. Murshudov, N. S.

Pannu, E. A. Potterton, H. R. Powell, R. J. Read, A. Vagin, and K. S. Wilson. 2011. "Overview of the CCP4 suite and current developments." *Acta Crystallographica D Biological Crystallography* 67 (Pt 4):235-42. doi: 10.1107/S0907444910045749.

Yamaguchi, Y., Y. Shimohigashi, T. Chijiwa, M. Nakai, T. Ogawa, S. Hattori, and M. Ohno. 2001. "Characterization, amino acid sequence and evolution of edema-inducing, basic phospholipase A_2 from *Trimeresurus flavoviridis* venom." *Toxicon* 39 (7):1069-76. doi: 10.1016/s0041-0101(00)00250-6.

Appendix

METHODS

6.1 *Na*Atm1 Purification

Two different methods were used for *Na*Atm1 purification; a flowchart of the two methods is shown in Figure 1. The first method involves membrane isolation. To isolate the membrane fraction, cells were first homogenized in lysis buffer to a final concentration of 0.1g cells per ml, with the lysis buffer containing 100 mM NaCl, 20 mM Tris pH7.5, DNase, lysozyme, and protease inhibitor. The cells were lysed with a microfluidizer with three passages. The lysate was spun down at ~10,000x g at 4˚C to remove cell debris and unlysed cells. The supernatant was taken and ultracentrifuged at ~125,000x g for an hour to isolate the membrane. The resulting supernatant was discarded, and the membrane pellet was washed with cold buffer containing 100 mM NaCl and 20 mM Tris, pH 7.5. The membrane pellet was resuspended in the same buffer to a final concentration of 100 mg membrane per ml. To store the membrane, aliquots of the resuspended membrane could be flash-frozen in liquid nitrogen and stored at -80 °C. For purification, the membrane could also further be solubilized with 1% detergent (final concentration) with stirring at 4˚ for an hour before ultracentrifugation again at ~113,000x g to remove the unsolubilized membrane. This supernatant from ultracentrifugation was subsequently loaded onto a pre-wash NiNTA column with 100 mM NaCl, 20 mM Tris, pH 7.5, 50 mM imidazole, pH 7.5 and 0.1% detergent. Elution was carried out with the same buffer containing 350 mM imidazole, pH 7.5. The eluent was then directly loaded onto HiLoad Superdex 200 16/60 (GE Healthcare) for gel filtration chromatography. Peak fractions were collected and concentrated with Amicon concentrator (EMD Millipore) with 100 kDa cutoff to ~20 mg/ml.

The second method involves lysis through detergent solubilization. 1% detergent was directly added to the resuspended cells in lysis buffer along with DNase, lysozyme, and protease inhibitor. The mixture was then stirred at 4˚C for three hours to solubilize the cells. The lysate was spun down at ~113,000x g at 4˚C to remove the unlysed cells and cell debris. The supernatant was then purified with NiNTA and gel filtration chromatography as described earlier. One point worth noting in this method is the choice of detergent. Not all detergents will solubilize the cells well.

6.2 Disulfide Crosslinking

Disulfide crosslinks were separately introduced near the Walker-B motif as described in Chapter 2. As the native *Na*Atm1 is cysteine-less, no reducing agent was used during purification. The crosslinking variants were all handled in the presence of reducing agent until crosslinking. Briefly, the cells were solubilized in lysis buffer containing 100 mM NaCl, 20 mM Tris pH7.5, DNase, lysozyme, protease inhibitor, 5 mM β-mercaptoethanol (BME), 0.5% n-dodecyl-β-D-maltopyranoside (DDM), and 0.5% octaethylene glycol monododecyl ether (C12E8) with stirring at 4˚C for three hours. The unlysed cells and cell debris were removed by ultracentrifugation at ~113,000x g. The supernatant was loaded onto a pre-wash NiNTA column with 100 mM NaCl, 20 mM Tris, pH 7.5, 50 mM imidazole, pH 7.5, 5 mM BME, 0.05% DDM, and 0.05% C12E8 and eluted with the same buffer containing 350 mM imidazole, pH 7.5 instead. The eluent was then subjected to desalting into 100 mM NaCl, 20 mM Tris, pH 7.5, 0.05% of DDM, and 0.05% C12E8. The desalted protein was then crosslinked with 1 mM Cu (II) (1,10-phenanthroline)$_3$ for an hour at 4˚C. The crosslinked sample was again desalted into the same buffer to remove the oxidant. The desalted sample was then concentrated and subjected to gel filtration chromatography with HiLoad Superdex 200 16/60 (GE Healthcare).

During the process of disulfide crosslinking optimization, we tried to improve the crosslinking efficiency by using different oxidants, altering the reaction pH, changing the reaction temperature, adding of nucleotides and/or substrates, and introducing bulky side-chain mutations or other functional (substrate and/or ATP binding) mutants, yet none of them seem to improve the crosslinking yield significantly. We further tried to separate the crosslinked and uncrosslinked products by affinity purification, ion exchange, and size exclusion chromatography, but due to the small molecular differences between the two populations, none of the above methods were able to separate the two populations. We further saw that the use of different detergent and detergent combinations would also affect the crosslinking efficiency (Figure 2), the presence of the two populations was clearly shown in the denaturing SDS-PAGE and the non-denaturing BN (blue native)-PAGE (Figure 2).

6.3 Small Scale Detergent Screen

For *Na*Atm1 detergent screen, nine different detergents from different detergent classes were chosen, including n-dodecyl-β-D-maltopyranoside (DDM), n-decyl-β-D-maltopyranoside (DM), n-nonyl-β-D-glucopyranoside (NG), n-octyl-β-D-glucopyranoside (OG), 5-cyclohexyl-1-pentyl-β-D-maltopyranoside (Cymal5), n-dodecyl-N,N-dimethylglycine (DDMG), octaethylene glycol monododecyl ether (C12E8), 3-[(3-cholamidopropyl)dimethylammonio]-2-hydroxy-1-propanesulfonate (CHAPSO), and n-dodecylphoscholine (FC12). All detergent solutions were prepared at 10% (w/v), and made into detergent mixtures with two, three, or four components to a final concentration of 10% using equivalent amounts of individual detergents (Table 1). 95 detergent mixtures were made and combined with a previously used detergent mixture (CHAPSO, OG, LDAO, and HEGA11) (Lee et al. 2014) into a detergent screen in 96-block format. The subsequent experiments were all done in a 96-well block format. The isolated membrane (90 μl of stock at 100 mg membrane/ml) was solubilized with 1% detergent (10 μl of 10% stock in 96-well block) for an hour at 4°C. The solubilized sample was then ultracentrifuged at ~192,000x g to remove the unsolubilized membrane. The supernatants were taken and prepared for SDS-PAGE. The results from this detergent extraction test were scored on a 0 to 3 scoring system (Figure 3a).

In a separate setting, the 96-well block was subjected to centrifugation at ~1,500x g to remove the cell debris. The supernatants were directly loaded onto a pre-washed NiNTA resin with buffer containing 100 mM NaCl, 20 mM Tris, pH 7.5, 50 mM imidazole, pH 7.5, and 0.1% detergent. The resin was washed with 10x column volumes of the same buffer and eluted with 3 column volumes of the same buffer containing 350 mM imidazole, pH 7.5 instead. The eluents were collected and ultracentrifuged at ~192,000x g. The supernatants were then subjected to dynamic light scattering to check monodispersity. Samples of the NiNTA eluents and supernatants were both analyzed by running on SDS-PAGE to check for sample quality. The results from this small scale NiNTA test were then scored on a 1 to 3 scoring system (Figure 3b). As a starting point for crystallization, the detergents or detergent mixtures with the highest total score were used to extract and purify *Na*Atm1 (Figure 3c).

6.4 Enzymatic ATPase Assay

In addition to the colorimetric ATPase activity assays described in Chapter 2 and 3, the ATPase activities of *Na*Atm1 were measured using an enzymatic quantification method. Limitations of this method include its non-applicability to proteoliposomes samples due to the scattering of proteoliposomes and its non-equimolar concentrations of Mg^{2+} and ATP in the initial reactions. The ATPase activity data obtained using this method was not used in any publication.

In this method, the ATPase activity was determined by measuring the amount of free phosphate generated upon ATP hydrolysis with the EnzCheck Phosphatase Assay kit (ThermoFisher Scientific) in a 96-well plate format by following the previous protocol (Lee et al. 2014). All reactions were done in 100 μL scale using 1 mg protein per reaction in 100 mM NaCl, 20 mM Tris, pH 7.5, 5 mM EDTA, and 0.3% w/v CHAPSO at various concentrations of ATP, pH 7.5. The reactions were initiated by the addition of 10 mM final concentration of $MgCl_2$. Reactions were done in triplicates, and monitored for 40-60 minutes, and the final linear rates obtained from the early timepoints were fitted with nonlinear least squares fit using Prism 8. This enzymatic assay was performed for all the cysteine crosslinking variants (*Na*A527C, *Na*S526C, and *Na*T525C), the ATP hydrolysis deficient variant *Na*E523Q, and the wild type protein *Na*Atm1 in detergent (Figure 4).

6.5 Figures

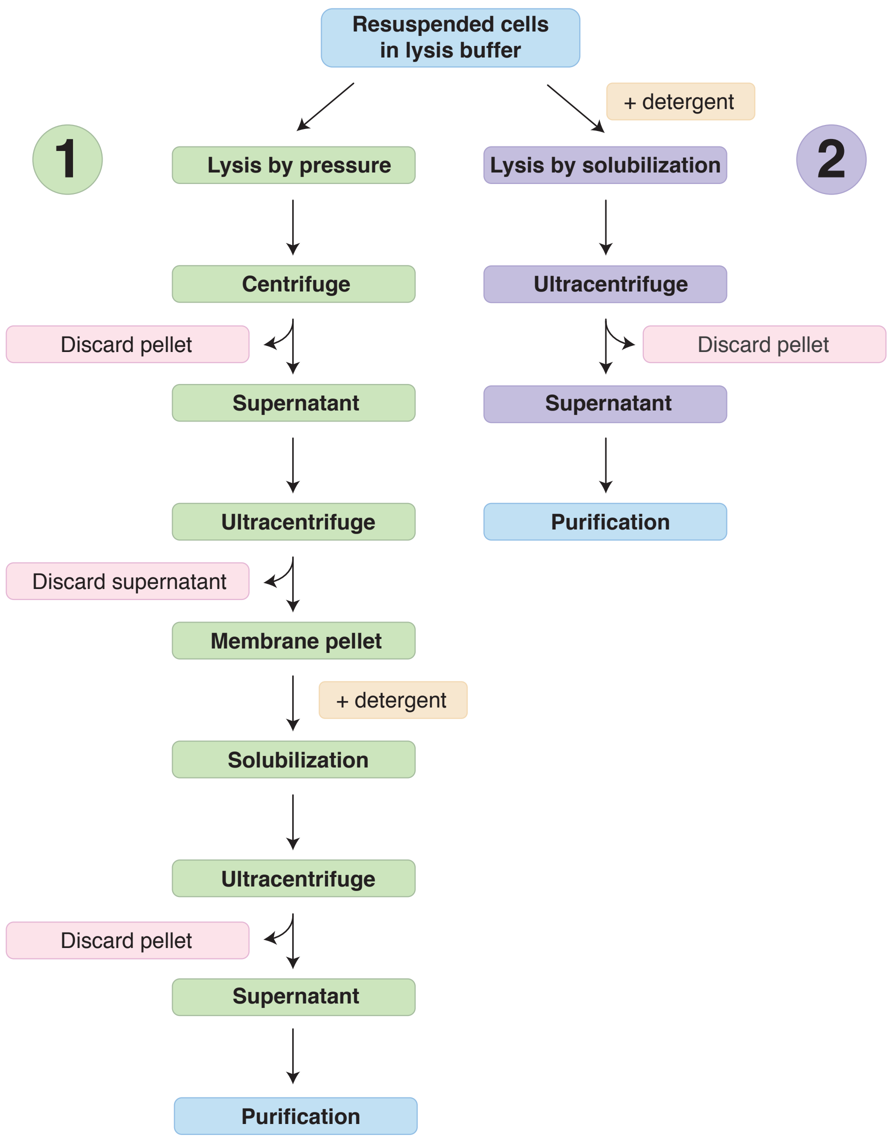

Figure 1. Membrane protein purification.

Schematic showing the two main membrane purification protocols used for *Na*Atm1 with method 1) involving membrane isolation, and method 2) involving lysis through solubilization using detergent.

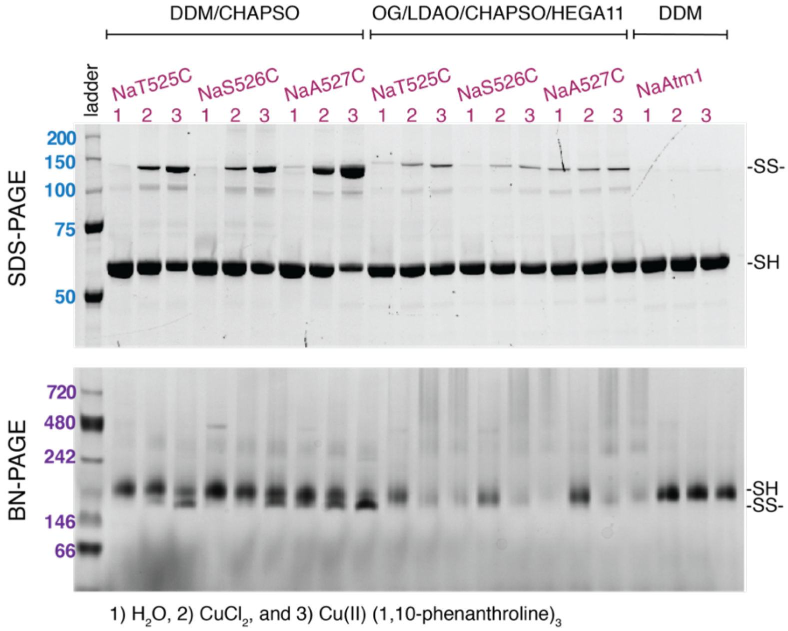

Figure 2. Polyacrylamide gel electrophoresis.

Top: SDS-PAGE showing disulfide crosslinking of different variants, purified in different detergent combinations. Bottom: BN-PAGE showing the crosslinked and uncrosslinked population with different migration features. (Note: presence of LDAO has effects on sample migration in BN-PAGE).

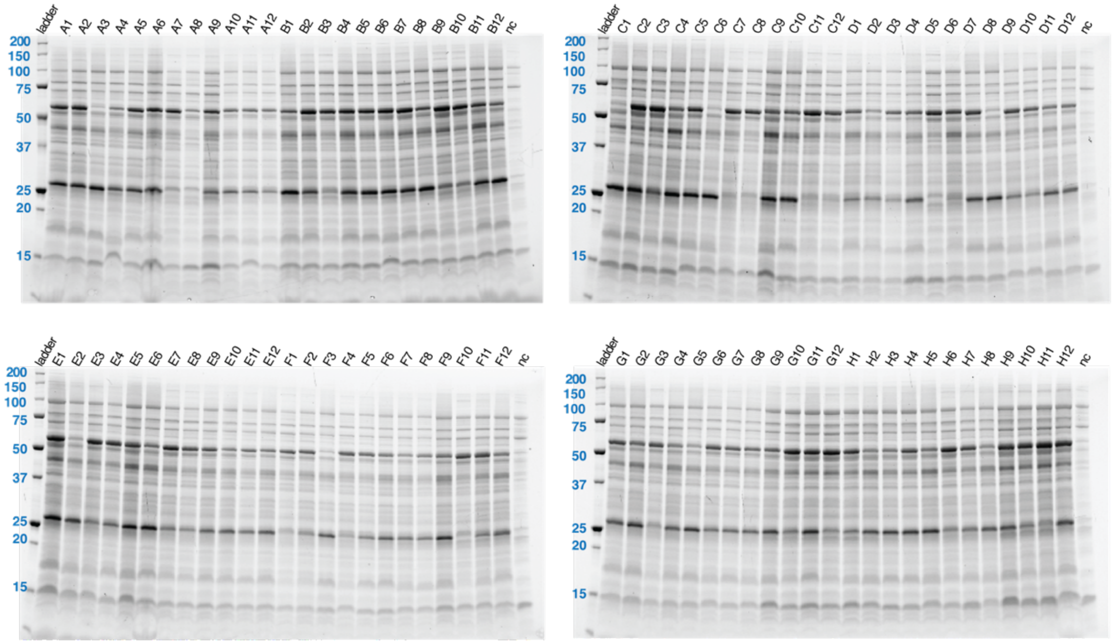

Figure 3. Small scale detergent extraction.

Extraction with 96 detergent mixtures from Table 1. Each lane is labeled with the corresponding well number with "nc" standing for negative control with ddH_2O addition for extraction instead of detergent.

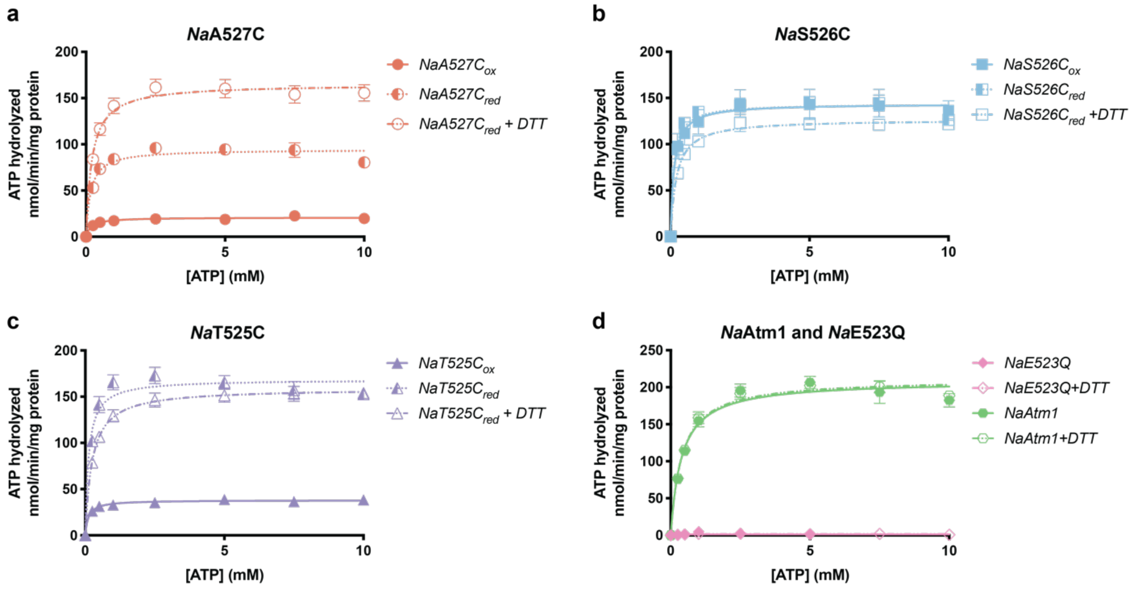

Figure 4. Enzymatic ATPase assay.

ATPase activities measured for (**a**) *Na*A527C, (**b**) *Na*S526C, and (**a**) *Na*T525C in crosslinked protein during purification (ox), reduced protein after purification (red), and the reduced protein with addition reducing agent (red + DTT (dithiothreitol)). (**d**) *Na*Atm1 and *Na*E523Q ATPase activities in the presence and absence of DTT as both constructs do not have cysteines.

6.6 Tables

Table 1. Detergent screen composition.

The screen was made from nine different individual detergents. The different detergent mixtures contain equal amounts of each detergent component, with a total concentration of 10% (w/v). The numbers (1-9) in the block represent individual detergents shown below the table.

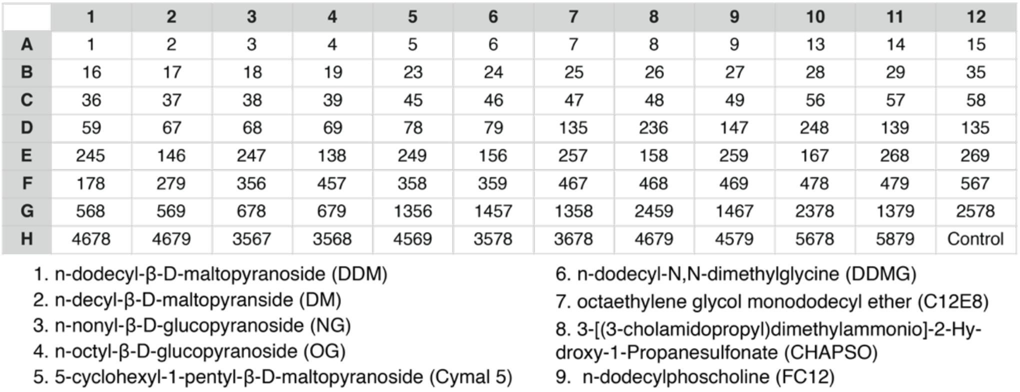

	1	2	3	4	5	6	7	8	9	10	11	12
A	1	2	3	4	5	6	7	8	9	13	14	15
B	16	17	18	19	23	24	25	26	27	28	29	35
C	36	37	38	39	45	46	47	48	49	56	57	58
D	59	67	68	69	78	79	135	236	147	248	139	135
E	245	146	247	138	249	156	257	158	259	167	268	269
F	178	279	356	457	358	359	467	468	469	478	479	567
G	568	569	678	679	1356	1457	1358	2459	1467	2378	1379	2578
H	4678	4679	3567	3568	4569	3578	3678	4679	4579	5678	5879	Control

1. n-dodecyl-β-D-maltopyranoside (DDM)
2. n-decyl-β-D-maltopyranside (DM)
3. n-nonyl-β-D-glucopyranoside (NG)
4. n-octyl-β-D-glucopyranoside (OG)
5. 5-cyclohexyl-1-pentyl-β-D-maltopyranoside (Cymal 5)
6. n-dodecyl-N,N-dimethylglycine (DDMG)
7. octaethylene glycol monododecyl ether (C12E8)
8. 3-[(3-cholamidopropyl)dimethylammonio]-2-Hydroxy-1-Propanesulfonate (CHAPSO)
9. n-dodecylphoscholine (FC12)

Table 2. Small scale detergent screen results.

(**a**) Manually scored small scale extraction results on a 0-3 scoring system, with 3 representing good, 2 representing ok, 1 representing bad, and 0 representing terrible extractions. (**b**) Manually scored small scale NiNTA purification results on a 1-3 scoring system, with 3 representing good, 2 representing ok, and 1 representing bad. (**c**) Total scores from both tests, shown in (**a**) and (**b**).

a

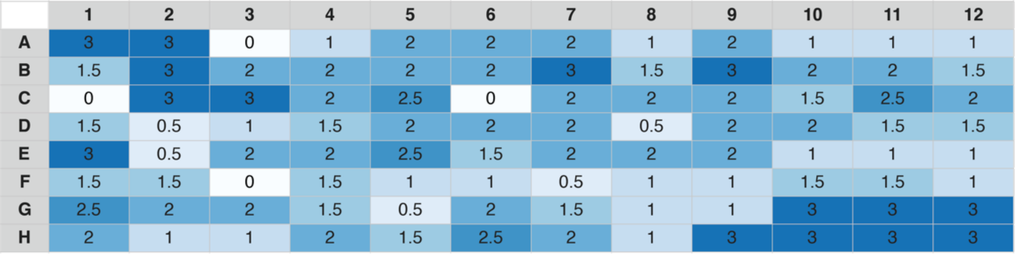

	1	2	3	4	5	6	7	8	9	10	11	12
A	3	3	0	1	2	2	2	1	2	1	1	1
B	1.5	3	2	2	2	2	3	1.5	3	2	2	1.5
C	0	3	3	2	2.5	0	2	2	2	1.5	2.5	2
D	1.5	0.5	1	1.5	2	2	2	0.5	2	2	1.5	1.5
E	3	0.5	2	2	2.5	1.5	2	2	2	1	1	1
F	1.5	1.5	0	1.5	1	1	0.5	1	1	1.5	1.5	1
G	2.5	2	2	1.5	0.5	2	1.5	1	1	3	3	3
H	2	1	1	2	1.5	2.5	2	1	3	3	3	3

b

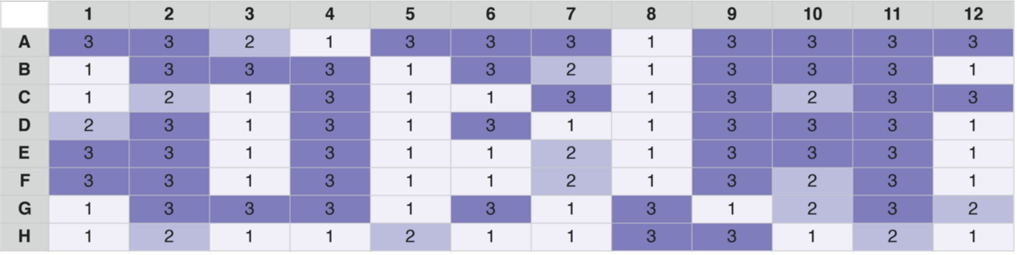

	1	2	3	4	5	6	7	8	9	10	11	12
A	3	3	2	1	3	3	3	1	3	3	3	3
B	1	3	3	3	1	3	2	1	3	3	3	1
C	1	2	1	3	1	1	3	1	3	2	3	3
D	2	3	1	3	1	3	1	1	3	3	3	1
E	3	3	1	3	1	1	2	1	3	3	3	1
F	3	3	1	3	1	1	2	1	3	2	3	1
G	1	3	3	3	1	3	1	3	1	2	3	2
H	1	2	1	1	2	1	1	3	3	1	2	1

c

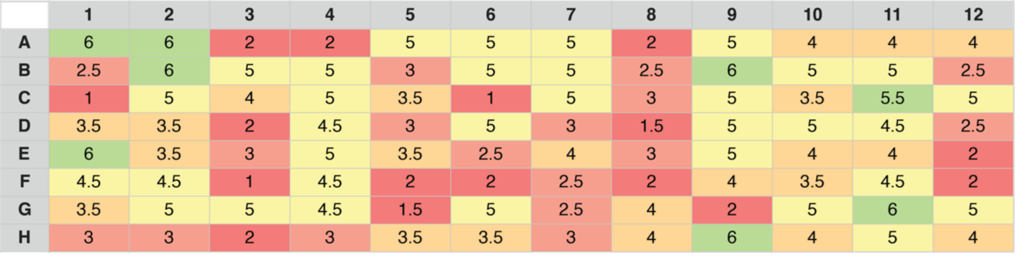

	1	2	3	4	5	6	7	8	9	10	11	12
A	6	6	2	2	5	5	5	2	5	4	4	4
B	2.5	6	5	5	3	5	5	2.5	6	5	5	2.5
C	1	5	4	5	3.5	1	5	3	5	3.5	5.5	5
D	3.5	3.5	2	4.5	3	5	3	1.5	5	5	4.5	2.5
E	6	3.5	3	5	3.5	2.5	4	3	5	4	4	2
F	4.5	4.5	1	4.5	2	2	2.5	2	4	3.5	4.5	2
G	3.5	5	5	4.5	1.5	5	2.5	4	2	5	6	5
H	3	3	2	3	3.5	3.5	3	4	6	4	5	4

6.7 References

Lee, J. Y., J. G. Yang, D. Zhitnitsky, O. Lewinson, and D. C. Rees. 2014. "Structural basis for heavy metal detoxification by an Atm1-type ABC exporter." *Science* 343 (6175):1133-6. doi: 10.1126/science.1246489.